UNIVERSITY OF CALIFORNIA, SAN DIEGO

Patient-specific Computational Models of Dyssynchronous Heart Failure and Cardiac Resynchronization Therapy for Clinical Diagnosis and Decision Support

A dissertation submitted in partial satisfaction of the
requirements for the degree
Doctor of Philosophy

in

Bioengineering with specialization in Multi-scale Biology

by

Christopher T. Villongco

Committee in charge:

Professor Andrew D. McCulloch, Chair
Professor Jeffrey H. Omens, Co-Chair
Professor Lawrence R. Frank
Professor David E. Krummen
Professor Alison L. Marsden
Professor John T. Watson

2015

The dissertation of Christopher T. Villongco is approved, and it is acceptable in quality and form for publication on microfilm and electronically:

_____

_____

_____

_____

_____
Co-Chair

_____
Chair

University of California, San Diego

2015

DEDICATION

To my loving family – David, Isabel, and Michael.

EPIGRAPH

There is something in humility which strangely exalts the heart.

— St. Augustine of Hippo (354 A.D. – 430 A.D.)

TABLE OF CONTENTS

LIST OF FIGURES

LIST OF TABLES

ACKNOWLEDGEMENTS

The content of Chapter 1 comprises an original document.

The content of Chapter 2 comprises an original document. The author gives thanks to Andrew McCulloch, Adarsh Krishnamurthy, Jeffrey Omens, and Matthew Gonzales for discussions and suggestions regarding finite element modeling, as well as to David Krummen for discussions on clinical imaging.

The content of Chapter 3 has been modified from a peer-reviewed publication to reflect the author's contribution to the work; the citation is Krishnamurthy A, Villongco CT, Chuang J, Frank LR, Nigam V, Belezzuoli E, Stark P, Krummen DE, Narayn S, Omens JH, McCulloch AD, Kerckhoffs RCP, "Patient-specific models of cardiac biomechanics," *Journal of Computational Physics* 2013. The author is indebted to Elliot Howard for performing the diffusion-weighted magnetic resonance scan of the excised human heart, and to Lawrence Frank and his research group for developing the diffusion-weighted magnetic resonance pulse sequence and image reconstruction algorithms and resources that resulted in a pristine human fiber data set. Thanks is also given to Andrew McCulloch for developing the ideas regarding the implementation of the diffusion tensor material coordinate model.

The majority of the content of Chapter 4 comprises an original document. The results and analysis of convergence of patient-specific electrophysiology simulations were performed by Kevin Vincent and appear in a manuscript in preparation; the citation is: Vincent K, Gonzales M, Gillette A, Villongco CT, Pezzuto S, Omens JH, Holst M, McCulloch AD, "High-order interpolation methods for cardiac monodomain simulations," *Frontiers Physiology, in review*, 2015. The author gives thanks to Matthew Gonzales and Andrew McCulloch for discussions regarding cardiac electrophysiology.

The content of Chapter 5 comprises the full content of a peer-reviewed publication; the citation is Villongco CT, Krummen DE, Stark P, Omens JH, McCulloch AD, "Patient-specific modeling of ventricular activation pattern using surface ECG-derived vectorcardiogram in bundle branch block," *Progress in Biophysics and Molecular Biology*, 2014. The author gives thanks to David Krummen, Alison Marsden, and Andrew McCulloch for discussions and suggestions regarding electrophysiology clinical data interpretation, modeling, and optimization strategies.

The content of Chapter 6 comprises a draft of a manuscript in preparation with shared first authorship; the citation is: Krishnamurthy A*, Villongco CT*, Krummen DE, Stark P, Kerckhoffs RCP, Omens JH, McCulloch AD. Cardiac resynchronization therapy reduces negative myocardial work in patient-specific models of dyssynchronous heart failure. *Science Translational Medicine, in preparation*, 2015. The author gives thanks to Adarsh Krishnamurthy, David Krummen, Jeffery Omens, and Andrew McCulloch for discussions and suggestions regarding clinical data interpretation, study design, modeling, and results analysis.

The majority of the content of Chapter 7 comprises an original document. The author is especially grateful to Valeriya Naumova for authoring the Methods section "Kernel-based regularization learning algorithm" in this chapter, developing the original mathematical theory, performing the analysis, and producing the prediction results. Model simulation data was provided by the author as inputs to the algorithm. The author gives thanks to Andrew McCulloch and David Krummen for discussions on clinical data and model considerations.

Thanks is given to the numerous doctors and staff at the Veteran's Administration Hospital. Gratuitous thanks to David Krummen and technicians of the electrophysiology catheter laboratory, Paul Stark and technicians of the radiology department, and technicians of the cardiac echocardiography lab, and all other workers at the Veteran's Administration Hospital for patiently providing the clinical data and expert advice in interpretation and processing. It was through their expert skill and support that enable cultivation of new collaborations between clinical practice and bioengineering research for the development of translational technologies to improve patient care.

Thanks to my colleagues and friends who have supported me through this most intellectually, creatively, and personally stimulating and challenging years of my life. Finally, thanks to my family for bearing witness to a relationship of unconditional love which is the source of fullness of liberty, life, happiness, and Truth.

VITA

2008	B. S. in Mechanical Engineering *magna cum laude*, Santa Clara University, Santa Clara
2011-2013	Graduate Teaching Assistant, University of California, San Diego
2012-2014	*Interfaces* Graduate Training Program with Multi-scale Biology Specialization
2015	Ph. D. in Bioengineering, University of California, San Diego

PUBLICATIONS

Krishnamurthy A*, Villongco CT*, Krummen DE, Stark P, Kerckhoffs RCP, Omens JH, McCulloch AD. Cardiac resynchronization therapy reduces negative myocardial work in patient-specific models of dyssynchronous heart failure. *Science Translational Medicine, in review*, 2015. ** indicates shared first authorship*

Vincent K, Gonzales M, Gillette A, Villongco CT, Pezzuto S, Omens JH, Holst M, McCulloch AD. High-order interpolation methods for cardiac monodomain simulations. *Frontiers Physiology, in review*, 2015.

Krishnamurthy A, Villongco CT, Beck A, Omens JH, McCulloch AD. Left ventricular diastolic and systolic material property estimation from image data. *Statistical atlases and computational models of the heart – Imaging and modelling challenges*, 2015.

Villongco CT, Krummen DE, Stark P, Omens JH, McCulloch AD. Patient-specific modeling of ventricular activation pattern using surface ECG-derived vectorcardiogram in bundle branch block. *Progress in Biophysics and Molecular Biology*, 2014.

Howard EJ, Kerckhoffs RCP, Vincent K, Krishnamurthy A, Villongco CT, Mulligan LJ, McCulloch AD, Omens JH. Myofiber prestretch magnitude determines regional systolic function during ectopic activation in the tachycardia-induced failing canine heart. *American Journal of Physiology*, 2013.

Krishnamurthy A, Villongco CT, Chuang J, Frank LR, Nigam V, Belezzuoli E, Stark P, Krummen DE, Narayn S, Omens JH, McCulloch AD, Kerckhoffs RCP. Patient-specific models of cardiac biomechanics. *Journal of Computational Physics*, 2013.

Zhang Y, Liang X, Ma J, Jing Y, Gonzales MJ, Villongco CT, Krishnamurthy A, Frank L, Stark P, Narayan SM, McCulloch AD. An atlas-based geometry pipeline for cardiac Hermite model construction and diffusion tensor reorientation. *Medical Image Analysis*, 2012.

Aguado-Sierra J, Krishnamurth A, Villongco CT, Chuang J, Howard E, Gonzales MJ, Omens J, Krummen DE, Narayan S, Kerckhoffs RCP, McCulloch AD. Patient-specific modeling of dyssynchronous heart failure: A case study. *Progress in Biophysics and Molecular Biology* 107, 147-155, 2011

ABSTRACT OF THE DISSERTATION

Patient-specific Computational Models of Dyssynchronous Heart Failure and Cardiac Resynchronization Therapy for Clinical Diagnosis and Decision Support

by

Christopher T. Villongco

Doctor of Philosophy in Bioengineering with specialization in Multi-scale Biology

University of California, San Diego, 2015

Professor Andrew D. McCulloch, Chair
Professor Jeffrey H. Omens, Co-Chair

Dyssynchronous heart failure (DHF) is a severe form of heart failure where conduction block in the left bundle branch causes delayed left ventricular electrical activation and discoordinated systolic contraction, dramatically reducing cardiac output. Cardiac resynchronization therapy (CRT) is a cost effective pacing treatment that has been shown to improve symptoms and survival, especially due to left ventricular reverse remodeling. However, approximately 50% of patients do not show objective evidence of reverse remodeling even after 6 months of CRT. A deeper understanding of the physiological mechanisms leading to positive long-term outcomes and identification of patients who are most likely to benefit are needed to maximize quality of care and mini-

mize health risks and economic costs. The ability to predict the outcome and personalize CRT application for an individual patient from clinical measurements alone is challenging given the wide inter-patient variability of clinical features and pathophysiological complexity of DHF.

In this work, we seek to answer questions regarding physiological mechanisms that are implicated in CRT response, baseline physiological features that are predictive of response, and personalized CRT application for an individual patient. For this purpose, we construct patient-specific computational models of DHF which integrate anatomical, electrophysiological, biomechanical, and hemodynamic clinical and empirical data to quantitatively characterize baseline and CRT physiology to understand how patients differ in response. The primary aims of this thesis will be to

1. construct patient-specific computational models of DHF incorporating clinical and empirical measurements to test whether the models can recapitulate characteristics of DHF and predict measured acute effects of CRT,

2. test the hypothesis that CRT response physiologically depends on the severity of baseline heterogeneity of mechanical loading caused by electrical dyssynchrony and ventricular dilation,

3. test the hypothesis that CRT response can be predicted from novel model-derived biomarkers of electrical dyssynchrony.

Through quantification and prediction of patient-specific cardiovascular physiology in disease and therapy, computational models have great potential to enhance the quality of medical care by providing novel diagnostic value to support clinical decisions regarding the best personalized approach to treat the individual patient.

Chapter 1

Introduction to the Dissertation

Abstract

In this introductory chapter, we review the physiology of heart failure, particularly dyssynchronous heart failure, and the current clinical standard of treatment. An improved understanding of the physiological mechanisms for improving dyssynchronous heart failure is urgently needed. Ineffective administration of clinical therapy increases patient risk and greater economic burdens.

We introduce the possibility of patient-specific, multi-scale computational models of dyssynchronous heart failure to serve as clinical decision support tools by elucidating the mechanisms of therapy and predicting the degree of benefit for individual patients. Computational models can incorporate a large array of clinical measurements to construct a holistic, quantitative representation of the pathophysiology and its treatment. We review computational modeling for dyssynchronous heart failure and cardiac resynchronization therapy. Finally, we set forth the aims of this dissertation work for contributing new tools and knowledge to answer questions of heart failure and treatment mechanisms by means of this new rapidly intensifying field of interdisciplinary research.

1.1 Heart Failure in the United States

The incidence of heart failure (HF) in the United States is a serious health issue amidst an epidemiological age of physical inactivity and obesity [42]. HF is suffered by an estimated 5.8 million Americans. Each year, an additional 650,000 new diagnoses are made clinically [44], and 1 million hospitalizations occur with HF as the primary diagnosis [43]. The HF mortality rate manifests in the death of about 50% of patients within 5 years of their initial diagnosis [97, 71]. HF incidence increases with age, quadrupling from 20 to 80 cases per 1,000 individuals from 65–69 years to 85 years of age [34]. At its current rate, the prevalence of HF is projected to increase by 46% to 8 million individuals over 18 years of age by 2030 [47]. By 2050, 1 in 5 Americans will have aged over 65 years into the high-risk HF group [46].

High HF incidence burdens the US health care system and the greater economy. In 2013, physician office visits alone cost $1.8 billion [44]. Hospitalizations are common after HF diagnosis, with 83% of patients hospitalized at least once and 43% hospitalized at least 4 times [117]. The mean cost of HF-related hospitalizations amounts to over $23,000 per patient [44]. Costs for diagnostic medical imaging is reported as one of the fastest growing segments of Medicare expenditures ($14 billion in 2006) with cardiovascular imaging accounting for nearly one-third of these costs [83]. Total expenditures related to HF reached $39.2 billion in costs both direct (cost of physicians and other professionals, hospital and nursing home services, prescribed medications, home health care, and other medical durables) and indirect (cost of morbidity, lost productivity, and mortality) in 2010 [72]. The greater cost of all cardiovascular disease (CVD) (including HF) and stroke was estimated at $503.2 billion during that year [72], and in 2006 CVD claimed more deaths ($\sim 800,000$) than all the leading causes of death including HIV/AIDS ($\sim 12,000$), Alzheimer's disease ($\sim 70,000$), accidents ($\sim 122,000$), and every form of cancer ($\sim 560,000$) combined [72].

HF is a complex clinical syndrome emerging from structural and functional defects in ventricular filling and/or ejection of blood. Damage or increased stress on the heart initially activates a compensatory response that provides short-term support of cardiovascular function, but over time adversely decompensates cardiac structure and function. Disorders of the cardiac pericardium, myocardium, endocardium, valves, or

great vessels or from metabolic abnormalities can lead to HF, but the majority of patients suffer from left ventricular (LV) myocardial dysfunction. An important feature of LV function is the ejection fraction (EF) defined as the relative blood volume ejected in a single beat of the filled ventricle. Normal EF ranges in 55%–70% with a total cardiac output between 4.0–8.0 L/min. HF with reduced EF (HFrEF or systolic HF) (EF$\leq$40%) affects approximately one half of all HF patients and is accompanied by varying degrees of dilated cardiomyopathy (DCM) wherein the ventricles are enlarged in size and depressed in contractility [23, 27, 59]. HF with preserved EF (HFpEF or diastolic HF) (EF$\geq$40%) affects the second half of all HF patients [85] but maintains normal ventricular size. Patients experience symptoms including dyspnea (discomfort while breathing), shortness of breath, chest pain, fatigue and reduced exercise tolerance, bloating, abdominal pain, loss of appetite, and fluid retention leading to pulmonary and splanchnic congestion and peripheral edema.

Risk factors for HF include hypertension, obesity and diabetes mellitus, metabolic syndromes, and atherosclerotic disease. Hypertension is a crucial modifiable risk factor in the US. Nearly a quarter of Americans are affected by hypertension, and the lifetime risk of developing it is >75% in the US [122]. Elevated levels of diastolic and systolic blood pressure are major risk factors for developing HF [124]. Incidence of HF is associated with higher levels of blood pressure, age, and longer duration of hypertension. Strategies to control hypertension are a vital part of public health effort to control HF. HFpEF due to hypertension and other hemodynamic complications constitute approximately 70% of cases in the US [17] and 60% worldwide, with mortality rates up to 60%. Long term treatment of systolic and diastolic hypertension reduces the risk for HF by approximately 50% [58].

1.1.1 Dyssynchronous heart failure

One third of patients with HFrEF and NYHA functional class III–IV symptoms have severely complicated dyssynchronous heart failure (DHF) due to a block in the cardiac conduction system commonly seen as left bundle branch block (LBBB). In LBBB, the left bundle branch in the interventricular septum fails to conduct intrinsic depolarizing action potentials to the LV to initiate myocardial contraction. Consequently,

depolarization begins in the RV, proceeds through the interventricular septum, and terminates in the inferior and lateral regions of the LV. The result is a significant delay (>60 ms) between the onset of LV and RV interventricular contraction [45, 125]. "Wide QRS complex" >120 ms is a primary marker for dyssynchrony introduced by LBBB [36]. Mechanical consequences of dyssynchrony include worsened LV function with increased metabolic demand, functional mitral regurgitation, paradoxical interventricular septal motion, adverse remodeling with increased LV dilation [53].

Electrical and mechanical dyssynchrony give rise to diastolic and systolic dysfunctions. Diastolic dysfunction occurs by valvular event delays. Delay of aortic valve closure results in a relative decrease in LV filling duration. Delayed depolarization or abnormal repolarization also causes contraction during early diastole, delaying mitral valve opening and shortening LV filling duration [45]. Systolic function is affected by abnormal interventricular septal wall motion resulting from abnormal pressure gradients caused by the delayed onset of contraction between the RV and LV. Abnormal septal motion increases LV end-systolic diameter and decreases the regional contribution of the septum to the ejection fraction. Delayed LV contraction following left atrial contraction may also develop an abnormal LV-LA pressure gradient leading to diastolic mitral regurgitation. Overall, these dysfunctions reduce global LV ejection fraction, cardiac output, mean arterial pressure, and the maximal rate of ventricular pressure generation $\frac{\mathrm{d}P}{\mathrm{d}t}$ [45, 21, 114]. The mechanical burden imposed by LBBB on the already-failing heart is associated with increased mortality rates in HF patients [128, 126, 9].

1.1.2 Standard clinical assessments for heart failure

The goal of clinical evaluation for HF is to determine its presence, define its underlying cause, assess its severity and the patient's prognosis, and identify comorbidities that might influence the response to treatment. The large inter-patient variation in non-specific signs and symptoms present a challenge to clinicians in making decisions for optimal treatment, and recitation of symptoms is a subjective process and an imprecise science. Clinical assessment depends on information including medical history, physical examination, laboratory test, cardiac imaging, and functional studies.

Typical clinical examinations evaluate a patient's medical and family history,

medication, diet, weight, blood pressure, body temperature, and severity of symptoms. Laboratory tests for biomarkers such as B-type natriuretic peptides (BNP) and cardiac troponins reflect various pathophysiological features of HF such as inflammation, myocardial injury, neurohormonal upregulation, and myocardial remodeling [127]. They are useful adjuncts for establishing prognosis and disease severity in chronic HF. Increasing plasma concentration of BNP's is associated with progressive worsening and reduced 5-year survival [86, 5].

Non-invasive evaluation of HF through cardiac imaging modalities involves assessments of cardiac structure and function and determining the underlying etiology to appropriately target therapies to patients. Two-dimensional (2D) transthoracic echocardiography (echo) with Doppler is the preferred imaging modality for its widespread availability, low cost, and lack of ionizing radiation. Its high temporal resolution make it an ideal technique for assessing LV geometry, volume, wall thickness, wall motion, valve function, flow patterns, and EF. Cardiac magnetic resonance (MR) and computed tomography (CT) can image the heart and surrounding structures in 3D with high spatial resolution, with the latter able to image the coronary arteries and characterize the myocardium. Structure, volume, and EF assessments can also be made, although image quality suffers at rapid heart rates. Contrast-enhanced MR and stress single-photon emission computed tomography (SPECT) are recommended for patients with known CAD to characterize myocardial ischemia, fibrosis, and viability. Invasive hemodynamic monitoring by cardiac catheterization is recommended for patients with respiratory distress or clinical evidence of impaired perfusion. Hemodynamic monitoring is indicated in patients with clinically indeterminate volume status and refractory to initial therapy, particularly if intracardiac filling pressures and cardiac output are unclear. Left heart catheterization or coronary angiography is indicated for patients with HF and LV dysfunction.

The presence and severity of HF are categorized according to the American College of Cardiology Foundation (ACCF)/American Heart Association (AHA) stages of HF [53] and the New York Heart Association (NYHA) functional classification [53, 30]. The ACCF/AHA stages characterize the development and progression of disease for individuals and populations based on risk factors and structural abnormalities. The NYHA

functional classification ranks by exercise capacity and symptomatic status in individuals. The NYHA functional classification has been shown to be an independent predictor of mortality [75] and is commonly used in clinical practice and research to determine the eligibility of patients for appropriate therapeutic strategies.

1.2 Standard Treatments for Heart Failure

In the long term, HF progresses toward gradual clinical deterioration of ventricular function. HF treatment strategies are recommended according to guideline-directed medical therapy defined by the ACCF/AHA. The aim of HF treatment is to improve a patient's health-related quality of life, especially with regards to physical ability and vitality [70, 48] by reducing risk, retarding deterioration, and even reversing progression. Reduced rates of rehospitalization and mortality are associated with increased quality of life [77, 96]. Optimal pharmacological therapy has been shown to modestly improve quality and delay HF progression [76]. At present, however, cardiac resynchronization therapy produces the best clinical outcomes [29].

1.2.1 Pharmacological therapy

Pharmacological therapy for HF primarily aims to control blood pressure. Optimal blood pressure control decreases risk of new HF by approximately 50% [11]. Pharmacological drug prescription can help improve symptoms and survival in early stages of heart failure, but without significant change in hemodynamics.

Diuretic-based antihypertensive therapy has been shown to prevent HF in wide range of target populations [109]. Diuretics aim to reduce fluid retention and alleviate hypertension by increasing urinary sodium excretion, leading to improved exercise endurance. Angiotensin-converting enzyme (ACE) inhibitors and beta antagonists are effective in prevention of HF. ACE inhibitors and beta-blocker therapy impedes maladaptive LV remodeling in patients with stage B HF and low LVEF to improve mortality and morbidity [57]. ACE inhibitors control blood pressure by increasing natriuresis and venous capacity and decreasing arteriolar resistance. Beta antagonists block epinephrine and norepinephrine stimulation of $\beta 1$ channels, reducing physical exertion

on heart rate (negative chronotropy) and force of contraction (negative inotropy). However, neither ACE inhibitors nor beta blockers as single therapies are superior to antihypertensive drugs, including calcium channel blockers, in reduction of all cardiovascular outcomes. Angiotensin-receptor blockers (ARBs) are an alternative anti-hypertensive therapy in patients intolerant of ACE inhibitor therapy. In patients with diabetes mellitus, angiotensin-converting enzyme (ACE) inhibitors and angiotensin-receptor blockers (ARBs) significantly reduce the incidence of HF in patients [133]. ACE inhibitors and ARBs can modestly improve or delay worsening of quality of life in HF [76]. However, positive outcomes of pharmacological therapy remain inconsistent.

1.2.2 Cardiac resynchronization therapy

Cardiac resynchronization therapy (CRT) aims to reduce ventricular dyssynchrony and its adverse effects by synchronous electromechanical activation using an implanted multi-site, biventricular pacing device [108, 115, 53, 6]. One pacing lead (V lead) is inserted retrograde through the coronary sinus and placed into a tributary overlying the LV free wall. Two other pacing leads are placed on the right atrium (A lead) and right ventricular septum (V lead). It is hypothesized that patients with LV dysfunction and delayed ventricular conduction can benefit from pacing by achieving faster depolarization times (reduced QRS width) and more synchronous electrical activation pattern, correcting interatrial and/or interventricular (V-V) conduction delay and maintaining optimal atrial-ventricular (A-V) synchrony. CRT can increase diastolic filling time through optimization of A-V delay; resynchronization of inter and intraventricular contraction through optimization of the V-V delay can improve efficient contraction and reduce mitral regurgitation. CRT has been shown to improve ventricular contractile function (ejection fraction), diminish secondary mitral regurgitation, reverse ventricular remodeling, and sustain improvement in HF. In persistently symptomatic patients, CRT alone results in significant improvement in quality of life, functional class, exercise capacity, LVEF [53, 6, 29], rate of repeated hospitalization and mortality due to NYHA functional class III to IV HF when compared to standard pharmacological therapy [29, 22, 20].

Functional improvement has been demonstrated in trials of patients with NYHA

class III or ambulatory class IV HF symptoms and QRS duration >150 ms. On average, a "clinical" responder exhibits a 1 to 2 mL/kg/min increase in peak oxygen consumption, 50 to 70 meter increase in 6 minute walk distance, and reduction of 10 points or more in the 0–105 point scale of the Minnesota Living with Heart Failure Questionnaire in patients with wide range of QRS durations [22]. Rehospitalization rates decrease by 30% and reductions in all-cause mortality is reduced to 24% to 36% as early as 3 months of therapy. Functional improvement may be more objectively observed using 2D echo to detect left ventricular reverse remodeling where the chamber size decreases and wall thickness increases [69, 113]. Patients who experience LV reverse remodeling >10% are classified as "echocardiographic" responders and have excellent survival rates >90% [131].

CRT is not without procedural risks and costs. CRT implant complications are similar to those with standard pacemaker and ICD technologies and include dissection or perforation of the coronary sinus, though rare. About 8% to 12% of CRT patients have a non-functional pacing systems [35]. Failure to ensure proper lead capture and placement can inhibit pacing and lead to further dyssynchrony. Optimal hemodynamic response from resynchronization depends on the site of LV stimulation [24] and on A-V [79] and V-V [107] delay optimization. Non-optimal A-V and V-V delay settings can also introduce dyssynchrony. Sufficiently short A-V interval is necessary to prevent intrinsic PR conduction from inhibiting biventricular pacing.

Clinical predictors of CRT response

The ACCF/AHA recommends guidelines for appropriate use of CRT in patients with HF. Current indications for CRT device candidacy are NYHA functional class II, III, ambulatory class IV symptoms (in spite of optimal pharmacological therapy), sinus rhythm, LVEF <35%, and cardiac dyssynchrony defined as prolonged QRS duration exceeding 150 ms [88, 127]. Despite these guidelines, about 30% of selected candidates fail to meet clinical response criteria, and up to 50% fail to meet echocardiographic response criteria [22, 29, 131]. Discovery of more reliable predictors of positive CRT outcomes from baseline pathophysiological conditions can help to direct and guide therapy.

Clinical imaging has been heavily utilized toward making quantitative assessments of possible predictors of outcome. Echocardiography is one of the most routinely available clinical imaging modalities for its low cost, portability, and non-invasiveness. High temporal resolution makes it an ideal modality for assessing mechanical dyssynchrony. Several observational studies have evaluated the value of echo in identifying and predicting response to CRT [25, 129, 15, 89]. Tissue Doppler imaging (TDI) has been shown to be superior to strain rate imaging and post-systolic shortening for predicting reverse remodeling in both ischemic and non-ischemic HF after CRT [132, 106]. However, large randomized trails using echo-based parameters have failed to reliably identify CRT responders [28, 16]. In patients with failure to respond to CRT or worsening clinical status, studies with echo have been used to maximize A-V intervals and programming of the CRT device while monitoring LV systolic function and mitral regurgitation [87, 100]. Echo has been shown to identify patients with dyssynchrony who are missed by electrocardiography criteria alone [90, 130]. MR in CRT candidates have shown that patients with area of fibrosis, specifically near potential lead placement areas, do not demonstrate clinical improvement with CRT [18]. One study found MR to be more sensitive for fibrosis than SPECT in prospective CRT patients. Available evidence does not yet support criteria for device therapy beyond LVEF; therefore, echo and MR testing are useful in patient selection.

Efforts to characterize baseline electrical dyssynchrony in LBBB using the electrocardiogram (ECG) have also been taken [111, 102, 19, 93, 1]. Conventional patient selection criteria uses a QRS duration >150 ms. A recent meta-analysis of the major randomized CRT trials in the past decade have shown that wide QRS complex >150 ms is still the strongest predictor of mortality in CRT candidates, surpassing echocardiographic indices of mechanical dyssynchrony [28]. ECG morphology between LBBB and RBBB pattern was considered and showed a present but statistically insignificant effect. Other workers suggest defining a new set of QRS features and morphologies that are reflective of a more strict or "true" LBBB pattern. Strauss et al. has characterized "true LBBB" morphology by a QS or rS morphology in leads V1-V2, duration $\geq$140 ms in men and $\geq$130 ms in women, and mid-QRS notching or slurring in >2 leads in I, aVL, V1, V2, V5, and V6. The two peaks of a mid-QRS notch is thought to reflect

two electrical activation events, first of the endocardial LV septum and second of the epicardial posterior wall. It is hypothesized that this specific electrical activation pattern is the precise substrate that is most amenable to CRT, therefore improving the chance of positive benefit. To date, however, no large study has been able to confirm the truth of these criteria. It is still not possible to confidently predict which patients will improve with CRT, and on average, benefit appears to be confined to patients with QRS duration of at least 150 ms and LBBB pattern.

1.3 Towards Personalized Treatment of Heart Failure

The concept of *appropriateness* guides clinical decisions to administer optimal, beneficial therapy to an individual patient. The AQA Principles for Appropriateness Criteria defines appropriateness as:

> The concept of appropriateness, as applied to health care, balances risk and benefit of a treatment, test, or procedure in the context of available resources for an individual patient with specific characteristics. Appropriateness criteria should provide guidance to supplement the clinician's judgment as to whether a patient is a reasonable candidate for the given treatment, test or procedure [4].

In the case of HF and treatment strategy, particularly by CRT, the question of which patients should receive a device, given the risks and costs, must answer two broad questions relating prediction and principle [8]. Determining the therapeutic outcome is a question of prediction of disease progression. However, predictive criteria cannot be known unless the pathological and therapeutic mechanisms of DHF and CRT are understood. Due to the complexity of the disease, wide variation of patient characteristics, and non-specific signs and symptoms, clear answers to questions of prediction and principle in DHF and CRT have been elusive.

Until the last few decades, contemporary views of human disease have been based on simple correlation between clinical syndromes and pathological analysis from trials of large, randomized patient populations (at best). Crude averages and other statistics of the results have served as recommendations for therapy. Though this approach has been useful for gaining insight into the general behaviors of pathologies, it does not

account for the unique features presented by an individual patient, perhaps not even for a patient in the trial population [60]. In reality, important pathological differences exist between patients (in addition to differences between any given patient and the "average" patient) which can significantly impact the likelihood of benefit from a particular therapy. Personalized therapy requires a clear delineation of subtle inter-individual differences which determine outcomes. A major barrier to individualized therapies has been the lack of a systematic analytic approach that describes how an individual patient's multiple pathological features combine to affect the fundamental determinants of therapeutic response and appropriateness of treatment.

1.3.1 The multi-scale biological hierarchy

The pathophysiology of diseases such as DHF reflects the emergent behavior of a hierarchical physiological network of stochastic and deterministic processes. Attempts to delineate therapeutic outcomes on such a network should consider the individual and ensemble behavior of its member components. The reductionist philosophy guiding biological researchers for centuries has uncovered the parts of a functional and structural biological hierarchy which exists across multiple scales of space (centimeters to nanometers) and time (seconds to nanoseconds). The hierarchy is roughly organized as follows: a biological organism is a collection of organs that support the organism; organs are compositions of particular types of tissues that support the organ; tissues are assemblages of specialized cells that support the tissue; an individual cell (with its own set of organelles, compartments, and structures) is a highly-specialized bioreactor which mediates a slew of tightly coupled and timed biochemical reactions of signaling and metabolism; subcellular reactions and structures are enacted by and constructed of proteins; proteins are specifically encoded by the genome; and the genome is regulated by the overlying biochemical environment. Not only does each scale presents a characteristic set of structure-related functions, one scale is susceptible to stimuli from any of the upward and downward scales. The function of one level depends on the synergism of lower levels and higher levels when feedback mechanisms are present (e.g. regulation of genetic expression by changes at the organ level). The final resulting pathophysiology is the emergent outcome of the complete network.

1.3.2 Computational models of physiology

Mathematical modeling provides a framework for capturing the dynamical behavior of physiological systems. Among the most sophisticated kinds of models to date are systems of ordinary (ODE) and partial (PDE) differential equations formulated with respect to time and space (independent variables) to quantify changes of important biophysical states and quantities (dependent variables) such as concentration, conformation, voltage, deformation, energy, stress, pressure, and flow, often within the complex geometric domains of biological structures. Various degrees of coupling can occur between member equations in a system and in other systems when common dependent variables are shared, allowing the ability to capture feed-back and feed-forward mechanisms. The dynamics of a particular mathematical system depend on the values of parameters represented in its equations. Specifying, optimizing, or tuning the model involves estimating a set of parameter values such that model behavior predicted by the equations matches corresponding empirical measurements. The solution quality of the parameter optimization depends on the granularity and robustness of the model and on the kind, quantity, and fidelity of the measured data.

The highly nonlinear, complex behaviors of the resulting systems often defy analytical solutions and require numerical approximation. Finite element analysis (FEA) is a suitable method for this purpose. It was originally developed in the 1950s from the mathematical foundation laid in the work of Hrennikoff [52] and Courant [32] to address design problems in civil and aeronautical engineering; FEA has since emerged as its own mathematical field with remarkable numerical applications in many other science and engineering disciplines. For physiological problems such as blood flow in the aorta or tissue deformation in the ventricles, FEA can approximate solutions to boundary value problems of PDE systems in complex geometric domains. FEA techniques consist of a variational formulation of the physical problem, a domain discretization strategy, solution algorithms, and post-processing procedures; for a standard reference text of FEA, see Zienkiewicz and Taylor [134]. FEA algorithms can be implemented in computer software code, and the resulting solution behavior of the model (and choice of algorithms) can be simulated on computer hardware. By this practical means, such a model is also referred to as a computational model.

Mathematical models of cardiovascular physiology have developed in the last century thanks to fundamental experimental work in physiology and theoretical developments in mathematics and other sciences. In the beginning of the 20th century, Otto Frank and Ernest Starling had introduced their Frank-Starling law of the heart observing length-dependent tension development where, within physiological limits, the stroke volume of the heart in a single beat is directly proportional to the total blood volume of the filled heart at end-diastole. Starling had also described fluid flow across a capillary [110], and Frank developed the idea of the *Windkessel* for pulsatile arterial blood flow [39]. Archibald Hill (considered one of the fathers of biophysics) described the cooperative binding effect of O_2 to hemoglobin by the Hill coefficient [50] in 1910. In 1938, he also published a treatise on the production of heat and mechanical work in contracting and lengthening muscle to derive the Hill equations for tetanized muscle contraction and the 3-element model of viscoelastic muscle properties [49]. In 1952, Alan Hodgkin and Andrew Huxley published their seminal mathematical model of action potential excitation and conduction based on observed flows of transmembrane ionic currents in nerve cells [51]. Huxley and Niedergerke later discovered the structural basis for muscle contraction with the sliding filament theory of muscle in 1954 [56]. Denis Noble applied Hodgkin's and Huxley's approach to describe action potentials in cardiac myocytes in terms of its ionic currents and unique pacemaker activity [80]. In the late 1970s, Tung described action potential wave propagation in cardiac tissue comprised of anisotropic intracellular and extracellular (bi-domain) media [119]; this was a generalization of cable theory originally presented by William Thomson (Lord Kelvin) in 1854 for telegraph communications [116]. Yuan Chen Fung fathered the field of modern biomechanics of soft biological tissue, notably by his namesake constitutive equation for exponential strain [40, 41]. He and other coworkers also highlighted the importance of residual stress in tissue mechanics [84, 26]. Fung's analytical framework enabled Richard Skalak in 1982 to consider a continuum description of tissue growth and remodeling [104, 103], leading to further developments by Rodriguez et al. [95]. Although this historical survey of the last century of physiological research is cursory, we may at once gain perspective and appreciation for the technical diversity and interdisciplinary basis of current physiological research.

1.3.3 A systems paradigm for pathophysiology

The progress of 20th century theoretical and experimental work in physiology, mathematics, and other sciences have gained tremendous knowledge of multi-scale physiology. In the last two decades, technical breakthroughs in computer power, experimental techniques, medical diagnostics, and large open-access, online databases with a wealth of physiologic data and analysis and modeling tools have brought the field of physiology to a new point in its history where it can begin to merge the isolated paths of reductionist research into holistic descriptions of physiological systems. Denis Noble recently remarked, "I'd be the first to admit that the complexities of biological systems are horrific. And I don't oppose the reductionist paradigm. I just say that it has to be complemented by an integrative paradigm" [74].

The "systems" paradigm integrates genetic, biochemical, cellular, physiological, and clinical data to create networks that can be used to predictively model disease behavior and response to therapy. These networks may be systematically constructed using a synergistic technical framework borrowing from the biological, chemical, physical, mathematical, and computational sciences and engineering. The NSF blue ribbon panel recently recognized that simulation-based engineering science applied to multi-scale study of simulation-based medicine may lead further toward realization of predictive, preventative, personalized, and participatory medicine [82]. Quantitative, holistic systems biology applied to human disease offers an exciting and unique approach for diagnosis for establishing disease, defining disease predilection, and developing personalized treatment strategies.

Applications toward cardiovascular medicine

To date, the heart is a preeminent example of an organ system whose centuries-old study of multi-scale structure and function lends it to highly interdisciplinary and collaborative research efforts through the systems paradigm [112, 66, 14, 98]. Several notable efforts have been established to foster and develop this new kind of research. The International Union of Physiological Sciences (IUPS) Human Physiome Project (HPP) is an international effort instigated in 1997 to provide a comprehensive framework for computational modeling of the human body, including databases, tools, and

standards for model development and exchange [33, 54]. The Cardiac Physiome Project is a branch of the HPP focused specifically on the heart [81, 37, 12, 105, 55]. The Cardiac Atlas Project is a large-scale database of cardiac imaging examinations and associated clinical data in order to develop a shareable, web-accessible, structural and functional atlas of the normal and pathological heart for clinical, research and educational purposes [38]. The National Institutes of Health (NIH) has provided support through the National Heart, Lung, and Blood Institute (NHLBI), committing over $45.6 M between 2006 and 2012 for programs for integrated computational and experimental approaches in heart, lung, blood, and sleep research [92]. The NIH also supports the National Biomedical Computation Resource (NBCR) to facilitate interaction among biomedical scientists and promote development of computing power at national supercomputer centers.

Studies of computational models of human and animal hearts integrating imaging, microstructure, and biophysical details have been used to develop subsequently validated hypotheses for complex physiological processes that elude simple empirical observations. Particularly important processes involve the electromechanical behavior of the heart in arrhythmia. Weiss et al. [123] studied the role of repolarization dynamics in initiating arrhythmias, particularly T wave alternans, by considering the intracellular coupling of Ca^{2+} and membrane voltage. Pop et al. [91] used a pig model to predict infarct-related ventricular tachycardia (VT) inducibility after programmed electrical stimulation, demonstrating correspondence between predicted and experimentally measured electroanatomical voltage maps. Arevalo et al. [7] examined the impact of the myocardial infarct border zone on arrhythmogenesis, suggesting that VT maintenance requires a minimum volume of remodeled scar tissue. Kerckhoffs et al. revealed mechanistic insights of regional to global effects of pacing normal [62, 121, 61] and failing [64, 63, 120] hearts. Examples of studies in defibrillation therapy mechanisms [3] have been undertaken by Sambelashvili to study the complex dynamics of virtual-electrode-induced scroll waves [99] and Rodriguez to characterize myocardial vulnerability to electric shock following an ischemic event [94].

1.3.4 Patient-specific models for clinical decision support

Patient-specific electromechanical models of the whole heart for optimization and advancement of therapy represent some of the most sophisticated models developed to date [118]. Supported by experimental and clinical data and techniques, such models can make predictions of therapeutic outcome and generate working hypotheses of cardiovascular function that are testable and reproducible [13]. This ability arises from its function as the framework that unifies diverse cardiac electrophysiology and electromechanics insight. Multi-scale, multi-physics models incorporating electromechanical and structural remodeling are poised to become a first line of screening for new therapies and approaches, including pharmacological intervention. Diagnostic developments stemming from mathematical models and simulation will be new approaches to patient screening and diagnosis. Whole-heart models of cardiovascular function have recently been used to the study wide range of mechanisms in the normal and diseased heart and have made a number of major contributions toward improving clinical practice in cardiology.

Electromechanical modeling studies have provided insight into mechanisms governing CRT efficacy. Kerckhoffs et al. [65, 64] showed that improvement of ventricular function following CRT in the failing heart with LBBB is diminished with increasing infarct size and infarct location; mechanical non-uniformity is also adversely affected by the synergistic effect of dilation and LBBB [67]. Niederer et al. [78] used one patient-specific model to suggest that a compromised Frank-Starling mechanism could be a clinical metric in identifying HF patients as potential responders to CRT; the model showed that hemodynamic benefit from CRT was improved when length-dependent tension regulation was attenuated. Electromechanics models have also been used to optimize CRT efficacy by the pacing parameters; it has been shown that CRT therapy without optimal individual adjustment introduces additional LV dyssynchrony and worsens acute and chronic outcomes [10]. To this end, Constantino et al. [31] proposed a strategy to optimize CRT response by placing LV pacing electrodes in regions with the most electromechanical delay. Other patient-specific electromechanical models with LBBB contractile dyssynchrony have been developed by Aguado-Sierra et al. [2] and Sermesant et al. [101], holding promise to become important clinical tools for treatment of

DHF.

Challenges and considerations for patient-specific modeling

The challenges of patient-specific computational modeling are formidable, but important aspects should be kept in mind to keep the task at hand reasonable and feasible. A model is a representation of reality designed to help us better understand that reality. A comprehensive multi-scale model that encompasses all biological detail on all levels for its own sake, however, would be neither practical nor particularly useful [66]. Prudent model formulation, implementation, and use should be driven by specific biological problems and questions; for patient-specific modeling, efforts should be directed at the pathology in question. Constructing integrative systems is difficult because of the enormous requirements for computational power, detailed data, and human effort. Parameters of a biological model are hard to measure and estimate, vary over disparate time and spatial scales, and reside in a noisy milieu of irrelevant signals [74].

A highly detailed computational model requires high computational effort which manifests in time and resources. High-performance computing is a major determinant for the implementation of computational costly models. Time costs add to computational cost in the physical number of computer flops it takes to solve the problem. Graphic Processing Units (GPUs) can be used to accelerate processing times of parallel problems, while existing software and technologies can serve as plug-in applications to a flexible architecture that can integrate these tools to solve multi-scale problems. For practical clinical use, computational costs must be kept at a minimum by compact mathematical models and efficient use of hardware resources by efficient software. Crampin [33] and Bassingthwaighte [13] have addressed need for simplified models at various physiologic levels. Bassingthwaighte proposed a strategy for the design of a multi-scale model of physiologic systems that involves a six step approach to design and validate an initial high-resolution multi-scale model. Specific components can be simplified to gain computational speed, but simplified components must be kept within a valid range. If necessary, inadequate components can be replaced by more detailed ones, and the resultant model will have to be validated again.

A patient-specific model requires input data from the patient. The availability of

non-invasive clinical imaging modalities in standard guidelines for clinical HF management presents an opportunity for patient-specific models of anatomy, electrophysiology, biomechanics, and hemodynamics to be developed and utilized. Models of ventricular anatomy can be constructed from detailed imaging data including CT, MR, and echo. Ventricular fiber architecture can be estimated using diffusion tensor MR. Myocardial infarction characterization can be made from SPECT and delayed-enhancement MR. Standard ECG measurements can infer properties of cardiac electrophysiology. Invasive intracardiac catheter measurements can also be used with empirical pressure-volume relations [68] to estimate passive and contractile parameters of ventricular myocardium.

The detail encompassed by the model is limited by the data used to construct it. Data type, amount, granularity, and management add to the costs associated with model development. Clinical data costs pertain to the cost of procedures used to obtain the measurements and associated risk/benefits of subjecting the patient to a procedure. Use of routinely obtained, minimally invasive data is preferred whenever possible. Since it is impractical to obtain a completely comprehensive data set for each patient, existing data, when appropriate, is needed for completion. For example, the specific *in-vivo* myofiber architecture of a patient from diffusion tensor MR imaging is currently impossible to obtain. Instead, a valid approximation can be made by mapping the fiber architecture of an atlas human heart to any particular patient's heart [73]. Online databases of other types of cardiac datasets will be useful for this purpose.

An advantage of computational models is that they can compute clinically relevant, biophysical quantities that cannot be measured directly. For example, stress cannot be measured accurately without damaging tissue. Similarly, computational models are based on parameters that are not typically measurable but may be clinically important. Predictions of patient-specific models should be validated by comparison against clinical follow-up whenever possible. If predictions and follow-up are incongruent, adjustments to the model should be considered: 1) components of the model may be too oversimplified and should be replaced with more accurate models, 2) the model may be based on an incomplete physiologic understanding of the disease, 3) additional theoretical or experimental studies may be needed to adequately revise the model.

In the overall clinical context, computational models are tools meant to provide

diagnostic and decision support. At point of care, the cardiologist must ultimately defer to real-life experience and acquired expertise. While a model may be idealized to minimize human bias and error in clinical decisions, they are inherently made from assumptions and limited knowledge. Work constantly progresses to improve the realism of models, but an incompleteness of knowledge will invariably exist in any representation of reality. Awareness of these limitations should promote prudent and appropriate use of computational models for diagnoses and decisions regarding patient health.

1.4 Aims of the Dissertation

The goal of this dissertation was to gain new insight into the physiological mechanisms and predictors of long-term outcomes of DHF treated by CRT. Long-term outcome was objectively defined by the degree of LV reverse remodeling (echo response criteria) after 3–6 months of CRT. A deeper understanding of the basic science of DHF and CRT will translate to improved clinical diagnostics, identification of likely CRT responders, and personalization of therapy. For this purpose, we aimed to utilize patient-specific computational models of the failing ventricles to quantitatively relate inter-patient physiologic differences during DHF and acute CRT with differences in long-term outcomes. We hypothesized that the pathological severity of mechanical loading and electrical activation caused by LBBB predicts better CRT outcomes. Optimization of CRT also depends on the amount of improvement gained by the particular patient-specific therapeutic parameters.

The first specific aim was to develop the tools and methods to construct patient-specific computational models incorporating clinical and empirical anatomical, electrophysiological, biomechanical, and hemodynamic data. We validated the models' ability to make accurate quantitative predictions to clinical data that was not used for parameterization. The second specific aim was to test the hypothesis that the heterogeneity of mechanical loading introduced by LBBB is an important indicator of the likelihood of improvement. Furthermore, the degree of load homogenization by CRT is mechanistically linked to the degree of LV reverse remodeling. The third specific aim was to test the hypothesis that the heterogeneity of electrical activation introduced by LBBB

is also an important indicator of long-term outcomes. The ability to make predictions from electrical biomarkers is particularly attractive due to the low cost and standardized use of the 12-lead ECG. Optimization of CRT parameters, specifically the V-V delay, is dependent upon the degree of improvement of synchronous electrical activation.

The study of patient-specific response to CRT in DHF is important. Clinical researchers have not yet reached a gold standard biomarker for reliable predictions of long-term CRT outcomes. This lack of detailed knowledge of the complex interactions of DHF and CRT is due to limited physiologic observability of clinical measurements and large inter-patient variability. The use of patient-specific models to overcome these limitations is beneficial in two ways. First, models are well-suited for investigating complex patient-specific physiological mechanisms by their ability to take an arbitrarily large number of quantitative measurements as inputs, simulate their interactions at baseline and acute CRT according to deterministic models of physiology, and predict the emergent outcome. Second, new mechanistic insight from the model results can inform better patient selection criteria for CRT using novel, immeasurable model outputs. A further step to take is to relate the model outputs to clinical measurements to discover new diagnostics directly from the clinical measurements. Second, the determination of the minimum clinical requirements to build models capable of sufficiently predicting the degree of CRT response will promote the feasibility and practicality of models as useful clinical diagnostic and decision support tools.

Acknowledgments

The content of this chapter comprises an original document.

Bibliography

1. Adelstein, E. C., Saba, S., 2009. Usefulness of baseline electrocardiographic qrs complex pattern to predict response to cardiac resynchronization. The American journal of cardiology 103 (2), 238–242.

2. Aguado-Sierra, J., Kerckhoffs, R. C., Lionetti, F., Hunt, D., Villongco, C., Gonzales, M., Campbell, S. G., McCulloch, A. D., 2010. A computational framework

for patient-specific multi-scale cardiac modeling. In: Patient-Specific Modeling of the Cardiovascular System. Springer, pp. 203–223.

3. Aguel, F., Eason, J., Trayanova, N., 2003. Advances in modeling cardiac defibrillation. International Journal of Bifurcation and Chaos 13 (12), 3791–3803.

4. Alliance, A., 2009. Aqa parameters for selecting measures for physician and other clinician performance. Retrieved April 19, 2010.

5. Ammar, K. A., Jacobsen, S. J., Mahoney, D. W., Kors, J. A., Redfield, M. M., Burnett, J. C., Rodeheffer, R. J., 2007. Prevalence and prognostic significance of heart failure stages application of the american college of cardiology/american heart association heart failure staging criteria in the community. Circulation 115 (12), 1563–1570.

6. Andrew, E., John, P., Kenneth, A., 2008. Acc/aha/hrs 2008 guidelines for device-based therapy of cardiac rhythm abnormalities. J Am Coll Cardiol 51 (1), 1–62.

7. Arevalo, H., Plank, G., Helm, P., Halperin, H., Trayanova, N., 2009. Volume of peri-infarct zone determines arrhythmogenesis in infarcted heart. Heart Rhythm 6 (5), S232–S233.

8. Arkin, A. P., Schaffer, D. V., 2011. Network news: innovations in 21st century systems biology. Cell 144 (6), 844–849.

9. Askenazi, J., Alexander, J. H., Koenigsberg, D. I., Belic, N., Lesch, M., 1984. Alteration of left ventricular performance by left bundle branch block simulated with atrioventricular sequential pacing. The American journal of cardiology 53 (1), 99–104.

10. Auger, D., Bleeker, G. B., Bertini, M., Ewe, S. H., Van Bommel, R. J., Witkowski, T. G., Ng, A. C., van Erven, L., Schalij, M. J., Bax, J. J., 2012. Effect of cardiac resynchronization therapy in patients without left intraventricular dyssynchrony. European heart journal 33 (7), 913–920.

11. Baker, D. W., 2002. Prevention of heart failure. Journal of cardiac failure 8 (5), 333–346.

12. Bassingthwaighte, J., Hunter, P., Noble, D., 2009. The cardiac physiome: perspectives for the future. Experimental physiology 94 (5), 597–605.

13. Bassingthwaighte, J. B., Chizeck, H. J., Atlas, L. E., 2006. Strategies and tactics in multiscale modeling of cell-to-organ systems. Proceedings of the IEEE 94 (4), 819–831.

14. Bassingthwaighte, J. B., Vinnakota, K. C., 2004. The computational integrated myocyte: a view into the virtual heart. Annals of the New York Academy of Sciences 1015 (1), 391–404.

15. Bax, J. J., Bleeker, G. B., Marwick, T. H., Molhoek, S. G., Boersma, E., Steendijk, P., Van Der Wall, E. E., Schalij, M. J., 2004. Left ventricular dyssynchrony predicts response and prognosis after cardiac resynchronization therapy. Journal of the American College of Cardiology 44 (9), 1834–1840.

16. Beshai, J. F., Grimm, R. A., Nagueh, S. F., Baker, J. H., Beau, S. L., Greenberg, S. M., Pires, L. A., Tchou, P. J., 2007. Cardiac-resynchronization therapy in heart failure with narrow qrs complexes. New England Journal of Medicine 357 (24), 2461–2471.

17. Bhuiyan, T., Maurer, M. S., 2011. Heart failure with preserved ejection fraction: persistent diagnosis, therapeutic enigma. Current cardiovascular risk reports 5 (5), 440–449.

18. Bilchick, K. C., Dimaano, V., Wu, K. C., Helm, R. H., Weiss, R. G., Lima, J. A., Berger, R. D., Tomaselli, G. F., Bluemke, D. A., Halperin, H. R., 2008. Cardiac magnetic resonance assessment of dyssynchrony and myocardial scar predicts function class improvement following cardiac resynchronization therapy. JACC: Cardiovascular Imaging 1 (5), 561–568.

19. Bilchick, K. C., Kamath, S., DiMarco, J. P., Stukenborg, G. J., 2010. Bundle-branch block morphology and other predictors of outcome after cardiac resynchronization therapy in medicare patients. Circulation 122 (20), 2022–2030.

20. Bradley, D. J., Bradley, E. A., Baughman, K. L., Berger, R. D., Calkins, H., Goodman, S. N., Kass, D. A., Powe, N. R., 2003. Cardiac resynchronization and death from progressive heart failure: a meta-analysis of randomized controlled trials. Jama 289 (6), 730–740.

21. Bramlet, D. A., Morris, K. G., Coleman, R. E., Albert, D., Cobb, F. R., 1983. Effect of rate-dependent left bundle branch block on global and regional left ventricular function. Circulation 67 (5), 1059–1065.

22. Bristow, M. R., Saxon, L. A., Boehmer, J., Krueger, S., Kass, D. A., De Marco, T., Carson, P., DiCarlo, L., DeMets, D., White, B. G., 2004. Cardiac-resynchronization therapy with or without an implantable defibrillator in advanced chronic heart failure. New England Journal of Medicine 350 (21), 2140–2150.

23. Bursi, F., Weston, S. A., Redfield, M. M., Jacobsen, S. J., Pakhomov, S., Nkomo, V. T., Meverden, R. A., Roger, V. L., 2006. Systolic and diastolic heart failure in the community. Jama 296 (18), 2209–2216.

24. Butter, C., Auricchio, A., Stellbrink, C., Fleck, E., Ding, J., Yu, Y., Huvelle, E., Spinelli, J., 2001. Effect of resynchronization therapy stimulation site on the systolic function of heart failure patients. Circulation 104 (25), 3026–3029.

25. Chung, E. S., Leon, A. R., Tavazzi, L., Sun, J.-P., Nihoyannopoulos, P., Merlino, J., Abraham, W. T., Ghio, S., Leclercq, C., Bax, J. J., 2008. Results of the predictors of response to crt (prospect) trial. Circulation 117 (20), 2608–2616.

26. Chuong, C., Fung, Y., 1986. Residual stress in arteries. In: Frontiers in Biomechanics. Springer, pp. 117–129.

27. Cleland, J., Torabi, A., Khan, N., 2005. Epidemiology and management of heart failure and left ventricular systolic dysfunction in the aftermath of a myocardial infarction. Heart 91 (suppl 2), ii7–ii13.

28. Cleland, J. G., Abraham, W. T., Linde, C., Gold, M. R., Young, J. B., Daubert, J. C., Sherfesee, L., Wells, G. A., Tang, A. S., 2013. An individual patient meta-analysis of five randomized trials assessing the effects of cardiac resynchronization therapy on morbidity and mortality in patients with symptomatic heart failure. European heart journal 34 (46), 3547–3556.

29. Cleland, J. G., Daubert, J.-C., Erdmann, E., Freemantle, N., Gras, D., Kappenberger, L., Tavazzi, L., 2005. The effect of cardiac resynchronization on morbidity and mortality in heart failure. New England Journal of Medicine 352 (15), 1539–1549.

30. Committee, N. Y. H. A. C., Association, N. Y. H., 1979. Nomenclature and criteria for diagnosis of diseases of the heart and great vessels. Little, Brown Medical Division.

31. Constantino, J., Hu, Y., Trayanova, N. A., 2012. A computational approach to understanding the cardiac electromechanical activation sequence in the normal and failing heart, with translation to the clinical practice of crt. Progress in biophysics and molecular biology 110 (2), 372–379.

32. Courant, R., 1943. Variational methods for the solution of problems of equilibrium and vibrations. Bull. Amer. Math. Soc 49 (1), 1–23.

33. Crampin, E. J., Halstead, M., Hunter, P., Nielsen, P., Noble, D., Smith, N., Tawhai, M., 2004. Computational physiology and the physiome project. Experimental Physiology 89 (1), 1–26.

34. Curtis, L. H., Whellan, D. J., Hammill, B. G., Hernandez, A. F., Anstrom, K. J., Shea, A. M., Schulman, K. A., 2008. Incidence and prevalence of heart failure in elderly persons, 1994-2003. Archives of Internal Medicine 168 (4), 418–424.

35. Daoud, E. G., Kalbfleisch, S. J., Hummel, J. D., Weiss, R., Augustini, R. S., Duff, S. B., Polsinelli, G., Castor, J., Meta, T., 2002. Implantation techniques and chronic lead parameters of biventricular pacing dual-chamber defibrillators. Journal of cardiovascular electrophysiology 13 (10), 964–970.

36. Epstein, A. E., DiMarco, J. P., Ellenbogen, K. A., Estes, N. M., Freedman, R. A., Gettes, L. S., Gillinov, A. M., Gregoratos, G., Hammill, S. C., Hayes, D. L., 2008. Acc/aha/hrs 2008 guidelines for device-based therapy of cardiac rhythm abnormalities: a report of the american college of cardiology/american heart association task force on practice guidelines (writing committee to revise the acc/aha/naspe 2002 guideline update for implantation of cardiac pacemakers and antiarrhythmia devices) developed in collaboration with the american association for thoracic surgery and society of thoracic surgeons. Journal of the American College of Cardiology 51 (21), e1–e62.

37. Fink, M., Niederer, S. A., Cherry, E. M., Fenton, F. H., Koivumäki, J. T., Seemann, G., Thul, R., Zhang, H., Sachse, F. B., Beard, D., 2011. Cardiac cell modelling: observations from the heart of the cardiac physiome project. Progress in biophysics and molecular biology 104 (1), 2–21.

38. Fonseca, C. G., Backhaus, M., Bluemke, D. A., Britten, R. D., Do Chung, J., Cowan, B. R., Dinov, I. D., Finn, J. P., Hunter, P. J., Kadish, A. H., 2011. The cardiac atlas projectâĂŤan imaging database for computational modeling and statistical atlases of the heart. Bioinformatics 27 (16), 2288–2295.

39. Frank, O., 1899. Die grundform des arteriellen pulses. Z Biol 37 (483-526), 19.

40. Fung, Y.-C., 1990. Biomechanics. Springer.

41. Fung, Y.-c., Fung, Y., 1965. Foundations of solid mechanics. Vol. 351. Prentice-Hall Englewood Cliffs, NJ.

42. Gaziano, J. M., 2010. Fifth phase of the epidemiologic transition: the age of obesity and inactivity. Jama 303 (3), 275–276.

43. Go, A. S., Mozaffarian, D., Roger, V. L., Benjamin, E. J., Berry, J. D., Blaha, M. J., Dai, S., Ford, E. S., Fox, C. S., Franco, S., 2014. Heart disease and stroke statistics–2014 update: a report from the american heart association. Circulation 129 (3), e28.

44. Go, A. S., Mozaffarian, D., Roger, V. L., Benjamin, E. J., Berry, J. D., Borden, W. B., Bravata, D. M., Dai, S., Ford, E. S., Fox, C. S., 2013. Heart disease and stroke statistics–2013 update: a report from the american heart association. Circulation 127 (1), e6.

45. Grines, C. L., Bashore, T., Boudoulas, H., Olson, S., Shafer, P., Wooley, C., 1989. Functional abnormalities in isolated left bundle branch block. the effect of interventricular asynchrony. Circulation 79 (4), 845–853.

46. Hardy, D., 2005. The booming dynamics of aging: From awareness to action. In: Report of the 2005 White House Conference on Aging.

47. Heidenreich, P. A., Trogdon, J. G., Khavjou, O. A., Butler, J., Dracup, K., Ezekowitz, M. D., Finkelstein, E. A., Hong, Y., Johnston, S. C., Khera, A., 2011. Forecasting the future of cardiovascular disease in the united states a policy statement from the american heart association. Circulation 123 (8), 933–944.

48. Heo, S., Doering, L. V., Widener, J., Moser, D. K., 2008. Predictors and effect of physical symptom status on health-related quality of life in patients with heart failure. American Journal of Critical Care 17 (2), 124–132.

49. Hill, A., 1938. The heat of shortening and the dynamic constants of muscle. Proceedings of the Royal Society of London B: Biological Sciences 126 (843), 136–195.

50. Hill, A. V., 1910. The possible effects of the aggregation of the molecules of haemoglobin on its dissociation curves. J Physiol (Lond) 40, 4–7.

51. Hodgkin, A. L., Huxley, A. F., 1952. A quantitative description of membrane current and its application to conduction and excitation in nerve. The Journal of physiology 117 (4), 500–544.

52. Hrennikoff, A., 1941. Solution of problems of elasticity by the framework method. Journal of applied mechanics 8 (4), 169–175.

53. Hunt, S. A., Abraham, W. T., Chin, M. H., Feldman, A. M., Francis, G. S., Ganiats, T. G., Jessup, M., Konstam, M. A., Mancini, D. M., Michl, K., 2009. 2009 focused update incorporated into the acc/aha 2005 guidelines for the diagnosis and management of heart failure in adults: a report of the american college of cardiology foundation/american heart association task force on practice guidelines developed in collaboration with the international society for heart and lung transplantation. Journal of the American College of Cardiology 53 (15), e1–e90.

54. Hunter, P. J., Borg, T. K., 2003. Integration from proteins to organs: the physiome project. Nature Reviews Molecular Cell Biology 4 (3), 237–243.

55. Hunter, P. J., Crampin, E. J., Nielsen, P. M., 2008. Bioinformatics, multiscale modeling and the iups physiome project. Briefings in bioinformatics 9 (4), 333–343.

56. Huxley, A. F., Niedergerke, R., 1954. Structural changes in muscle during contraction. Nature 173 (4412), 971–973.

57. Investigators, S., 1992. Effect of enalapril on mortality and the development of heart failure in asymptomatic patients with reduced left ventricular ejection fractions. N Engl j Med 327, 685–691.

58. Izzo Jr, J. L., Gradman, A. H., 2004. Mechanisms and management of hypertensive heart disease: from left ventricular hypertrophy to heart failure. Medical Clinics of North America 88 (5), 1257–1271.

59. Kannel, M. W. B., 2000. Incidence and epidemiology of heart failure. Heart failure reviews 5 (2), 167–173.

60. Kent, D. M., Hayward, R. A., 2007. Limitations of applying summary results of clinical trials to individual patients: the need for risk stratification. Jama 298 (10), 1209–1212.

61. Kerckhoffs, R., Bovendeerd, P., Prinzen, F., Smits, K., Arts, T., 2003. Intra-and interventricular asynchrony of electromechanics in the ventricularly paced heart. Journal of Engineering Mathematics 47 (3-4), 201–216.

62. Kerckhoffs, R., Faris, O. P., Bovendeerd, P., Prinzen, F. W., Smits, K., McVeigh, E. R., Arts, T., 2005. Electromechanics of paced left ventricle simulated by straightforward mathematical model: comparison with experiments. American Journal of Physiology-Heart and Circulatory Physiology 289 (5), H1889–H1897.

63. Kerckhoffs, R. C., Healy, S. N., Usyk, T. P., McCulloch, A. D., 2006. Computational methods for cardiac electromechanics. Proceedings of the IEEE 94 (4), 769–783.

64. Kerckhoffs, R. C., McCulloch, A. D., Omens, J. H., Mulligan, L. J., 2007. Effect of pacing site and infarct location on regional mechanics and global hemodynamics in a model based study of heart failure. In: Functional Imaging and Modeling of the Heart. Springer, pp. 350–360.

65. Kerckhoffs, R. C., McCulloch, A. D., Omens, J. H., Mulligan, L. J., 2009. Effects of biventricular pacing and scar size in a computational model of the failing heart with left bundle branch block. Medical image analysis 13 (2), 362–369.

66. Kerckhoffs, R. C., Narayan, S. M., Omens, J. H., Mulligan, L. J., McCulloch, A. D., 2008. Computational modeling for bedside application. Heart failure clinics 4 (3), 371–378.

67. Kerckhoffs, R. C., Omens, J. H., McCulloch, A. D., Mulligan, L. J., 2010. Ventricular dilation and electrical dyssynchrony synergistically increase regional mechanical nonuniformity but not mechanical dyssynchrony a computational model. Circulation: Heart Failure 3 (4), 528–536.

68. Klotz, S., Hay, I., Dickstein, M. L., Yi, G.-H., Wang, J., Maurer, M. S., Kass, D. A., Burkhoff, D., 2006. Single-beat estimation of end-diastolic pressure-volume relationship: a novel method with potential for noninvasive application. American Journal of Physiology-Heart and Circulatory Physiology 291 (1), H403–H412.

69. Koitabashi, N., Kass, D. A., 2012. Reverse remodeling in heart failure–mechanisms and therapeutic opportunities. Nature Reviews Cardiology 9 (3), 147–157.

70. Lesman-Leegte, I., Jaarsma, T., Coyne, J. C., Hillege, H. L., Van Veldhuisen, D. J., Sanderman, R., 2009. Quality of life and depressive symptoms in the elderly: a comparison between patients with heart failure and age-and gender-matched community controls. Journal of cardiac failure 15 (1), 17–23.

71. Levy, D., Kenchaiah, S., Larson, M. G., Benjamin, E. J., Kupka, M. J., Ho, K. K., Murabito, J. M., Vasan, R. S., 2002. Long-term trends in the incidence of and survival with heart failure. New England Journal of Medicine 347 (18), 1397–1402.

72. Lloyd-Jones, D., Adams, R. J., Brown, T. M., Carnethon, M., Dai, S., De Simone, G., Ferguson, T. B., Ford, E., Furie, K., Gillespie, C., 2010. Heart disease and stroke statistics–2010 update a report from the american heart association. Circulation 121 (7), e46–e215.

73. Lombaert, H., Peyrat, J., Croisille, P., Rapacchi, S., Fanton, L., Cheriet, F., Clarysse, P., Magnin, I., Delingette, H., Ayache, N., 2012. Human atlas of the cardiac fiber architecture: study on a healthy population. Medical Imaging, IEEE Transactions on 31 (7), 1436–1447.

74. Macilwain, C., 2011. Systems biology: evolving into the mainstream. Cell 144 (6), 839–841.

75. Madsen, B., Hansen, J., Stockholm, K., Husum, D., Mortensen, L., 1994. Chronic congestive heart failure. description and survival in 190 patients with heart failure based on clinical signs and symptoms. Eur Heart J 15, 303–310.

76. Majani, G., Giardini, A., Opasich, C., Glazer, R., Hester, A., Tognoni, G., Cohn, J. N., Tavazzi, L., 2005. Effect of valsartan on quality of life when added to usual therapy for heart failure: results from the valsartan heart failure trial. Journal of cardiac failure 11 (4), 253–259.

77. Moser, D. K., Yamokoski, L., Sun, J. L., Conway, G. A., Hartman, K. A., Graziano, J. A., Binanay, C., Stevenson, L. W., Investigators, E., 2009. Improvement in health-related quality of life after hospitalization predicts event-free survival in patients with advanced heart failure. Journal of cardiac failure 15 (9), 763–769.

78. Niederer, S. A., Plank, G., Chinchapatnam, P., Ginks, M., Lamata, P., Rhode, K. S., Rinaldi, C. A., Razavi, R., Smith, N. P., 2010. Length-dependent tension in the failing heart and the efficacy of cardiac resynchronisation therapy. Cardiovascular research, cvq318.

79. Nishimura, R. A., Hayes, D. L., Holmes, D. R., Tajik, J., 1995. Mechanism of hemodynamic improvement by dual-chamber pacing for severe left ventricular dysfunction: an acute doppler and catheterization hemodynamic study. Journal of the American College of Cardiology 25 (2), 281–288.

80. Noble, D., 1962. A modification of the hodgkin–huxley equations applicable to purkinje fibre action and pacemaker potentials. The Journal of Physiology 160 (2), 317–352.

81. Noble, D., Garny, A., Noble, P. J., 2012. How the hodgkin–huxley equations inspired the cardiac physiome project. The Journal of physiology 590 (11), 2613–2628.

82. Oden, J., Belytschko, T., Hughes, T., Johnson, C., Keyes, D., Laub, A., Petzold, L., Srolovitz, D., Yip, S., 2006. Revolutionizing engineering science through simulation: A report of the national science foundation blue ribbon panel on simulation-based engineering science. Arlington, VA: National Science Foundation.

83. Office, U. G. A., 2008. Medicare part b imaging services: rapid spending growth and shift to physician offices indicate need for cms to consider additional management practices. GAO Report 08-452.

84. Omens, J. H., Fung, Y.-C., 1990. Residual strain in rat left ventricle. Circulation Research 66 (1), 37–45.

85. Owan, T. E., Hodge, D. O., Herges, R. M., Jacobsen, S. J., Roger, V. L., Redfield, M. M., 2006. Trends in prevalence and outcome of heart failure with preserved ejection fraction. New England Journal of Medicine 355 (3), 251–259.

86. Palladini, G., Barassi, A., Klersy, C., Pacciolla, R., Milani, P., Sarais, G., Perlini, S., Albertini, R., Russo, P., Foli, A., 2010. The combination of high-sensitivity cardiac troponin t (hs-ctnt) at presentation and changes in n-terminal natriuretic peptide type b (nt-probnp) after chemotherapy best predicts survival in al amyloidosis. Blood 116 (18), 3426–3430.

87. Parreira, L., Santos, J., Madeira, J., Mendes, L., Seixo, F., Caetano, F., Lopes, C., Venancio, J., Mateus, A., Ines, J., 2005. Cardiac resynchronization therapy with sequential biventricular pacing: impact of echocardiography guided vv delay optimization on acute results. Revista portuguesa de cardiologia: orgao oficial da Sociedade Portuguesa de Cardiologia – Portuguese journal of cardiology: an official journal of the Portuguese Society of Cardiology 24 (11), 1355–1365.

88. Patel, M. R., White, R. D., Abbara, S., Bluemke, D. A., Herfkens, R. J., Picard, M., Shaw, L. J., Silver, M., Stillman, A. E., Udelson, J., 2013. 2013 accf/acr/ase/asnc/scct/scmr appropriate utilization of cardiovascular imaging in heart failure: a joint report of the american college of radiology appropriateness

criteria committee and the american college of cardiology foundation appropriate use criteria task force. Journal of the American College of Cardiology 61 (21), 2207–2231.

89. Penicka, M., Bartunek, J., De Bruyne, B., Vanderheyden, M., Goethals, M., De Zutter, M., Brugada, P., Geelen, P., 2004. Improvement of left ventricular function after cardiac resynchronization therapy is predicted by tissue doppler imaging echocardiography. Circulation 109 (8), 978–983.

90. Perry, R., De Pasquale, C. G., Chew, D. P., Aylward, P. E., Joseph, M. X., 2006. Qrs duration alone misses cardiac dyssynchrony in a substantial proportion of patients with chronic heart failure. Journal of the American Society of Echocardiography 19 (10), 1257–1263.

91. Pop, M., Sermesant, M., Mansi, T., Crystal, E., Ghate, S., Peyrat, J., Lashevsky, I., Qiang, B., McVeigh, E., Ayache, N., 2011. Correspondence between simple 3-d mri-based computer models and in-vivo ep measurements in swine with chronic infarctions. Biomedical Engineering, IEEE Transactions on 58 (12), 3483–3486.

92. Qasba, P., Larkin, J., 2013. Nhlbi support of systems biology. Frontiers in physiology 4.

93. Rickard, J., Kumbhani, D. J., Gorodeski, E. Z., Baranowski, B., Wazni, O., Martin, D. O., Grimm, R., Wilkoff, B. L., 2010. Cardiac resynchronization therapy in non-left bundle branch block morphologies. Pacing and clinical electrophysiology 33 (5), 590–595.

94. Rodríguez, B., Tice, B. M., Eason, J. C., Aguel, F., Trayanova, N., 2004. Cardiac vulnerability to electric shocks during phase 1a of acute global ischemia. Heart Rhythm 1 (6), 695–703.

95. Rodriguez, E. K., Hoger, A., McCulloch, A. D., 1994. Stress-dependent finite growth in soft elastic tissues. Journal of biomechanics 27 (4), 455–467.

96. Rodríguez-Artalejo, F., Guallar-Castillón, P., Pascual, C. R., Otero, C. M., Montes, A. O., García, A. N., Conthe, P., Chiva, M. O., Banegas, J. R., Herrera, M. C., 2005. Health-related quality of life as a predictor of hospital readmission and death among patients with heart failure. Archives of Internal Medicine 165 (11), 1274–1279.

97. Roger, V. L., Weston, S. A., Redfield, M. M., Hellermann-Homan, J. P., Killian, J., Yawn, B. P., Jacobsen, S. J., 2004. Trends in heart failure incidence and survival in a community-based population. Jama 292 (3), 344–350.

98. Rudy, Y., 2000. From genome to physiome: integrative models of cardiac excitation. Annals of biomedical engineering 28 (8), 945–950.

99. Sambelashvili, A., Efimov, I. R., 2004. Dynamics of virtual electrode-induced scroll-wave reentry in a 3d bidomain model. American Journal of Physiology-Heart and Circulatory Physiology 287 (4), H1570–H1581.

100. Sawhney, N. S., Waggoner, A. D., Garhwal, S., Chawla, M. K., Osborn, J., Faddis, M. N., 2004. Randomized prospective trial of atrioventricular delay programming for cardiac resynchronization therapy. Heart rhythm 1 (5), 562–567.

101. Sermesant, M., Chabiniok, R., Chinchapatnam, P., Mansi, T., Billet, F., Moireau, P., Peyrat, J.-M., Wong, K., Relan, J., Rhode, K., 2012. Patient-specific electromechanical models of the heart for the prediction of pacing acute effects in crt: A preliminary clinical validation. Medical image analysis 16 (1), 201–215.

102. Sipahi, I., Carrigan, T. P., Rowland, D. Y., Stambler, B. S., Fang, J. C., 2011. Impact of qrs duration on clinical event reduction with cardiac resynchronization therapy: meta-analysis of randomized controlled trials. Archives of internal medicine 171 (16), 1454–1462.

103. Skalak, R., 1982. Growth as a finite displacement field. In: Proceedings of the IUTAM Symposium on Finite Elasticity. Springer, pp. 347–355.

104. Skalak, R., Dasgupta, G., Moss, M., Otten, E., Dullemeijer, P., Vilmann, H., 1982. Analytical description of growth. Journal of Theoretical Biology 94 (3), 555–577.

105. Smith, N. P., Hunter, P. J., Paterson, D. J., 2009. The cardiac physiome: at the heart of coupling models to measurement. Experimental physiology 94 (5), 469–471.

106. Søgaard, P., Egeblad, H., Kim, W. Y., Jensen, H. K., Pedersen, A. K., Kristensen, B. Ø., Mortensen, P. T., 2002. Tissue doppler imaging predicts improved systolic performance and reversed left ventricular remodeling during long-term cardiac resynchronization therapy. Journal of the American College of Cardiology 40 (4), 723–730.

107. Sogaard, P., Egeblad, H., Pedersen, A. K., Kim, W. Y., Kristensen, B. Ø., Hansen, P. S., Mortensen, P. T., 2002. Sequential versus simultaneous biventricular resynchronization for severe heart failure evaluation by tissue doppler imaging. Circulation 106 (16), 2078–2084.

108. Solomon, S. D., Foster, E., Bourgoun, M., Shah, A., Viloria, E., Brown, M. W., Hall, W. J., Pfeffer, M. A., Moss, A. J., 2010. Effect of cardiac resynchronization therapy on reverse remodeling and relation to outcome multicenter automatic defibrillator implantation trial: Cardiac resynchronization therapy. Circulation 122 (10), 985–992.

109. Staessen, J. A., Wang, J.-G., Thijs, L., 2001. Cardiovascular protection and blood pressure reduction: a meta-analysis. The Lancet 358 (9290), 1305–1315.

110. Starling, E. H., 1896. On the absorption of fluids from the connective tissue spaces. The Journal of physiology 19 (4), 312–326.

111. Stavrakis, S., Lazzara, R., Thadani, U., 2012. The benefit of cardiac resynchronization therapy and qrs duration: A meta-analysis. Journal of cardiovascular electrophysiology 23 (2), 163–168.

112. Summers, R., Abdulla, T., Houyel, L., Schleich, J. M., 2011. Progress with a multiscale systems engineering approach to cardiac development. AUTOMATIKA: časopis za automatiku, mjerenje, elektroniku, računarstvo i komunikacije 52 (1), 49–57.

113. Sutton, M. G. S. J., Plappert, T., Abraham, W. T., Smith, A. L., DeLurgio, D. B., Leon, A. R., Loh, E., Kocovic, D. Z., Fisher, W. G., Ellestad, M., 2003. Effect of cardiac resynchronization therapy on left ventricular size and function in chronic heart failure. Circulation 107 (15), 1985–1990.

114. Takeshita, A., Basta, L. L., Kioschos, J. M., 1974. Effect of intermittent left bundle branch block on left ventricular performance. The American journal of medicine 56 (2), 251–255.

115. Tang, A. S., Wells, G. A., Talajic, M., Arnold, M. O., Sheldon, R., Connolly, S., Hohnloser, S. H., Nichol, G., Birnie, D. H., Sapp, J. L., 2010. Cardiac-resynchronization therapy for mild-to-moderate heart failure. New England Journal of Medicine 363 (25), 2385–2395.

116. Thomson, W., 1854. On the theory of the electric telegraph. Proceedings of the Royal Society of London 7, 382–399.

117. Titler, M. G., Jensen, G. A., Dochterman, J. M., Xie, X.-J., Kanak, M., Reed, D., Shever, L. L., 2008. Cost of hospital care for older adults with heart failure: medical, pharmaceutical, and nursing costs. Health services research 43 (2), 635–655.

118. Trayanova, N. A., 2011. Whole-heart modeling applications to cardiac electrophysiology and electromechanics. Circulation Research 108 (1), 113–128.

119. Tung, L., 1978. A bi-domain model for describing ischemic myocardial dc potentials. Ph.D. thesis, Massachusetts Institute of Technology.

120. Usyk, T. P., McCulloch, A. D., 2003. Electromechanical model of cardiac resynchronization in the dilated failing heart with left bundle branch block. Journal of electrocardiology 36, 57–61.

121. Usyk, T. P., McCulloch, A. D., 2003. Relationship between regional shortening and asynchronous electrical activation in a three-dimensional model of ventricular electromechanics. Journal of cardiovascular electrophysiology 14 (s10), S196–S202.

122. Vasan, R. S., Beiser, A., Seshadri, S., Larson, M. G., Kannel, W. B., D'Agostino, R. B., Levy, D., 2002. Residual lifetime risk for developing hypertension in middle-aged women and men: The framingham heart study. Jama 287 (8), 1003–1010.

123. Weiss, J. N., Karma, A., Shiferaw, Y., Chen, P.-S., Garfinkel, A., Qu, Z., 2006. From pulsus to pulseless the saga of cardiac alternans. Circulation Research 98 (10), 1244–1253.

124. Wilhelmsen, L., Rosengren, A., Eriksson, H., Lappas, G., 2001. Heart failure in the general population of men–morbidity, risk factors and prognosis. Journal of internal medicine 249 (3), 253–261.

125. Wyndham, C., Smith, T., Meeran, M. K., Mammana, R., Levitsky, S., Rosen, K., 1980. Epicardial activation in patients with left bundle branch block. Circulation 61 (4), 696–703.

126. Xiao, H., Lee, C., Gibson, D., 1991. Effect of left bundle branch block on diastolic function in dilated cardiomyopathy. British heart journal 66 (6), 443–447.

127. Yancy, C. W., Jessup, M., Bozkurt, B., Butler, J., Casey, D. E., Drazner, M. H., Fonarow, G. C., Geraci, S. A., Horwich, T., Januzzi, J. L., 2013. 2013 accf/aha guideline for the management of heart failure: a report of the american college of cardiology foundation/american heart association task force on practice guidelines. Journal of the American College of Cardiology 62 (16), e147–e239.

128. Young, J. B., Abraham, W. T., Smith, A. L., Leon, A. R., Lieberman, R., Wilkoff, B., Canby, R. C., Schroeder, J. S., Liem, L. B., Hall, S., 2003. Combined cardiac resynchronization and implantable cardioversion defibrillation in advanced chronic heart failure: the miracle icd trial. Jama 289 (20), 2685–2694.

129. Ypenburg, C., van Bommel, R. J., Delgado, V., Mollema, S. A., Bleeker, G. B., Boersma, E., Schalij, M. J., Bax, J. J., 2008. Optimal left ventricular lead position predicts reverse remodeling and survival after cardiac resynchronization therapy. Journal of the American College of Cardiology 52 (17), 1402–1409.

130. Yu, C., Lin, H., Zhang, Q., Sanderson, J., 2003. High prevalence of left ventricular systolic and diastolic asynchrony in patients with congestive heart failure and normal qrs duration. Heart 89 (1), 54–60.

131. Yu, C.-M., Bleeker, G. B., Fung, J. W.-H., Schalij, M. J., Zhang, Q., van der Wall, E. E., Chan, Y.-S., Kong, S.-L., Bax, J. J., 2005. Left ventricular reverse remodeling but not clinical improvement predicts long-term survival after cardiac resynchronization therapy. Circulation 112 (11), 1580–1586.

132. Yu, C.-M., Fung, J. W.-H., Zhang, Q., Chan, C.-K., Chan, Y.-S., Lin, H., Kum, L. C., Kong, S.-L., Zhang, Y., Sanderson, J. E., 2004. Tissue doppler imaging is superior to strain rate imaging and postsystolic shortening on the prediction of reverse remodeling in both ischemic and nonischemic heart failure after cardiac resynchronization therapy. Circulation 110 (1), 66–73.

133. Yusuf, S., Sleight, P., Pogue, J., Bosch, J., Davies, R., Dagenais, G., 2000. Effects of an angiotensin-converting-enzyme inhibitor, ramipril, on cardiovascular events in high-risk patients. the heart outcomes prevention evaluation study investigators. The New England journal of medicine 342 (3), 145–153.

134. Zienkiewicz, O. C., Taylor, R. L., Zienkiewicz, O. C., Taylor, R. L., 1977. The finite element method. Vol. 3. McGraw-hill London.

Chapter 2

Patient-specific Models of Ventricular Anatomy
Part I: Ventricular Geometry

Abstract

The geometry of the cardiac ventricles is an important determinant of physiological function, especially at the organ and systemic scale. Patient-specific models of the heart must necessarily begin with a compact mathematical representation of its geometry obtained by medical imaging data. In the context of dyssynchronous heart failure, key geometric features are dilation of the ventricular chambers and decreased wall thickness (particularly in the septum). Myocardial infarction often presents as a confounder of mechanical and electrical function.

Here we develop a process for constructing patient-specific mathematical models of biventricular geometry for 8 patients diagnosed with dyssynchronous heart failure and left bundle branch block. We utilized a combined anatomical image data set including computed tomography, magnetic resonance images, and singe-photon emission computed tomography. Computed tomography and magnetic resonance images were pre-processed to remove noise, masked, segmented, and triangulated. From these data, we construct 3D high-order finite element meshes of the geometry and region of my-

ocardial infarction. Finite element mesh atlases were registered to the processed image data in a semi-automated fashion. We also use singe-photon emission computed tomography images to localize myocardial infarctions. Myocardial infarct geometry was localized to the finite element meshes by an expert clinical cardiac electrophysiologist. The resulting models serve as the basis for further finite element analyses integrating multi-scale cardiovascular physiology.

2.1 Introduction

The vital function of the heart is to drive the circulation of blood through the pulmonary and systemic circulation for the transport of nutrients and metabolic wastes to and from every cell in the body. The cardiac ventricles are responsible for this most central physiologic role. Therefore, ventricular topography, shape, and geometry are optimally configured to perform this task. The ventricles are partitioned into left and right sides by three mutually intersecting muscular segments: the left and right free walls and the interventricular septum. The pumping mechanism exploits a balanced interplay between the thickness, curvature, pressure, and wall tension of these structures. Optimal geometry is required for maximal pump efficiency. Based on the principle of minimal work and Laplace's Law, Hutchins et al. observed that for diastolic filling, a spherical ventricular geometry would require the least energetic expenditure. During systole, on the other hand, a conical ventricular geometry is most energetically efficient [5]. As the compromise geometry between the two extremes, a prolate hemispheroid optimally minimizes the energy expenditure of cycling between diastolic and systolic geometries.

One of the primary structural changes in dyssynchronous heart failure (DHF) is dilated cardiomyopathy (DCM) which is marked by dilation of the ventricular chambers, depressed myocardial contractility under normal loading conditions, and susceptibility to electromechanical delays. The particular patient-specific geometry of the heart is an important determinant of pump function and is among the first physiological features to account for in assessing the severity of DHF.

2.1.1 Clinical imaging of failing ventricular anatomy

Non-invasive measures of patient-specific cardiac structure and function are of primary interest in assessing the condition of DHF and are made possible through non-invasive clinical imaging. Structural features include ventricular chamber geometry, dimensions, and wall thickness, valve dimensions, and presence of myocardial infarction. Functional features include ejection fraction, stroke volume, ventricular filling, and valve regurgitation. The primary purpose of imaging in the context of assessing DHF, particularly for determining CRT candidacy, is to evaluate left ventricular (LV) systolic function which is typically quantified by the ejection fraction (LVEF). Identification of cardiac vein anatomy for CRT lead placement and cardiac catheterization. Among the most commonly used 3D imaging modalities for HF assessment are computed tomography (CT), magnetic resonance (MR), and single-photon emission computed tomography (SPECT).

Standard use of non-invasive clinical imaging modalities presents an opportunity for detailed models of patient-specific ventricular geometry and function to be created. The different modalities each have strengths and weaknesses, advantages and disadvantages for the purposes of capturing important structural and functional details relevant to different facets of cardiovascular physiology. As a practical matter, anatomical model development must consider the balance between sufficient accuracy and the costs, risks, and feasibility of procuring the necessary data. We briefly overview of current standard clinical imaging modalities for DHF assessment to gain an appreciation of these considerations.

Computed tomography

CT scanners emit ionizing radiation in the form of an x-ray beam which penetrates a patient's body. An array of detectors located behind the patient on the opposite side of the source measures the attenuation or "shadow" of the x-ray beam as a result of non-homogeneous absorption properties of a 2D cross-section of biological tissue. The emitter and detectors are mounted on a toroidal gantry which measures beam projections over a range of angular orientations 180°–360° about the long axis of the patient. A 3D image of the field of view (e.g. a patient's thoracic cavity) is reconstructed by

computing the back-projection of the collection of projections at the measured angular orientations.

CT is capable of high spatial resolution imaging of the cardiac anatomy and surrounding structures. In this study, images of the ventricles were acquired at end-diastole with voxel size on the order of $0.5\times0.5\times2.5$ mm ($512\times512\times80$ voxels). For evaluating patients before CRT, CT can resolve the coronary anatomy for lead placement. It also has moderate temporal resolution (64-slice CT is on the order of 160 ms for assessing LV dyssynchrony and LVEF, though at variable and high heart rate it can be susceptible to motion artifacts. The use of ionizing radiation is the primary disadvantage of CT.

Magnetic resonance

MR utilizes the property of the nuclear magnetic resonance of atomic nuclei. Microscopic magnetic dipoles in hydrogen nuclei which are abundantly present in the water content of biological tissue are excited by application of a precise pulse sequence of radio waves and magnetic gradients in the presence of a static, macroscopic magnetic field (rated at 1.5 Tesla for clinical use) spanning the imaging field of view within the scanner bore where the patient lies stationary. As the dipoles relax following excitation, they produce the measured radio frequency signal which, given the known parameters of the pulse sequence, is reconstructed into a final image. Images are acquired slice by slice through the volume of the patient and reconstructed into a three-dimensional image.

The spatial resolution of clinical MR is comparable to CT and is capable of accurate measurement of ventricular chamber volumes, ventricular mass, and LVEF [6]. Myocardial perfusion imaging may also be achieved by contrast-enhanced MR which makes use of a gadolinium contrast agent [13]. This is important to assess fibrosis. For example, one study on CRT candidates have identified areas of fibrosis near potential lead placement locations and do not improve with CRT [12]. Gadolinium may also be used to enhance contrast of the ventricular chambers for volume measurements.

MR is also capable of higher temporal resolution that CT, acquiring on the order of 10 to 50 images per second, making it suitable for real-time imaging. In this study, images for model construction were derived from ECG-gated 4D image sequences of

the cardiac cycle (25 images per second). Typical in-plane spatial resolution was on the order of 1 mm with a slice thickness of 2 mm with 5 mm between each slice. A major advantage of MR is that it does not expose the subject to ionizing radiation.

Single-photon emission computed tomography

Single-photon emission computed tomography is a nuclear modality which relies on the radioactive signal of substances introduced to the body by inhalation, injection, or ingestion to produce images. These substances or radiotracers gain their source of the radioactivity from radionuclide labels attached to biochemically active drugs which are taken up by the tissues of imaging interest.

In HF cases with indications for ischemic etiology, SPECT measures local myocardial perfusion by the uptake of the radiotracer by the myocardium. Images of regional perfusion density are typically taken at resting and elevated (stress) heart rate. The difference between the resting and stress distributions gives a clear picture of the region of ventricular myocardial infarction. In addition, SPECT measures of dyssynchrony for CRT candidates have been correlated with echocardiographic measures to predict likely responders [1].

2.2 Methods

2.2.1 Finite element models of ventricular geometry

The objective of a multi-scale model of the heart is to quantitatively describe and analyze cardiovascular physiological processes over time and space, linking the behaviors of the cell to the organ, using mathematical and computational models. Finite element analysis is an ideal approach suited for this task, providing a mathematical framework for quantitative analyses of cardiac function including anatomy, biomechanics, electrophysiology, and hemodynamics. A fundamental component of this framework is a finite element mesh providing a realistic description of the three dimensional geometry of the ventricles. The mesh embodies the spatial domain for posing and solving the various mathematical models of physiology. Accurate and reliable solutions require the

meshes to be geometrically accurate and computationally stable.

A finite element mesh discretizes a continuous geometric domain into a collection of discrete sub-domains called *elements*. Within each element, spatial coordinates (or more generally any scalar, vector, or tensor *field variable*) are approximated by interpolation. Elements may take on a variety of shapes. Tetrahedral elements with linear interpolation are popularly used for a large class of solid and fluid mechanics problems on account of their simplicity, well-characterized properties, and wide availability of meshing and analysis software [8]. For problems of cardiovascular physiology, such as soft tissue mechanics and reaction-diffusion, however, this scheme is prone to numerical error without fine discretization of the spatiotemporal domain incurring greater computational cost [11]. Hexahedral elements, on the other hand, are more efficient in terms of solution stability and computational cost, though are less amenable to automatic mesh generation, especially for complex geometries. In this work, we utilize hexahedral finite elements with high-order cubic Hermite basis functions using recent techniques for handling complex geometries.

In a cubic Hermite finite element, the geometry is parameterized by the position and curvature (spatial derivatives) at each of the eight element vertices. Eight parameters or degrees of freedom are specified at each node for a total of 64 degrees of freedom per element. Elements are C^1 continuous, meaning that their coordinates and first derivatives vary continuously between neighboring elements. This feature allows us to smoothly approximate the geometry in a piecewise fashion over the total collection of elements in the mesh using cubic polynomial basis functions. The shape of a hexahedral element in real space $\mathbf{Y} = (Y_1, Y_2, Y_3)$ may be mathematically expressed as the weighted sum of basis functions and parameters with respect to the local element coordinate frame (parametric space) $\xi = (\xi_1, \xi_2, \xi_3)$ where $\xi \in [0,1]$:

$$\mathbf{Y}(\xi_1, \xi_2, \xi_3) = \sum_{l=1}^{8} \sum_{m=1}^{8} \phi_{lm}(\xi_1, \xi_2, \xi_3) \cdot \mathbf{y}_l(m), \tag{2.1}$$

$$\mathbf{y}_l = \left(\mathbf{y}, \frac{\partial \mathbf{y}}{\partial \xi_1}, \frac{\partial \mathbf{y}}{\partial \xi_2}, \frac{\partial \mathbf{y}}{\partial \xi_3}, \frac{\partial^2 \mathbf{y}}{\partial \xi_1 \partial \xi_2}, \frac{\partial^2 \mathbf{y}}{\partial \xi_1 \partial \xi_3}, \frac{\partial^2 \mathbf{y}}{\partial \xi_2 \partial \xi_3}, \frac{\partial^3 \mathbf{y}}{\partial \xi_1 \partial \xi_2 \partial \xi_3} \right), \tag{2.2}$$

$$\phi_{lm} = \psi_{1lm}(\xi_1) \cdot \psi_{2lm}(\xi_2) \cdot \psi_{3lm}(\xi_3), \tag{2.3}$$

where ϕ_{lm} is the triple-product of the 3D Hermite basis functions ψ_{nlm} in each local

element dimension ξ_n, for each local element node l, for which m Hermite parameters are defined in $\mathbf{y}_l$ (8 total parameters comprised of 1 value, 3 simple derivatives, 3 cross derivatives, and 1 triple-cross derivative). In the simple case of a 1D element with two nodes, each with two parameters, (2.1) expands to:

$$\mathbf{Y}(\xi) = \psi_1^0(\xi)y_1 + \psi_2^0(\xi)y_2 + \psi_1^1(\xi)\frac{\mathrm{d}y}{\mathrm{d}\xi}\Big|_1 + \psi_2^1(\xi)\frac{\mathrm{d}y}{\mathrm{d}\xi}\Big|_2, \tag{2.4}$$

with basis functions ψ_j^i

$$\begin{aligned} \psi_1^0 &= 1-3\xi^2+2\xi^3, \\ \psi_2^0 &= \xi^2(3-2\xi), \\ \psi_1^1 &= \xi(\xi-1)^2, \\ \psi_2^1 &= \xi^2(\xi-1), \end{aligned} \tag{2.5}$$

where index j refers to the local node conferred with C^i continuity by its corresponding basis function. The complete equations for three dimensional cubic Hermite basis functions may be derived from permutations of the triple-products of the 1D basis functions in (2.5) and are omitted here. More comprehensive coverage of cubic Hermite elements is given by Nielsen et al. [10] and Hunter et al. [4].

Specification of the parameters $\mathbf{y}_l$ with respect to the local element coordinate frame ξ ensures smoothness and continuity throughout the mesh, provided the elements are of identical unit size and shape. Since this is generally not the practical case in real geometries, continuity may be enforced by accounting for the actual element sizes according to their arc lengths. Nielsen proposed element "scale factors" to map the global element arc lengths $\mathbf{s}$ to the local element frame ξ [10]. In the case of a 2D quadrilateral cubic Hermite element with parameters $\frac{\partial \mathbf{Y}}{\partial \xi_1}$, $\frac{\partial \mathbf{Y}}{\partial \xi_2}$, and $\frac{\partial \mathbf{Y}}{\partial \xi_1 \xi_2}$, the scale factors may be related accordingly:

$$\begin{aligned} \frac{\partial \mathbf{Y}}{\partial \xi_1} &= \frac{\partial \mathbf{Y}}{\partial s_1}\frac{\mathrm{d}s_1}{\mathrm{d}\xi_1}, \\ \frac{\partial \mathbf{Y}}{\partial \xi_2} &= \frac{\partial \mathbf{Y}}{\partial s_2}\frac{\mathrm{d}s_2}{\mathrm{d}\xi_2}, \\ \frac{\partial^2 \mathbf{Y}}{\partial \xi_1 \xi_2} &= \frac{\partial^2 \mathbf{Y}}{\partial s_1 s_2}\frac{\mathrm{d}s_1}{\mathrm{d}\xi_1}\frac{\mathrm{d}s_2}{\mathrm{d}\xi_2}, \end{aligned} \tag{2.6}$$

where $\frac{\mathrm{d}s_1}{\mathrm{d}\xi_1}$ and $\frac{\mathrm{d}s_2}{\mathrm{d}\xi_2}$ are the element scaling factors. The scaling factors may be thought

of as tangent vectors in $\mathbf{Y}$ space that are coincidental with their corresponding nodal parameters in ξ at the global element nodes. Note that, by this definition, s_1 does not vary with ξ_2. The finite element model of ventricular geometry is fully defined by the local element parameters and scaling factors.

Gonzales et al. [3] generalized the above definition of scale factors to elements with so-called "extraordinary" vertices. As a consequence of scale factors definition in (2.6), continuity is enforced for elements defined by ordinary vertices which are required to have four neighboring vertices (valence 4). The motivation for the introduction of extraordinary vertices was to gain the ability to capture increasingly complex anatomical detail using cubic Hermite elements by introducing the possibility of new regional element topologies. Extraordinary vertices are allowed variable valence, typically 3 or 5. This new arrangement requires additional transformation components in the mapping from local to global parametric space, thereby requiring a "scale factor matrix".

The particular geometry of a finite element mesh may be customized or fitted to a patient's clinical images by solving for the Hermite parameters or degrees of freedom $\frac{\partial \mathbf{Y}}{\partial \mathbf{s}}$ throughout the mesh. We use a regularized least-squares fitting scheme to estimate the mesh parameters [2]:

$$F(\mathbf{u}) = \sum_d \|\mathbf{u}(\xi_d) - \mathbf{u}_d\|^2 + \int_\Omega \Big(\alpha_1 \left\| \frac{\partial \mathbf{u}}{\partial \xi_1} \right\|^2 + \alpha_2 \left\| \frac{\partial \mathbf{u}}{\partial \xi_2} \right\|^2 + \alpha_3 \left\| \frac{\partial^2 \mathbf{u}}{\partial \xi_1^2} \right\|^2 + \alpha_4 \left\| \frac{\partial^2 \mathbf{u}}{\partial \xi_2^2} \right\|^2 + \alpha_5 \left\| \frac{\partial^2 \mathbf{u}}{\partial \xi_1 \partial \xi_2} \right\|^2 \Big) \, \mathrm{d}\Omega, \tag{2.7}$$

where $\mathbf{u}$ is a vector of field variables (e.g. spatial coordinates $\mathbf{Y}$), d is an index over the data points (segmented image in this case), $\mathbf{u}_d$ is the value of the field for data point d, ξ_d are the parameters of the d^{th} data point projected onto the mesh surface, $\mathbf{u}(\xi_d)$ are the interpolated field values for data point d, Ω is the finite element domain, and α_k are Sobolev smoothing weights for the k^{th} derivative term. Smoothing weights were chosen to balance geometric accuracy and mesh smoothness [9]. Smoothing weights on the first and second derivatives may be intuitively understood as the resistance of the mesh surface to stretching and bending, respectively. Values for the weights are typically in the range of 10–0.1. More comprehensive guidelines for choice of smoothing weight

are described by Mazhari et al. [9].

2.2.2 Clinical image data

Eight male patients (ages 67, 71, 85) (74 ± 9 years) with left bundle branch block, NYHA class III heart failure, and dilated cardiomyopathy were enrolled from the Veteran's Administration San Diego Healthcare System (San Diego, CA) into an Institutional Review Board (IRB)-approved protocol after obtaining informed, written consent. End-diastolic cardiac anatomy was surveyed with CT (GE Lightspeed, GE Medical Systems, Milwaukee, WI, in-plane resolution of 0.49×0.49 mm, thickness 2.5 mm) in six patients and MR (in-plane resolution of 0.9×0.9 mm, thickness 7 mm) in two patients. Five patients with indications for myocardial ischemia underwent SPECT imaging (technetium sestamibi, ECAM-2, Siemens Medical Solutions, Hoffman Estates, IL, resolution of $6.59 \times 6.59 \times 1$ mm) during stress and rest states. Regions of myocardial infarction were identified from the images by an expert clinical electrophysiologist David E. Krummen.

2.2.3 Mesh fitting to clinical images

The ventricular myocardium in the end-diastolic state was segmented from the obtained images in a semi-automated fashion by intensity thresholding and 3D "snake" segmentation via geodesic level sets in ITK-SNAP (www.itksnap.org; [15]). The ventricular region of interest spans from the apex to the basal valve plane. Extraneous anatomical features such as trabeculae, papillary muscles, epicardium, fat, connective tissue were excluded. The segmented volume was triangulated via a marching-cubes algorithm in ITK-SNAP and smoothed using GAMer (www.fetk.org/gamer [14]). The final segmented volume was partitioned into epicardial, LV and RV endocardial, and septal surfaces.

Two types of cubic Hermite finite element meshes were constructed for each patient, one with ordinary and another with extraordinary vertices, for biomechanics and electrophysiology simulations, respectively. Gonzales et al. developed a technique extending cubic Hermite interpolation with C^0 and C^1 continuity to meshes with "ex-

traordinary" vertices [3]. Ordinary vertices are constrained to only four neighbors. Extraordinary vertices are more generally allowed 3 or 5 neighboring vertices. This allows greater freedom to arrange the mesh vertices to strategically conform to the natural local topologies (e.g. radial versus rectangular topology) of the modeled shape. This allows for a more compact and natural representation of curvilinear geometries by reducing the total number elements which are more uniformly shaped, improving the computational stability and accuracy of the solution and reducing computational cost. The two types of meshes are illustrated in Figure (2.2). A more comprehensive treatment on meshes with extraordinary vertices may be found in the work of Gonzales et al. [3].

The mesh with ordinary vertices (OV mesh) was constructed first. A 2D template mesh with 64 bi-linear elements was partitioned into LV and RV endocardial, septal, mid-wall, and epicardial surfaces. Each surface was manually "snapped" to its corresponding measured surface using the "Retopo" tool in Blender (www.blender.org). LV and RV endocardial, septal, mid-wall, and epicardial surfaces were fitted to their respective surface in the segmentation in prolate spheroidal coordinates. The μ and θ coordinates were held constant, the nodal parameters for λ were fit. the remaining Hermite derivative parameters were estimated by a regularized least-squares fitting scheme in (2.7). The fitted 2D surfaces were joined transmurally to form hexahedral cubic Hermite elements, and the mesh was refined to a final total of 128 elements.

The mesh with extraordinary vertices (EV mesh) was constructed from a 3D template mesh with 132 tri-linear elements was co-registered to the first mesh in Blender. Twelve extraordinary vertices of valence 3 were placed at approximately 1/3 of the apex to base distance on the endocardial and epicardial surfaces to form a rectangular "patch" topology at the apex. A total of 54 vertices of valence 5 were placed at the LV and RV septal junctions to form a rectangular topology at the interventricular septum. Each of the LV and RV anterior, lateral, and posterior walls are formed by a continuous rectangular patch topology of ordinary vertices. Vertices were snapped to the surfaces of a refined version of the OV mesh in Blender. Cubic Hermite parameters were computed by a subdivision scheme developed by Gonzales et al. [3]. Regions of normal and infarcted myocardium identified from the SPECT images were manually demarcated onto the segmented image volume and fitted as a binary scalar field in both meshes using the

above regularized fitting scheme.

2.3 Results

The finite element mesh templates with ordinary and extraordinary vertices were fitted to the segmented CT or MR images of each patient. Meshes with ordinary vertices are illustrated in Figure (2.4), and meshes with extraordinary vertices are shown in Figure (2.5). The spatial accuracy of the meshes was assessed by the RMS fitting error taken as the mean projection distance of the segmented image data to corresponding mesh surfaces. For all patients, iterative fitting of geometric nodal parameters was performed until the error was on the order of the in-plane voxel size ~ 1 mm. Manual placement of vertices of the EV mesh directly on to the fitted surfaces of OV mesh effectively ensured similar geometric accuracy of the EV meshes. Ventricular dimensions including left ventricular volume, long axis length, LV inner diameter, and septal and lateral LV wall thickness were also compared to echocardiographic measurements. Right ventricular dimensions were not measured in the echocardiography images and were not compared. A summary of the geometric comparisons is shown in Table (2.1). The scaled Jacobian J [16] was used as an element quality metric to ensure smooth and well-behaved numerical solutions; a value of 1 indicates an element as a perfect cube with orthogonal edges of equal length. All elements for all meshes satisfied $J > 0.6$. Regions of myocardial infarction from the SPECT images are illustrated in Figure (2.6).

2.4 Discussion

We developed a process for high-order finite element model construction of ventricular geometry from available clinical images. While in a research setting, high-fidelity data and models are desirable, for the prospect of being used in translational medicine, the cost of such model construction is an issue of utmost importance. This pipeline was developed with economic feasibility in mind, and therefore considered the appropriateness of use and overall cost of obtaining the clinical data as well as efficient computational methods for developing geometric models of patient-specific ventricles.

Improvements to the pipeline could incorporate automation of manual steps. For one, a single mesh template with ordinary or extraordinary topologies was manually fitted each time to patient image data. One method to automate this step could exploit ventricular mapping from an atlas to automatically generate a mesh of necessary quality by mapping one patient's image data set to another patient's. Work by Lamata et al. is an example of an automated method that is capable of rapidly producing meshes from 3D image data with spatial accuracy on the order of the image resolution [7]. The method presented in this chapter can be made independent of the data set, though at its current state the process has been optimized for using CT and MR images. The best clinical data set to obtain for geometric modeling is echocardiography for its low cost, widespread availability, and non-invasiveness. Image data from 2D and 3D echocardiography are able to be accommodated into this general meshing process.

2.5 Conclusion

The patient-specific geometry of dilated ventricles in DHF was modeled using available clinical image data and a high-order finite element method. Biventricular meshes with ordinary and extraordinary vertices were constructed for eight patients with accuracy on the order of the available clinical images. The geometric domain defined by the finite element meshes will serve as the basis for further continuum analyses of cardiovascular properties and function.

Acknowledgments

The content of this chapter comprises an original document. The author gives thanks to Andrew McCulloch, Adarsh Krishnamurthy, Jeffrey Omens, and Matthew Gonzales for discussions and suggestions regarding finite element modeling, as well as to David Krummen for discussions on clinical imaging.

Table 2.1: Geometric model validation to measured dimensions. Dimensions of the fitted OV mesh were compared to measurements obtained from imaging data. The following measurements were obtained from 2D echocardiography: LVLd – LV long dimension; IVSd – interventricular septal dimension; LVIDd – LV inner diameter dimension; LVPWd – LV posterior wall dimension. LV end-diastolic volume was obtained from CT/MR: LV EDV – LV end-diastolic volume.

	Measured Data					Model				
Patient	LVLd (cm)	IVSd (cm)	LVIDd (cm)	LVPWd (cm)	LV EDV (mL)	LVLd (cm)	IVSd (cm)	LVIDd (cm)	LVPWd (cm)	LV EDV (mL)
BiV1	9.32	0.74	5.15	0.98	242	9.66	1.18	6.89	0.99	270
BiV2	8.70	0.89	6.19	0.57	162	8.66	1.08	5.54	0.63	168
BiV3	8.22	1.48	6.34	1.29	256	9.98	0.91	6.97	1.03	319
BiV4	9.50	1.30	7.40	1.30	290	9.74	1.60	7.12	1.37	307
BiV5	10.20	1.57	6.38	1.52	238	9.11	1.50	6.67	1.56	225
BiV6	8.91	1.53	5.25	1.55	116	8.90	1.73	4.70	1.57	113
BiV7	9.44	1.04	4.13	0.88	200	8.88	1.87	4.80	1.54	240
BiV8	9.11	1.00	6.20	0.80	162	8.13	1.41	5.35	0.92	157

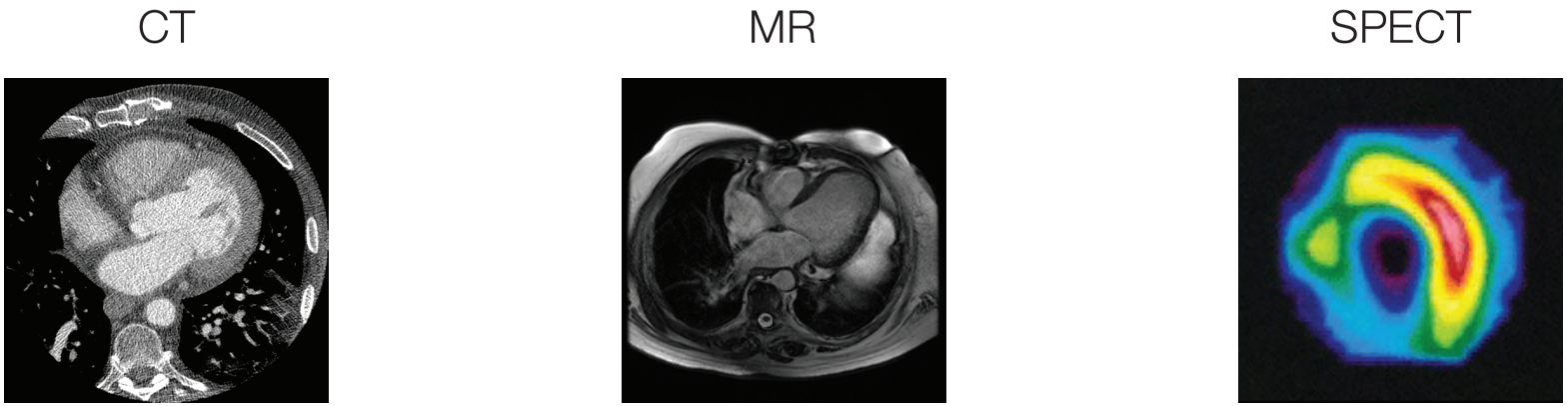

Figure 2.1: Clinical imaging modalities for modeling ventricular geometry. Examples of each different imaging modality used in this study: CT – computed tomography; MR – magnetic resonance; SPECT – Single-photon emission computed tomography.

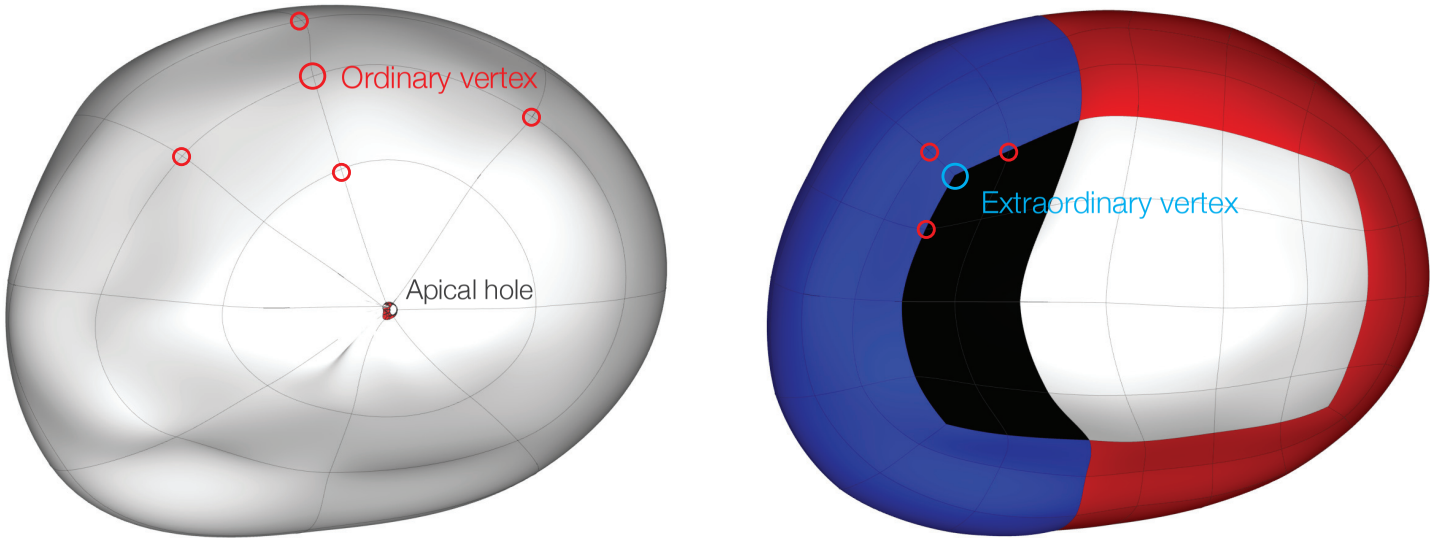

Figure 2.2: Meshes with ordinary (left) and extraordinary (right) vertices. Ordinary vertices are limited to valence 4; extraordinary vertices may have valence 3 or 5. In a biventricular mesh with ordinary vertices, epicardial elements assume a radial topology. Elements converge at the apex, and the valence 4 constraint requires a hole remaining at the apex. This results in poor element isotropy and introduces the possibility of spurious boundary conditions or singularities in mesh solutions. In a mesh with extraordinary vertices, the radial element topology at the apex is replaced with a rectangular patch with elements that are more isotropic and uniform. Transitions between element topologies occur at extraordinary vertices placed at saddle points.

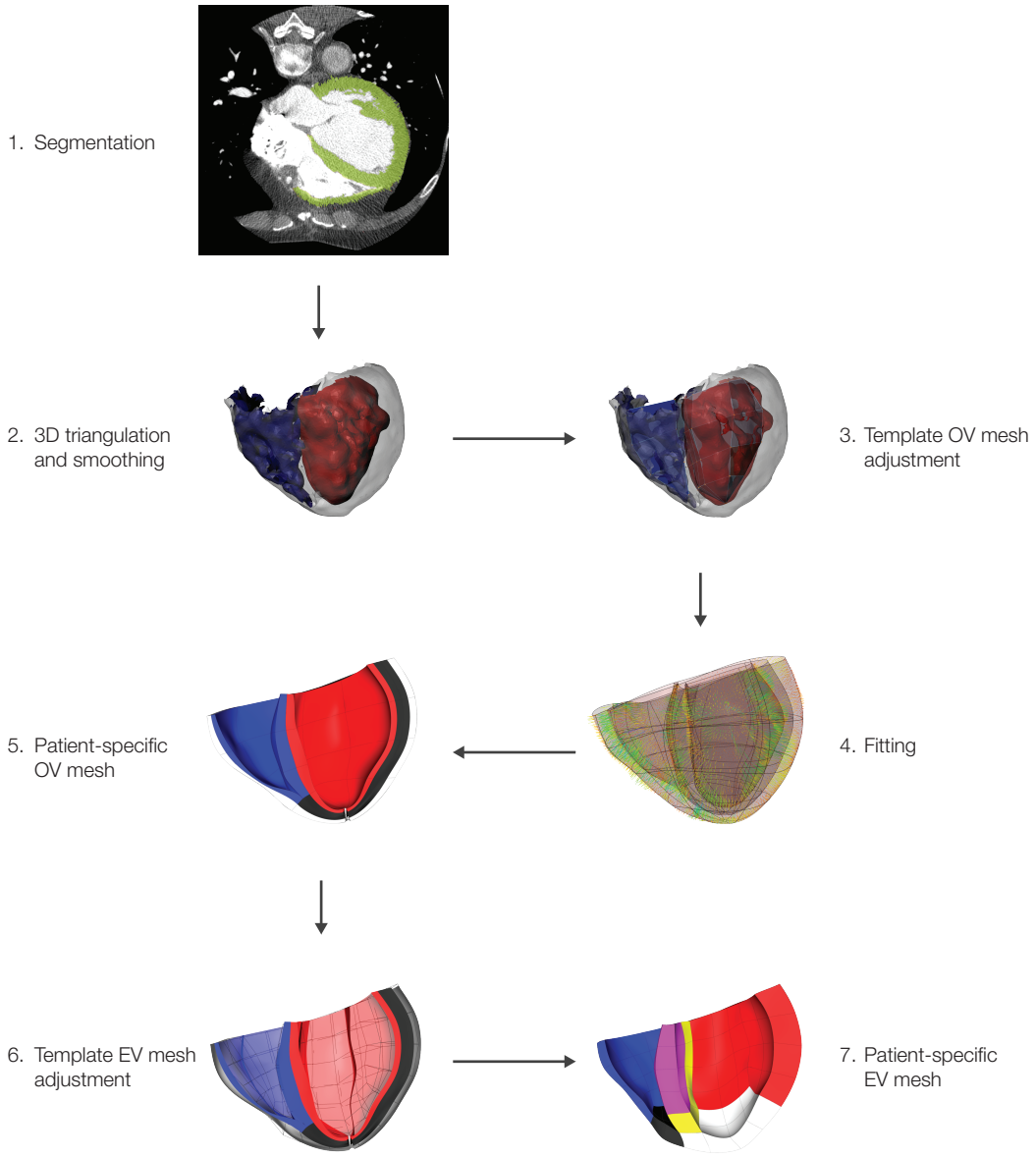

Figure 2.3: Summary of mesh construction from 3D image data. 1) Image voxels containing ventricular myocardium are masked using segmentation software (i.e. ITK-SNAP). 2) A smooth 3D triangulation is computed using the segmentation software, and endocardial and epicardial surfaces are extracted. 3) The 2D template OV mesh with linear quadrilateral elements is manually snapped on to the extracted surfaces. 4) The 2D mesh is iteratively fitted to the segmented surfaces by computing cubic Hermite mesh parameters that minimize (2.7). 5) The fitted quadrilaterals are converted to hexahedral elements, and the patient-specific OV mesh is obtained. 6) A 3D template EV mesh with linear hexahedral elements is manually snapped on to the surfaces of the OV mesh. 7) Cubic Hermite scale factors are computed, and the patient-specific EV mesh is obtained.

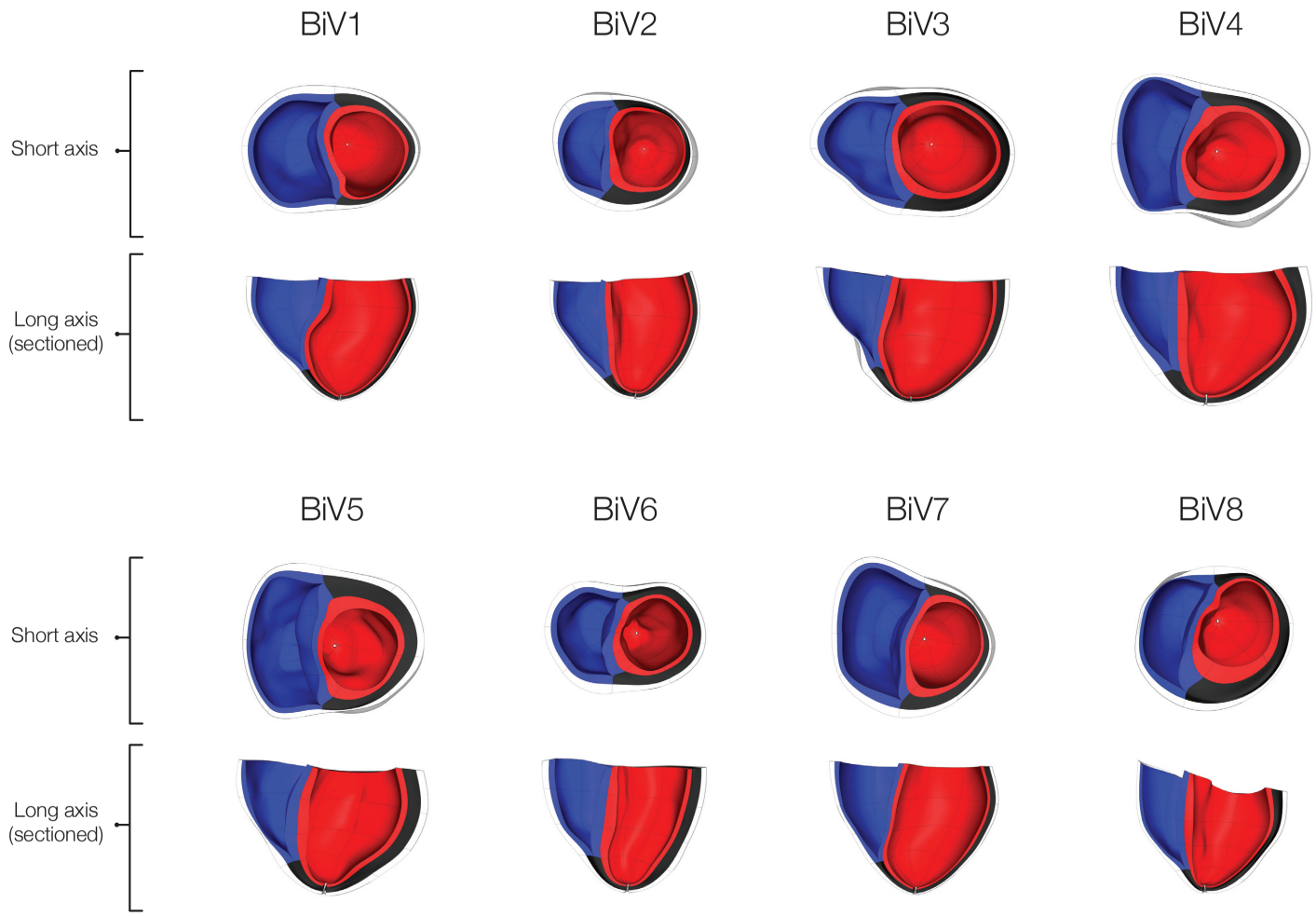

Figure 2.4: Patient-specific finite element meshes with ordinary vertices. Myocardial regions include LV endocardium (red), RV endocardium (blue), mid-wall myocardium (black), and epicardium (white).

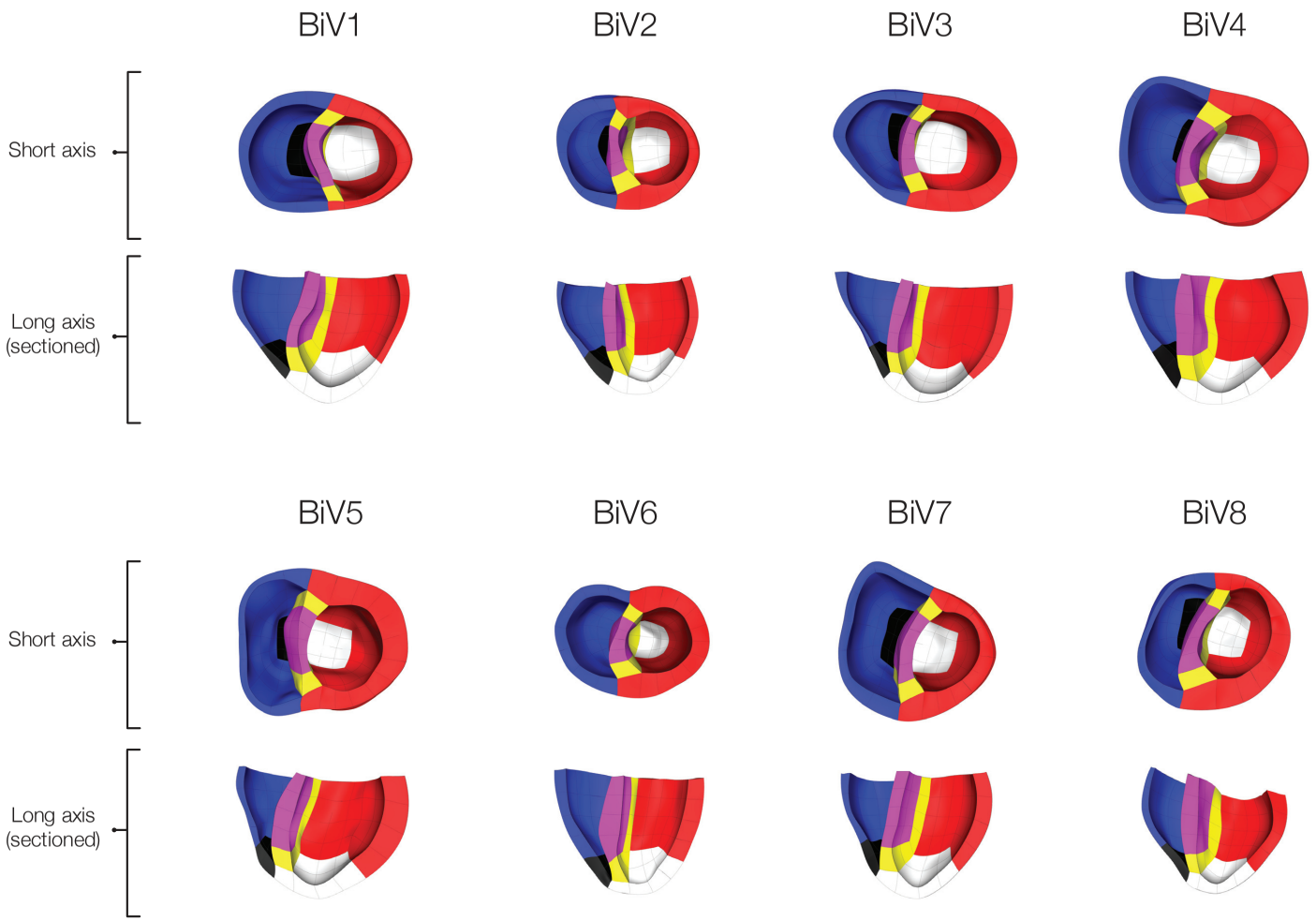

Figure 2.5: Patient-specific finite element meshes with extraordinary vertices. Topology regions include LV free wall (red), LV apex (white), RV free wall (blue), RV apex (black), interventricular septal junction (yellow), and interventricular septum (magenta).

Figure 2.6: Patient-specific myocardial infarctions. SPECT images at rest and stress states were used to manually mask the infarct region on to the image segmentation. The masked voxels were fitted as a binary 3D scalar field in the geometric mesh. Normal regions are colored blue, and infarct regions are colored black.

Bibliography

1. Boogers, M. M., Van Kriekinge, S. D., Henneman, M. M., Ypenburg, C., Van Bommel, R. J., Boersma, E., Dibbets-Schneider, P., Stokkel, M. P., Schalij, M. J., Berman, D. S., 2009. Quantitative gated spect–derived phase analysis on gated myocardial perfusion spect detects left ventricular dyssynchrony and predicts response to cardiac resynchronization therapy. Journal of Nuclear Medicine 50 (5), 718–725.

2. Fernandez, J., Mithraratne, P., Thrupp, S., Tawhai, M., Hunter, P., 2004. Anatomically based geometric modelling of the musculo-skeletal system and other organs. Biomechanics and modeling in mechanobiology 2 (3), 139–155.

3. Gonzales, M. J., Sturgeon, G., Krishnamurthy, A., Hake, J., Jonas, R., Stark, P., Rappel, W.-J., Narayan, S. M., Zhang, Y., Segars, W. P., 2013. A three-dimensional finite element model of human atrial anatomy: new methods for cubic hermite meshes with extraordinary vertices. Medical image analysis 17 (5), 525–537.

4. Hunter, P., Pullan, A., 2001. Fem/bem notes. Department of Engineering Science, The University of Auckland, New Zeland.

5. Hutchins, G. M., Bulkley, B. H., Moore, G. W., Piasio, M. A., Lohr, F. T., 1978. Shape of the human cardiac ventricles. The American journal of cardiology 41 (4), 646–654.

6. Jenkins, C., Moir, S., Chan, J., Rakhit, D., Haluska, B., Marwick, T. H., 2009. Left ventricular volume measurement with echocardiography: a comparison of left ventricular opacification, three-dimensional echocardiography, or both with magnetic resonance imaging. European heart journal 30 (1), 98–106.

7. Lamata, P., Niederer, S., Nordsletten, D., Barber, D. C., Roy, I., Hose, D., Smith, N., 2011. An accurate, fast and robust method to generate patient-specific cubic hermite meshes. Medical image analysis 15 (6), 801–813.

8. Löhner, R., 1997. Automatic unstructured grid generators. Finite Elements in Analysis and Design 25 (1), 111–134.

9. Mazhari, R., Omens, J. H., Waldman, L. K., McCulloch, A. D., 1998. Regional myocardial perfusion and mechanics: a model-based method of analysis. Annals of biomedical engineering 26 (5), 743–755.

10. Nielsen, P., Le Grice, I., Smaill, B., Hunter, P., 1991. Mathematical model of geometry and fibrous structure of the heart. Am. J. Physiol 260 (29), H1365–H1378.

11. Pathmanathan, P., Gavaghan, D., Whiteley, J., 2009. A comparison of numerical methods used for finite element modelling of soft tissue deformation. The Journal of Strain Analysis for Engineering Design 44 (5), 391–406.

12. Roes, S. D., Borleffs, C. J. W., van der Geest, R. J., Westenberg, J. J., Marsan, N. A., Kaandorp, T. A., Reiber, J. H., Zeppenfeld, K., Lamb, H. J., de Roos, A., 2009. Infarct tissue heterogeneity assessed with contrast-enhanced mri predicts spontaneous ventricular arrhythmia in patients with ischemic cardiomyopathy and implantable cardioverter-defibrillator. Circulation: Cardiovascular Imaging 2 (3), 183–190.

13. Valle-Muñoz, A., Estornell-Erill, J., Soriano-Navarro, C. J., Nadal-Barange, M., Martinez-Alzamora, N., Pomar-Domingo, F., Corbí-Pascual, M., Payá-Serrano, R., Ridocci-Soriano, F., 2009. Late gadolinium enhancement–cardiovascular magnetic resonance identifies coronary artery disease as the aetiology of left ventricular dysfunction in acute new-onset congestive heart failure. European Journal of Echocardiography, jep115.

14. Yu, Z., Holst, M. J., Cheng, Y., McCammon, J. A., 2008. Feature-preserving adaptive mesh generation for molecular shape modeling and simulation. Journal of Molecular Graphics and Modelling 26 (8), 1370–1380.

15. Yushkevich, P. A., Piven, J., Hazlett, H. C., Smith, R. G., Ho, S., Gee, J. C., Gerig, G., 2006. User-guided 3d active contour segmentation of anatomical structures: significantly improved efficiency and reliability. Neuroimage 31 (3), 1116–1128.

16. Zhang, Y., Bajaj, C., 2006. Adaptive and quality quadrilateral/hexahedral meshing from volumetric data. Computer methods in applied mechanics and engineering 195 (9), 942–960.

Chapter 3

Patient-specific Models of Ventricular Anatomy
Part II: Fiber Architecture

Abstract

Patient-specific models of the cardiac ventricles require a realistic representation of the myocardial fiber architecture to accurately capture the regional variation of anisotropic biomechanical and electrophysiological properties. The fiber architecture can be measured using diffusion tensor magnetic resonance imaging, however *in vivo* measurements are currently impractical to obtain for individual patients. The aim of this chapter is to develop a method for constructing the fiber architecture of a ventricular fiber atlas defined by an *ex vivo* human donor heart and mapping the result to patient-specific geometric models.

Human cardiac ventricles provided by an organ donor heart were subject to a diffusion-weighted magnetic resonance scan. Measurements were registered into a corresponding geometric model of the ventricles and fitted using a log-Euclidean interpolation framework. Local material coordinates axes representing the fiber, sheet, and sheet-normal directions of the myocardium were defined by the principal directions of interpolated diffusion tensors. A measure of dyadic tensor overlap was used to quan-

tify the error between measured and interpolated principal directions; 74% of the fitted tensors (112,419 of 152,651 voxels) had average errors of $12.5^\circ \pm 7^\circ$ in the fiber, $20^\circ \pm 11.5^\circ$ in the sheet, and $18^\circ \pm 11.6^\circ$ in the sheet-normal directions. Finally, the fiber architecture in patient-specific ventricular geometries was estimated by large deformation diffeomorphic mapping from the model of the organ donor ventricles.

3.1 Introduction

Cardiomyocytes are structured within the ventricular myocardium according to a complex architecture that is important for the electrical, mechanical, and hemodynamic properties at the tissue and organ scales. A realistic, quantitative description of this fiber architecture is therefore necessary in a patient-specific, multi-scale model of ventricular anatomy. Patient-specific models can be constructed feasibly from clinical data thanks to advances in computing power and technology [34, 1, 23, 22, 21, 30]. Where patient-specific clinical data are not available, approximations must be made with empirical data. Diffusion tensor magnetic resonance imaging (DT-MRI) is a conventional non-invasive imaging modality for measuring the underlying microstructure of biological tissue with high spatial resolution. However, DT-MRI is not routinely available in the clinic, nor is it feasible to obtain *in vivo* measurements for an individual patient. In this chapter, we review the description of cardiac tissue microstructure and how it is measured with DT-MRI. We present a method for incorporating DT-MRI measurements of an excised human ventricle into patient-specific models.

3.1.1 Myocyte organization in cardiac tissue

Important functional aspects of cardiac tissue emerge as a result of the properties and spatial organization of its cellular constituents. Cardiac tissue is composed of various kinds of cells, primarily myocytes and fibroblasts, embedded in a structural network of collagen and elastin fibers called the extracellular matrix (ECM). Myocytes are responsible for producing contractile force when excited electrically by action potentials. Fibroblasts and cardiofibroblasts maintain the integrity of the ECM, mediate inflammatory responses, and develop fibrosis in tissue injury.

Ventricular myocytes constitute the majority of the heart muscle by volume, numbering close to 7 billion cells in a healthy human heart [25]. A myocyte is approximately cylindrical in shape with branched appendages, measuring about 50–150 μm in length (longitudinal or "fiber" direction) and 10–20 μm in diameter (transverse or "cross-fiber" direction). A single myocyte attaches to an average of ten neighboring myocytes at intercalated disks distributed throughout its sarcolemma. Protein junctions at the intercalated disks provide mechanical and electrical coupling between myocytes: desmosomes anchor neighboring sarcolemmas together, and low-resistance gap junctions allow flow of ions and other small molecules between the sarcoplasms of neighboring cells. Intercalated disks are more abundant at the longitudinal ends of the myocyte (70%) but are also found transversely (30%) [27]. This anisotropic spatial distribution at the cell level is partly responsible for anisotropic properties at the tissue level, where passive stiffness (3:1 ratio) and electrical conductance (3:1 ratio) are greater in the fiber than the transverse direction.

Collagenous fibers of the ECM provide higher ordering of myocytes. Collagen fiber thickness ranges from 40 nm in normal conditions and up to 300 nm in pathologic conditions [7]. Endomysial collagen fibers surround individual myocytes and bind it to its neighbors. Perimysial collagen envelops groups of myocytes into laminar sheets approximately 3-4 cells thick [17]. The laminar sheets are separated from each other by vacuous cleavage planes but remain loosely tethered by long perimysial collagen. The degree of sheet coupling varies throughout the ventricle and introduces another source of mechanical and electrical anisotropy. Loose sheet coupling contributes to slowed conduction in the direction normal to the sheet plane [17, 15]. It also allows greater deformability (shearing) of the myocardium, particularly at the endocardium where substantial wall thickening is attributed to sheet sliding and reorientation [31, 8].

Variation of fiber-sheet orientation throughout the ventricle occurs in a characteristic pattern which has been shown to be remarkably conserved between species [19], suggesting its fundamental importance for whole organ function. Streeter et al. [32] first observed a smooth rotation of fiber orientation across the ventricular wall in canine hearts, varying from -70° to 60° (relative to the circumferential direction) from the epicardium to endocardium; fibers wrap around the ventricle in a left-handed helix at the

epicardium and a right-handed helix at the endocardium. Sheets and cleavage planes are oriented radially through the wall [17], remaining within 45° of the normal to the epicardial tangent plane [8]. While these orientational trends are generally observed, they can vary to a greater extent depending on the ventricular region [29] and even change discontinuously [12] which may have important local consequences on tissue properties. The overall architecture influences the anisotropic conduction of action potentials and biomechanical stress and strain distributions throughout the ventricular myocardium.

3.1.2 Diffusion-weighted imaging of fiber orientation

Measurements of myocardial fiber-sheet orientations have relied on histological [32] and optical [28] techniques for prepared chunks of tissue. More recent imaging modalities are capable of making whole-heart measurements in high spatial resolution. Diffusion tensor magnetic resonance imaging (DT-MRI) spatially maps the extent of proton movement in fluid-permeated anisotropic media like biological tissue. Proton movement is carried by Brownian motion or diffusion of water molecules along mean free paths constrained by the local microstructure (e.g. intracellular compartments, cell membranes, ECM). In DT-MRI, the measured MR signal (i.e. intensity) at each image voxel is weighted by the magnitude and relative orientation of diffusion along a known direction within a given time. Diffusion-weighted images are captured for at least six independent directions and are used to estimate an effective 3D diffusion tensor for every voxel. For more details on DT-MRI physics and principles, see Basser et al. [5].

The diffusion tensor $\mathbf{D}$ relates the macroscopic concentration gradient $\nabla\mathbf{C}$ to the macroscopic diffusion flux $\mathbf{J}$ in an anisotropic medium:

$$\mathbf{J} = -\mathbf{D}\nabla\mathbf{C}, \tag{3.1}$$

where

$$\mathbf{D} = \begin{vmatrix} D_{xx} & D_{xy} & D_{xz} \\ D_{yx} & D_{yy} & D_{yz} \\ D_{zx} & D_{zy} & D_{zz} \end{vmatrix} \tag{3.2}$$

$\mathbf{D}$ is a 3×3 symmetric, positive-definite covariance matrix of voxel-averaged flux coefficients (mm^2/s); diagonal terms scale fluxes and concentration gradients in the same

directions, and off-diagonal terms couple fluxes and concentration gradients in orthogonal directions. The orientation of the surrounding tissue structure can be measured by the principal directions or eigenvectors **v** of **D** [3]. Figure (3.1) illustrates a geometric representation of the diffusion tensor. Comparison of histological and DT-MRI measurements of fiber orientation have confirmed that the fiber axis coincides with the primary principal direction [16, 29, 14] and the sheet-normal axis coincides with the tertiary principal direction [12].

By this relationship, we may construct a model of ventricular fiber architecture by registering (fitting) DT-MRI measurements in a finite element geometry of the corresponding ventricles. Fiber, sheet, and sheet-normal directions in the model can be defined by the local eigenvectors of the fitted **D**. Methods and strategies for tensor interpolation and local fiber-sheet axis parameterization are required. It is also important to note that **D** assumes voxel-averaged representation of diffusion (intra-voxel fiber orientation populations are smeared out) and does not vary with time.

3.1.3 Estimation of *in vivo* human fiber architecture

A current limitation of DT-MRI is its inability to make reliable, high quality *in vivo* measurements of the beating, moving heart. An alternative strategy for incorporating DT-MRI measurements of fiber architecture into a patient-specific computational model may use an explanted human heart, especially from a human organ donor, as an atlas which can be subsequently mapped to the specific ventricular geometry of *in vivo* patient hearts.

A recent statistical analysis [19] of fiber architecture variation in a large population of human hearts has shown that fiber orientations are well-preserved between individuals. This suggests that it is reasonable to model the fibers in a patient-specific anatomy with measurements from another human heart after accounting for the variations in fiber orientation due to differences in ventricle size and shape. Geometric shape changes can be quantified between the anatomical models of the donor and patient-specific hearts by large deformation diffeomorphic maps (LDDMs). Diffeomorphic transformations are smooth one-to-one mappings of one anatomical model domain to another that preserve geometric features. Smoothness and bijectivity ensure that con-

tours remain contours, surfaces remains surfaces, and volumes remain volumes through the transformation.

A caveat of this approach is the rare availability of explanted hearts from healthy human organ donors; pristine specimens are typically reserved for transplantation rather than research. A single organ donor heart was acquired for the present study. The heart was used in accordance with the requirements of the Institutional Review Board under a condition of nondisclosure regarding the health state of the heart prior to donation.

3.2 Methods

3.2.1 Diffusion-weighted imaging study

The explanted donor heart was subjected to a DT-MRI scan (3T Discovery MR 750, GE Medical Systems, Milwaukee, WI) which utilized a novel three-dimensional fast spin echo pulse sequence with variable density spiral acquisition to efficiently eliminate eddy current and motion artifacts [11]. The field of view was 12 cm with a resolution of $0.93 \times 0.93 \times 2$ mm resolution ($128 \times 128 \times 56$ voxels). Diffusion gradients were applied in 32 non-collinear directions with a b value of 1000 s/mm^2. Scan duration was 2 hours with a TR of 1000 ms. Image reconstruction required a special least squares algorithm to correctly invert the non-uniformly sampled data was performed in parallel on a Linux cluster [11].

3.2.2 Model of ventricular geometry

Hexahedral cubic-Hermite finite element meshes of the ventricular geometries for the each patient and the explanted donor heart were constructed from the clinical and empirical image data. Endocardial and epicardial contours (left ventricle, right ventricle, septum, and epicardium) of the patient hearts at end-diastole were manually segmented from the CT images. The contours of the donor heart were segmented from fractional anisotropy (FA) images of the DT-MRI scan to differentiate between myocardial and pericardial tissue such as fat; the two are otherwise indistinguishable in the null gradient images. Clear identification of myocardium was necessary to prevent modeling noise

from diffusion directions from non-myocardial regions.

The 3D coordinates of the segmented voxels were reconstructed to generate a cloud of points representing left and right ventricular, septal, and epicardial surfaces. The cloud was reoriented such that the base of the heart was parallel to the horizontal plane and the long axis passed through the apex of the left ventricle; this ensures consistent application of displacement and pressure boundary conditions to the final constructed patient meshes.

An initial 2D cubic-Hermite template mesh (129 nodes, 108 elements) consisting of four nested surfaces representing the endocardial and epicardial surfaces was defined in prolate spheroidal coordinates. The geometry of the template mesh was pre-fitted to each patient by placing the nodes at common anatomical landmarks (left ventricular free wall, right ventricular free wall, base, apex, and the septum-right ventricular junctions) to preserve the structure of the mesh relative to each heart. Following the methods of Nielsen and colleagues [24], the pre-fitted meshes were fitted in the radial (λ) coordinate to the reconstructed data by a linear least squares minimization of the projection distance of the data to the interpolated mesh surfaces parameterized at the nodes; fitting in only the λ coordinate has the advantage of reducing the number of degrees of freedom of the fit.

The fitted surfaces were converted to hexahedral cubic-Hermite elements in rectangular Cartesian coordinates and refined transmurally to a final resolution of 209 nodes and 128 elements (5,016 geometric degrees of freedom). The accuracy of the results was verified by ensuring that the remaining RMS projection error was on the order of the spatial resolution of the image data (0.48 mm) and the LV cavity volume agreed to within %5 of the measured volume from the clinical data.

The DT-MRI measurements were registered into the anatomic mesh by first segmenting the myocardial area from the FA images described previously. In order to exactly align the segmented image volume with the anatomical model, overlapping voxels in the area and contour masks were used to compute the 4×4 affine transformation matrix T to rotate and translate the segmented volume. Since we are dealing with tensor images, the tensors themselves need to be reoriented to correct for the alignment to the anatomical model. A rotated tensor $\mathbf{D}'$ is computed by applying the rotational

component $\mathbf{R}$ of the affine transformation by $\mathbf{D}' = \mathbf{R}^T\mathbf{D}\mathbf{R}$. The rotated tensor $\mathbf{D}'$ was finally transformed to $\mathbf{L}'$ in LE space, and their independent components were fitted by the same methods as the anatomical models.

3.2.3 Diffusion tensor fitting and interpolation

Tensor interpolation is complicated by a number of factors. Tensor fields interpolated in usual Euclidean space are corrupted by null, non-positive-definite, and swollen tensor artifacts [9] which have no physical meaning and unrepresentative of real tissue structure [10]. Affine invariant Riemannian frameworks have been proposed which overcome these artifacts but are computationally expensive [26]. Tensor interpolation using a Log-Euclidian (LE) framework has the advantage of being much simpler to implement while preserving the positive definiteness, symmetry, and determinant of the diffusion tensor [2]. In the LE framework, the diffusion tensor $\mathbf{D}$ is transformed to $\mathbf{L}$ by the matrix logarithm: $\mathbf{L} = \log(\mathbf{D})$; the symmetry and positive-definiteness of $\mathbf{L}$ is preserved. Computations in LE space such as interpolation of the components of $\mathbf{L}$ proceed in the same fashion as scalar quantities in Euclidian space.

The fiber architecture model takes advantage of this implementation by directly interpolating the six independent components of $\mathbf{L}$ as separate 3D scalar fields fitted to the log-transformed components of the DT-MRI measurements in the domain of the finite element mesh. A locally interpolated $\mathbf{D}$ is recovered by reassembling $\mathbf{L}$ from the locally interpolated log fields and transforming it to Euclidian space by the matrix exponential $\mathbf{D} = \exp(\mathbf{L})$. $\mathbf{D}$ is finally decomposed into λ_i and v_i to obtain the fiber-sheet material axes. Figure (3.4) illustrates the result of this implementation strategy.

3.2.4 Diffeomorphic mapping of fiber architecture

The present method employs high-order finite element 3D kinematic analysis to compute a parametrically represented large deformation diffeomorphic map between the host and target anatomical geometries. A diffeomorphic map f transforms a material point $\mathbf{Y}$ in the host domain to point $\mathbf{y}(\mathbf{Y})$ in the target domain. The transformation f in a kinematic sense is equivalent to a field of deformation gradients $\mathbf{F} = \partial y_i/\partial Y_j$

$i, j = 1, 2, 3$. Smoothness is satisfied if the Jacobian of $\mathbf{F}$ is nonsingular everywhere. The relative smoothness of f can be measured in terms of its harmonic energy [36] which is defined as the spatial averaging of the squared Frobenius norm of the Jacobian.

Application of the diffeomorphic transformation f on the fiber architecture requires a material coordinate reorientation strategy. The most suitable strategy is the so-called preservation of principal directions (PPD). Compared to the finite strain (FS) strategy, PPD reorients the fibers in a way that is more representative of the mechanical deformation in the reshaping of the donor anatomy to the patient anatomy. In addition to the rotational component of $\mathbf{F}$, PPD accounts for reorientation due to axial stretch and compression.

The fiber architecture transformation was implemented by calculating $\mathbf{F}$ between the donor model and a patient model at the locations of the previously registered DT-MRI measurements. The interpolated material coordinate axes at these locations were reoriented according to the PPD strategy and recomposed into diffusion tensors $\mathbf{D}'$ using the original λ_i; preservation of the eigenvalues is reasonable as it implies that tissue anisotropy is maintained during the deformation ([6]). The reoriented tensors were registered in the patient model and the local material coordinate system was computed in the same manner as the donor heart.

3.3 Results

The DT-MRI measurements $\mathbf{D}$ of the donor heart were registered into its corresponding geometric model by fitting a linear variation of the six components of $\mathbf{L}$ as separate scalar nodal fields. An interpolated tensor $\mathbf{D_i}$ at a given location within an element was recovered by taking the matrix exponential of the interpolated components of $\mathbf{L}$. Material axes v_i were computed by eigen decomposition of $\mathbf{D_i}$. Interpolated tensors in the fitted donor heart are illustrated in Figure (3.6).

Since the fiber model only computes the eigenvectors of $\mathbf{D_i}$, the quality of the fit was measured by a dyadic tensor overlap metric [4] between $\mathbf{D_i}$ and $\mathbf{D}$ for all registered DT measurements within the geometric model:

$$\text{overlap} = \frac{\sum_{i=1}^{3} \lambda_i \lambda_i' \left(v_i \cdot v_j\right)^2}{\sum_{i=1}^{3} \lambda_i \lambda_i'} , \tag{3.3}$$

where λ_i and v_i are the principal components and directions of the compared tensors; the metric is essentially a weighted average of the dot products between the principal diffusion axes, where a maximum value of 1 indicates perfect overlap. The frequency of the overlap metric for all registered measurements is shown in the histogram in Figure (3.7). Linear interpolation of the LE components of $\mathbf{D_i}$ in the cubic-Hermite domain of the donor model registered 74% (112,419 of 152,651 voxels) of the DT measurements with an overlap greater than 0.7; the highest agreement was located in the LV, septum, and apex Figure (3.8). In terms of angles, average errors were $12.5^\circ \pm 7^\circ$ in the fiber, $20^\circ \pm 11.5^\circ$ in the sheet, and $18^\circ \pm 11.6^\circ$ in the sheet-normal directions. Linear basis functions apparently are sufficient to capture the characteristic variation of fiber and sheet orientation where the quality of measurements is high. Areas of poor overlap occurred in the RV where DT measurements were less reliable.

Diffeomorphic maps were computed as distributions of large deformation gradients between the host geometry and each of the patient-specific geometries at the element locations of the registered DT data. Local interpolated fiber-sheet material coordinates in the host geometry were reoriented according to the PPD strategy using the local deformation gradients. The reoriented axes were fitted in each of the patient-specific geometries. The result of one patient is illustrated in Figure (3.9)

3.4 Discussion

In the present study, we used human DT-MRI measurements of an *ex vivo* heart to reconstruct an atlas of the fiber-sheet anatomy that was mapped to patient-specific models to define local material coordinate axes. This strategy is valid since it has been shown that fiber architecture is conserved over a wide range of conditions between individuals [19]. However, we did not take into account the disease state of the patients' hearts which have been shown to exhibit increased dispersion in fiber directions [20].

Recently, *in vivo* DT-MRI measurements [33] were used to reconstruct my-

ocardial fiber architecture. Those workers used a diffeomorphic demons algorithm to map DT-MRI measurements to a prolate-spheroidal model of the left ventricle and an anisotropic kernel estimator to interpolate regions of sparse measurements from the mid ventricle to the apex. However, reliable measurements were restricted by the image quality to the region between the base and mid-ventricle where cardiac motion was at a minimum. Nevertheless, there is the promise to reconstruct patient-specific models of *in vivo* fiber architecture, with improved *in vivo* imaging. The techniques used here should be useful for registering and interpolating *in vivo* DT-MRI data.

We were unable to quantitatively validate the reconstructed fiber anatomy with histological measurements, though others have reported good agreement between fiber and sheet-normal directions with the principal directions (primary and tertiary, respectively) of water diffusion measured using DT-MRI [29, 12, 13]. We also cannot validate the registration of the ex-vivo data to the patient-specific cardiac model, however other workers have validated the use of diffeomorphic [35] and statistical [18] maps and similar tensor reorientation strategies to map the myofiber architecture between anatomical models.

3.5 Conclusion

We have demonstrated a feasible method for creating patient-specific models of fiber architecture using DT-MRI measurements from an *ex vivo* human heart atlas. The ability to make reliable estimates of patient-specific fiber architecture by mapping techniques will enhance as databases of cardiac fiber atlases from more patients are constructed. The resulting estimates of fiber architecture in patient-specific geometries will facilitate the modeling of anisotropic properties of electrophysiology and biomechanics.

Acknowledgments

The content of this chapter has been modified from a peer-reviewed publication to reflect the author's contribution to the work; the citation is Krishnamurthy A, Villongco CT, Chuang J, Frank LR, Nigam V, Belezzuoli E, Stark P, Krummen DE,

Narayn S, Omens JH, McCulloch AD, Kerckhoffs RCP, “Patient-specific models of cardiac biomechanics,” *Journal of Computational Physics* 2013. The author is indebted to Elliot Howard for performing the diffusion-weighted magnetic resonance scan of the excised human heart, and to Lawrence Frank and his research group for developing the diffusion-weighted magnetic resonance pulse sequence and image reconstruction algorithms and resources that resulted in a pristine human fiber data set. Thanks is also given to Andrew McCulloch for developing the ideas regarding the implementation of the diffusion tensor material coordinate model.

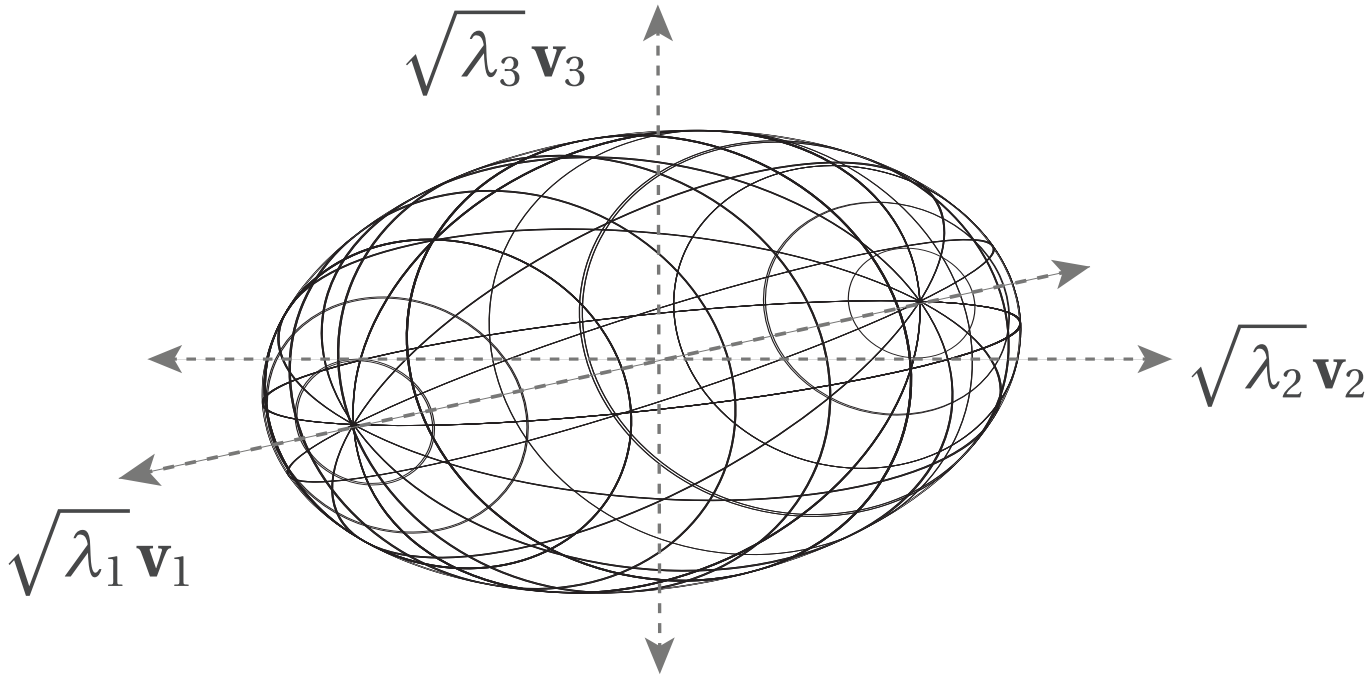

Figure 3.1: Geometric representation of a diffusion tensor. The diffusion tensor may be represented by an ellipsoid whose principal axes $\mathbf{v}$ coincide with the fiber, sheet, and sheet-normal directions of the cardiac fiber-sheet microstructure. The principal values λ determine the fiber (largest value), sheet, and sheet-normal directions. The lengths of the principal semi-axes are given by $\sqrt{\lambda}\mathbf{v}$.

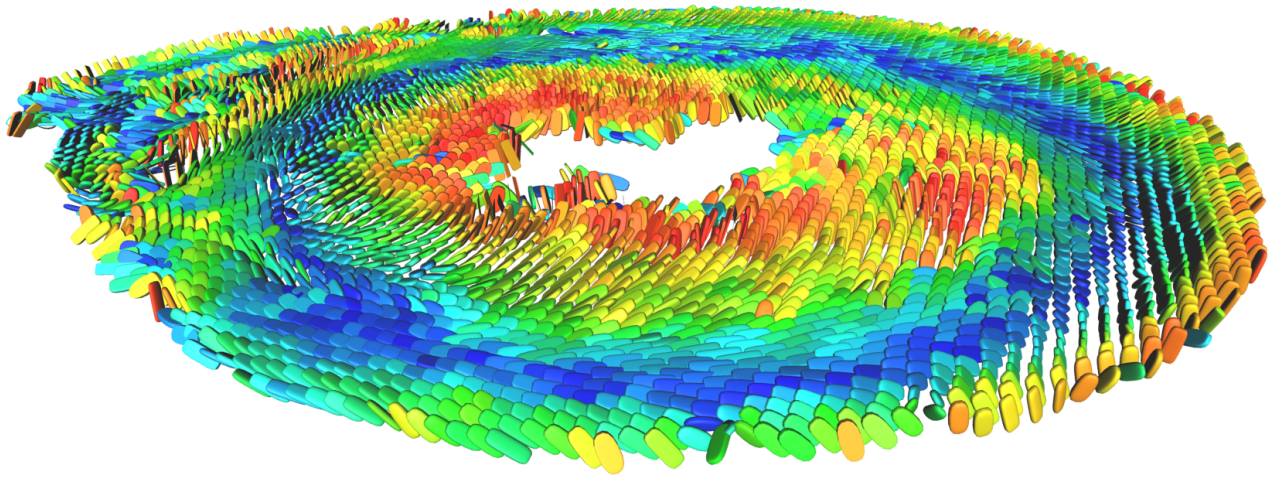

Figure 3.2: Short-axis slice of reconstructed diffusion tensors. The example slice is located in the LV of the explanted donor heart. The tensors are represented by glyphs whose axes are scaled by the eigenvalues and surfaces are colored by the orientation of the primary eigenvector with respect to the circumferential axis; blue indicates circumferentially oriented fiber directions, and red indicates longitudinally oriented fiber directions.

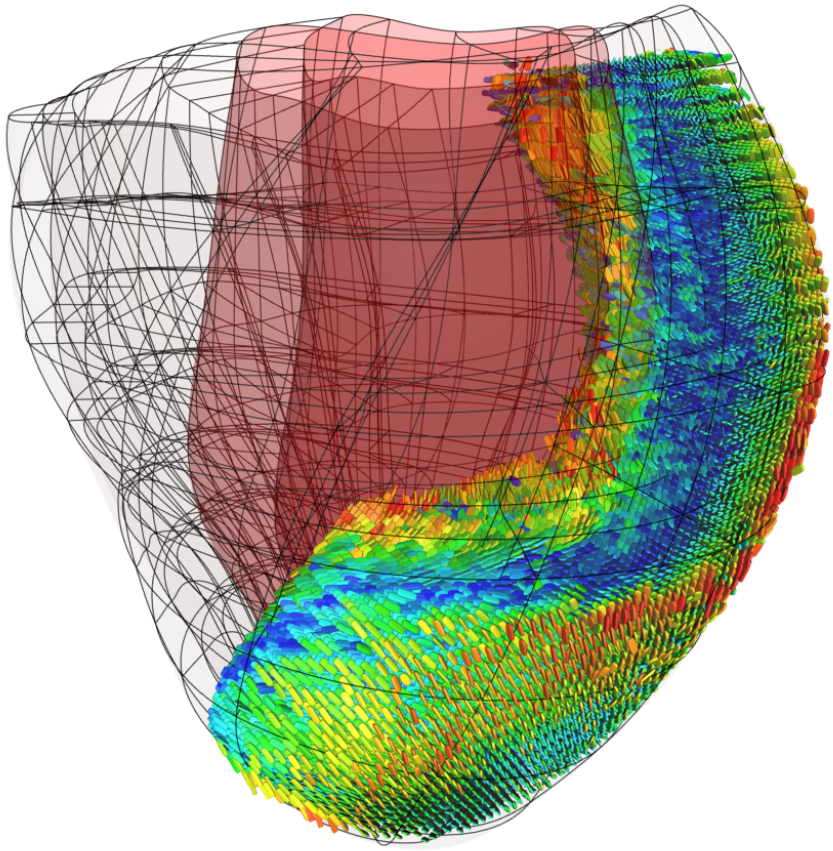

Figure 3.3: Spatial alignment of DT-MRI data with mesh. This example shows a cut view of a lateral section of diffusion tensors in the LV free wall. The characteristic variation of fiber orientation is evident.

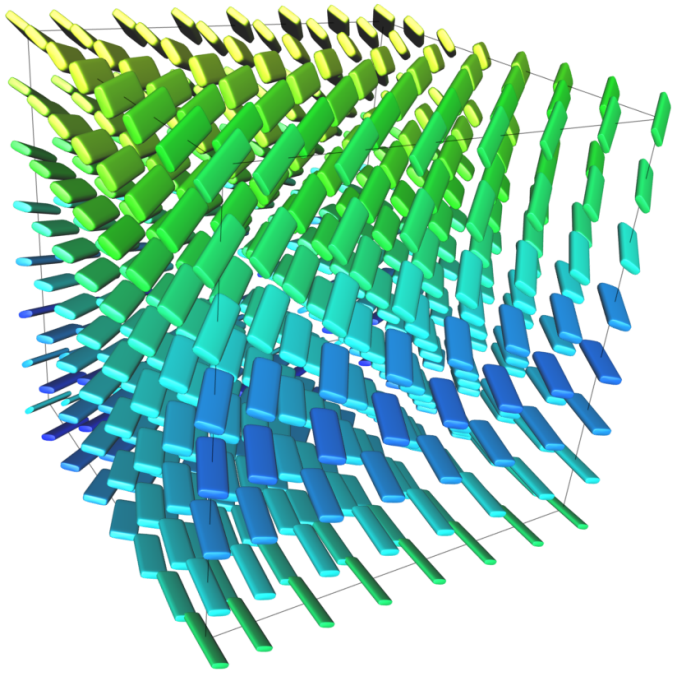

Figure 3.4: Log-Euclidean tensor interpolation. This example illustrates the result of LE interpolation in a cube. Eight arbitrary tensors were defined at the vertices by scalar fields for six independent components of matrix-log diffusion tensors. The components were linearly interpolated through the cube. The interpolated Euclidean tensor was computed by taking the matrix exponential of the interpolated components.

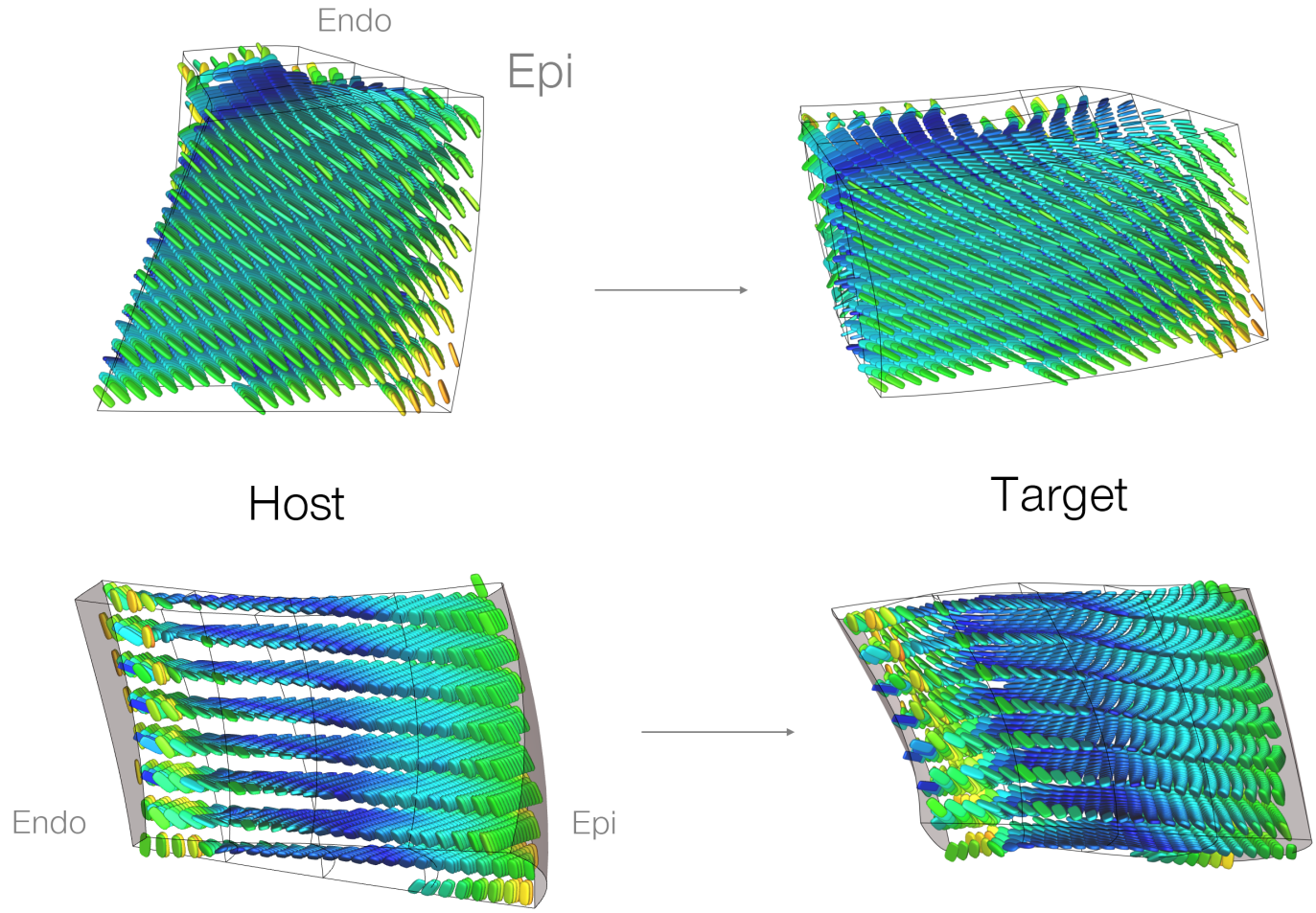

Figure 3.5: Large deformation diffeomorphic mapping and tensor reorientation. Two views of the results of the large deformation diffeomorphic mapping and the tensor reorientation strategy from the host to a target patient. The interpolated fiber architecture is shown in four transmural elements in the LV lateral wall. The fiber-sheets were reoriented using the PPD strategy by computing the deformation gradient $\mathbf{F}(\mathbf{Y})$ between corresponding material points in the host and the patient anatomical models.

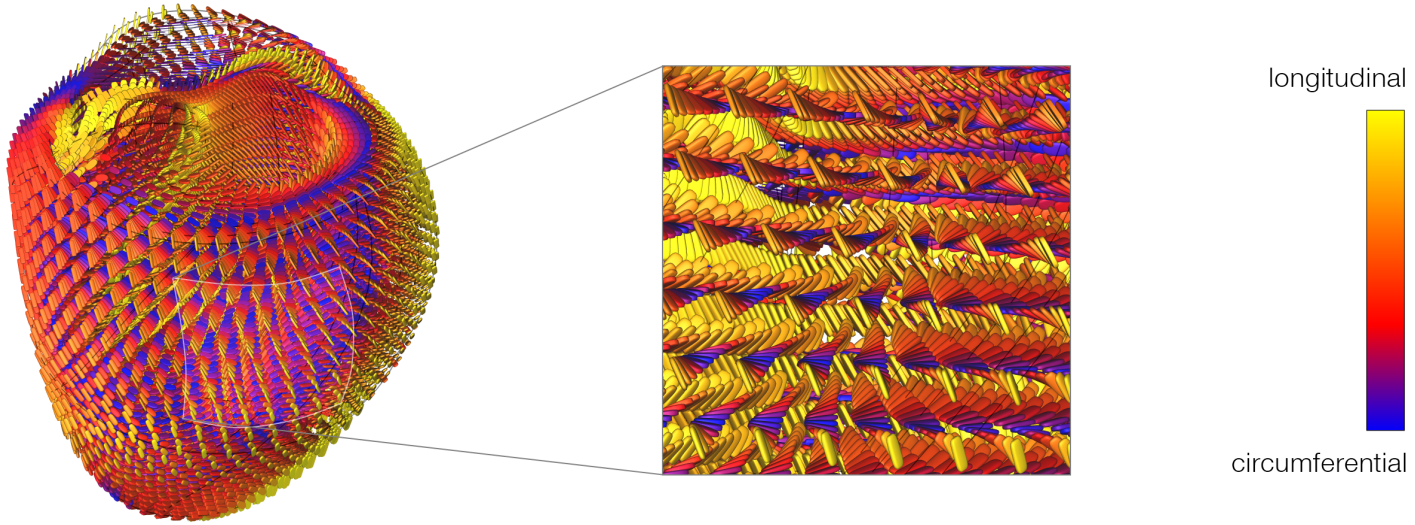

Figure 3.6: Fiber architecture model of host human heart. Eigen-decomposition of the interpolated diffusion tensors yields the fiber architecture shown. The diffusion tensors are represented as scaled glyphs depicting the orientation of the myofiber-sheet structure. The glyphs are colored according to their z-axis component. A close-up of the anterio-lateral wall of the left ventricle reveals the well-established characteristic organization of the fibers through the thickness of the wall.

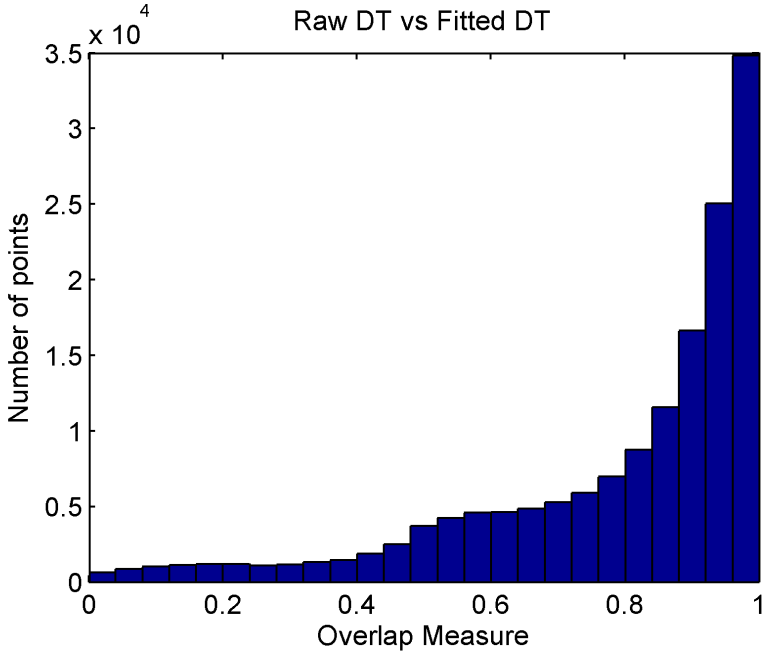

Figure 3.7: Distribution of dyadic tensor overlap metric. The quality of the fit was assessed by computing the overlap between the measured and modeled material axes at corresponding locations in the model. 74% (112,419 of 152,651 voxels) of the DT measurements have overlap greater than 0.70.

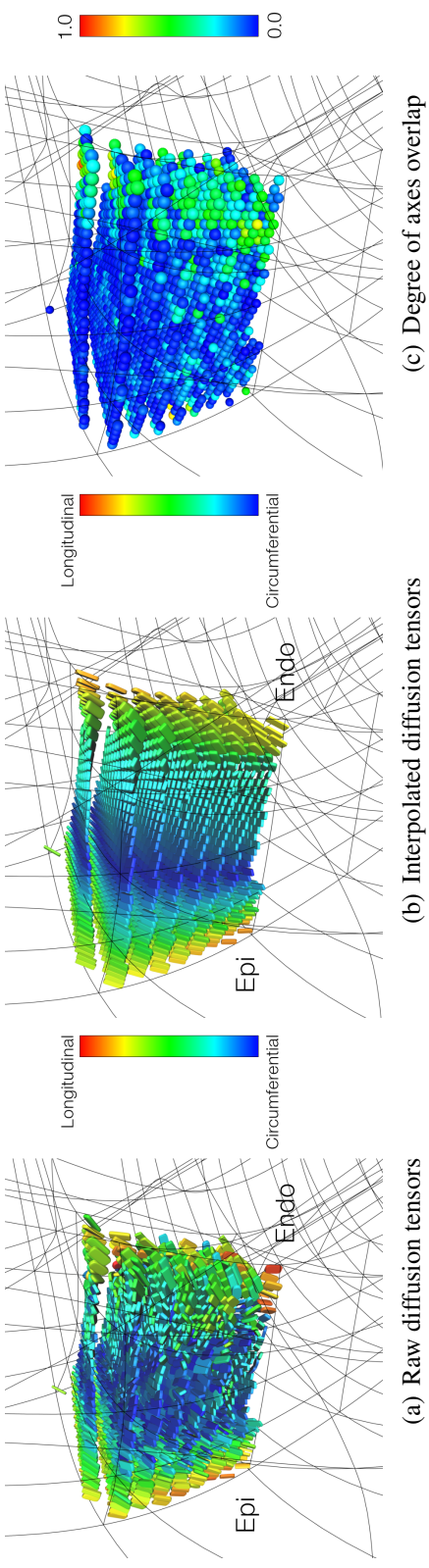

(a) Raw diffusion tensors (b) Interpolated diffusion tensors (c) Degree of axes overlap

Figure 3.8: Diffusion tensor fitting validation. (a) Raw diffusion tensor data in four transmural elements located in the lateral LV wall. (b) Interpolated diffusion tensors from the fit of the log-Euclidean components. (c) Degree of overlap between (a) and (b). Points of high tensor overlap are colored blue; points of lower overlap are colored green. Note the smoothing achieved by linear interpolation of the DT components.

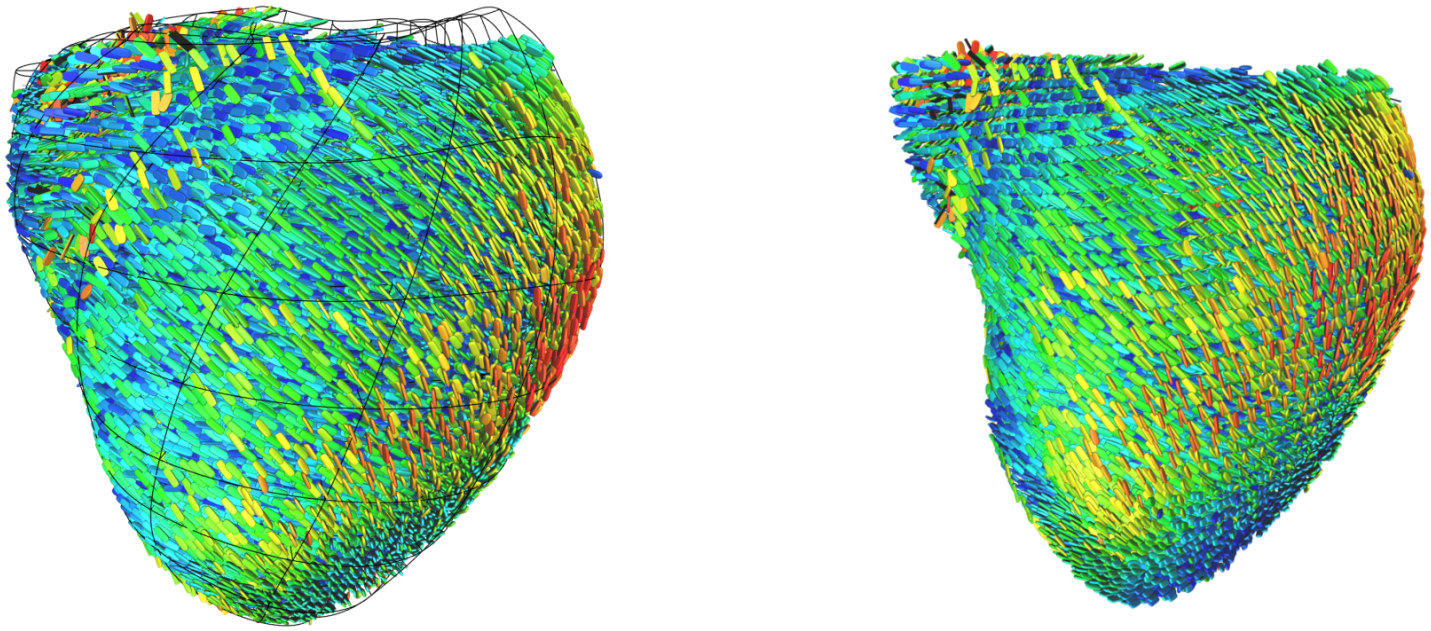

Figure 3.9: Fiber mapping from host to patient-specific ventricles. In this example, the measured DT data in the host *ex vivo* heart (left) was mapped to patient BiV2 (right) according to a diffeomorphic deformation between the two ventricular geometries. Diffusion tensors were reoriented by preservation of principal direction; epicardial fiber orientations in BiV2 are slightly elevated due to its increased aspect ratio compared to the host.

Bibliography

1. Aguado-Sierra, J., Krishnamurthy, A., Villongco, C., Chuang, J., Howard, E., Gonzales, M., Omens, J., Krummen, D., Narayan, S., Kerckhoffs, R., 2011. Patient-specific modeling of dyssynchronous heart failure: A case study. Progress in Biophysics and Molecular Biology.

2. Arsigny, V., Fillard, P., Pennec, X., Ayache, N., 2005. Fast and simple calculus on tensors in the log-euclidean framework. Medical Image Computing and Computer-Assisted Intervention–MICCAI 2005, 115–122.

3. Basser, P., 1995. Inferring microstructural features and the physiological state of tissues from diffusion-weighted images. NMR in Biomedicine 8 (7), 333–344.

4. Basser, P., Pajevic, S., 2000. Statistical artifacts in diffusion tensor mri (dt-mri) caused by background noise. Magnetic Resonance in Medicine 44 (1), 41–50.

5. Basser, P. J., Mattiello, J., LeBihan, D., 1994. Estimation of the effective self-diffusion tensor from the nmr spin echo. Journal of Magnetic Resonance, Series B 103 (3), 247–254.

6. Cao, Y., Miller, M., Mori, S., Winslow, R., Younes, L., 2006. Diffeomorphic matching of diffusion tensor images. Computer Vision and Pattern Recognition Workshop, 67.

7. Clayton, R., Bernus, O., Cherry, E., Dierckx, H., Fenton, F., Mirabella, L., Panfilov, A., Sachse, F., Seemann, G., Zhang, H., 2011. Models of cardiac tissue electrophysiology: progress, challenges and open questions. Progress in biophysics and molecular biology 104 (1), 22–48.

8. Costa, K., Takayama, Y., McCulloch, A., Covell, J., 1999. Laminar fiber architecture and three-dimensional systolic mechanics in canine ventricular myocardium. American Journal of Physiology-Heart and Circulatory Physiology 276 (2), H595.

9. Fillard, P., Arsigny, V., Pennec, X., Ayache, N., 2006. Joint estimation and smoothing of clinical DT-MRI with a Log-Euclidean metric.

10. Fillard, P., Pennec, X., Arsigny, V., Ayache, N., 2007. Clinical DT-MRI estimation, smoothing, and fiber tracking with Log-Euclidean metrics. IEEE Trans Med Imaging 26 (11), 1472–82.

11. Frank, L., Jung, Y., Inati, S., Tyszka, J., Wong, E., 2010. High efficiency, low distortion 3D diffusion tensor imaging with variable density spiral fast spin echoes 3D DW VDS RARE. Neuroimage 49 (2), 1510–1523.

12. Helm, P., Beg, M., Miller, M., Winslow, R., 2005. Measuring and mapping cardiac fiber and laminar architecture using diffusion tensor MR imaging. Annals - New York Academy of Sciences 1047, 296.

13. Helm, P., T, H., Younes, L., McVeigh, E., Winslow, R., 2005. Ex vivo 3d diffusion tensor imaging and quantification of cardiac laminar structure. Magnetic resonance in medicine 54 (4), 850–859.

14. Holmes, A., Scollan, D., Winslow, R., 2000. Direct histological validation of diffusion tensor MRI in formaldehyde-fixed myocardium. Magnetic resonance in medicine 44 (1), 157–161.

15. Hooks, D., Trew, M., Caldwell, B., Sands, G., LeGrice, I., Smaill, B., 2007. Laminar arrangement of ventricular myocytes influences electrical behavior of the heart. Circulation research 101 (10), e103–e112.

16. Hsu, E., Muzikant, A., Matulevicius, S., Penland, R., Henriquez, C., 1998. Magnetic resonance myocardial fiber-orientation mapping with direct histological correlation. American Journal of Physiology-Heart and Circulatory Physiology 274 (5), H1627.

17. LeGrice, I., Smaill, B., Chai, L., Edgar, S., Gavin, J., Hunter, P., 1995. Laminar structure of the heart: ventricular myocyte arrangement and connective tissue architecture in the dog. American Journal of Physiology-Heart and Circulatory Physiology 38 (2), H571.

18. Lekadir, K., Hoogendoorn, C., Pereanez, M., Albà, X., Pashaei, A., Frangi, A., 2014. Statistical personalization of ventricular fiber orientation using shape predictors.

19. Lombaert, H., Peyrat, J., Croisille, P., Rapacchi, S., Fanton, L., Clarysse, P., Delingette, H., Ayache, N., 2011. Statistical analysis of the human cardiac fiber architecture from DT-MRI. Functional Imaging and Modeling of the Heart, 171–179.

20. Lombaert, H., Peyrat, J., Fanton, L., Cheriet, F., Delingette, H., Ayache, N., Clarysse, P., Magnin, I., Croisille, P., 2012. Statistical atlas of human cardiac fibers: Comparison with abnormal hearts, 207–213.

21. Lumens, J., Blanchard, D., Arts, T., Mahmud, E., Delhaas, T., 2010. Left ventricular underfilling and not septal bulging dominates abnormal left ventricular filling hemodynamics in chronic thromboembolic pulmonary hypertension. American Journal of Physiology-Heart and Circulatory Physiology 299 (4), H1083.

22. Neal, M., Kerckhoffs, R., 2010. Current progress in patient-specific modeling. Briefings in bioinformatics 11 (1), 111.

23. Niederer, S. A., Plank, G., Chinchapatnam, P., Ginks, M., Lamata, P., Rhode, K. S., Rinaldi, C. A., Razavi, R., Smith, N. P., 2011. Length-dependent tension in the failing heart and the efficacy of cardiac resynchronization therapy. Cardiovascular Research 89 (2), 336–43.

24. Nielsen, P. M., LeGrice, I. J., Smaill, B. H., Hunter, P., 1991. Mathematical model of geometry and fibrous structure of the heart. American Journal of Physiology-Heart and Circulatory Physiology 260 (4), H1365.

25. Olivetti, G., Cigola, E., Maestri, R., Corradi, D., Lagrasta, C., Gambert, S. R., Anversa, P., 1996. Aging, cardiac hypertrophy and ischemic cardiomyopathy do not affect the proportion of mononucleated and multinucleated myocytes in the human heart. Journal of molecular and cellular cardiology 28 (7), 1463–1477.

26. Pennec, X., Fillard, P., Ayache, N., 2006. A riemannian framework for tensor computing. International Journal of Computer Vision 66 (1), 41–66.

27. Saffitz, J. E., Kanter, H. L., Green, K. G., Tolley, T. K., Beyer, E. C., 1994. Tissue-specific determinants of anisotropic conduction velocity in canine atrial and ventricular myocardium. Circulation research 74 (6), 1065–1070.

28. Sands, G. B., Gerneke, D. A., Hooks, D. A., Green, C. R., Smaill, B. H., Legrice, I. J., 2005. Automated imaging of extended tissue volumes using confocal microscopy. Microscopy research and technique 67 (5), 227–239.

29. Scollan, D., Holmes, A., Zhang, J., Winslow, R., 2000. Reconstruction of cardiac ventricular geometry and fiber orientation using magnetic resonance imaging. Annals of Biomedical Engineering 28 (8), 934–944.

30. Sermesant, M., Razavi, R., 2010. Personalized computational models of the heart for cardiac resynchronization therapy. Patient-Specific Modeling of the Cardiovascular System, 167–182.

31. Spotnitz, H., Spotnitz, W., Cottrell, T., Spiro, D., Sonnenblick, E., 1974. Cellular basis for volume related wall thickness changes in the rat left ventricle. Journal of molecular and cellular cardiology 6 (4), 317–331.

32. Streeter Jr, D., Spotnitz, H., Patel, D., Ross Jr, J., Sonnenblick, E., 1969. Fiber orientation in the canine left ventricle during diastole and systole. Circulation research 24 (3), 339.

33. Toussaint, N., Sermesant, M., Stoeck, C., Kozerke, S., Batchelor, P., 2010. In vivo human 3D cardiac fibre architecture: reconstruction using curvilinear interpolation of diffusion tensor images. Med Image Comput Comput Assist Interv 13 (Pt 1), 418–25.

34. Trayanova, N., 2011. Whole-heart modeling. Circulation Research 108 (1), 113–128.

35. Vadakkumpadan, F., Arevalo, H., Ceritoglu, C., Miller, M., Trayanova, N., 2012. Image-based estimation of ventricular fiber orientations for personalized modeling of cardiac electrophysiology. Medical Imaging, IEEE Transactions on 31 (5), 1051–1060.

36. Yeo, B., Vercauteren, T., Fillard, P., Peyrat, J., Pennec, X., Golland, P., Ayache, N., Clatz, O., 2009. DT-REFinD: Diffusion tensor registration with exact finite-strain differential. Medical Imaging, IEEE Transactions on 28 (12), 1914–1928.

Chapter 4

Computational Models of Ventricular Electrophysiology

Abstract

This chapter reviews the biophysics of ventricular electrophysiology in heart failure, descriptive mathematical models at the tissue and cellular level, and computational considerations for simulations. Impulse propagation of electrical depolarization in tissue is governed by the structure and composition of the ventricular myocardium and can be mathematically described via a reaction-diffusion process. At the level of the individual cell, propagation is supported by action potentials generated by the flow of numerous ionic currents through the myocyte membrane. In heart failure, structural changes in the myocardium affect tissue-level properties, while subcellular changes affect normal features of the action potential and has further emergent consequences for tissue-level impulse propagation.

We consider the computational requirements and performance of patient-specific models of electrophysiology, specifically the convergence of numerical solutions of activation time. We make use of the Thiele modulus to estimate the level of convergence based on the spatial resolution of the geometric mesh and electrical conductivities. We compared electrophysiology solutions between fully-converged (540,672 elements) and less-converged (1,056, 8,448, and 67,584 elements) models to justify an appropriate

balance between numerical accuracy and computational cost. We found that the RMS error was less than 5 msec for all three unconverged simulations which is on the order of accuracy of invasive clinical measurements of electrical activation times.

4.1 Introduction

Dyssynchronous heart failure (DHF) arises as a consequence of impaired multi-scale electrophysiological activity of the ventricles. At the organ level, conduction block of action potentials (AP) in the left bundle branch leads to an abnormal ventricular activation sequence that begins in the RV and causes intra- and inter-ventricular electromechanical time delays [8]. At the tissue and cellular level, chronic remodeling in HF causes detrimental changes to important myocyte electrical properties for action potential generation and propagation, which in turn affect activation at the organ scale. Mathematical models of cellular and tissue AP electrogenesis and propagation are capable of quantitatively recapitulating important pathological features of DHF and predicting ventricular activation sequences which can be further incorporated into models of biomechanics and hemodynamics to study their effects on local and global function. For a more in-depth treatment of cardiac electrophysiology, the reader is referred to a review by Rudy [26].

Practical considerations for patient-specific model development, implementation, and interpretation, especially for clinical decision support, often involve a compromise between numerical accuracy and computational effort; a higher resolution model will produce more accurate solutions at the cost of computational effort and overall model feasibility and economy. Realistic limits on model accuracy requirements may be defined by the resolution of clinical measurements used for model parameterization and validation. The goal of this chapter is to examine the effect of electrophysiology model properties (e.g. level of discretization, electrical conductivity) on the behavior and accuracy of local activation time solutions predicted by simulations of AP propagation in LBBB throughout the ventricle with regards to the gold standard of clinical measurements.

4.1.1 Genesis and propagation of cardiac action potential

Cardiomyocytes, like neurons, are excitable, having the ability to generate and sustain propagating AP waves. In nerve, APs lasting several milliseconds conduct down axons and signal release of neurotransmitters into synapses. In cardiomyocytes, APs lasting several hundred milliseconds conduct through the ventricular myocardium and are responsible for initiating contraction. The AP shape or *morphology* is defined by the time course of its magnitude. AP morphology is modulated by properties of the cell membrane and is important for synchronous electrophysiology and biomechanics.

Myocyte-level electrogenesis

The myocyte intracellular space is permeated by sarcoplasmic fluid which consists of ionic species, particularly Na^+, Ca^{2+}, K^+, among other lipids, carbohydrates, and proteins. The sarcolemma is a semi-permeable, capacitative lipid membrane that encapsulates the intracellular space and is embedded with protein channels, pumps, and exchangers. At rest (phase 4), inwardly-rectifying K^+ channels carry outward K^+ current I_{K1} which polarizes the membrane (about -85 mV for a human ventricular myocyte). An externally applied or spontaneously generated local depolarization of sufficient rate and size of membrane/tissue causes a number of voltage-gated membrane channels to open and conduct current. Opening of fast Na^+ channels carries an initial inward surge of Na^+ current I_{Na} which leads to an immense and rapid depolarization upstroke (phase 0) (+50 mV) which excites and activates the immediate and surrounding parts of membrane, causing further Ca^{2+} and K^+ voltage-gated channels to open.

Excitation triggers a transient outward K^+ current I_{to} which, in combination with inactivation of the fast Na^+ channels, causes initial rapid repolarization (phase 1) appearing as a "notch" in the AP morphology. Excitation also opens voltage-gated L-type (long activation, long recovery) Ca^{2+} channels which carry depolarizing inward Ca^{2+} current I_{CaL}. During the action potential plateau (phase 2), membrane voltage steadies due to competing fluxes between depolarizing inward I_{CaL} and repolarizing outward K^+ currents including the delayed rectifier K^+ current I_K (comprised of rapid I_{Kr} and slow I_{Ks} components) and inwardly rectifying I_{K1}. The depolarizing inward Ca^{2+} current induces intracellular Ca^{2+} release from the sarcoplasmic reticulum (SR)

which drives myocyte excitation-contraction coupling [2]. Eventual inactivation of I_{CaL} and continued K^+ outflux rapidly repolarize (phase 3) the membrane back to its resting potential. Other activated currents include $I_{\text{Na-Ca}}$ by Na^+/Ca^{2+} exchanger which pumps Na^+ inward and Ca^{2+} outward at resting potential and $I_{\text{Na-K}}$ by Na^+/K^+ exchanger which pumps Na^+ outward and K^+ inward.

Following inactivation, channels require some recovery time for voltage-sensitive gates to return to the closed resting state, and the channels become refractory to new depolarizing stimuli and will not sustain new APs, even at rest potential. Recovery rates vary among types of voltage-gated channels and can range from milliseconds (fast Na^+ channel) to seconds (some K^+ channels). The total cardiac action potential duration lasts 200–300 milliseconds at normal heart rates. This tightly regulated, orchestrated interplay between voltage-gated ion channels in active, inactive, and recovery states thus shapes AP morphology. Normal regional variations of ion channel concentrations, kinetics, and types cause AP morphology and durations to vary widely in the ventricle, particularly by known transmural variations between endocardial, mid-wall, and epicardial myocytes.

Tissue-level propagation

AP propagation at the tissue level occurs by electrotonic spread of current in addition to AP electrogenesis at the myocyte level. Normal myocardium behaves as a synchronized, continuous syncytium with anisotropic conduction properties due to low-resistance intercellular gap junctions and the fiber-sheet tissue microstructure (see Section 3.1.1). In the weakly excitable limit and in conditions of gap junction uncoupling (e.g. myocardial infarction), propagation can occur discretely and may be important for propagation failure and arrhythmia [25, 30]. Direction of propagation is crucial because of the influence of anisotropy and fiber architecture. Propagating APs are sustained by macroscopic membrane currents that form closed circuits: currents pass through gap junctions and exit across the sarcolemma. The transmembrane potential of each myocyte thereby influences its neighbors due to passive flow of current sustained by AP electrogenesis in the myocyte. The speed of conduction depends on passive properties of the membrane including myocyte excitability (ability to reach threshold), intracel-

lular resistance (determined by ionic composition in the sarcoplasm), gap junctional resistance, and the cross-sectional area of the cell. The magnitude of the I_{Na} upstroke, V_{max} is also an important determinant of AP conduction velocity. The conduction velocity in the fiber direction for normal human ventricular myocardium is 68 cm/s [33]. Normal tissue level electrophysiology promotes uni-directional propagation of the AP.

Alterations in heart failure

In HF, AP morphology is altered by changes in membrane protein channel activity affecting intracellular Ca^{2+} dynamics and repolarization. The APD in failing myocytes is prolonged in human ventricular myocytes compared to non-failing myocytes. The main causes include enhanced Na^+/Ca^{2+} exchanger activity and reduced inward rectifying K^+ and Na^+/K^+ current [3, 23]. These changes slow the rate of repolarization by decreasing outflow of positive charge from the sarcolemma. For example, decrease in I_{K1} activity retards repolarization and resting membrane depolarization [14]. In addition, reduced I_{to} current density [3] which leads to delayed and blunted phase 1 repolarization and loss of the notch. Increased enhanced Na^+/Ca^{2+} exchanger current and reduced activity of the Ca^{2+} ATPase [9, 29], especially at high heart rates, leads to slowed Ca^{2+} uptake into the SR which reduces the available SR Ca^{2+} and depresses the Ca^{2+} transient peak for subsequent beats. I_{CaL} current density and kinetics remain unchanged. Other evidence has shown that K^+ leak current I_{Kleak} is increased, and the slow part of repolarization I_{Ks} is decreased.

Consequences of the cellular alterations in heart failure manifest on the tissue scale. Delayed membrane repolarization increases susceptibility to arrhythmogenesis; spontaneous Ca^{2+} release events from the sarcoplasmic reticulum can trigger afterdepolarizations and initiate ectopic beats [6, 12]. In DCM, the ventricles dilate and increase in volume while the wall thins. Fibrosis also blunts conduction velocity and anisotropy. Depressed $[Ca^{2+}]$ levels weaken contractility. Slowed or blocked conduction through ischemic or infarcted myocardium can interrupt AP propagation and electrical activation pattern.

4.1.2 Numerical methods for electrophysiology simulation

Solution techniques

Solutions to the systems of ODE and PDE equations for electrophysiology can be approximated by various numerical methods that are implemented by computer code [16]. Time-dependent ODE's are integrated by explicit [35], implicit [11], and semi-implicit [13] Euler, Runge-Kutta, or Rush-Larsen [31] schemes and variants. Time- and space-dependent PDE's for distributed currents in the ventricle are solved on a discretized geometric domain of a given type of element and interpolation function, (e.g. hexahedral cubic Hermite finite elements) using matrix solvers of the direct (e.g. Cholesky factorization) [15, 28] or iterative (e.g. conjugate gradient) [27, 28] type. Additional strategies and techniques for increasing computational speed include various forms of matrix preconditioning, mass matrix lumping, and operator splitting [32]. The complete simulation and solution code can be deployed on system architectures with shared memory, distributed memory, serial memory, etc. The total composition of numerical solution techniques complexly affects the behavior, stability, and accuracy of the model [19].

Convergence analysis

An important aspect of numerical performance and accuracy is the resolution of time and space discretizations of ODE and PDE integration; ODE solvers take finite time steps Δt, and the discretized mesh is comprised of elements with a mean edge length $\Delta \bar{x}$. Adequate spatiotemporal resolution is necessary not only to capture rapid details of AP electrogenesis and propagation, but also to ensure correct numerical solution behavior and stability. In realistic electrophysiology models of human ventricular tissue, high resolution is requisite by the presence of large potential gradients on the 1 mm and 1 ms space and time scales due to the rapid Na^+ depolarization current. Inadequate resolution of time and space steps produces spurious model behavior and inaccurate solutions such as errors in conduction velocity and appearance of corners in smoothly curved wavefronts or oscillations near the AP upstroke and wavefront [21].

As spatiotemporal resolution increases, discretization errors decrease and solu-

tions converge to true values. For a given model (with a constant set of parameters, initial and boundary conditions) and solution code, convergence is evaluated by comparing differences in results at different spatiotemporal resolutions. Convergence is established at a resolution where solutions are within 10% of an established benchmark solution computed from a model with extremely fine resolution (0.0001 cm). The choice of convergence criteria and accuracy requirements depends on which properties are most relevant to the question of the model. For problems of uni-directional AP propagation, the local activation time defined by the zero potential-crossing of the AP upstroke is a simple spatiotemporal metric of conduction velocity that is easily computed, stored, and compared for solution verification.

Depending on the implementation, computational costs can scale nonlinearly with problem size, as is the case where doubling 3D spatial resolution can increase expense by a factor of eight [4]. Furthermore, an economic balance between model accuracy and computational cost is crucial for feasibility of patient-specific modeling in the clinic. Simulation times should be on the order of minutes to several hours to support timely clinical decision making. Model accuracy should be practically limited by the resolution of clinical measurements used to parameterize and validate the model in the first place; excess model accuracy relative to measurement would not have clinically meaningful value and thus expend unnecessary computational resource. Electroanatomic mapping is a gold standard clinical modality for measuring regional endocardial activation times to within 5 ms accuracy and may be used to establish reasonable limits to patient-specific electrophysiology simulations of activation time.

Therefore, it is important to define a patient-specific model of electrophysiology of sufficient accuracy and reasonable computational cost. We will run simulations of reaction-diffusion AP propagation using multiple resolutions of a high-order finite element geometry of human ventricles and compute local activation times. We will further characterize convergence based on the physicality of the reaction-diffusion problem, verify it by comparing solutions to a benchmark case, and estimate the cost of running such simulations.

4.2 Methods

4.2.1 Computational models of electrophysiology

Biophysically detailed mathematical models of electrophysiology quantitatively reflect an integrated system of molecular, electrical, and structural properties at the cellular and tissue scales. We briefly review the underlying mathematical basis, based on biophysical principles, in order to highlight key electrophysiological features and how their multi-scale changes in HF can be accounted for in the model. For a more critical overview of electrophysiology modeling, see the review by Clayton et al [4].

It is important to first consider several implicit assumptions of cellular and tissue models that are important for the interpretation of simulation results. Cardiac tissue is assumed to be a continuum whose conduction properties are time independent. Moreover, properties are uniformly distributed or varied smoothly through space. The properties of the cardiac tissue continuum arise from the properties of myocytes or extracellular space only; explicit contributions from other types of cells (e.g. fibroblasts) and structures (e.g. ECM) are ignored. Parameter values have important consequences for accuracy, validity, and interpretation of models, but are often are difficult to obtain and verify. In the case of patient-specific model development, clinical measurements of the AP are not standard, and it is currently not possible to adjust parameters on an individual basis. Therefore, patient-specific models of cell electrophysiology are uniformly based on experimentally observed, qualitative features of failing ventricular myocytes.

Action potential electrogenesis in cardiomyocytes

At the scale of myocyte, the AP is generated by a specific time course of membrane depolarization and repolarization modulated by the transmembrane flow of ionic species through the activation, inactivation, and recovery of voltage-sensitive protein channels. The total current density I_{m} ($\mathrm{A/m^3}$) across the capacitative membrane is the sum of ionic currents generated by the flow of various ionic species through their associated protein channels:

$$I_{\mathrm{m}} = C_{\mathrm{m}} \frac{\mathrm{d}V_{\mathrm{m}}}{\mathrm{d}t} + \sum_s I_s, \tag{4.1}$$

where C_{m} is the cellular membrane capacitance (F/m^2), V_{m} is the membrane potential (mV), I_s is the total current density generated by ionic species s (e.g. Na^+, Ca^{2+}, and K^+), and t is time. Ohmic ion currents are described by a Hodgkin-Huxley formalism where current density is a function of channel conductance, various channel protein subunits or "gate" states, and the driving potential:

$$I_s = G_s x_s^1 x_s^2 \ldots x_s^n (V_{\mathrm{m}} - V_s), \tag{4.2}$$

where G_s is the maximal conductance of the ion channel for species s, x_s is the time-dependent state of the nth gating variable, and V_s is the equilibrium (Nernst) potential of species s. Gating variable state values vary in $[0,1]$ and represent active, inactive, and refractory states. The state dynamics of each gating variable are time-dependent and can be generally formulated as:

$$\frac{\mathrm{d}x_s}{\mathrm{d}t} = \frac{x_{s\infty}(V_{\mathrm{m}}) - x_s}{\tau_s(V_{\mathrm{m}})}, \tag{4.3}$$

where $x_{s\infty}$ is the steady-state value of the gating variable and τ_s is the time constant for recovery to steady-state following perturbation of membrane voltage. The kinetic properties of the channel gates can be determined by fitting model parameters to match measured dynamic and steady-state currents obtained by voltage-clamp experiments [10]. More recent ionic models account for the concentration of important ionic species $[s]$ (i.e. Ca^{2+}) which is affected by k types of ion channels and pump and exchanger currents which carry the species s:

$$\frac{\mathrm{d}[s]}{\mathrm{d}t} = \sum_k I_s^k(V_{\mathrm{m}}, s). \tag{4.4}$$

Such a description allows realistic simulation of Ca^{2+} transients to study how changes in AP morphology affect excitation excitation-contraction coupling.

To date, the most biophysically detailed and realistic model of human ventricular myocyte electrophysiology has been developed by Ten Tusscher and Panfilov [33]. It includes descriptions of all major channel, pump, exchanger, and background currents

for Na^+, Ca^{2+}, and K^+ (19 ODEs in total) fitted to measurements from voltage-clamp experiments. Heterogeneous channel properties are described for epicardial, mid-wall, and endocardial myocytes which differ primarily in APD. Furthermore, detailed descriptions of intracellular Ca^{2+} handling include diffusion between cell compartments (dyadic cleft and intracellular space) and Ca^{2+} release and uptake by the SR. Realistic Ca^{2+} transients allows the possibility for direct coupling to realistic models of sarcomere excitation-contraction.

Known alterations of channel kinetics in DHF can be incorporated by augmenting or diminishing parameter values including maximum conductivities and state transition rates to match quantitative experimental measurements or qualitative behavior if measurements are not available. To capture AP morphology changes in DHF, parameters in the Ten Tusscher model were adjusted accordingly: transient-outward channel conductance G_{to} was reduced to 65% of its normal value, maximal current I_{NaCa} was elevated by 200% of its normal value, SR Ca^{2+} handling was reduced by reducing the SR volume to 60%, maximal conductance G_{leak} of background Ca^{2+} leak current was increased by 32%, maximal conductance G_{Ks} of I_{Ks} was decreased by 40%, and maximal conductance G_{K1} of I_{K1} was decreased by 50%.

Cardiac action potential propagation in tissue

Models of AP propagation cardiac tissue describe the electrotonic flow of current within an excitable continuum with smooth variations in properties such as fiber orientations. The passive electrical conductivities of the extracellular (ECM) and intracellular (sarcoplasm) cardiomyocyte domains determine the conduction velocity. Excitable cardiomyocytes actively generate APs through the total transmembrane ionic current fluxes I_{m}. The macroscopic behavior of electric current flow is governed by Kirchhoff's current law, where the total intracellular (i) and extracellular (e) current is conserved:

$$\nabla \cdot (\mathbf{J}_{\text{i}} + \mathbf{J}_{\text{e}}) = 0, \tag{4.5}$$

where

$$\begin{aligned} \mathbf{J}_\mathrm{i} &= -\mathbf{G}_\mathrm{i}\nabla\Phi_\mathrm{i} \\ \mathbf{J}_\mathrm{e} &= -\mathbf{G}_\mathrm{e}\nabla\Phi_\mathrm{e}. \end{aligned} \tag{4.6}$$

$\mathbf{J}_\mathrm{i}$ and $\mathbf{J}_\mathrm{e}$ are current densities, $\mathbf{G}_\mathrm{i}$ and $\mathbf{G}_\mathrm{e}$ are conductivity tensors, and Φ_i and Φ_e are potentials in the intracellular and extracellular domains. The negative sign defines current flow in the direction of decreasing potential (negative gradient). The transmembrane potential V_m is the difference between the intracellular and extracellular domain potentials:

$$V_\mathrm{m} = \Phi_\mathrm{i} - \Phi_\mathrm{e}. \tag{4.7}$$

In terms of the transmembrane potential, the final system of equations becomes:

$$\begin{aligned} \nabla\cdot((\mathbf{G}_\mathrm{i}+\mathbf{G}_\mathrm{e})\Phi_\mathrm{e}) &= -\nabla\cdot(\mathbf{G}_\mathrm{i}\nabla V_\mathrm{m}), \\ \nabla\cdot\mathbf{G}_\mathrm{i}(\nabla V_\mathrm{m}+\nabla\Phi_\mathrm{e}) &= \chi(C_\mathrm{m}\tfrac{\mathrm{d}V_\mathrm{m}}{\mathrm{d}t}+\textstyle\sum_s I_s), \end{aligned} \tag{4.8}$$

where χ is the cellular surface-to-volume ratio. I_m is the total transmembrane current density in ((4.1)), and it is at this point where the cellular AP reaction is coupled to electrotonic diffusion . This system is known as the "bidomain" model because it captures the change in the transmembrane potential due to differences in conduction anisotropy between the extracellular and intracellular domains. Mathematically, the bidomain equations describe a PDE system of the Poisson type. Boundary conditions are typically prescribed as zero potential flux in the normal direction $\mathbf{n}$ to the ventricular borders:

$$\begin{aligned} \mathbf{n}\cdot(\mathbf{G}_\mathrm{e}\nabla\Phi_\mathrm{e}) &= 0 \\ \mathbf{n}\cdot(\mathbf{G}_\mathrm{i}\nabla(V_\mathrm{m}+\Phi_\mathrm{e})) &= 0. \end{aligned} \tag{4.9}$$

If conduction anisotropies for intracellular and extracellular domains are assumed to be related linearly by a constant:

$$\mathbf{G}_\mathrm{e} = \lambda\mathbf{G}_\mathrm{i}, \tag{4.10}$$

the bidomain equations ((4.8)) simplify to the monodomain equation:

$$\frac{\mathrm{d}V_\mathrm{m}}{\mathrm{d}t} = \nabla\cdot(\mathbf{D}\nabla V_\mathrm{m}) - \frac{I_\mathrm{m}+I_\mathrm{applied}}{C_\mathrm{m}}, \tag{4.11}$$

where $\mathbf{D}$ is the local conductivity tensor (m^2/s) and I_{applied} is an externally injected current (e.g. pacemaker lead stimulation). The conductivity tensor $\mathbf{D}$ is a scaling of the original intracellular conductivity:

$$\mathbf{D} = \frac{\mathbf{G}_i}{\chi C_{\text{m}}}. \tag{4.12}$$

The monodomain approximation is warranted in cases where current injection into the extracellular domain can be ignored; even without taking into account unequal anisotropy ratios, the bidomain and monodomain models produce similar activation patterns in unidirectional propagation [22] and spiral tip trajectories in reentrant rotor [24] simulations. The conductivity tensor $\mathbf{D}$ varies spatially with the local fiber orientation and is defined as:

$$\mathbf{D} = D_1\mathbf{f}\mathbf{f}^T + D_2\mathbf{s}\mathbf{s}^T + D_3\mathbf{n}\mathbf{n}^T, \tag{4.13}$$

where D_1, D_2, D_3 are principal conductivities in orthotropic fiber, sheet, and sheet-normal directions coincided by unit vectors $\mathbf{f}$, $\mathbf{s}$, and $\mathbf{n}$ such that $\mathbf{f}\mathbf{f}^T + \mathbf{s}\mathbf{s}^T + \mathbf{n}\mathbf{n}^T = \mathbf{I}$ ($\mathbf{I}$ is the identity matrix).

4.2.2 Numerical convergence

A convenient means to evaluate system behavior in different parameter regimes involves algebraic combinations of parameter variables into dimensionless numbers. For reaction-diffusion systems (defined originally for catalyst pellet reactions), the Thiele modulus captures the ratio of reaction rate to diffusion rate [34], reflecting the nonlinearity of the system. Dimensionless numbers are also useful for evaluating numerical system behavior to estimate the ease of achieving converged solutions. In a numerical reaction-diffusion system, the local or *cell* Thiele modulus characterizes system behavior as:

$$\text{Th}_{\text{C}} = \frac{kh^2}{D}, \tag{4.14}$$

where k is the reaction rate, h is the mean element line length, and D is the conductivity. Th_{C} describes the numerical system behavior as affected by the mesh, ionic model, and conduction parameters. The value of Th_{C} reflects the ratio of the numerical characteristic reaction rate (ODE time step) and length (mean element edge length) to the diffusion

constant. Quarteroni et al. showed how spurious oscillations appear near rapid features of the solution, particularly at the AP upstroke, when $Th_C > 1$ and disappear $Th_C < 1$, resulting in truer AP profiles. The cell Thiele modulus, as a descriptor for the effect of model parameters on solution convergence, provides an index by which parameter combinations may be judiciously chosen to guarantee converged solutions. Th_C number can therefore serve as a useful metric for convergence behavior given the parameters of the numerical system.

4.2.3 Numerical solution scheme

Operator splitting [32] was employed to separate the reaction (ODE) and diffusion (PDE) components of the monodomain equation and solve them in series. The system of ODEs representing the cell ionic model was first updated using a single-iteration backwards Euler solver [17]. The ODEs were evaluated at each Gauss-Legendre quadrature point in the computational mesh, and these calculations were accelerated by solving them on an NVIDIA GPU. The voltages and local derivatives at the quadrature points were interpolated to nodal voltages. The global linear system was solved with a biconjugate gradient method implemented in PyTrilinos [28] using an incomplete LU factorization for the preconditioner. Finally, the updated voltage solution was evaluated at the quadrature points before the next time step. All computations were performed using the finite element software Continuity 6 (http://continuity.ucsd.edu/).

4.2.4 Patient-specific model and simulations

Action potential propagation simulations were conducted in a previously described patient-specific finite element model of dilated ventricles [36]. Chapter 2 deals in detail with patient-specific mesh generation from clinical image data, and Chapter 3 discusses a method to estimate the fiber architecture. In summary, CT images of a patient (BiV2) with DCM in DHF were segmented, triangulated, and smoothed. A template 3D hexahedral mesh with 132 linear elements and extraordinary vertices was manually fitted to the triangulation. High-order Hermite parameters were estimated by a subdivision-surface scheme [7] resulting in a smooth C1 continuous geometry with a

total of 8,448 degrees of freedom. The RMS error of the mesh surfaces to the triangulated surfaces was on the order of 2 mm. The mean edge length of the final mesh was $h = 1.2$ cm.

The parent mesh was further subdivided in a 1-to-8 fashion to generate child meshes of incrementally decreasing line lengths. The resulting meshes had of $h = 0.6$ cm (1,056 elements), $h = 0.3$ cm (8,448 elements), $h = 0.15$ cm (67,584 elements), and $h = 0.075$ cm (540,672 elements). Fiber architecture was estimated for the mesh with 1,056 elements and interpolated in further subdivisions. Transversely anisotropic conductivities were assigned at 0.0346 mS/mm in the fiber direction and 0.00494 mS/mm in the cross-fiber and sheet directions. A stimulus was applied at 50,000 μA/cm^3 for a duration of 2 ms to a small region on the endocardium of the right ventricular free wall to simulate LBBB.

4.3 Results

4.3.1 Action potential morphology

AP and Ca^{2+} transients were simulated for normal and failing epicardial, mid-wall, and endocardial myocytes. Figure (4.1) shows the AP's and Ca^{2+} transients. APD prolongation for all failing myocyte types compared to normal myocytes is evident; prolongation differs between cell types (endocardial: 75 ms; mid-wall: 50 ms; epicardial: 100 ms). The degree of early phase 1 repolarization is also blunted and delayed, evident in the the loss of the notch. The rate of phase 3 repolarization is also slowed in all cell types. The intracellular Ca^{2+} transient is slowed, and its peak magnitude is blunted by as much as 50% in all types of failing myocytes. Diastolic recovery is also delayed and monotonically decreases. These features in AP morphology and Ca^{2+} are consistent with findings of AP morphology in failing myocytes and reflect changes in Ca^{2+} and K^+ channel dynamics and currents.

4.3.2 Activation pattern

We compared the nodal activation times between one fully converged electrophysiology solution and three less-converged solutions to determine the sufficiency of convergence of the latter solutions; sufficient convergence was achieved when the global error compared to the fully converged solution was on the order of uncertainty as clinical measurements of electrical activation time obtained by electroanatomic mapping; the uncertainty of clinical measurements is on the order of 5 msec [36].

Electrical propagation in a patient-derived human biventricular mesh was simulated at four levels of spatial refinement resulting in simulations with an average cell Thiele modulus in the primary direction of propagation of 1.0, 4.0, 16.2, and 64.8 for the four mesh refinements. For this exercise, the simulation with Th_C = 1.0 was considered fully converged. Activation times in the three less-converged simulations were compared to the converged activation times at node locations from the coarsest mesh (Figure (4.2)). Since propagation of the high cell Thiele modulus simulations was too fast, the total activation time for those simulations was scaled to give a regression line with a slope of 1.0. The Bland-Altman plot in Figure (4.2) B comparing the scaled activation times and the fully converged activation times identifies a pattern of outliers (>2 standard deviations) that were too fast compared to the fully converged solution. These outliers were located in the basal right ventricular free wall. The root-mean-squared (RMS) error between fully converged activation pattern and the scaled unconverged activation patterns decreases as the Thiele modulus decreases toward 1.0 (Figure (4.2) C). The RMS error was less than 5 msec for all three unconverged simulations and twice the RMS error was less than 5 msec for the Th_C = 4.0 and Th_C = 16.2 simulations.

4.4 Discussion

The verification of model results computed by complex solution codes presents a challenging task. Recently, Niederer et al. [18] introduced an N-version benchmark problem for which research groups in the electrophysiology simulation community can participate to solve a canonical problem in order to verify the correctness of solutions obtained by their respective implementations and codes. The problem posed well-defined

geometries, fiber orientations, conductivity, and AP propagation parameters. The solution method was left for the participating groups to freely choose. Activation time solutions at the mesh nodes were compared (rigorously by the L^2 norm). The study found large discrepancies in total (latest) activation time in the mesh, even at high spatial and temporal resolutions, attributed to differences in solution techniques (e.g. mass lumping [19] and ionic current solution interpolation [20]), revealing important sources of solution bias and error that were previously unknown. A main conclusion of the benchmark study was that spatial resolution required for activation time convergence was higher (0.1 mm) than previously thought (0.25 mm) [5]. One limitation of the study is that it did not evaluate solutions produced by high-order interpolation techniques. High-order schemes of the monodomain problem have been shown to have better convergence properties compared to linear interpolation schemes with the same number of degrees of freedom [1]. Here we have demonstrated that that high-order solution methods indeed have faster convergence properties with fewer elements. Moreover, the Thiele modulus is a more useful estimator of convergence than mean element line length alone.

For patient-specific modeling, identification of suitable convergence criteria and subsequent validation are important for model accuracy and economy. The local cell Thiele modulus shows that for a given mesh of mean line length h and chosen ionic model with characteristic reaction rate k, the electrical conductivity D determines the value of $\mathrm{Th_C}$ and the degree of convergence. The value for D is roughly estimated by the total activation time (QRS duration). However, in the case of DCM with LBBB, prolonged QRS durations are a result of enlarged ventricles, abnormal activation sequence, and slowed conduction. In terms of modeling, slowed conduction and larger elements will result in a higher $\mathrm{Th_C}$ and less-converged solutions, particularly when computational costs limit the minimum h and total number of elements in the mesh. We have demonstrated that although the absolute activation times solved by the model vary as a function of conductivity, the activation pattern remains similar for different conductivities. Therefore, one is able to scale activation times solved from a converged simulation with fast conduction to a situation with prolonged QRS duration in order to estimate absolute activation times and patterns in models of LBBB. This provides a strategy to

execute simulations of cardiac electrophysiology with better accuracy at greatly reduced computational cost.

4.5 Conclusion

We have described the basis for electrophysiology models of action potential genesis and propagation in failing myocytes and important numerical considerations for simulation. The main quantity of interest for patient-specific electrophysiology modeling is the electrical activation pattern. We demonstrated that fully converged simulations were not required for the purposes of validating simulated electrical activation times to electroanatomic mapping measurements with sufficient accuracy. The cell Thiele modulus Th_C is a useful index to estimate the degree of solution convergence and determine suitable model parameters (i.e. conductivity, mesh resolution, reaction kinetics) to achieve sufficient convergence.

Acknowledgments

The majority of the content of this chapter comprises an original document. The results and analysis of convergence of patient-specific electrophysiology simulations were performed by Kevin Vincent and appear in a manuscript in preparation; the citation is Vincent K, Gonzales M, Gillette A, Villongco CT, Pezzuto S, Omens JH, Holst M, McCulloch AD, "High-order interpolation methods for cardiac monodomain simulations," *Frontiers Physiology, in review*, 2015. The author gives thanks to Matthew Gonzales and Andrew McCulloch for discussions regarding cardiac electrophysiology.

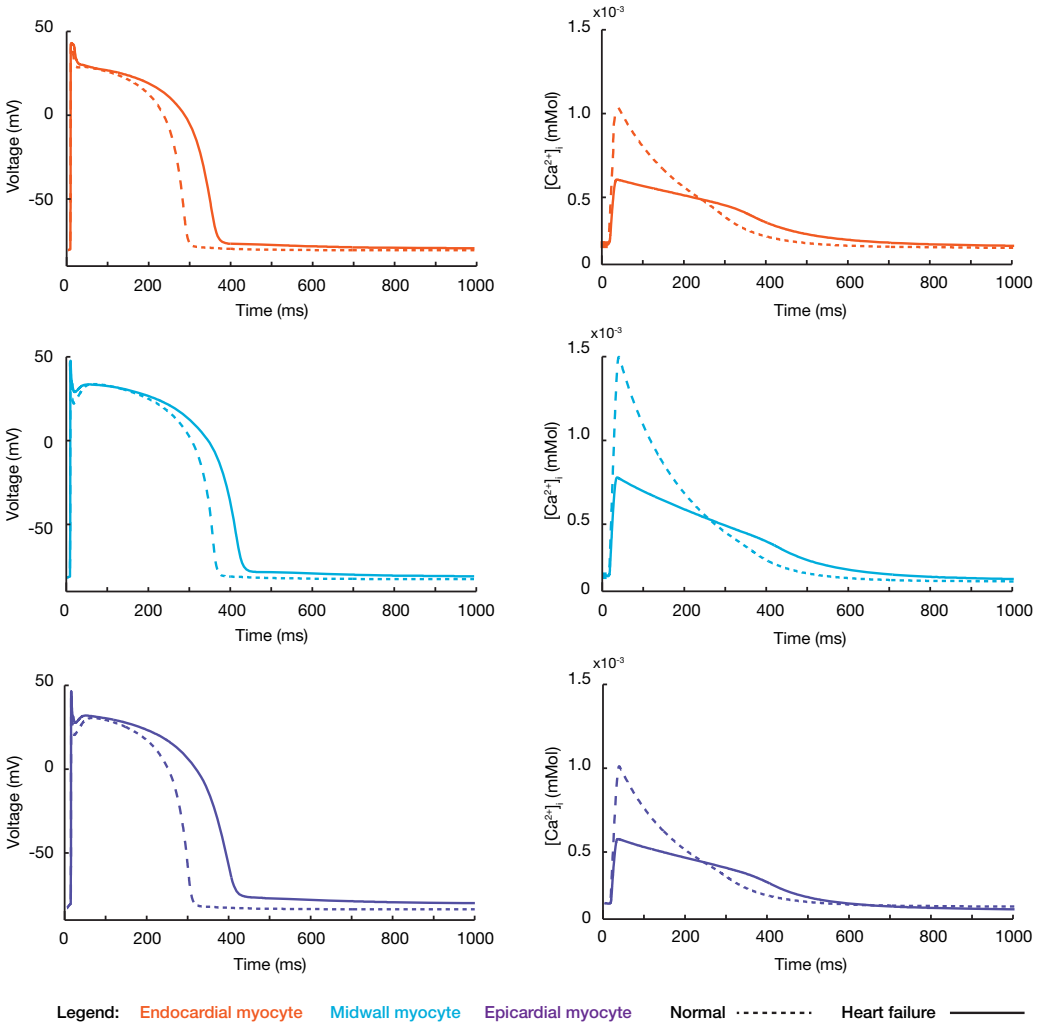

Figure 4.1: Action potentials and Ca^{2+} transients in normal and failing myocytes. Shown here are single-cell simulations of normal and failing myocytes in endocardial, mid-wall, and epicardial regions [33]. Prominent features of AP morphology in failing myocytes include prolonged APD and slowed repolarization rates. $[Ca^{2+}]$ transients in failing myocytes feature depressed peak $[Ca^{2+}]$ and slowed diastolic recovery.

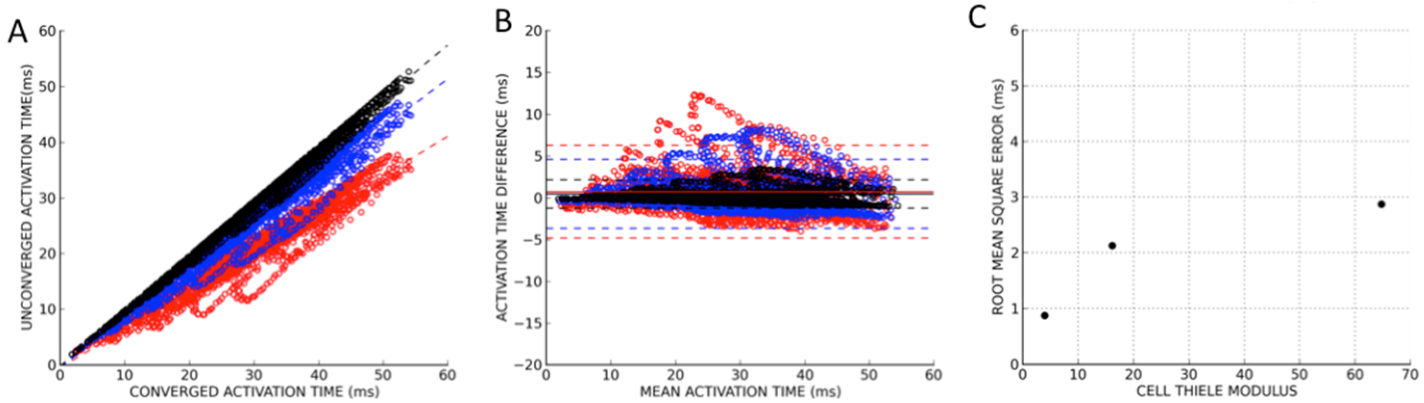

Figure 4.2: Activation time convergence comparison. (A) Activation times from three unconverged electrophysiology simulations (black - Th_C = 4.0; blue - Th_C = 16.2; and red - Th_C = 64.8) are plotted against activation times at the same location on the mesh from a converged (Th_C = 1.0) reference solution. Regression lines are shown for each unconverged solution as a broken line. (B) The activation times in the unconverged location were then scaled to give the regression line a slope of 1.0. These scaled activation times are compared to the converged activation times using a Bland-Altman plot where solid lines represent the mean difference between the two solutions and the broken lines are two standard deviations in the residuals from the regression line. (C) The root mean squared error between the unconverged and fully converged activation patterns decreases with the cell Thiele modulus of the simulation.

Bibliography

1. Arthurs, C. J., Bishop, M. J., Kay, D., 2012. Efficient simulation of cardiac electrical propagation using high order finite elements. Journal of computational physics 231 (10), 3946–3962.

2. Bers, D. M., 2002. Cardiac excitation–contraction coupling. Nature 415 (6868), 198–205.

3. Beuckelmann, D. J., Näbauer, M., Erdmann, E., 1993. Alterations of k+ currents in isolated human ventricular myocytes from patients with terminal heart failure. Circulation research 73 (2), 379–385.

4. Clayton, R., Bernus, O., Cherry, E., Dierckx, H., Fenton, F., Mirabella, L., Panfilov, A., Sachse, F., Seemann, G., Zhang, H., 2011. Models of cardiac tissue electrophysiology: progress, challenges and open questions. Progress in biophysics and molecular biology 104 (1), 22–48.

5. Clayton, R., Panfilov, A., 2008. A guide to modelling cardiac electrical activity in anatomically detailed ventricles. Progress in biophysics and molecular biology 96 (1), 19–43.

6. Curran, J., Brown, K. H., Santiago, D. J., Pogwizd, S., Bers, D. M., Shannon, T. R., 2010. Spontaneous ca waves in ventricular myocytes from failing hearts depend on ca 2+-calmodulin-dependent protein kinase ii. Journal of molecular and cellular cardiology 49 (1), 25–32.

7. Gonzales, M. J., Sturgeon, G., Krishnamurthy, A., Hake, J., Jonas, R., Stark, P., Rappel, W.-J., Narayan, S. M., Zhang, Y., Segars, W. P., 2013. A three-dimensional finite element model of human atrial anatomy: new methods for cubic hermite meshes with extraordinary vertices. Medical image analysis 17 (5), 525–537.

8. Grines, C. L., Bashore, T., Boudoulas, H., Olson, S., Shafer, P., Wooley, C., 1989. Functional abnormalities in isolated left bundle branch block. the effect of interventricular asynchrony. Circulation 79 (4), 845–853.

9. Hasenfuss, G., Reinecke, H., Studer, R., Meyer, M., Pieske, B., Holtz, J., Holubarsch, C., Posival, H., Just, H., Drexler, H., 1994. Relation between myocardial function and expression of sarcoplasmic reticulum ca (2+)-atpase in failing and nonfailing human myocardium. Circulation research 75 (3), 434–442.

10. Hodgkin, A. L., Huxley, A. F., 1952. A quantitative description of membrane current and its application to conduction and excitation in nerve. The Journal of physiology 117 (4), 500–544.

11. Hooke, N., Henriquez, C., Lanzkron, P., Rose, D., 1994. Linear algebraic transformations of the bidomain equations: implications for numerical methods. Mathematical biosciences 120 (2), 127–145.

12. Hove-Madsen, L., Llach, A., Bayes-Genís, A., Roura, S., Font, E. R., Arís, A., Cinca, J., 2004. Atrial fibrillation is associated with increased spontaneous calcium release from the sarcoplasmic reticulum in human atrial myocytes. Circulation 110 (11), 1358–1363.

13. Keener, J., Bogar, K., 1998. A numerical method for the solution of the bidomain equations in cardiac tissue. Chaos: An Interdisciplinary Journal of Nonlinear Science 8 (1), 234–241.

14. Koumi, S., Backer, C. L., Arentzen, C. E., 1995. Characterization of inwardly rectifying k+ channel in human cardiac myocytes alterations in channel behavior in myocytes isolated from patients with idiopathic dilated cardiomyopathy. Circulation 92 (2), 164–174.

15. Li, X. S., Demmel, J. W., 2003. Superlu_dist: A scalable distributed-memory sparse direct solver for unsymmetric linear systems. ACM Transactions on Mathematical Software (TOMS) 29 (2), 110–140.

16. Lines, G., Buist, M., Grottum, P., Pullan, A., Sundnes, J., Tveito, A., 2003. Mathematical models and numerical methods for the forward problem in cardiac electrophysiology. Computing and visualization in science 5 (4), 215–239.

17. Lionetti, F. V., McCulloch, A. D., Baden, S. B., 2010. Source-to-source optimization of cuda c for gpu accelerated cardiac cell modeling. In: Euro-Par 2010-Parallel Processing. Springer, pp. 38–49.

18. Niederer, S. A., Kerfoot, E., Benson, A. P., Bernabeu, M. O., Bernus, O., Bradley, C., Cherry, E. M., Clayton, R., Fenton, F. H., Garny, A., 2011. Verification of cardiac tissue electrophysiology simulators using an n-version benchmark. Philosophical Transactions of the Royal Society A: Mathematical, Physical and Engineering Sciences 369 (1954), 4331–4351.

19. Pathmanathan, P., Bernabeu, M., Niederer, S., Gavaghan, D., Kay, D., 2012. Computational modelling of cardiac electrophysiology: explanation of the variability of results from different numerical solvers. International journal for numerical methods in biomedical engineering 28 (8), 890–903.

20. Pathmanathan, P., Mirams, G. R., Southern, J., Whiteley, J. P., 2011. The significant effect of the choice of ionic current integration method in cardiac electrophysiological simulations. International Journal for Numerical Methods in Biomedical Engineering 27 (11), 1751–1770.

21. Pezzuto, S., 2013. On the effect of a coarse space discretization in electrophysiology.

22. Potse, M., Dubé, B., Richer, J., Vinet, A., Gulrajani, R. M., 2006. A comparison of monodomain and bidomain reaction-diffusion models for action potential propagation in the human heart. Biomedical Engineering, IEEE Transactions on 53 (12), 2425–2435.

23. Priebe, L., Beuckelmann, D. J., 1998. Simulation study of cellular electric properties in heart failure. Circulation research 82 (11), 1206–1223.

24. Roth, B. J., 2001. Meandering of spiral waves in anisotropic cardiac tissue. Physica D: Nonlinear Phenomena 150 (1), 127–136.

25. Rudy, Y., Quan, W., 1987. A model study of the effects of the discrete cellular structure on electrical propagation in cardiac tissue. Circulation Research 61 (6), 815–823.

26. Rudy, Y., Silva, J. R., 2006. Computational biology in the study of cardiac ion channels and cell electrophysiology. Quarterly reviews of biophysics 39 (01), 57–116.

27. Saad, Y., 2003. Iterative methods for sparse linear systems. Siam.

28. Sala, M., Spotz, W. F., Heroux, M. A., 2008. Pytrilinos: High-performance distributed-memory solvers for python. ACM Transactions on Mathematical Software (TOMS) 34 (2), 7.

29. Schwinger, R. H., Böhm, M., Schmidt, U., Karczewski, P., Bavendiek, U., Flesch, M., Krause, E.-G., Erdmann, E., 1995. Unchanged protein levels of serca ii and phospholamban but reduced ca2+ uptake and ca2+-atpase activity of cardiac sarcoplasmic reticulum from dilated cardiomyopathy patients compared with patients with nonfailing hearts. Circulation 92 (11), 3220–3228.

30. Spach, M. S., Kootsey, J. M., 1983. The nature of electrical propagation in cardiac muscle. American Journal of Physiology-Heart and Circulatory Physiology 244 (1), H3–H22.

31. Sundnes, J., Artebrant, R., Skavhaug, O., Tveito, A., 2009. A second-order algorithm for solving dynamic cell membrane equations. Biomedical Engineering, IEEE Transactions on 56 (10), 2546–2548.

32. Sundnes, J., Lines, G. T., Tveito, A., 2005. An operator splitting method for solving the bidomain equations coupled to a volume conductor model for the torso. Mathematical biosciences 194 (2), 233–248.

33. ten Tusscher, K. H., Panfilov, A. V., 2006. Alternans and spiral breakup in a human ventricular tissue model. American Journal of Physiology-Heart and Circulatory Physiology 291 (3), H1088–H1100.

34. Thiele, E., 1939. Relation between catalytic activity and size of particle. Industrial & Engineering Chemistry 31 (7), 916–920.

35. Vigmond, E. J., Aguel, F., Trayanova, N. A., 2002. Computational techniques for solving the bidomain equations in three dimensions. Biomedical Engineering, IEEE Transactions on 49 (11), 1260–1269.

36. Villongco, C. T., Krummen, D. E., Stark, P., Omens, J. H., McCulloch, A. D., 2014. Patient-specific modeling of ventricular activation pattern using surface ecg-derived vectorcardiogram in bundle branch block. Progress in biophysics and molecular biology 115 (2), 305–313.

Chapter 5

Estimation of Ventricular Activation Pattern During Bundle Branch Block Using Vectorcardiograms

Abstract

Patient-specific computational models have promise to improve cardiac disease diagnosis and therapy planning. Here a new method is described to simulate left bundle branch block (LBBB) and RV-paced ventricular activation patterns in three dimensions from non-invasive, routine clinical measurements. Activation patterns were estimated in three patients using vectorcardiograms (VCG) derived from standard 12-lead electrocardiograms (ECG). Parameters of a monodomain model of biventricular electrophysiology were optimized to minimize differences between the measured and computed VCG. Electroanatomic maps of local activation times measured on the LV and RV endocardial surfaces of the same patients were used to validate the simulated activation patterns. For all patients, the optimal estimated model parameters predicted a time-averaged mean activation dipole orientation within $6.7 \pm 0.6^{\circ}$ of the derived VCG. The predicted local activation times agreed within 11.5 ± 0.8 ms of the measured electroanatomic maps, on the order of the measurement accuracy.

5.1 Introduction

The sequence of electrical excitation in the ventricles of the heart is an important indicator of cardiac health and disease. Intrinsic cardiac electrical conduction disorders, such as left bundle branch block (LBBB), are detrimental to normal mechanical synchrony and pump efficiency. In device-based treatments for heart failure (HF) such as cardiac resynchronization therapy (CRT) (i.e. biventricular pacing), the therapeutic response is dependent on the patient-specific baseline electrophysiological substrate [28, 40]. The most important electrophysiological characteristic is the myocardial activation pattern.

Electrocardiographic imaging (ECGI) [33, 41] and noninvasive imaging of cardiac electrophysiology (NICE) [27] have advanced rapidly in the last decade, and their clinical use has grown. ECGI and NICE estimate distributions of extracellular potential and electrical activation, respectively, on the epicardial surface of the heart from body-surface potential recordings on a subject's torso. Estimates are based finding inverse solutions to the forward problem of electrophysiology:

$$\Phi_B = Z\Phi_H \tag{5.1}$$

where Φ_H is a vector of the electrical source distribution on the surface of the heart, Φ_B is a vector of the potential distribution on the body surface, and Z is the transfer matrix of the passive volumetric conduction of the thoracic cavity tissue and fluids. ECGI makes use of a pericardial potential source model for Φ_H, while NICE uses an equivalent double layer source model. The potentials Φ_B are typically sampled over the torso (~ 250 locations in ECGI, ~ 64 locations in NICE) and recorded as electrocardiograms; Z can be modeled as an isotropic conducting medium (using the boundary element method) or as a three-dimensional torso with prescribed conductivities (using finite volume or finite element methods). Though a unique relationship between body-surface and epicardial potentials exists in certain conditions [30, 43], the inverse problem is ill-conditioned and sensitive to noise in Z or Φ_B. This problem is usually handled with numerical regularization techniques [30, 26, 16, 25, 37, 14]. ECGI and NICE methods have been successfully applied to a range of physiologic conditions including normal sinus rhythm,

ventricular pacing, atrial flutter, ventricular tachycardia, bundle branch block [29], and Wolff-Parkinson-White syndrome [5].

Preconditioning the inverse problem may also take the form of model-based constraints by conditioning Φ_B a priori with solutions from forward models of ventricular excitation. Recent model-based approaches have been implemented and validated in animal [19, 18, 24, 45, 20, 23] and human [10] studies. Using electrical activation models based on artificial neural networks and cellular automata, the results of these studies agreed with measured surface electrocardiograms, activation times, and known source locations within reasonable error bounds. One limitation of these approaches is the computational expense of detailed excitation models. Recent advances in computing power and GPU architecture, however, make physiologically detailed forward models more feasible. Recently, Cluitmans et al. found that, compared with conventional regularization techniques alone, a training model with patient-specific epicardial geometry and FitzHugh-Nagumo membrane kinetics, optimized to match vectorcardiographic features, significantly improved the agreement between recorded electrocardiograms and localization accuracy of known pacing sites compared to numerical regularization alone [8].

In light of these advancements, we propose a model-based approach for estimating patient-specific myocardial electrical activation patterns. We used a forward monodomain model of human ventricular action potential propagation in patient-specific anatomical models approximated using high-order 3D biventricular geometry, human fiber architecture, and regions of heterogeneous conductivities due to the presence of myocardial infarction. From our excitation model, we approximated the total cardiac dipole at each time and compared it to the vectorcardiogram (VCG) derived from the 12-lead surface electrocardiogram (ECG). We hypothesized that the optimal combination of excitation model parameters that minimizes a VCG objective function could predict activation patterns within measurement limits. We validated computed activation patterns directly using invasive electroanatomic maps of endocardial activation isochrones.

5.2 Methods

5.2.1 Clinical study

Three male patients (ages 67, 71, 85) (74 ± 9 years) with left bundle branch block, NYHA class III heart failure, and dilated cardiomyopathy were enrolled from the Veteran's Administration San Diego Healthcare System (San Diego, CA) into an Institutional Review Board (IRB)-approved protocol after obtaining informed, written consent. End-diastolic cardiac anatomy was obtained with CT imaging (GE Lightspeed, GE Medical Systems, Milwaukee, WI, in-plane resolution of 0.49×0.49 mm, thickness 2.5 mm). Two patients with indications for myocardial ischemia underwent nuclear perfusion imaging (technetium sestamibi, ECAM-2, Siemens Medical Solutions, Hoffman Estates, IL, resolution of $6.59 \times 6.59 \times 1$ mm) to localize the affected regions; one patient had an inferoseptal infarct, and another an inferior infarct. In the following invasive electrophysiology study, standard 12-lead body-surface electrocardiograms were recorded (Bard Pro, Bard Electrophysiology, Lowell, MA) at 1 kHz simultaneously with non-fluoroscopic electroanatomic contact mapping (NavX, St. Jude Medical, St. Paul, MN) of biventricular endocardial geometry and activation times. The electrocardiograms were printed to XPS file format, rasterized at 600 dpi (1.6 ms, 0.004 mV), and resampled to 1 kHz. Intracardiac electrograms at the LV and RV endocardial surfaces were recorded using a roving catheter with 3D tip localization [32, 42]. Activation times were computed by first identifying the global activation time reference $(t = 0)$ at the earliest onset of the QRS complex in body-surface leads I, II, aVF, and V1. Local activation at the catheter in contact with the endocardial surface was then marked (with respect to the global activation time reference) by the onset of the largest deflection in the recorded electrogram.

5.2.2 Vectorcardiogram derivation

The cardiac dipole or "heart vector" is the net intracellular current that flows from regions of higher intracellular potential to regions of lower potential at the activation and recovery wave fronts at a given instant in the myocardium. The magnitude of the cardiac dipole is proportional to the effective intracellular conductivity of the tissue

and the strength of the potential gradients, and its orientation is in the mean direction of the propagating wave front:

$$\Phi_H = -\int_\Omega \sigma_i \nabla \Phi_i d\Omega \tag{5.2}$$

where σ_i is the intracellular conductivity, Φ_i is the intracellular potential, and Ω is the geometric domain of the ventricular myocardium. Burger was one of the first to investigate the relationship between the cardiac dipole and body-surface electrocardiogram recordings [6]:

$$\Phi_H = A\Phi_B \tag{5.3}$$

where Φ_H is the cardiac dipole, Φ_B is the vector of electrocardiogram recordings on the body surface ECG, and A is the matrix of transfer coefficients accounting for the passive conductivity of the thoracic cavity tissue and fluids. This system is similar to the inverse problem with the exception of the reduced dimensionality of Φ_H as a lumped vector representing the magnitude and mean orientation of the instantaneous potential distribution in the myocardium. Prior studies [21, 11, 12] have determined general transformations between the cardiac dipole and surface electrocardiograms by obtaining simultaneous measurements of 12-lead ECG and Frank-lead VCG in a wide patient population and minimizing the differences between derived and measured signals. In this study, we utilize the inverse Dower and Kors transformations to derive VCGs from the surface ECGs. The transformation coefficients are given in Table (5.1).

5.2.3 Patient-specific computational model

Anatomical model

Patient-specific finite element meshes of ventricular anatomy were generated from the clinical CT and perfusion images together with previously described diffusion tensor magnetic resonance images (DTI) from a cadaver heart [1]. Ventricular myocardium from apex to the basal valve plane was identified in the CT images, manually

segmented, and triangulated in ITK-SNAP (www.itksnap.org; [44]). The coordinate frame of the resulting geometry was rotated to coincide with the ECG reference frame: the positive x-direction corresponds to right to left (lead I), the positive y-direction corresponds to superior to inferior (lead aVF), and the z-direction corresponds to anterior to posterior ($\sim$ lead -V1).

A generic biventricular control mesh (132 elements, $\overline{\Delta x} \sim 12.5$ mm) with linear hexahedral elements was manually overlaid onto the endocardial and epicardial surfaces of the triangulated segmentations. The resulting linear mesh was converted into a high-order cubic Hermite mesh with extraordinary vertices [15]. The mesh was subdivided thrice in a 1-8 fashion to the final level of refinement (67,584 elements, $\overline{\Delta x} \sim 2$ mm) for electrophysiology simulations.

Regions of myocardial infarction were identified from sestamibi perfusion images during stress and rest in the two ischemic patients. The boundaries of the regions were manually demarcated on the anatomical meshes by an expert cardiac electrophysiologist (DEK); Patient 1 had a posteroseptal infarction, and Patient 2 had an inferior infarction. The regions were registered in the anatomical model as a binary field of normal and infarcted tissue.

The myofiber architecture was estimated empirically using a log-Euclidean interpolation framework previously described [22, 1, 13, 3] for registering DT-MR measurements to the anatomical models. Briefly, DT-MR images of an isolated human donor heart were obtained. The reconstructed diffusion tensors were fitted as a field of the log-transformed components in a corresponding anatomical mesh to interpolate local fiber, sheet, and sheet-normal axes. The fiber orientations in the resulting model were mapped to each patient via large-deformation diffeomorphic mapping [7] and reoriented based on the 3D deformation gradients between the atlas and target patient ventricular geometries to account for the effect of ventricular shape differences on fiber orientation [2]. The resulting fiber-sheet model formed the local basis of transversely isotropic electrical conductivity with a fiber-sheet anisotropy ratio of 7.

Electrophysiology model

Myocyte transmembrane potentials are described by a recent model of human ventricular myocytes [36] which was modified to accommodate changes in channel kinetics during heart failure [1]. Action potential propagation was modeled in a monodomain reaction-diffusion framework. Electrical conductivity in the ventricular domain was partitioned into LV and RV subendocardial regions ($\sim$ 3 mm transmurally), infarct region, and the remaining bulk myocardium. The conductivity in the endocardial regions was allowed to vary up to 10 times that of bulk myocardium [1] to account for the fast conduction of the Purkinje system which was not explicitly modeled. In infarcted regions, conductivity was isotropic and allowed to vary between 10%–90% of that in the bulk myocardium.

5.2.4 Model parameter optimization to derived VCG

Electrophysiological parameters including a single ectopic stimulus site and electrical conductivity values were optimized to simulate an activation sequence with a VCG that best matched the measured VCG. Parameter ranges are summarized in Table (5.2). Stimulus sites were sampled at 118 locations ($\sim$ 4 mm spacing) in the RV endocardium spanning from apex to base and anterior to posterior septal junctions. Stimuli were applied for a duration of 5 ms at a magnitude of 80,000 μA/cm^3. Electrical conductivity in the sheet direction of the bulk myocardial regions (σ_{bulk}) was sampled in the range of 0.0001–0.004 cm^2/ms. Electrical conductivity ratios with respect to σ_{bulk} in the LV (λ_{LV}) and RV (λ_{RV}) subendocardial regions were sampled in the range of 1 (myocardial conduction) and 10 (fast Purkinje conduction). A simulation database of the solutions of all possible parameter combinations was created for each patient (approximately 600 per patient). Due to the computational cost of searching the parameter space, we made a first approximation of the optimal parameters in a coarse mesh (8448 elements, $\overline{\Delta x} \sim 4$ mm). The approximate optimal stimulus location for the coarse mesh was found and applied in the nominal mesh. The conductivities in the nominal mesh were adjusted to match the total activation time of the initial optimal approximation.

We utilized an objective function θ to compare the orientations of the simulated

and measured cardiac dipoles:

$$\theta = \frac{1}{t_{\text{tot}}} \sum_{t=1}^{t_{\text{tot}}} \frac{|\tilde{v}_t^m|}{|\tilde{v}_R^m|} \left(\frac{\arccos\left(\frac{\tilde{v}_t^s \cdot \tilde{v}_t^m}{|\tilde{v}_R^s||\tilde{v}_R^m|} \right)}{\pi} \right) \tag{5.4}$$

where at time t, $\tilde{v}_t^m$ is the measured dipole (VCG), $\tilde{v}_t^s$ is the simulated dipole, $\tilde{v}_R^m$ is measured dipole at the R peak, $\tilde{v}_R^s$ is the simulated dipole at the R peak, and t_{tot} is the total measured activation time. The objective function computes the weighted time-average of the dot products between the two dipoles. Note that θ is computed between 3D dipoles and represents the maximal angle in the plane containing them. Weighting by the relative strength of the measured signal gives more importance to deviations between dipoles with greater magnitude.

5.3 Results

5.3.1 Clinical electrophysiological measurements

The recorded ECG and computed VCG for each patient are shown in Figure (5.1). Indications for LBBB [9] include the following: QRS durations for Patient 1, Patient 2, and Patient 3 were 152 ms, 148 ms, and 115 ms, respectively. All ECGs exhibited rS patterns in leads V1–V3 which transitioned into RS patterns in the lateral leads. Discordant T waves are also a consistent feature in the precordial leads for all patients. Mid-QRS notching was present in lead I and V6 for Patient 1 and lead II for Patient 2. In Patient 3, measurements were taking during right ventricular apex pacing which closely approximates LBBB activation pattern. The RV pacing lead was positioned at the posterior septal surface near the RV apex during an ICD insertion procedure. The derived VCG loops were oriented primarily from RV to LV and apex to base, indeed confirming a right to left activation sequence. In Patient 3, the loop was oriented anteriorly. We estimated a $12.5 \pm 2.2^\circ$ variability in the derived VCGs between the Kors and inverse Dower transformations by computing θ between the two derived VCGs for each patient.

We estimated the measurement error in the activation times and spatial coordi-

nates of the electroanatomic contact maps. To estimate the timing error, we measured the variability of the QRS onset as automatically detected for all beats in the surface ECG for each patient and found it to be in the range of 7–11 ms. Assuming the same uncertainty in the intracardiac electrogram of the roving catheter, the combined uncertainty results in an activation time noise floor in the range of 10–16 ms. We accounted only for measurements made by physical contact with the endocardial surface in our analysis to minimize systematic and methodological bias by the electroanatomic mapping software which can densely interpolate endocardial surface geometries for the LV and RV. The total number of contact measurements were 63 for Patient 1 (25 RV, 38 LV), 21 for Patient 2 (7 RV, 14 LV), and 22 for Patient 3 (11 RV, 11 LV). The contact measurements were registered to the anatomical model by translation and rigid rotation of the interpolated endocardial surfaces to the centers of the LV and RV cavities; interpolated measurements representing the lateral walls were positioned closest to the lateral walls of the model. Separate affine transformations were applied to the LV and RV electroanatomic measurements for direct comparison to the nearest points on the endocardial surface of the anatomical model. The mean distance of the final measurement locations to the model surfaces was 5 mm.

5.3.2 Optimization of cardiac dipole orientation

The objective θ was computed for VCGs derived from both Kors and inverse Dower transformations. A parameter set was identified as optimal if it ranked in the top ten best parameter sets in both VCG comparisons and were within 10 ms of the measured total activation time. The simulated total activation times were 157 ms (152 ms measured) for Patient 1, 150 ms (148 ms measured) for Patient 2, and 120 ms (115 ms measured) for Patient 3. Figure (**??**) lists the optimal parameter values and corresponding θ values (compared to Kors only): 7.6° for Patient 1, 6.1° for Patient 2, and 6.5° for Patient 3. The time course of θ is shown in Figure (5.3) (A). For all patients, instantaneous θ values were typically less than 10° and deviated by no larger than 20°. The VCG traces of the measured and optimal VCG are compared in Figure (5.3) (B). The morphologies and relative magnitudes of the simulated VCG components agree with the measurements. The 3D orientations of the VCG loops are compared with respect to the

ventricular anatomy in Figure (5.4). Predicted early activation sites in the RV shown in Figure (5.5) (B) are located anteriorly in Patient 1, laterally in Patient 2, and close to the known RV apex lead location in Patient 3.

5.3.3 Validation to electroanatomic maps

We compared the optimal activation maps with the registered electroanatomic measurements. Figure (5.5) shows the point-by-point comparison of the electroanatomic measurements and the corresponding nearest point on the endocardial surface. We computed a linear regression of the corresponding activation times and measured the scatter σ_{AT} (one standard deviation) of local activation times about the line to determine goodness-of-fit. The scatter was 12.6 ms for Patient 1, 10.9 ms for Patient 2, and 11.0 ms for Patient 3. Overall, the activation time scatter was on the order of the estimated measurement precision.

5.4 Discussion

In the present study, we have demonstrated that patient-specific models of ventricular depolarization can estimate LBBB and RV-paced activation sequences from VCGs generically derived from routine 12-lead body-surface ECGs within the accuracy of invasive measurements. We estimated the activation sequence of a single depolarization wave by recapitulating the time course of the total cardiac dipole with an optimal set of electrophysiology model parameters. We show good agreement between the predicted activation sequence and invasive electroanatomic measurements of endocardial activation times to within measurement precision. In addition to providing a quantitative estimation of 3D activation pattern in patient-specific ventricles, a detailed transmembrane current model which includes calcium kinetics also allows extension of the model to contractile ventricular mechanics [22].

A reduced ionic model would have been sufficient to predict similar LBBB and RV paced activation patterns as those obtained with the ten Tusscher model. Simplified FHN-like models are of lower computational cost partly due to slower depolarization kinetics. Though the predicted activation patterns may be similar, the reduced rate of

the potential upstroke at the wave front of a FHN-like model would result in different potential gradients and cardiac dipoles. Though this difference does not necessarily invalidate our approach, it could obfuscate comparison of simulations to measurements.

Activation patterns were estimated on the basis of the objective function θ which compares deviations between simulated and measured cardiac dipole orientations. Since a direct comparison of absolute time-voltage tracings was not possible due to incomplete lead position data, θ was intended to compare the relative magnitudes of orthogonal dipole components over the course of activation. Deviations in dipole orientations are weighted by the R-peak normalized magnitude of the measured dipole. Since VCG loop shape and size are functions of the absolute dipole magnitude, it may be possible for loops of different shape and size to show good agreement if the relative ratios of the VCG components agree at times near the peaks of the measured signal.

Numerical convergence

We verified the numerical convergence of the simulated dipole orientations and activation times by comparing the results of the coarse and nominal meshes. For our purposes, a sufficiently converged wave front was taken as one that could recapitulate the dominant morphology and features of the measured VCG and produce activation patterns that were independent of mesh resolution. We compared the mean cost values in a representative solution for a coarse and nominal mesh with the same parameters (stimulus location, scar and endocardial conductivities and adjusted bulk conductivity for equal total activation time). The mean difference in dipole orientation between the coarse and nominal meshes was less than 5°. Considering that the uncertainty of the dipole orientations derived from measurements due to a generic transformation is approximately 10°, the VCGs are converged to within estimated limits of accuracy of the measured signals. The predicted activation times of the coarse and nominal meshes at corresponding anatomical locations also have a RMS difference of approximately 4 ms which is within the limits of the accuracy of the data (10 ms).

Limitations

The validity of the activation pattern estimation approach using the VCG rests on the condition that depolarization wave dynamics can can be simplybe approximated by a single dominant excitation wave and described unambiguously by a single rotating fixed dipole. This assumption holds for activation patterns such as true LBBB [35, 4, 31] and RV pacing. The electrophysiology model assumes this condition by including a single RV activation site without a detailed description of the cardiac conduction system. Intact cardiac conduction in the present model is approximated by allowing rapid electrical conduction of the LV and RV subendocardial layers relative to the bulk myocardium. Our results show that with the current degrees of freedom, the model can capture the features of a simple rotating dipole representation of depolarization in conditions of LBBB and RV paced activation within the measurement limits of accuracy. However, most arrhythmias and activation sequences in disease states typically involve complex wave dynamics with multiple wave fronts [39]. In these more general cases, a single activation site and fixed dipole equivalent source model would be unable to describe ventricular depolarization patterns in any meaningful detail.

The lack of precise lead position information warranted the use of a patient-generic ECG to VCG transformation. Transformations such as Kors represent the average effects of heart size, body size, lead position, and heart orientation of a wide patient population and do not account for patient-specific torso properties. We estimated the error due to different transformations (Kors vs. inverse Dower) to approximately 10° to limit the accuracy we can expect to match measurements. We attempted to normalize out the effects of heart size, location, and body habitus by considering only the relative signal magnitudes and dipole orientation relative to the cardiac anatomy. We estimated the relative orientation of simulated dipoles to the measurements by co-registering the ventricles and VCG reference frame using the CT images. Compression of the 12-lead ECG to three orthogonal leads has been shown by factor analysis to preserve 99% of the original data content, with little information added by additional leads [34]. A full 12-lead description of the signal would be more valuable for patient-specific torso models where the individual lead positions are known. Future studies may include lead position measurements by leaving the 12-lead ECG electrodes in place during the CT scan or

applying radio-opaque markers in the same locations as the leads. Detailed lead position information in a patient-specific torso model would also allow direct comparison of the simulated voltage-time traces to actual body-surface electrocardiograms or invasive electrograms as an additional validation of the model.

The present model focuses on ventricular depolarization in heart failure. Heart failure is a complex disease state with changes in ventricular shape, fiber orientation, and ion channel expression remodeling. The anatomical model accounts for the gross fiber architecture remodeling in dilated ventricles by mapping the architecture of a human DT-MRI dataset according to differences in ventricular shape. Similar approaches to estimating fiber architecture have been described and validated by other groups [38]. It is currently impractical to measure patient-specific fiber orientations using *in vivo* DT-MRI. A generic phenotype of HF-induced electrophysiological ion channel remodeling is described by a modified ten Tusscher transmembrane current model [1] and does not fully account for patient-specific HF ionic remodeling. The present model may be extended to estimate ventricular repolarization and atrial activation. Transmural ion channel heterogeneities of action potential morphology in HF remodeling and more stringent steady state convergence of electrical properties (e.g. APD restitution and conduction velocity) are required for accurate steady and non-steady state predictions of T-wave morphology. A more detailed description of the geometry, conductivity, and fiber orientation in infarcted regions are also necessary to account for T-wave modulations effected by a scar. Estimation of atrial activation from the P-wave would require at least a different generic VCG transformation to account for the difference in the location of the origin of the atrial dipole from the ventricular dipole [17]. An appropriate anatomical model must also incorporate the geometry and fiber orientations of the valvular plane and atrial chambers.

5.5 Conclusion

We have described a method to estimate three dimensional LBBB and RV-paced activation patterns based on VCG derived from routine body-surface ECG using patient-specific computational models of HF electrophysiology. The early RV stimulus site and

myocardial conductivities in the model are optimized by minimizing the total deviation of simulated and measured cardiac dipole orientations during activation. The activation pattern predicted by the optimal parameters agrees with invasive measurements of endocardial activation time. This approach has potential to advance solution techniques for non-invasive electrocardiographic imaging and extend the utility of patient-specific computational models in clinical diagnosis and therapy planning.

Acknowledgments

The content of this chapter comprises the full content of a peer-reviewed publication; the citation is Villongco CT, Krummen DE, Stark P, Omens JH, McCulloch AD, "Patient-specific modeling of ventricular activation pattern using surface ECG-derived vectorcardiogram in bundle branch block," *Progress in Biophysics and Molecular Biology*, 2014. The author gives thanks to David Krummen, Alison Marsden, and Andrew McCulloch for discussions and suggestions regarding electrophysiology clinical data interpretation, modeling, and optimization strategies.

Table 5.1: ECG to VCG transformations using the inverse Dower and Kors methods.

	Inverse Dower				Kors		
	X	Y	Z		X	Y	Z
V1	-0.17	0.06	-0.23	V1	-0.13	0.06	-0.43
V2	-0.07	-0.02	-0.31	V2	0.05	-0.02	-0.06
V3	0.12	-0.11	-0.25	V3	-0.01	-0.05	-0.14
V4	0.23	-0.02	-0.06	V4	0.14	0.06	-0.2
V5	0.24	0.04	0.06	V5	0.06	-0.17	-0.11
V6	0.19	0.05	0.11	V6	0.54	0.13	0.31
I	0.16	-0.23	0.02	I	0.38	-0.07	0.11
II	-0.01	0.89	0.10	II	-0.07	0.93	-0.23

Table 5.2: Range of tested electrophysiology parameter values.

Stimulus locations	σ_{bulk} (cm^2/ms)	λ_{LV}, λ_{RV}	λ_{scar}
118	0.0001–0.004	1–10	0.1–0.9

Table 5.3: Optimal electrophysiology parameter values and corresponding VCG objective (θ) and local activation time σ_{AT} errors. Patient 3 did not have a myocardial infarction.

Patient	Stimulus location	σ_{bulk} (cm^2/ms)	λ_{LV}	λ_{RV}	λ_{scar}	θ	σ_{AT}
1	Anterior RV	0.0002	1	1	0.9	7.6	12.6
2	Lateral RV	0.0006	1	3.3	0.9	6.1	10.9
3	Postero-apical RV	0.0005	1	1	-	6.5	11.0

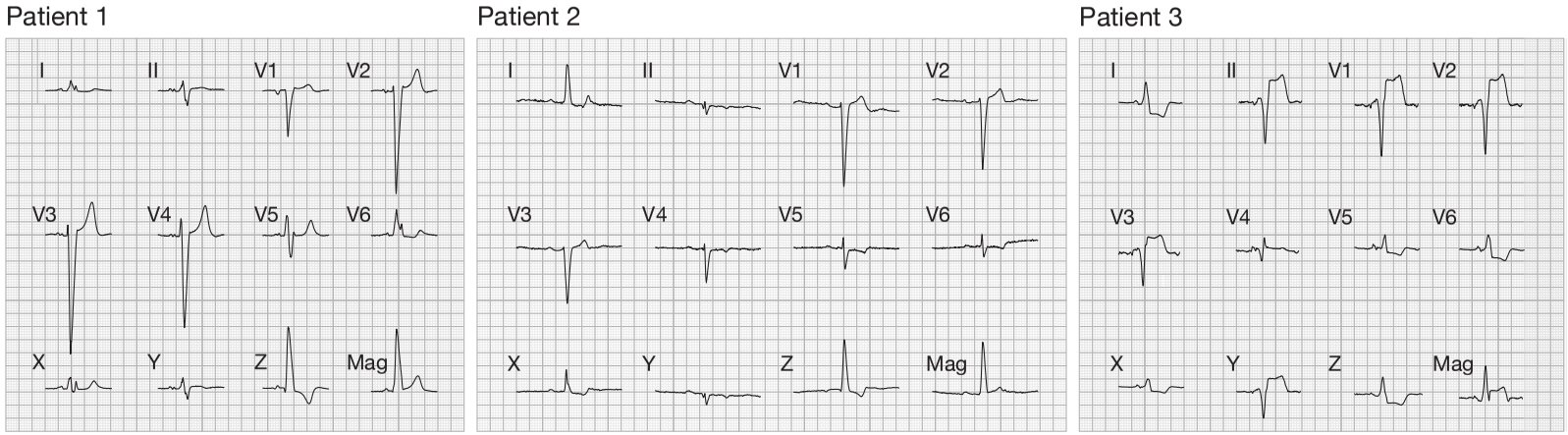

Figure 5.1: Recorded surface ECG and derived VCG traces for a single beat for all three patients. The top two rows show the recorded limb leads I–II and precordial leads V1–V6 for VCG derivation. The computed VCG components and magnitude (Kors transformation) are shown in the third row. One large grid has dimensions 200 ms$\times$0.5 mV.

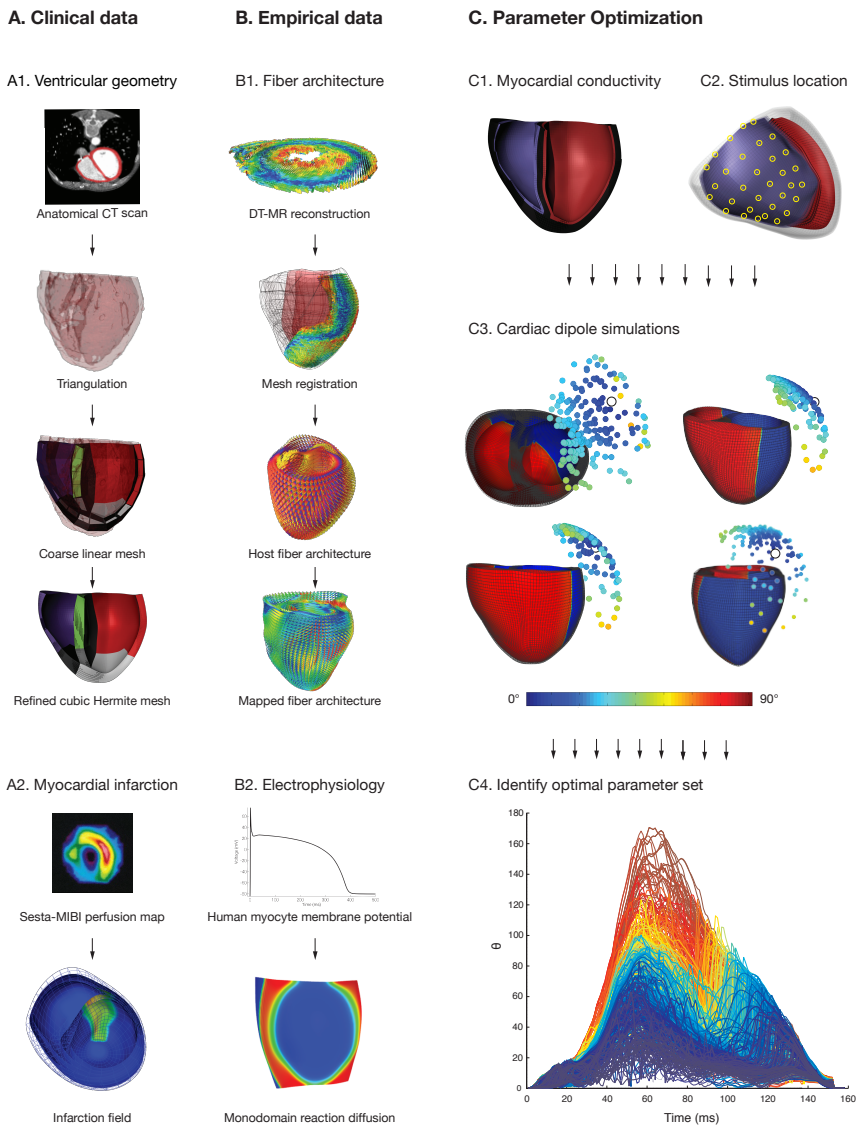

Figure 5.2: Overview of the patient-specific model of LBBB activation. The four main components of the model are derived from clinical measurements (A) of ventricular geometry (A1) and myocardial infarction (A2) and empirical data (B) of fiber architecture (B1) and cellular and tissue electrophysiology (B2). Parameter optimization (C) is performed by simulating activation from combinations of prescribed regional conductivity values (C1) and stimulus locations (C2). The deviation (θ) in dipole orientation between the measured and simulated dipoles during activation was computed for all parameter combinations (shown here at $t = 80$ ms for Patient 1; R at 56 ms) (C3); the circles represent the vector tips of simulated unit dipoles, and the color (blue to green to red) reflects the orientation deviation ($0^\circ < 45^\circ < 90^\circ$) with the measured vector (tip marked by white circle). The time course of deviations for all simulated parameter sets in one patient, with the value of θ ($0^\circ < 90^\circ < 180^\circ$) for each trace represented by the color (blue to green to red) (C4); the solution of the parameter set with minimal θ and total activation time within 5 ms of the measured duration was chosen as optimal.

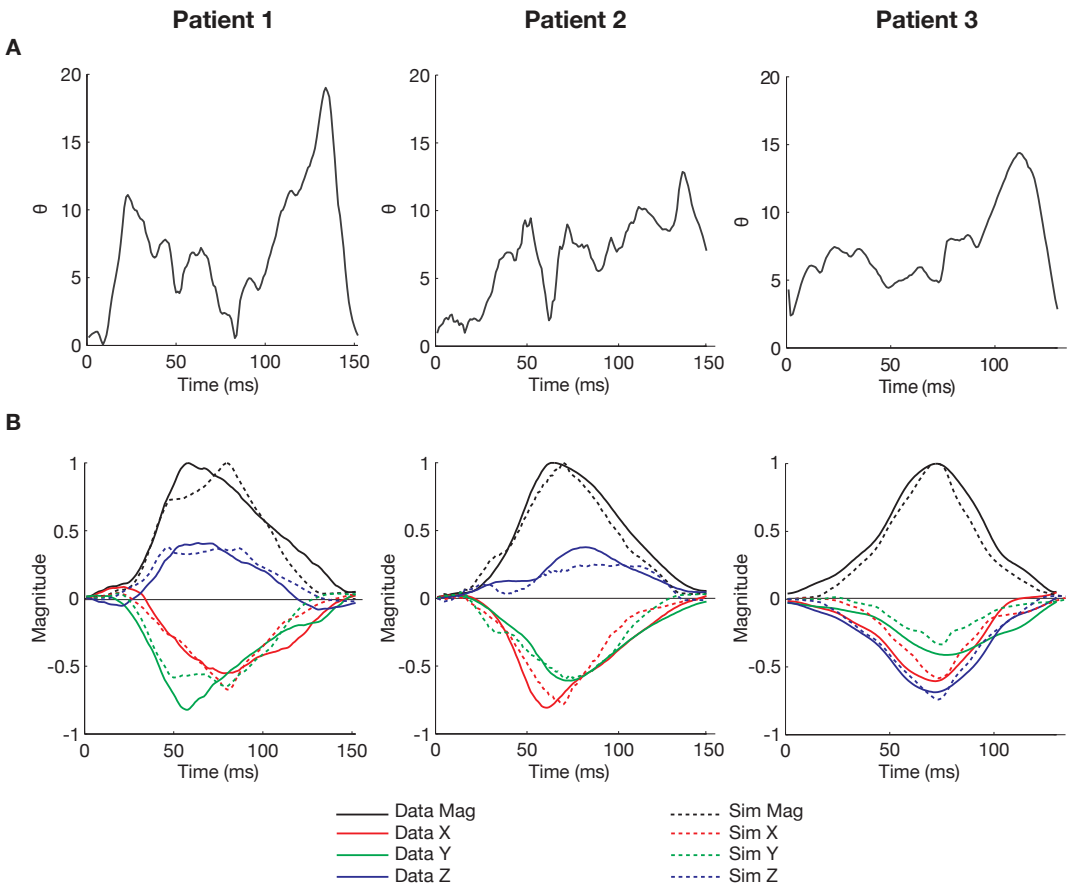

Figure 5.3: Summary comparisons between optimal and measured VCGs. A. The time course of the cost value θ (°) during activation. B. Comparison of the peak-normalized magnitude (Mag), X, Y, and Z components of the optimal simulated (dashed line) and measured (solid line) VCGs (for Kors transformation).

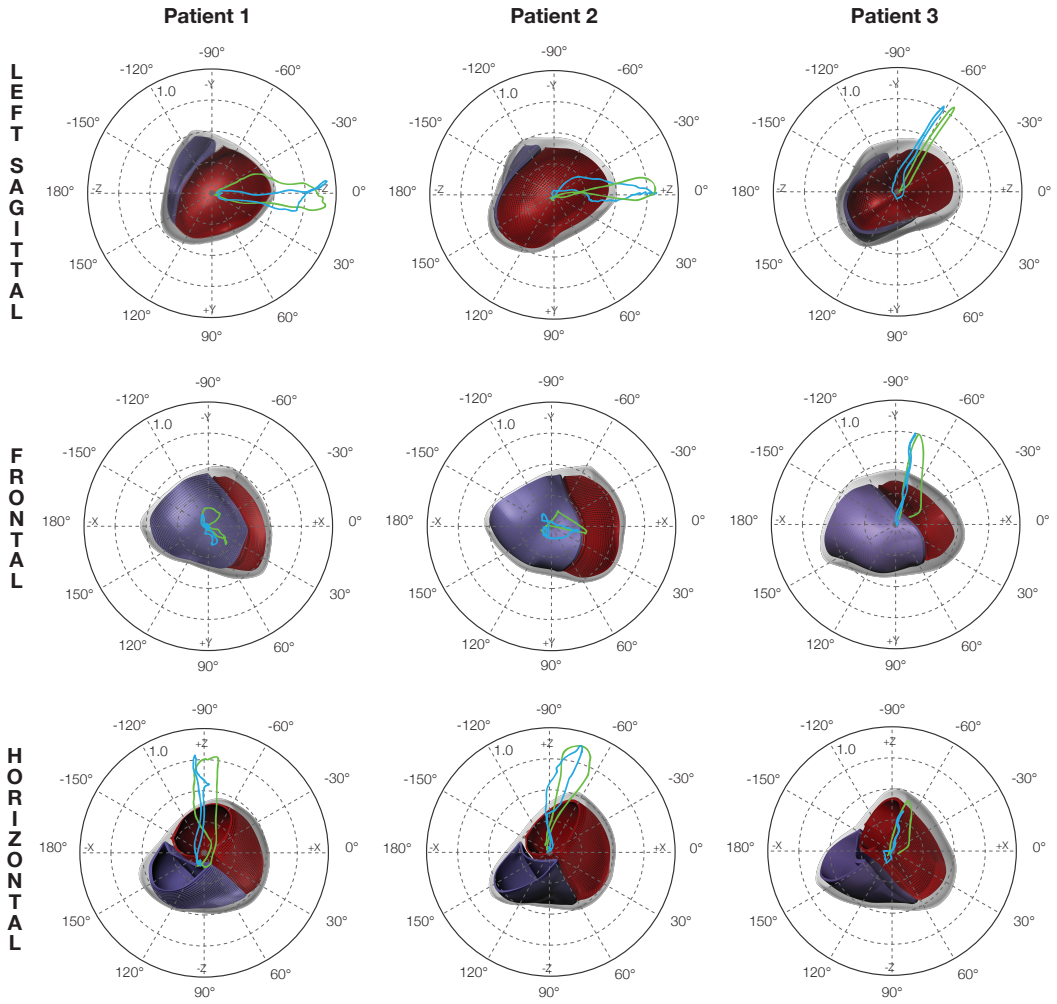

Figure 5.4: Comparison between optimal simulated and measured VCG loops. The loops represent the spatial trajectory of the tip of the cardiac dipole with its tail at the origin. The polar plots show the projections of the simulated (blue) and measured (green) VCG loops (Kors transformation) on to the left sagittal, frontal, and horizontal planes. The relative orientation of the loops to the anatomical meshes (red – LV endocardial surface; blue – RV endocardial surface) is illustrated.

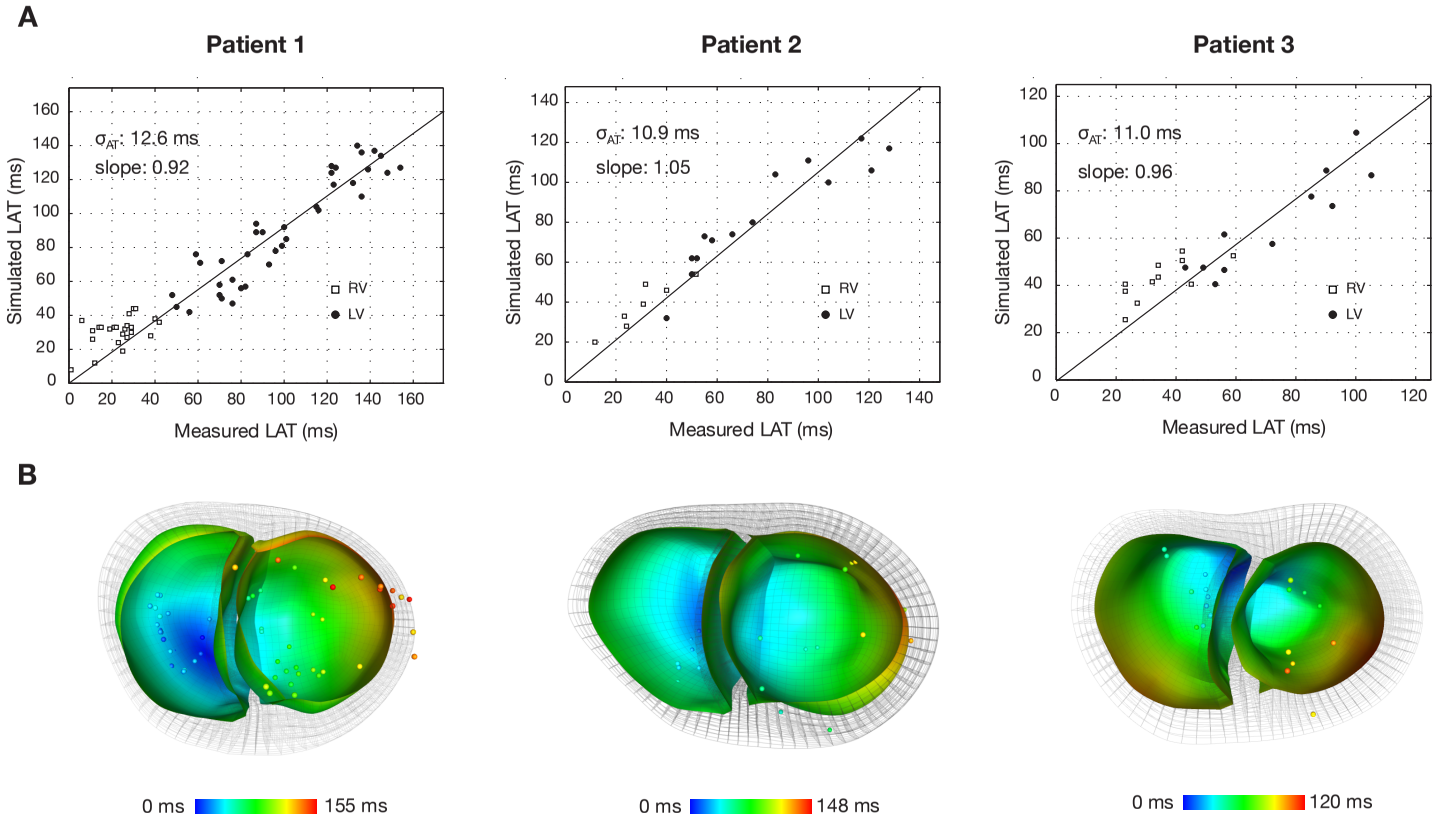

Figure 5.5: Comparison of optimal simulated and measured activation patterns. Simulated activation times were validated to electroanatomic measurements at corresponding points on the endocardial surface. A. Plots of the simulated and measured activation times with parameters of the regression line are shown. B. Short-axis views of the optimal activation patterns on the RV and LV endocardial surfaces of the anatomical mesh with electroanatomic measurements superimposed at corresponding locations.

Bibliography

1. Aguado-Sierra, J., Krishnamurthy, A., Villongco, C., Chuang, J., Howard, E., Gonzales, M., Omens, J., Krummen, D., Narayan, S., Kerckhoffs, R., et al., 2011. Patient-specific modeling of dyssynchronous heart failure: A case study. Progress in Biophysics and Molecular Biology.

2. Alexander, D., Pierpaoli, C., Basser, P., Gee, J., 2001. Spatial transformations of diffusion tensor magnetic resonance images. Medical Imaging, IEEE Transactions on 20 (11), 1131–1139.

3. Arsigny, V., Fillard, P., Pennec, X., Ayache, N., 2005. Fast and simple calculus on tensors in the log-euclidean framework. Medical Image Computing and Computer-Assisted Intervention–MICCAI 2005, 115–122.

4. Auricchio, A., Fantoni, C., Regoli, F., Carbucicchio, C., Goette, A., Geller, C., Kloss, M., Klein, H., 2004. Characterization of left ventricular activation in patients with heart failure and left bundle-branch block. Circulation 109 (9), 1133–1139.

5. Berger, T., Fischer, G., Pfeifer, B., Modre, R., Hanser, F., Trieb, T., Roithinger, F. X., Stuehlinger, M., Pachinger, O., Tilg, B., et al., 2006. Single-beat noninvasive imaging of cardiac electrophysiology of ventricular pre-excitation. Journal of the American College of Cardiology 48 (10), 2045–2052.

6. Burger, H., Van Milaan, J., 1946. Heart-vector and leads. British heart journal 8 (3), 157.

7. Cao, Y., Miller, M., Mori, S., Winslow, R., Younes, L., 2006. Diffeomorphic matching of diffusion tensor images. Computer Vision and Pattern Recognition Workshop, 67.

8. Cluitmans, M. J., Bonizzi, P., Karel, J. M., Volders, P. G., Peeters, R. L., Westra, R. L., 2013. Inverse reconstruction of epicardial potentials improved by vectorcardiography and realistic potentials. In: Computing in Cardiology Conference (CinC), 2013. IEEE, pp. 369–372.

9. Daubert, J.-C., Saxon, L., Adamson, P. B., Auricchio, A., Berger, R. D., Beshai, J. F., Breithard, O., Brignole, M., Cleland, J., DeLurgio, D. B., et al., 2012. 2012 ehra/hrs expert consensus statement on cardiac resynchronization therapy in heart failure: implant and follow-up recommendations and management a registered branch of the european society of cardiology (esc), and the heart rhythm society; and in collaboration with the heart failure society of america (hfsa), the american society of echocardiography (ase), the american heart association (aha), the european association of echocardiography (eae) of the esc and the heart failure association of the esc (hfa). endorsed by the governing bodies of aha, ase, eae, hfsa, hfa, ehra, and hrs. Europace 14 (9), 1236–1286.

10. Dossel, O., Bauer, W., Farina, D., Kaltwasser, C., Skipa, O., 2006. Imaging of bioelectric sources in the heart using a cellular automaton model. In: Engineering in Medicine and Biology Society, 2005. IEEE-EMBS 2005. 27th Annual International Conference of the. IEEE, pp. 1067–1070.

11. Dower, G. E., Yakush, A., Nazzal, S. B., Jutzy, R. V., Ruiz, C. E., 1988. Deriving the 12-lead electrocardiogram from four (easi) electrodes. Journal of electrocardiology 21, S182–S187.

12. Edenbrandt, L., Pahlm, O., 1988. Vectorcardiogram synthesized from a 12-lead ecg: superiority of the inverse dower matrix. Journal of electrocardiology 21 (4), 361–367.

13. Fillard, P., Pennec, X., Arsigny, V., Ayache, N., 2007. Clinical DT-MRI estimation, smoothing, and fiber tracking with Log-Euclidean metrics. IEEE Trans Med Imaging 26 (11), 1472–82.

14. Golub, G. H., Reinsch, C., 1970. Singular value decomposition and least squares solutions. Numerische Mathematik 14 (5), 403–420.

15. Gonzales, M. J., Sturgeon, G., Krishnamurthy, A., Hake, J., Jonas, R., Stark, P., Rappel, W.-J., Narayan, S. M., Zhang, Y., Segars, W. P., et al., 2013. A three-dimensional finite element model of human atrial anatomy: new methods for cubic hermite meshes with extraordinary vertices. Medical image analysis 17 (5), 525–537.

16. Greensite, F., Huiskamp, G., 1998. An improved method for estimating epicardial potentials from the body surface. Biomedical Engineering, IEEE Transactions on 45 (1), 98–104.

17. Guillem, M., Sahakian, A., Swiryn, S., 2006. Derivation of orthogonal leads from the 12-lead ecg. accuracy of a single transform for the derivation of atrial and ventricular waves. In: Computers in Cardiology, 2006. IEEE, pp. 249–252.

18. Han, C., Pogwizd, S. M., Killingsworth, C. R., He, B., 2011. Noninvasive imaging of three-dimensional cardiac activation sequence during pacing and ventricular tachycardia. Heart Rhythm 8 (8), 1266–1272.

19. Han, C., Pogwizd, S. M., Killingsworth, C. R., He, B., 2012. Noninvasive reconstruction of the three-dimensional ventricular activation sequence during pacing and ventricular tachycardia in the canine heart. American Journal of Physiology-Heart and Circulatory Physiology 302 (1), H244–H252.

20. He, B., Li, G., Zhang, X., 2002. Noninvasive three-dimensional activation time imaging of ventricular excitation by means of a heart-excitation model. Physics in medicine and biology 47 (22), 4063.

21. Kors, J., Van Herpen, G., Sittig, A., Van Bemmel, J., 1990. Reconstruction of the frank vectorcardiogram from standard electrocardiographic leads: diagnostic comparison of different methods. European heart journal 11 (12), 1083–1092.

22. Krishnamurthy, A., Villongco, C. T., Chuang, J., Frank, L. R., Nigam, V., Belezzuoli, E., Stark, P., Krummen, D. E., Narayan, S., Omens, J. H., et al., 2013. Patient-specific models of cardiac biomechanics. Journal of computational physics 244, 4–21.

23. Li, G., He, B., 2001. Localization of the site of origin of cardiac activation by means of a heart-model-based electrocardiographic imaging approach. Biomedical Engineering, IEEE Transactions on 48 (6), 660–669.

24. Liu, C., Skadsberg, N. D., Ahlberg, S. E., Swingen, C. M., Iaizzo, P. A., He, B., 2008. Estimation of global ventricular activation sequences by noninvasive three-dimensional electrical imaging: Validation studies in a swine model during pacing. Journal of cardiovascular electrophysiology 19 (5), 535–540.

25. Messinger-Rapport, B. J., Rudy, Y., 1988. Regularization of the inverse problem in electrocardiography: A model study. Mathematical biosciences 89 (1), 79–118.

26. Oster, H. S., Rudy, Y., 1992. The use of temporal information in the regularization of the inverse problem of electrocardiography. Biomedical Engineering, IEEE Transactions on 39 (1), 65–75.

27. Pfeifer, B., Hanser, F., Seger, M., Fischer, G., Modre-Osprian, R., Tilg, B., 2008. Patient-specific volume conductor modeling for non-invasive imaging of cardiac electrophysiology. The open medical informatics journal 2, 32.

28. Ploux, S., Lumens, J., Whinnett, Z., Montaudon, M., Strom, M., Ramanathan, C., Derval, N., Zemmoura, A., Denis, A., De Guillebon, M., et al., 2013. Noninvasive electrocardiographic mapping to improve patient selection for cardiac resynchronization therapy: beyond qrs duration and left bundle branch block morphology. Journal of the American College of Cardiology 61 (24), 2435–2443.

29. Ramanathan, C., Ghanem, R. N., Jia, P., Ryu, K., Rudy, Y., 2004. Noninvasive electrocardiographic imaging for cardiac electrophysiology and arrhythmia. Nature medicine 10 (4), 422–428.

30. Ramanathan, C., Jia, P., Ghanem, R., Calvetti, D., Rudy, Y., 2003. Noninvasive electrocardiographic imaging (ecgi): application of the generalized minimal residual (gmres) method. Annals of biomedical engineering 31 (8), 981–994.

31. Rodriguez, L., Timmermans, C., Nabar, A., Beatty, G., Wellens, H. J., 2003. Variable patterns of septal activation in patients with left bundle branch block and heart failure. Journal of cardiovascular electrophysiology 14 (2), 135–141.

32. Rotter, M., Takahashi, Y., Sanders, P., Haïssaguerre, M., Jaïs, P., Hsu, L.-F., Sacher, F., Pasquié, J.-L., Clementy, J., Hocini, M., 2005. Reduction of fluoroscopy exposure and procedure duration during ablation of atrial fibrillation using a novel anatomical navigation system. European heart journal 26 (14), 1415–1421.

33. Rudy, Y., 2013. Noninvasive electrocardiographic imaging of arrhythmogenic substrates in humans. Circulation research 112 (5), 863–874.

34. Schreck, D. M., Tricarico, V. J., Frank, J. D., Thielen, L. E., Chhibber, P., Brotea, C., Leber, I. B., 1998. Statistical methodology: Vi. mathematical modeling of the electrocardiogram using factor analysis. Academic emergency medicine 5 (9), 929–934.

35. Strauss, D. G., Selvester, R. H., Wagner, G. S., 2011. Defining left bundle branch block in the era of cardiac resynchronization therapy. The American journal of cardiology 107 (6), 927–934.

36. ten Tusscher, K. H., Panfilov, A. V., 2006. Alternans and spiral breakup in a human ventricular tissue model. American Journal of Physiology-Heart and Circulatory Physiology 291 (3), H1088–H1100.

37. Tikhonov, A., Arsenin, V. Y., 1977. Methods for solving ill-posed problems. John Wiley and Sons, Inc.

38. Vadakkumpadan, F., Arevalo, H., Ceritoglu, C., Miller, M., Trayanova, N., 2012. Image-based estimation of ventricular fiber orientations for personalized modeling of cardiac electrophysiology. Medical Imaging, IEEE Transactions on 31 (5), 1051–1060.

39. Vaquero, M., Calvo, D., Jalife, J., 2008. Cardiac fibrillation: from ion channels to rotors in the human heart. Heart Rhythm 5 (6), 872–879.

40. Varma, N., Jia, P., Rudy, Y., 2007. Electrocardiographic imaging of patients with heart failure with left bundle branch block and response to cardiac resynchronization therapy. Journal of electrocardiology 40 (6), S174–S178.

41. Wang, Y., Cuculich, P. S., Zhang, J., Desouza, K. A., Vijayakumar, R., Chen, J., Faddis, M. N., Lindsay, B. D., Smith, T. W., Rudy, Y., 2011. Noninvasive electroanatomic mapping of human ventricular arrhythmias with electrocardiographic imaging. Science translational medicine 3 (98), 98ra84–98ra84.

42. Wittkampf, F. H., Wever, E. F., Derksen, R., Wilde, A. A., Ramanna, H., Hauer, R. N., De Medina, E. O. R., 1999. Localisa new technique for real-time 3-dimensional localization of regular intracardiac electrodes. Circulation 99 (10), 1312–1317.

43. Yamashita, Y., 1982. Theoretical studies on the inverse problem in electrocardiography and the uniqueness of the solution. Biomedical Engineering, IEEE Transactions on (11), 719–725.

44. Yushkevich, P. A., Piven, J., Hazlett, H. C., Smith, R. G., Ho, S., Gee, J. C., Gerig, G., 2006. User-guided 3d active contour segmentation of anatomical structures: significantly improved efficiency and reliability. Neuroimage 31 (3), 1116–1128.

45. Zhang, X., Ramachandra, I., Liu, Z., Muneer, B., Pogwizd, S. M., He, B., 2005. Noninvasive three-dimensional electrocardiographic imaging of ventricular activation sequence. American Journal of Physiology-Heart and Circulatory Physiology 289 (6), H2724–H2732.

Chapter 6

Cardiac Resynchronization Therapy Reduces the Amount of Myocardium Performing Negative Work

Abstract

In patients with dyssynchronous heart failure (DHF), the distribution of myocardial work in the dilated ventricles becomes heterogeneous as a result of non-uniform mechanical function. During cardiac resynchronization therapy (CRT), the redistribution of myocardial work may play an important mechanistic role in favorable CRT response by linking synchronous tissue-level function to cell-level processes leading to left ventricular (LV) reverse remodeling. In the present study, regional myocardial work during DHF and acute CRT was quantified using patient-specific, multi-scale models constructed from clinical measurements of individual patients at baseline. We found that, during acute CRT, the degree of reduction of septal myocardium performing negative work relates to the degree of LV reverse remodeling at 6 months of CRT.

6.1 Introduction

Heart failure (HF) affects 5.7 million people in the US causing more than 550,000 deaths annually. Half of all HF patients exhibit reduction in left ventricular ejection fraction and dilated cardiomyopathy (DCM), particularly in dyssynchronous heart failure (DHF) caused by left bundle branch block (LBBB). Cardiac resynchronization therapy (CRT) is a cost effective device-based treatment aimed to improve ventricular synchrony using an implantable, programmed pacemaker. Patients who respond to CRT exhibit improvement of symptoms and evidence of left ventricular (LV) reverse remodeling (>10% reduction in LV end-systolic volume [19]). Conventional clinical guidelines recommend CRT use based on patient etiology, severity of symptoms, and various features of cardiac structure and function measured by standard clinical modalities [48, 37]. Identification of patients who will likely benefit from CRT has proven difficult given a 30-40% rate of non-response wherein patient symptoms do not improve or in some cases worsen. With over 50,000 implant procedures (at a 10% failure rate) performed annually at a cost of over $7B in the US and over $17B globally, there is an urgent socio-economic need for clinical decision support tools to help cardiologists improve overall care by maximizing patient benefit and minimizing risks and costs.

An important physiological effect of CRT is thought to be improved mechanical pump efficiency by synchronous ventricular function, resulting in increased cardiac output at diminished energy cost to the myocardium [32]. Patients with evidence of severe dyssynchrony at baseline are therefore more likely to improve. In the last decade, clinical researchers have sought non-invasive markers of electromechanical dyssynchrony in DHF (baseline) to predictive acute improvements in hemodynamic performance and chronic LV reverse remodeling in CRT. Electrical dyssynchrony, marked by a QRS duration > 150 ms on a 12-lead body-surface electrocardiogram (ECG), remains the strongest predictor of CRT on morbidity and mortality [13]. Markers of mechanical dyssynchrony (e.g. regional delays in onset of shortening, peak velocity, septal flash) (refs) and mechanical dis-coordination (e.g. internal shortening fraction (ISF) [47] circumferential uniformity ratio estimate (CURE) [18], septal rebound stretch [28, 16]), have proven to be of value but are inconsistent [12], possibly due to technical challenges of echocardiographic imaging and analysis [44, 15]. Acute hemodynamic improvement during CRT

depends on patient-specific anatomical lead positions [9] and programmed A-V [8, 34] and V-V delays [41], however stroke work and dP/dt only relate weakly with outcomes [7].

The pathophysiological consequence of dyssynchronous function on the ventricular myocardium manifests as a redistribution of regional mechanical work [39, 17, 4]. In DHF caused by LBBB with DCM, work is depressed in the early-activated septum and elevated in the late-activated LV lateral wall. Kerckhoffs et al demonstrated that the coefficient of variation of work (COVW) is a sensitive measure of work heterogeneity introduced by mechanical dis-coordination in dogs [23], suggesting its utility as a marker for distinguishing responders and non-responders at baseline. Corresponding with changes in regional myocardial work are recently observed changes in myocardial perfusion [43, 45, 38], metabolism [35, 17], and structural remodeling [31], suggesting that that the altered mechano-energetic condition elicits pathophysiological adaptations in the local myocardium. Furthermore, recent molecular studies have characterized remarkable degrees of cellular adaptation [11, 22] that coincide with redistributions in perfusion and metabolism in early- and late-activated regions, including myocyte gene expression [5], electrical properties [2], and cell survival [10].

The regional distribution of work in DHF and CRT may therefore play an important role in cellular responses underlying mechanisms of adverse and reverse remodeling. However, non-invasive estimation of regional mechanical work in human individuals remains a challenge for standard clinical practice. In the present study, we develop patient-specific, multi-scale computational models using clinical measurements to estimate the regional work heterogeneity in DHF and investigate its impact on the benefit from CRT by long-term LV reverse remodeling.

6.2 Methods

6.2.1 Clinical study

Eight male patients aged (66 ± 11 years) with NYHA class III heart failure, dilated cardiomyopathy, left bundle branch block (LBBB) (QRS duration 145 ± 22 ms), and left ventricular ejection fraction (LVEF) $28 \pm 7\%$ were enrolled from the Veteran's

Administration San Diego Healthcare System (San Diego, CA) in 2008–2014. Patients gave informed consent to participate in the human subject protocol approved by the Institutional Review Board. One patient (BiV6) had a previously implanted RV pacemaker. Anatomical, electrophysiological, and hemodynamic measurements for each patient were obtained at baseline LBBB and immediately after pacemaker (St. Jude Medical) implantation and operation (acute CRT).

Several types of imaging data sets were obtained before device implantation. End-diastolic ventricular geometry was imaged by 64-slice computed tomography (CT) (Lightspeed VCG, GE Medical Systems, Milwaukee, WI) with an isotropic in-plane resolution of 0.49 mm (256$\times$256 pixels) and slice thickness of 0.625 mm. In two patients, end-diastolic geometry was imaged by magnetic resonance (MR) imaging (specifications) with an in-plane resolution of 0.9 mm (128$\times$128 pixels) and slice thickness of 2 mm. In five patients with myocardial infarction, affected regions were localized by singe-photon emission computed tomography (SPECT) (technetium sestamibi, ECAM-2, Siemens Medical Solutions, Hoffman Estates, IL) during rest and stress with an isotropic in-plane resolution of 6.59 mm and 10 mm slice thickness.

Electrophysiology and hemodynamic measurements were obtained before and after device implantation. Standard 12-lead body-surface electrocardiograms (ECGs) were recorded (Bard Pro, Bard Electrophysiology, Lowell, MA) over 5-6 beats at 1 kHz sampling rate. Vectorcardiograms (VCGs) were derived from the ECGs [26]. Left and right ventricular cavity pressures were continuously monitored by cardiac catheterization over several beats at 1 kHz sampling rate. Mean aortic pressure was recorded by sphygmomanometer measurements. Two-dimensional (2D) transthoracic echocardiography (TTE) (Sonos, Philips Medical IE33, Bothell, WA) recorded two- and four-chamber long-axis views of the ventricles over two beats. End–diastolic LV volumes and valve diameters (aortic and mitral annuli) were computed from the images. Continuous-wave Doppler TTE estimated regurgitated and forward stroke volumes by the velocity time integral (VTI) of hemodynamic flows through the mitral and aortic valves. Table (6.1) summarizes patient characteristics at baseline.

BiVP's were implanted with pace/sense leads placed on the right atria (lead A), RV septal surface (lead V), and the LV free wall (lead V) epicardial surface through

a coronary vein. Final V-lead positions on the ventricles were localized from bi-plane chest x-ray images by an expert electrophysiologist (David E. Krummen). A-V delays were programmed to 161.25 ± 21 ms (paced) and 121.25 ± 14 ms (sensed). The V-V delay, (w.r.t. the V-lead on the LV) was programmed to 19.4 ± 16.6 ms according to an algorithm (QuickOpt, St. Jude) to maximize cardiac output from Doppler TTE. Following 3 ± 1 months of bi-ventricular pacing, the V-V delays were reprogrammed to 27.5 ± 17.9 ms to maintain maximum stroke volume. After 6 months of pacing, a follow up 2D TTE study assessed changes in cardiac output and ventricular volumes (LV reverse remodeling). CRT responders were identified by > 10% decrease in LV end-systolic volume from baseline.

6.2.2 Patient–specific cardiovascular model

Anatomy

Biventricular anatomical model construction from clinical and empirical data have been described previously [27, 1]. Briefly, CT or MR images of the ventricles at end-diastole were segmented and triangulated. A high-order cubic Hermite biventricular mesh atlas with 64 hexahedral elements was fitted to the triangulation using an iterative linear least squares algorithm [33]. The resulting mesh was refined to a total of 128 elements for biomechanics simulations. A child mesh atlas with 132 linear hexahedral elements was co-registered to its parent, converted to cubic Hermite hexahedral elements [20], and refined to 8448 elements for electrophysiology simulations [46].

Human ventricular fiber architecture was estimated using diffusion tensor MR (DT-MR) images of an explanted human donor heart [27]. Reconstructed tensors in myocardial regions were registered to a high-order mesh of the explanted heart using a log-Euclidean tensor interpolation framework. Local orthogonal fiber, sheet, and sheet-normal axes were computed from the eigenvectors of the fitted tensors. The fiber architecture of the explanted heart was mapped to each patient-specific geometry via large deformation diffeomorphic mapping and tensor reorientation to account for changes in fiber structure due to differences in ventricular shape.

Regions of myocardial infarction were localized from rest and stress SPECT by

an expert cardiac electrophysiologist/nuclear radiologist (David E. Krummen). Regions of depressed perfusion were manually demarcated on the CT/MR triangulations and registered in each patient-specific mesh as binary fields of normal and infarcted tissue.

Electrophysiology

Action potential propagation was modeled as mono-domain reaction-diffusion with human ventricular myocyte ionic currents [42]. Ion channel properties were adjusted to approximate observed changes in AP morphology during HF [1]. Patient-specific 3D regional depolarization times at baseline were estimated by optimizing the location of an ectopic stimulus in the RV sub-endocardium and myocardial electrical conductivities to match vectorcardiograms derived from measured ECGs [46]. Using the optimized baseline electrophysiology properties, acute CRT depolarization patterns for paced beats were simulated by applying stimuli according the prescribed V-V lead delays and locations in the anatomical model; programmed A-V delays were less than 180 ms.

Biomechanics

The unloaded ventricular geometry at zero pressure and active and passive biomechanics properties at baseline were estimated as described in previous work [27, 1]. Using an empirical PV relation [25] and transversely isotropic passive stiffness [21], the diastolic pressure-volume (PV) loading curves for the unloaded ventricles were matched to the observed end-diastolic pressure and volume measured by intra-cardiac catheterization and echocardiography. The estimated unloaded geometry served as the reference configuration for subsequent stress and strain computations. Left and right systolic pressure traces were matched to the observed pressure traces (particularly peak systolic pressure, dP/dt max, and dP/dt min) and end-systolic volume by adjusting parameters of an active contraction model [29]. Local onset of contraction was defined by the estimated local depolarization times in the electrophysiology model.

Hemodynamics

A closed-loop, self-adaptive model of the systemic and pulmonary circulation [3] was coupled to the biomechanics model via pressure boundary conditions to compute systolic and diastolic pressure traces [27, 1]. Measured valve annuli diameters from 2D TTE were input directly as dimensional parameters, while others (e.g. atrial diameter) were predetermined within normal human physiologic limits. Aortic and pulmonary arterial length parameters were manually adjusted to match measured systolic pressures. Remaining circulatory parameters (e.g. vessel compliance) were self-adapted during non-steady state beats to match the cardiac output (accounting for mitral regurgitation) measured from Doppler TTE and aortic pressure measured by sphygmomanometer. The fully parameterized hemodynamic model was simulated over 11 beats at measured heart rates until steady-state pressure traces were obtained.

6.2.3 Global and regional myocardial work metrics

Principal (fiber, sheet, and sheet-normal) myocardial stresses and strains (referenced to the unloaded geometry) were computed during the 10th steady-state beat at the Gauss-Legendre quadrature points (27 per element, 3,456 total) of the biomechanics meshes. The external myocardial work density (kJ/m^3) over the complete cardiac cycle beat was calculated by the areas enclosed by the stress-strain loops; clockwise and counter-clockwise loops were defined as positive and negative work, respectively; positive work indicates work performed by myocardium on the blood volume, and negative work indicates work performed by the blood volume on the myocardium. Global (i.e. stroke work, total LV myocardial work, efficiency η, and COVW) and regional (i.e. RV, septal, and LV) work metrics were examined to determine significant ($p<0.05$) differences between responders and non-responders during LBBB and CRT. Significant differences were determined by student's t-tests and 2-way ANOVA between responders versus non-responders and LBBB versus CRT. Metrics which differed significantly between response groups and physiologic states were correlated with the measured ΔESV_{LV} to determine significant relations with LV reverse remodeling. Significance was defined by the critical values for Pearson's correlation coefficient.

6.2.4 Work sensitivity analysis

The sensitivity of important work metrics to patient-specific variations in physiological components was assessed. Work metrics during steady-state beats were recomputed in 8 knock-out simulations (6 for LBBB, 2 for CRT) where, for the complete set of 8 patients, patient-specific parameters of each model component were replaced by patient-averaged parameters for a total of 64 additional simulations. The patient-averaged geometry (–G) was computed from the spatial average of the patient-specific geometries. The patient-averaged LBBB activation pattern (–A) was simulated using the spatial average of the ectopic stimulus location in the RV and myocardial conductivities in the patient-averaged geometry. Patient-averaged CRT activation pattern was simulated using the average of the V-lead locations and V-V delays. Patient-averaged biomechanics (–M) and hemodynamics (–H) were obtained by averaging optimized parameters. The patient-averaged unloaded geometry was re-estimated from the averaged biomechanics parameters. Regions of myocardial infarction were removed (–I) entirely in ischemic patients. Finally, the simultaneous interaction effect of patient-specific geometry and LBBB activation pattern (–GA) was evaluated.

The recomputed work metrics from each knock-out simulation were compared against ΔESV_{LV}. An important patient-specific variation of physiological property was identified when a knock-out resulted in a loss of the original significant correlation with ΔESV_{LV}. The contribution of each physiological component on the original patient-specific work metrics was assessed by the correlation coefficient (R^2) and normalized root-mean-squared deviation (nRMSD) between paired (fully patient-specific vs patient-averaged) sets of work metric values.

6.3 Results

6.3.1 Clinical outcomes

After 6 months of pacing, CRT responders were identified by a reduction (+) in LV end-systolic volume $\Delta ESV_{LV} > +10\%$ measured by 2D TTE. The responders were BiV6 (+50 mL; +59%), BiV3 (+14 mL; +16%), BiV5 (+32 mL; +15%), and BiV1 (+17

mL; +12%). Non-responders with a sub-threshold reduction or increase (-) in LV end-systolic volume included BiV8 (+8 mL; +7%), BiV2 (-3 mL; -2%), BiV4 (-22 mL; -12%), and BiV7 (-55 mL; -36%). BiV7 was classified as a clinical non-responder due to mortality.

Baseline clinical measurements including QRS duration, LVEF, LV end-diastolic volume, LV peak systolic pressure, dP/dt max, dP/dt min, LV end-diastolic volume, and LV mass were compared (Figure (6.2)) against ΔESV_{LV} to determine possible correlates with CRT response. None of the clinical measurements showed a correlation with ΔESV_{LV}.

6.3.2 Patient-specific CRT model validation

Patient-specific electromechanical function during acute CRT was validated to measured hemodynamic features. Peak LV systolic pressure and dP/dt max are compared in Figure (6.3). The RMS error values were 5 mmHg and 0.3 mmHg/s for peak LV pressure and dP/dt max, respectively. Changes in QRS duration were not validated since electrical resynchronization has been shown to be unrelated to hemodynamic response, and pacing may still provide clinical benefit despite QRS duration prolongation [14].

6.3.3 Regional work distributions

Stresses and strains were computed from steady-state beats during LBBB and CRT. Figure (6.5) illustrates regional stress-strain loop distributions of a representative CRT responder (BiV6) and non-responder (BiV7) during LBBB. In LBBB, early-activated regions in the RV and septum feature loops with little contained area, resulting in low total cycle work performed by the myocardium. Loops in septal regions near the apex tend to feature intersections, revealing systolic periods when work is done on the myocardium (negative work) attributed by blunted systolic stress and systolic stretch. In contrast, late-activated regions in the LV lateral wall produce large loops with augmented positive work magnitudes due to increased systolic stress. Peak shortening did not differ significantly between the two regions. In CRT, stress-strain loops with the

regional distribution is reversed, with early-activated regions occurring at the LV lateral wall near the pacing site.

6.3.4 Baseline work heterogeneity and efficiency

We first determined whether regional work heterogeneity distinguishes responders and non-responders during LBBB and CRT. Regional work heterogeneity was computed as the COVW from total cardiac cycle work sampled at the Gauss-Legendre points (3,456 in total) of the patient-specific meshes. Figure (6.4) (A) shows box plots of the COVW distributions for responders and non-responders at baseline LBBB and CRT. COVW values were significantly ($p<0.05$) different in responders (1.55 ± 0.12) and non-responders (1.28 ± 0.2) at baseline LBBB, confirming the utility of COVW as a marker for CRT outcome as suggested by Kerckhoffs [23]. During acute CRT, work heterogeneity was reduced overall for both responders and non-responders, but not significantly. Responders had a marginally significant ($p=0.05$) difference in COVW at baseline and CRT compared to non-responders, indicating that global work homogenization is not strongly related to outcomes.

Next, we assessed whether improved pump efficiency during acute CRT is greater in responders compared to non-responders. We defined the global pump efficiency η to be the simulated LV stroke work normalized by the LV myocardial work. Box plots of the LV stroke work, myocardial work, and efficiency are shown in Figure (6.4) (B). At baseline, LV stroke work (mean$\pm$std) and myocardial work (mean$\pm$std) were similar between responders and non-responders. During CRT, there was a minute increase in LV stroke work and decrease in myocardial work in responders and non-responders, resulting in increased η for both groups. Interestingly, non-responders saw a significantly increased η, while responders did not. No significant difference in η was observed between LBBB and CRT for all patients or between responders and non-responders at LBBB and CRT. Therefore, η does not appear to be an important distinguishing feature between responders and non-responders.

6.3.5 Negative work and late systolic stretch in the LV and septum

Features of the regional work distribution were examined in detail. Histograms of the work density as fractions of the myocardium were partitioned among LV free wall (LVFW), septum, and RV free wall (RVFW) regions in Figure (6.6) for LBBB and Figure (6.6) for CRT. Apparent features of the distributions are long tails of positive work values, primarily in the LV free wall, and short tails of negative work values, particularly in the RV and septum. No trend between CRT response and reduction of high work values (truncation of the positive tail) was observed; during acute CRT, the fraction of LV lateral wall performing high positive work (upper quartiles of baseline work distributions) decreased on average by 4% for responders and 6% for non-responders. However, significant differences in the volume fraction of negative work in the LV (LVNW) and septum (STNW) were observed. Figure (6.7) shows box plots comparing LVNW and STNW for responders and non-responders at baseline LBBB and CRT. A significant difference in the baseline fraction of LVNW (p=0.04) and STNW (p=0.02) between responders and non-responders was observed. There was also a significant difference in LVNW (p=0.04) and STNW (p=0.003) between LBBB and CRT in responders. Notably, STNW was significantly different (p=0.002) between LBBB and CRT for all patients. A significantly ($p<0.05$) larger fraction of LV performing negative work at baseline, particularly in the septum, was present in responders compared to non-responders. A significant reduction in the fraction of septum performing negative work during CRT.

Reduction of systolic stretch, particularly in the septum, has been associated with mechanical dyssynchrony, acute hemodynamic improvement, and long-term LV reverse remodeling [30, 28, 16]. As a possible kinematic surrogate of the work distribution, the fraction of septum with late systolic stretch, ST λ_{late}, referenced to the end-diastolic configuration) was quantified during LBBB and CRT. Late systolic stretch was defined as $\lambda_{\text{late}} > 1$ during or following peak shortening of myocardium in high work, late-activated regions of the LVFW. Figure (6.7) illustrates the stretch traces for a representative responder (BiV6) and non-responder (BiV7) in the septum and LVFW during LBBB and CRT. Both responders and non-responders have evidence of ST λ_{late} during LBBB. During CRT, the amount of ST λ_{late} is visibly reduced to a greater degree compared to non-responders. The box plot in Figure (6.8) shows a marginally signifi-

cant (p=0.05) difference in ST λ_{late} during LBBB and CRT in responders. There was a significant (p=0.03) difference in ST λ_{late} among all patients between LBBB and CRT.

6.3.6 Reduction of myocardium performing negative work correlates with CRT response

Having identified critical differences in LVNW, STNW, and ST λ_{late} in responders and non-responders, the patient-specific values during LBBB, CRT, and the change (defined as LBBB value - CRT value) were correlated directly with measured ΔESV_{LV} (Figure (6.9)). At baseline, significant correlations were found for LVNW (R^2=0.82; p<0.01) and STNW (R^2=0.68; p<0.02), but not for ST λ_{late}. None of the metrics correlated during acute CRT. However, the change in the work metric values between LBBB and CRT correlated with outcomes: ΔLVNW (R^2=0.52; p<0.05) was modest, but ΔSTNW (R^2=0.78; p<0.01) and ΔST λ_{late} (R^2=0.74; p<0.01) were strong. The latter results in particular suggest a causal mechanism for the degree of benefit from CRT.

6.3.7 Work is sensitive to hemodynamics, geometry, and electrical activation

We determined the sensitivity of LVNW, STNW, and ΔSTNW to patient-specific variations in physiology model components by substituting each with patient-averaged parameters. The summary results are shown in Table (6.2). The original correlation between CRT outcomes and baseline LVNW and STNW were lost with the removal of patient-specific variations in hemodynamics (–H) (LVNW – 0.815 to 0.374; STNW – 0.675 to 0.130) and combined geometry and electrical activation pattern (–GA) (LVNW – 0.815 to 0.478; STNW – 0.675 to 0.466). During CRT, the original correlation between CRT outcomes and ΔSTNW was lost with the removal of patient-specific variations in the geometry (–G) (ΔSTNW – 0.779 to 0.499) and pacing protocol (–A) (ΔSTNW – 0.779 to 0.044).

The significance of removing patient-specific model components to the patient-specific variation of work was also evaluated by computing the R^2 and normalized root mean squared deviations (nRMSDs) between the work values produced by the origi-

nal patient-specific and patient-averaged model components. Substitution of patient-averaged hemodynamics (–H) at baseline left only 9.2% and 30.3% of the original variation remaining in LVNW and STNW, respectively; this corresponded with nRMSD values of 31% and 33%. Substitution of patient-averaged geometry and electrical activation (–H) at baseline left 81.2% and 58.6% of the original variation remaining in LVNW and STNW, respectively; this corresponded with nRMSD values of 14% and 31%. Substitution of patient-averaged geometry (–G) alone also resulted in a significant impact on baseline LVNW (85.7%; 14% nRMSD) and STNW (66.3%; 33% nRMSD). During CRT, ΔSTNW was significantly affected by substitution of patient-averaged geometry (–G) (46.3%; 41% nRMSD) and activation pattern (–A) produced by the averaged CRT pacing protocol (11.7%; 47% nRMSD).

6.4 Discussion

This is the first study to demonstrate in human patients the significance of the regional work distribution during DHF and CRT on LV reverse remodeling. These results suggest that LV reverse remodeling as a long-term outcome of CRT is not due to an acute increase in work efficiency, but rather an acute and sustained improvement of the distribution of myocardial work in the LV, particularly in the septum (STNW). Furthermore, LV reverse remodeling is more likely in patients with more severe baseline electromechanical dyssynchrony (as estimated by LVNW) and have greater capacity for improvement.

The finding that the improvement of septal myocardial work is supported by recent experimental evidence. Studies in DHF patients have demonstrated that depressed septal glucose metabolism at baseline [6] and improvement in septal perfusion during CRT [36] predicts long-term LV reverse remodeling. These findings strongly suggest that tissue-level mechano-energetics, particularly in the septum, have important effects on cell-level mechanisms which underlie DHF pathophysiology and CRT remodeling. Specifically, transcripts for proteins involved in metabolic (oxidative phosphorylation, fatty acid, amino acid, and glucose metabolism) and signaling (MAPK, JAK-STAT, TGF-beta) pathways were down- and up-regulated, respectively, cardiomyocytes sam-

pled from early-activated regions [5]. CRT was shown to reverse the levels of transcripts across the genome to normal. Other cellular changes include regional heterogeneities in activity of stress kinases (affecting muscle function, survival, and fibrosis), electrical properties (affecting arrhythmogenesis), Ca^2+ handling (affecting contractility), and micro-RNAs. mIRs in particular are responsible for modulating myocyte hypertrophy, excitation-contraction coupling, apoptosis, and fibrosis [40]. Global changes are characterized by blunted beta-adrenergic response, contractility, and cell survival. CRT has been found to restore Ca^2+ sensitivity of myofilaments through GSK-3B reactivation and phosphorylation at sites on Z-disk and M-band proteins [24]. For stress signaling, CRT reversed regional heterogeneities of stress signaling caused by increased p38 MAPK and Ca-calmodulin kinase II (CaMKII) activity and increased tumor necrosis factor (TNF)-alpha expression. Localized differences in stress kinase activation were shown to be consistent with disparities in regional work load in DHF and its equalization by CRT.

The analysis of sensitivity of the myocardial work revealed that patient-specific variations in baseline hemodynamics and ventricular geometry and electrical activation combined were important determinants of baseline regional work. This suggests that the degree of ventricular dilation and dyssynchrony introduced by LBBB are important properties that determine CRT outcomes, supporting the original hypothesis by Kerckhoffs et al. [23]. While the degree of dilation is measurable by clinical imaging, the severity of dyssynchrony is less obvious to measure from standard ECGs alone. Because the width of the QRS reflects the increased size of the ventricles, slowing of myocardial conductivity, and activation of the LV and RV, a more specific clinical measure of electrical delay in the LV is needed for an accurate assessment of dyssynchrony. Hemodynamics was also found to be an important determinant of regional work. The model of hemodynamics used in this study contained a large amount of parameters which made identification of a specific significant hemodynamic property more difficult. Further sensitivity analysis of hemodynamic outputs (e.g. LV and RV time-courses of pressures and volumes) to input patient data could reveal which clinical measurement(s) are important for estimating baseline severity of DHF and long-term CRT outcomes. Finally, the improvement in septal work due to CRT was also dependent on ventricular geom-

etry and pacing protocol parameterized by lead position and V-V delay. This finding underscores the importance of patient-specific application of CRT to maximize work improvement. The electrical activation pattern produced by a given lead position and V-V delay depends on the geometry and electrophysiological properties of given patient's ventricles. Further model analysis of the individual contributions of geometry, myocardial conductivity, lead location, and V-V delay on the regional work will identify the most important pacing parameters to consider for maximizing CRT outcomes for a given patient's baseline condition.

6.5 Conclusion

This work suggests a possible mechano-energetic mechanism for LV reverse remodeling due to CRT for the first time in human patients. Specifically, the fraction of myocardium performing negative work at baseline is a strong indicator of the likelihood of LV reverse remodeling measured after 6 months of CRT. Reduction of the fraction of septal myocardium performing negative work is also strongly correlated with the degree of LV reverse remodeling. The fact that the models can reliably predict outcomes based solely on baseline data suggests that more diagnostic information from clinical measurements can be extracted and integrated using models than the measurements alone. We have also identified patient-specific hemodynamics, geometry, and electrical activation sequence as important determinants of the work distribution. Since the heart adapts to changes in its environment by growth and remodeling, acute changes predicted by the model are still insufficient to answer questions relating to the long-term development of optimal intervention therapies. Future work can develop computational models that can predict chronic response to pacing by allowing for changes in the heart geometry due to local tissue growth.

Acknowledgments

The content of this chapter comprises a draft of a manuscript in preparation with shared first authorship; the citation is: Krishnamurthy A*, Villongco CT*, Krummen

DE, Stark P, Kerckhoffs RCP, Omens JH, McCulloch AD. Cardiac resynchronization therapy reduces negative myocardial work in patient-specific models of dyssynchronous heart failure. *Science Translational Medicine, in preparation*, 2015. The author gives thanks to Adarsh Krishnamurthy, David Krummen, Jeffery Omens, and Andrew McCulloch for discussions and suggestions regarding clinical data interpretation, study design, modeling, and results analysis.

Table 6.1: Summary of patient characteristics at baseline. Patient characteristics include age (years), forward ejection fraction (fEF) (%), QRS duration (QRSd) (ms), mitral valve regurgitant volume (MRV) (mL), heart rate (HR) (beats per minute), and anatomical location of myocardial infarct.

Measure	BiV1	BiV2	BiV3	BiV4	BiV5	BiV6	BiV7	BiV8
Age	84	65	79	64	61	55	68	54
fEF (%)	38	26	35	25	17	32	21	29
QRSd (ms)	156	148	162	130	182	119	140	120
MRV (mL)	—	16	—	36	14	—	—	—
HR (bpm)	70	70	70	70	60	70	70	75
Infarct Location	—	septo posterior	septal	posterior	septo posterior	—	—	posterior

Table 6.2: Summary results of work sensitivity analysis. Reduction of negative work in the LV and septum correlates with the degree of LV reverse remodeling. The sensitivity of negative work in the LV (LVNW) and septum (STNW) during baseline and CRT to patient-specific variations in different physiological aspects was assessed. The original patient-specific (Ps) parameters were substituted by patient-averaged parameters for the geometry (G), activation times (A), mechanics (M), and hemodynamics (H). In patients with myocardial infarction, the infarct was removed (I). Patient-averaged hemodynamics and simultaneous geometry and electrical activation times (GA) eliminated the significant correlation between outcome and negative work at LBBB. The significant correlation between ΔESV_{LV} and ΔSTNW was also eliminated using average geometry and electrical activation pattern during acute CRT.

State	LBBB							CRT		
Case	Ps	–G	–I	–A	–M	–H	–GA	Ps	–G	–A
Model Component										
Geometry	●	○	●	●	●	●	○	●	○	●
Infarct	●	●	○	●	●	●	●	●	●	●
Activation times (LBBB)	●	●	●	○	●	●	○	-	-	-
Bioechanics	●	●	●	●	○	●	●	●	●	●
Hemodynamics	●	●	●	●	●	○	●	●	●	●
Activation times (CRT)	-	-	-	-	-	-	-	●	●	○
Regional work metric	$R^2(\Delta ESV_{LV})$									
LVNW	**0.815***	0.580*	0.823*	0.733*	0.797*	0.374	0.478	0.250	0.375	0.417
STNW	**0.675***	0.546*	0.752*	0.605*	0.629*	0.130	0.466	0.060	0.277	0.267
ΔSTNW	-	-	-	-	-	-	-	**0.779***	0.499	0.044
	R^2 (Ps)									
LVNW	**1.000**	0.857	0.996	0.971	0.997	0.092	0.812	**1.000**	0.754	0.114
STNW	**1.000**	0.663	0.916	0.924	0.996	0.303	0.586	**1.000**	0.220	0.261
ΔSTNW	-	-	-	-		-	-	**1.000**	0.463	0.117
	nRMSD (Ps)									
LVNW	**0%**	14%	2%	9%	3%	31%	14%	**0%**	35%	60%
STNW	**0%**	33%	11%	13%	3%	33%	31%	**0%**	48%	70%
ΔSTNW	-	-	-	-	-	-	-	**0%**	41%	47%

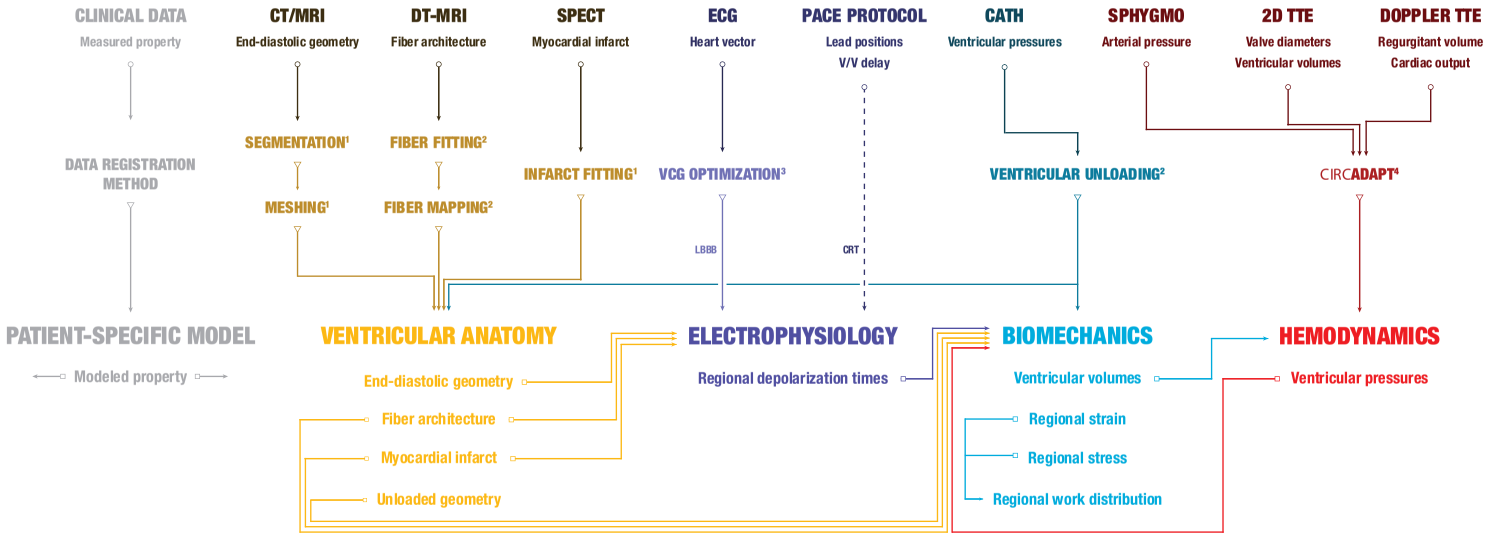

Figure 6.1: [Overview of clinical data, registration methods, and patient-specific model. Patient clinical data of measured pathophysiological features in DHF were obtained from standard clinical modalities (CT/MRI, SPECT, ECG, intracardiac catheterization, sphygmomanometer, 2D trans-thoracic echocardiography, Doppler trans-thoracic echocardiography). DT-MRI measurements were obtained from a human donor heart. Previously described data registration methods were used for parameterization of patient-specific model components including ventricular anatomy (yellow), electrophysiology (purple), biomechanics (blue) and hemodynamics (red) model components (1 [1]; 2 [27]; 3 [46]). Input/output relationships of model features between model components are illustrated with arrows. Patient-specific ventricular anatomy includes the end-diastolic geometry, fiber architecture, myocardial infarct, and unloaded geometry [27]. The patient-specific electrophysiology model predicts regional depolarization times in the end-diastolic geometry during LBBB and CRT. Forward coupling from electrophysiology to biomechanics is achieved by prescription of activation of systolic contraction. Patient-specific biomechanics computes ventricular volumes, stresses, and strains. Pressure boundary conditions are coupled to the biomechanics model by a model of closed-loop, adaptive systemic and pulmonary circulation (CircAdapt [3]). Regional myocardial work is computed from the simulated stresses and strains of during a steady-state beat in LBBB and CRT.

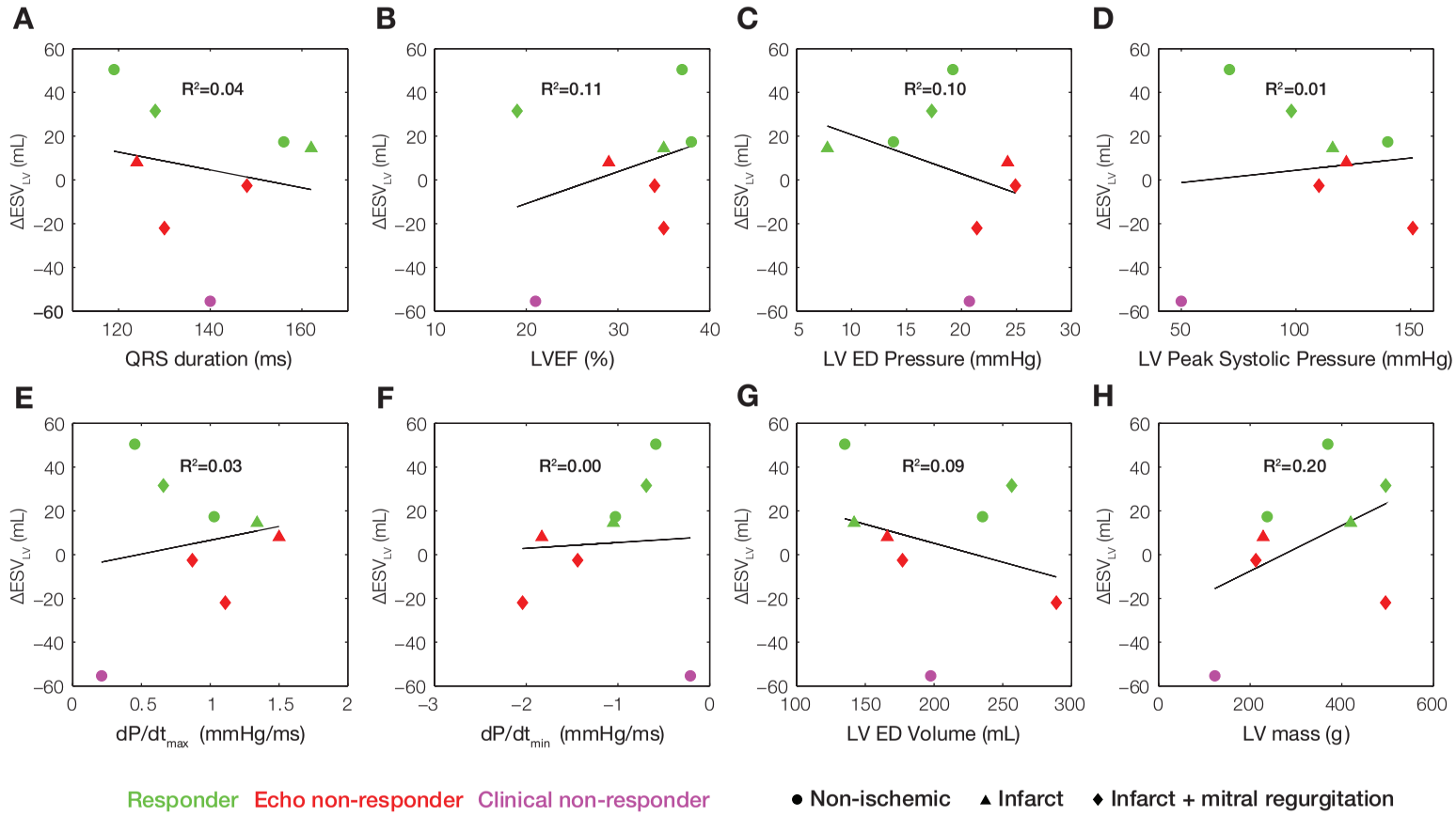

Figure 6.2: Clinical measures of LV function at baseline (LBBB) do not correlate with CRT outcome. Baseline clinical measurements such as (A) QRS duration, (B) left ventricular ejection fraction (LVEF), (C) LV end-diastolic (ED) pressure, (D) LV peak systolic pressure, (E) dP/dt max, (F) dP/dt min, (G) LV ED volume, and (H) LV mass do not correlate with measured ΔESV_{LV} after 6 months of CRT.

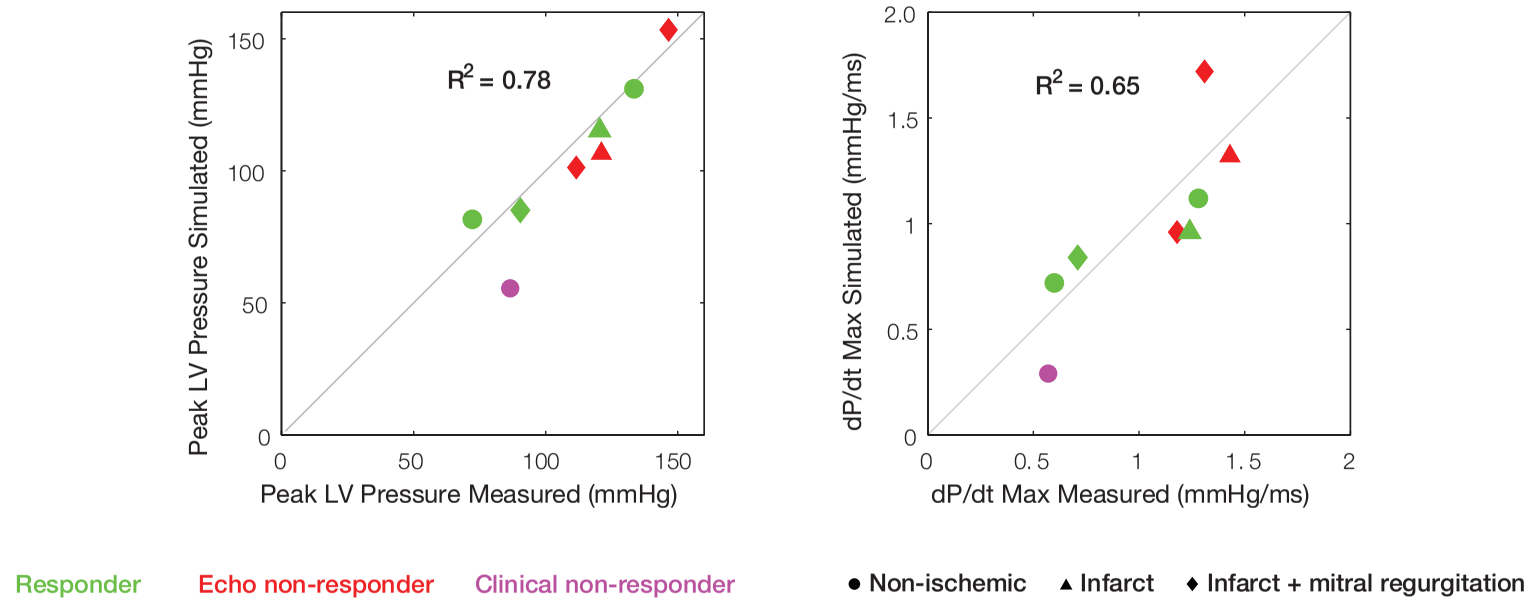

Figure 6.3: Patient-specific CRT model validation. Predicted and measured dP/dt max and peak systolic pressure are compared after acute CRT pacing.

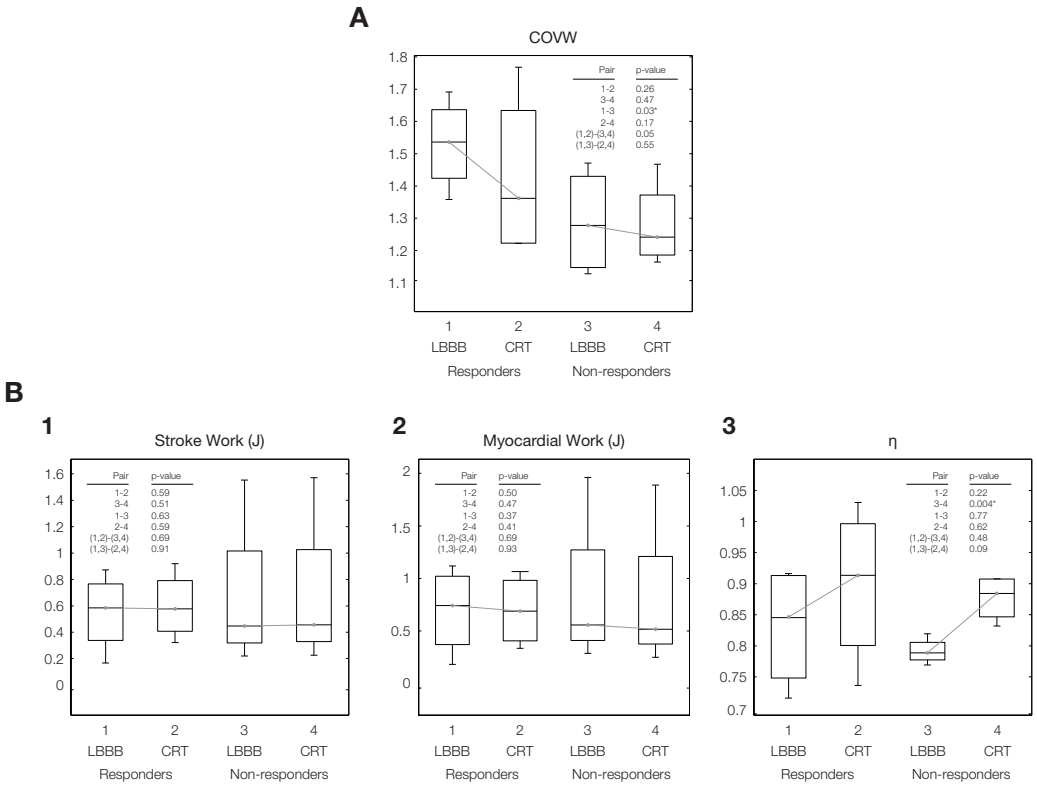

Figure 6.4: Differences in global work metrics between responders and non-responders. Regional work heterogeneity in LBBB differs between responders and non-responders, but LV stroke work, myocardial work, and efficiency do not. Box plots of computed distributions of (A) coefficient of variation of work (COVW) and (B) global work metrics (including LV (B1) stroke work, (B2) myocardial work, and (B3) efficiency (Îů)) show few differences between responders and non-responders during LBBB and CRT. Regional work heterogeneity (COVW) is significantly ($p<0.05$) different between responders and non-responders in LBBB (A) (Pair 1-3). Decrease in work heterogeneity during CRT is marginally significant between responders and non-responders (Pair (1,3)-(2,4)). LV stroke work increases and myocardial work decreases insignificantly among responders and non-responders between LBBB and CRT (B1, B2). Work efficiency η increases significantly among non-responders (Pair 3-4) during CRT, but insignificantly among all patients (B3) (Pair (1,3)-(2,4)).

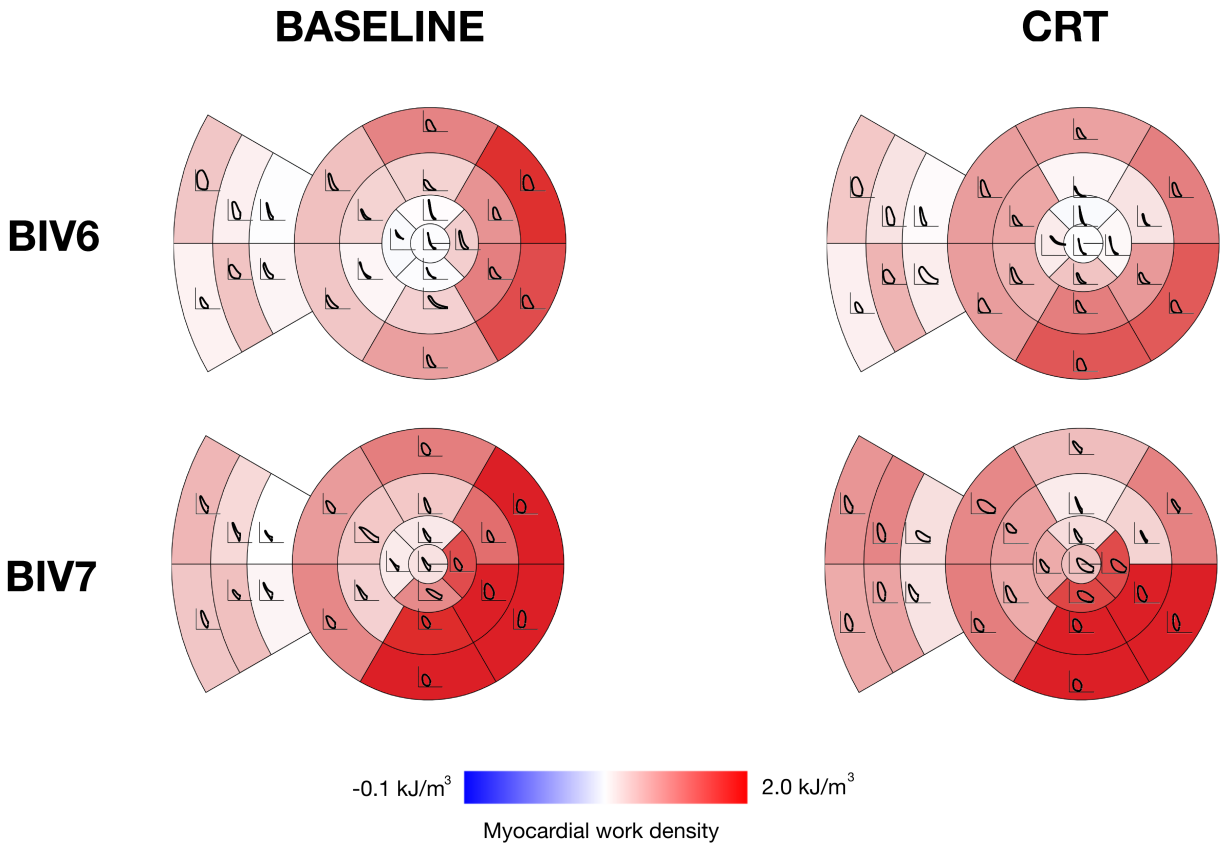

Figure 6.5: Myocardial work distributions during LBBB and CRT. Myocardial work density was computed from the predicted stress/strain loops during LBBB and CRT for the best responder (BiV6) (left) and worst non-responder (BiV7) (right). The LV is shown in a bulls-eye plot style with are overlaid on to its corresponding region. The color of the area within the loop quantifies the magnitude of work averaged over each section of the bulls-eye plot. Stress strain loops are overlaid onto their corresponding ventricular regions and are color coded by the total magnitude of work through the cardiac cycle.

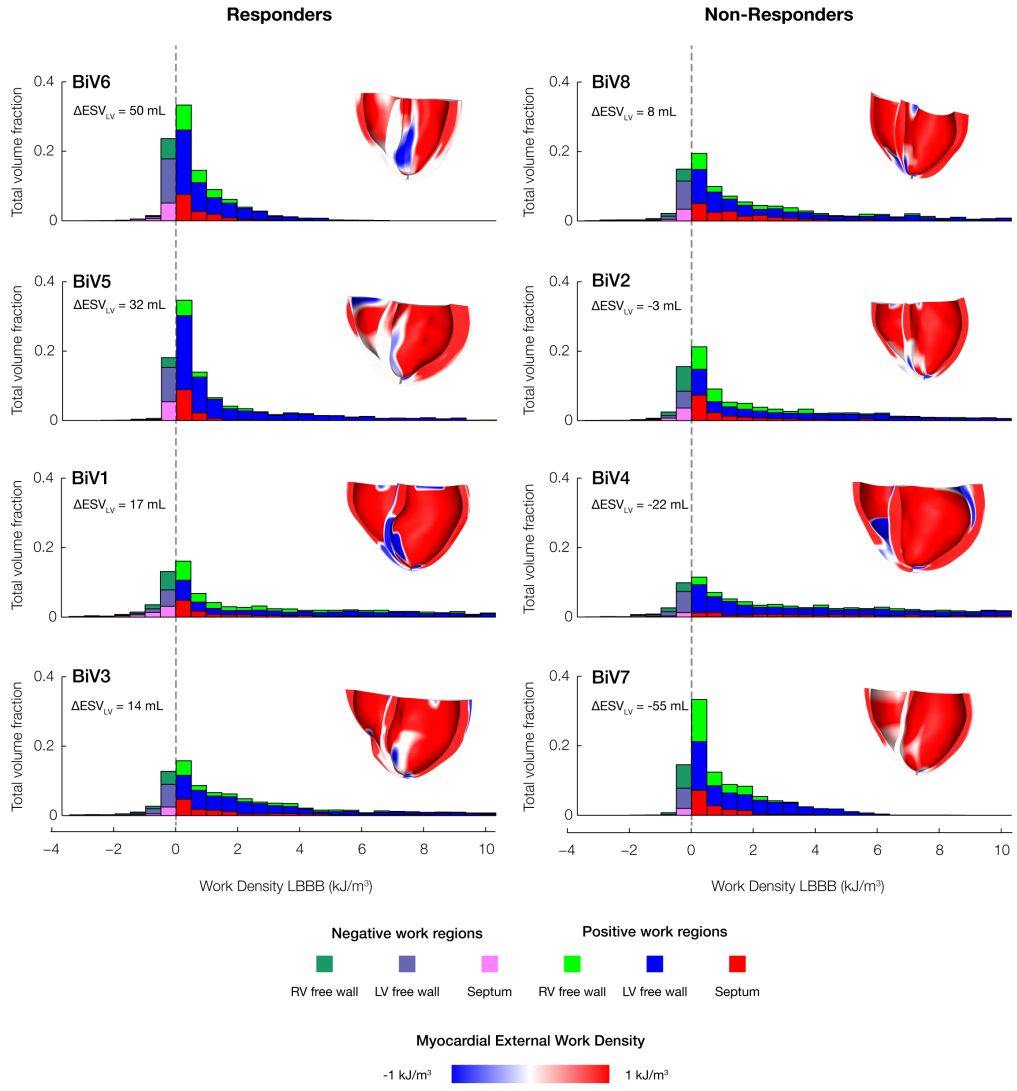

Figure 6.6: Regional volume fractions of work in the ventricles. Parts of the LV and septum perform negative work in LBBB and CRT. The regional volume fraction frequency of the predicted values of the myocardial work density (at Gauss-Legendre quadrature) points were enumerated as fractions of regional volumes partitioned into septum, LV free wall, and RV free wall regions. The fraction of negative work values (left of the solid line at zero) is associated with the degree of measured CRT response (ΔESV_{LV}). Patients are ordered column-wise according to degree of measured improvement (BiV6 was the strongest responder, and BiV7 was the weakest responder). The frequency of the predicted values of the myocardial work density (computed at the Gauss/Legendre integration points) were enumerated as fractions of regional volumes partitioned into septum, LV free wall, and RV free wall regions. The fraction of negative work values (left of the solid line at zero) is associated with the degree of measured CRT response (ΔESV_{LV}). Patients are ordered column-wise according to degree of measured improvement (BiV6 was the strongest responder, and BiV7 was the weakest responder).

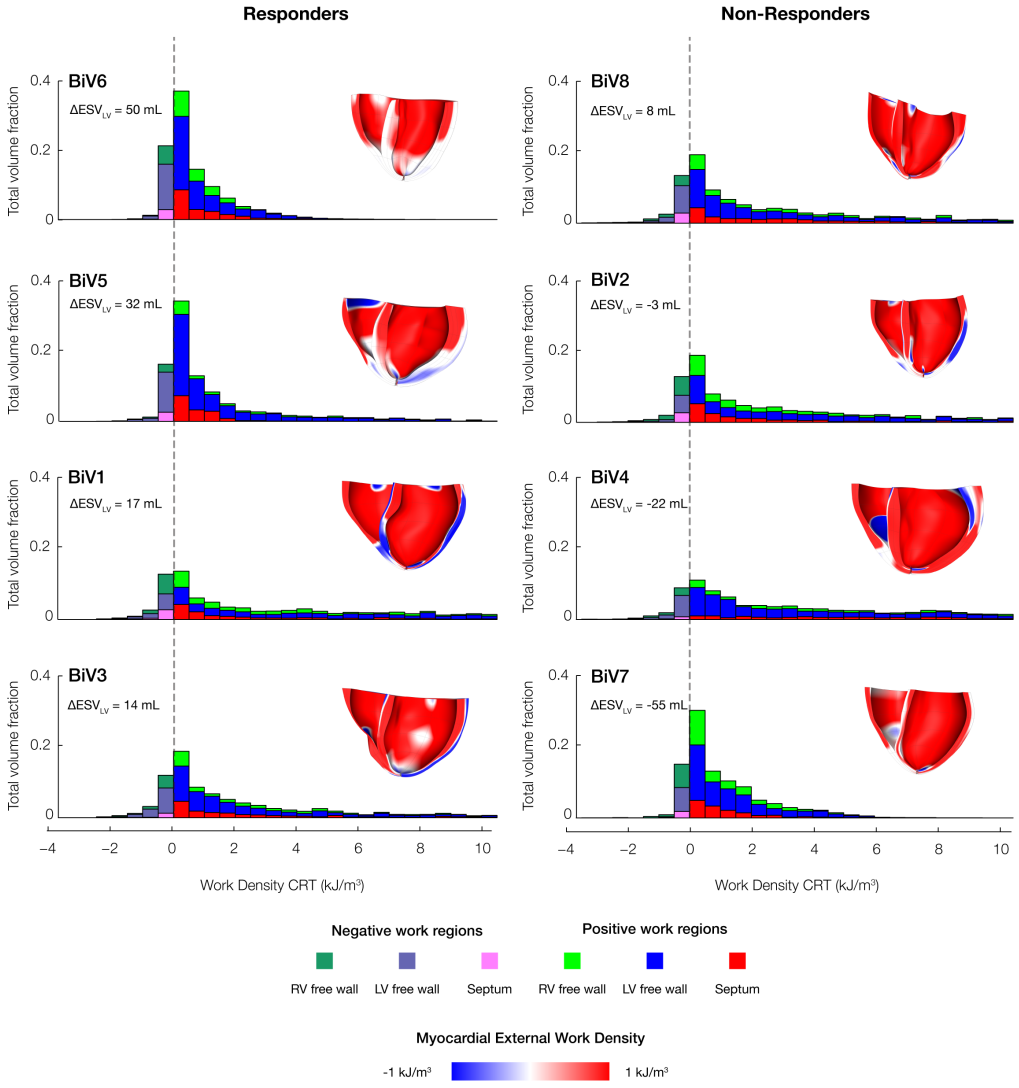

Figure 6.6: Regional volume fractions of work in the ventricles (continued).

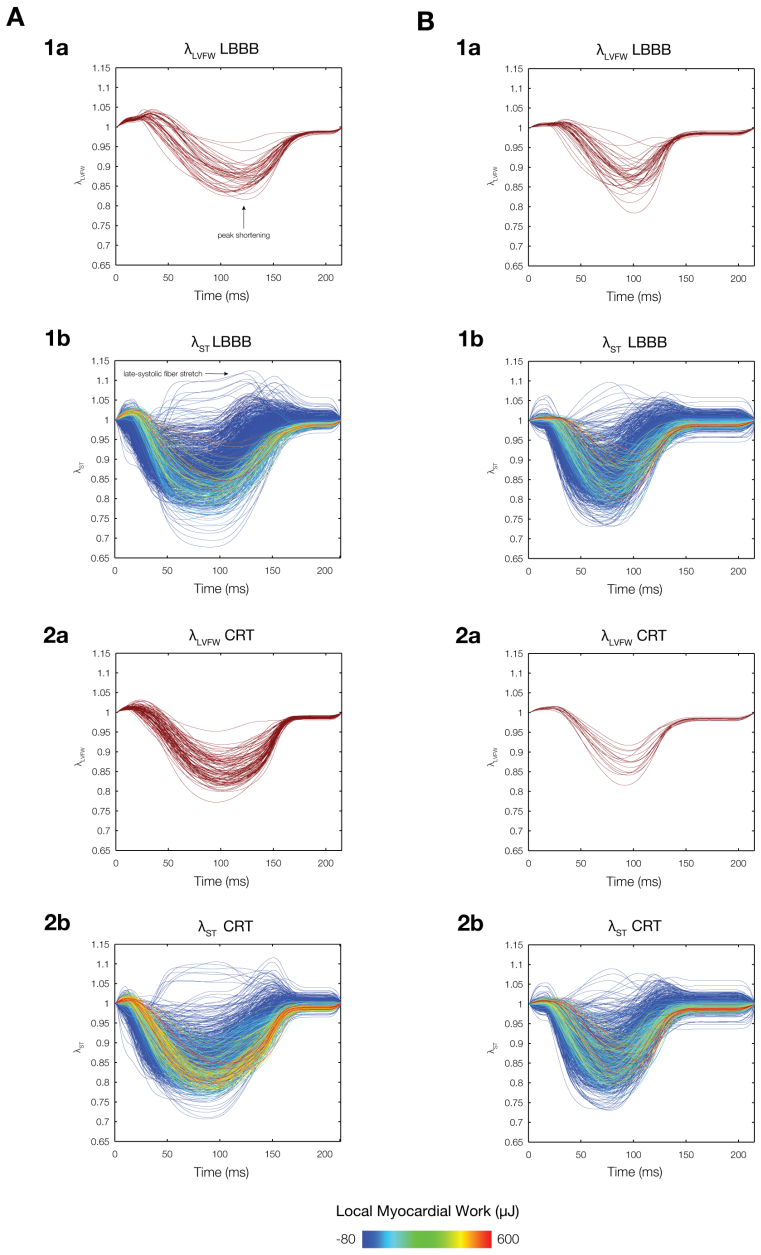

Figure 6.7: Late-systolic fiber stretch in the septum. Late stretch occurs in the septum following peak shortening in the LV free wall. The time-course of fiber stretch λ during a steady-state beat for a representative (A) responder (BiV6) and (B) non-responder (BiV7) are shown during (1) LBBB and (2) CRT for (a) regions of high (>98%ile) work in the LV free wall (LVFW) and (b) all work regions of the septum (ST). Traces are colored by the total local myocardial work over a single beat. In LBBB, peak systolic shortening in regions of high work in the LVFW (A-1a, B-1a) is followed by prominent late-systolic fiber stretch (ST λ_{late}>1) in the septum (A-1b, B-1b). During CRT, time to peak shortening is hastened (A-2a, B-2a), and the amount of septal myocardium with late fiber stretch is apparently reduced in a responder (A-2b) compared to a non-responder (B-2b).

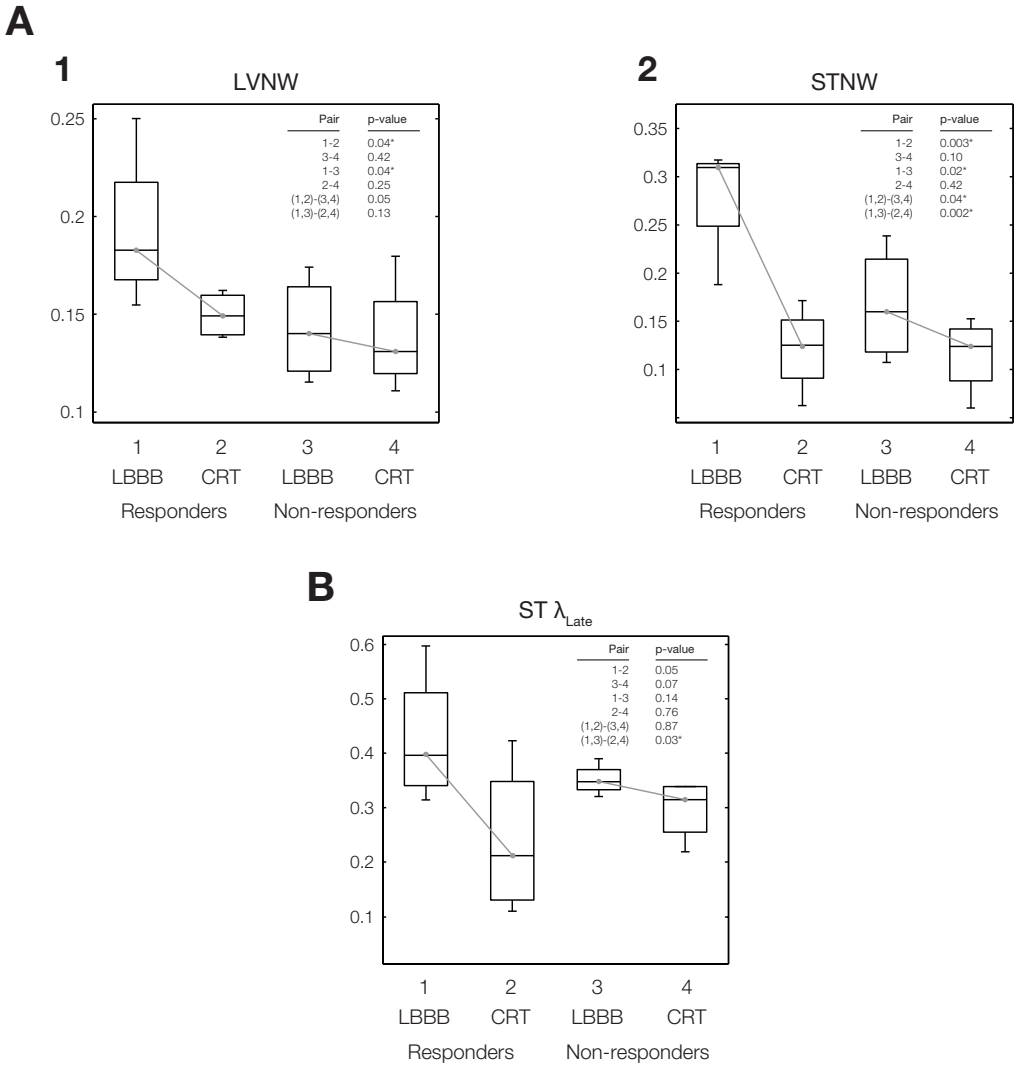

Figure 6.8: Differences in regional work metrics between responders and non-responders. Regional fractions of myocardium with negative work and late-systolic stretch differ between responders and non-responders during LBBB and CRT. Box plots of computed distributions of work (LVNW, STNW) and kinematic metrics (ST λ_{late}) show significant ($p<0.05$) differences between responders and non-responders during LBBB and CRT. The volume fractions of LV with negative work (LVNW) (A1) and septum with negative work (STNW) (A2) are significantly different among responders during LBBB compared with CRT (Pair 1-2) and during LBBB between responders and non-responders (Pair 1-3). STNW is also significantly different for all patients during LBBB and CRT (Pair (1,2)-(3,4) and Pair (1,3)-(2,4)). The volume fraction of septum with late systolic stretch (ST λ_{late}) (B) is significantly different among all patients during LBBB compared with CRT.

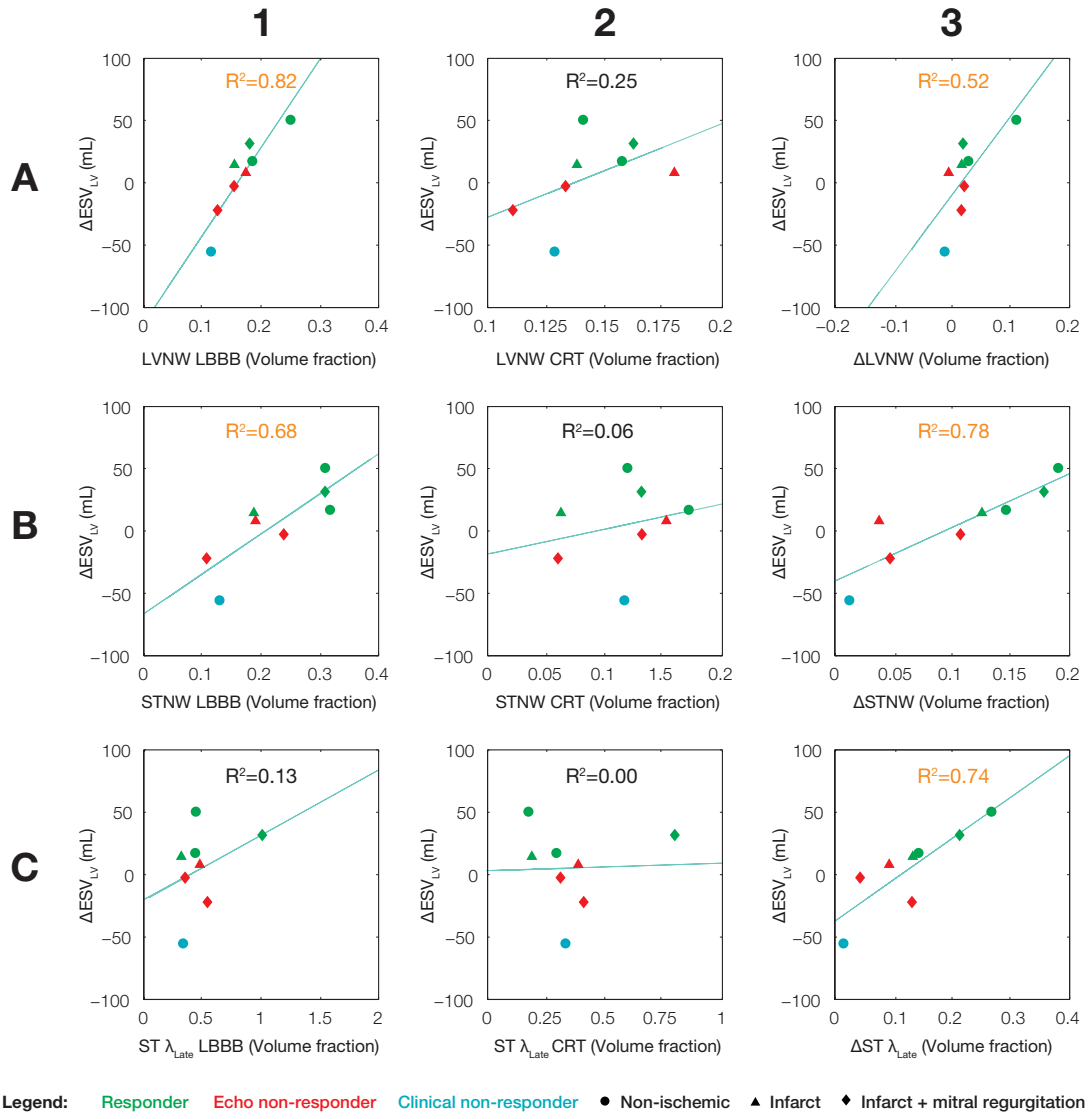

Figure 6.9: Reduction of regions of negative work correlates with CRT outcomes. Reduction of negative work in the LV and septum correlates with the degree of LV reverse remodeling. Correlations between LV reverse remodeling (ΔESV_{LV}) and volume fractions of the (A) LV with negative work (LVNW), (B) septum with negative work (STNW), and (C) septum with late-systolic stretch (ST λ_{late}) are shown for simulated values at (1) baseline LBBB, (2) CRT, and (3) the change (defined as LBBB value - CRT value; reduction is positive). Marker colors denotes patient responders (green), echo non-responders (ΔESV_{LV} <10%) (red), and clinical non-responders (pink); shapes denote non-ischemic (circle), ischemic (triangle), and ischemic with mitral regurgitation (diamond). At baseline, larger fractions of LVNW (A1) and STNW (B1) are associated with greater ΔESV_{LV} outcomes. Volume fractions during acute CRT (A2, B2, C2) do not relate to outcomes. However, the magnitudes of ΔLVNW (A3), ΔSTNW (B3), and ΔST λ_{late} (C3) relate to the magnitude of ΔESV_{LV}, implicating improved septal mechano-energetic function as an important feature leading to reverse remodeling.

Bibliography

1. Aguado-Sierra, J., Krishnamurthy, A., Villongco, C., Chuang, J., Howard, E., Gonzales, M., Omens, J., Krummen, D., Narayan, S., Kerckhoffs, R., 2011. Patient-specific modeling of dyssynchronous heart failure: A case study. Progress in Biophysics and Molecular Biology.

2. Aiba, T., Hesketh, G. G., Barth, A. S., Liu, T., Daya, S., Chakir, K., Dimaano, V. L., Abraham, T. P., O'Rourke, B., Akar, F. G., 2009. Electrophysiological consequences of dyssynchronous heart failure and its restoration by resynchronization therapy. Circulation 119 (9), 1220–1230.

3. Arts, T., Delhaas, T., Bovendeerd, P., Verbeek, X., Prinzen, F. W., 2005. Adaptation to mechanical load determines shape and properties of heart and circulation: the circadapt model. American Journal of Physiology-Heart and Circulatory Physiology 288 (4), H1943–H1954.

4. Badke, F. R., Boinay, P., Covell, J. W., 1980. Effects of ventricular pacing on regional left ventricular performance in the dog. American Journal of Physiology-Heart and Circulatory Physiology 238 (6), H858–H867.

5. Barth, A. S., Aiba, T., Halperin, V., DiSilvestre, D., Chakir, K., Colantuoni, C., Tunin, R. S., Dimaano, V. L., Yu, W., Abraham, T. P., 2009. Cardiac resynchronization therapy corrects dyssynchrony-induced regional gene expression changes on a genomic level. Circulation: Cardiovascular Genetics 2 (4), 371–378.

6. Birnie, D., De Kemp, R. A., Tang, A. S., Ruddy, T. D., Gollob, M. H., Guo, A., Williams, K., Thomson, K., DaSilva, J. N., Beanlands, R. S., 2012. Reduced septal glucose metabolism predicts response to cardiac resynchronization therapy. Journal of Nuclear Cardiology 19 (1), 73–83.

7. Bogaard, M. D., Houthuizen, P., Bracke, F. A., Doevendans, P. A., Prinzen, F. W., Meine, M., Gelder, B. M., 2011. Baseline left ventricular dp/dtmax rather than the acute improvement in dp/dtmax predicts clinical outcome in patients with cardiac resynchronization therapy. European journal of heart failure 13 (10), 1126–1132.

8. Bogaard, M. D., Meine, M., Tuinenburg, A. E., Maskara, B., Loh, P., Doevendans, P. A., 2012. Cardiac resynchronization therapy beyond nominal settings: who needs individual programming of the atrioventricular and interventricular delay? Europace, eus170.

9. Butter, C., Auricchio, A., Stellbrink, C., Fleck, E., Ding, J., Yu, Y., Huvelle, E., Spinelli, J., 2001. Effect of resynchronization therapy stimulation site on the systolic function of heart failure patients. Circulation 104 (25), 3026–3029.

10. Chakir, K., Daya, S. K., Tunin, R. S., Helm, R. H., Byrne, M. J., Dimaano, V. L., Lardo, A. C., Abraham, T. P., Tomaselli, G. F., Kass, D. A., 2008. Reversal of global apoptosis and regional stress kinase activation by cardiac resynchronization. Circulation 117 (11), 1369–1377.

11. Cho, H., Barth, A. S., Tomaselli, G. F., 2012. Basic science of cardiac resynchronization therapy molecular and electrophysiological mechanisms. Circulation: Arrhythmia and Electrophysiology 5 (3), 594–603.

12. Chung, E. S., Leon, A. R., Tavazzi, L., Sun, J.-P., Nihoyannopoulos, P., Merlino, J., Abraham, W. T., Ghio, S., Leclercq, C., Bax, J. J., 2008. Results of the predictors of response to crt (prospect) trial. Circulation 117 (20), 2608–2616.

13. Cleland, J. G., Abraham, W. T., Linde, C., Gold, M. R., Young, J. B., Daubert, J. C., Sherfesee, L., Wells, G. A., Tang, A. S., 2013. An individual patient meta-analysis of five randomized trials assessing the effects of cardiac resynchronization therapy on morbidity and mortality in patients with symptomatic heart failure. European heart journal 34 (46), 3547–3556.

14. Daubert, J.-C., Saxon, L., Adamson, P. B., Auricchio, A., Berger, R. D., Beshai, J. F., Breithard, O., Brignole, M., Cleland, J., DeLurgio, D. B., 2012. 2012 ehra/hrs expert consensus statement on cardiac resynchronization therapy in heart failure: implant and follow-up recommendations and management a registered branch of the european society of cardiology (esc), and the heart rhythm society; and in collaboration with the heart failure society of america (hfsa), the american society of echocardiography (ase), the american heart association (aha), the european association of echocardiography (eae) of the esc and the heart failure association of the esc (hfa). endorsed by the governing bodies of aha, ase, eae, hfsa, hfa, ehra, and hrs. Europace 14 (9), 1236–1286.

15. De Boeck, B. W., Meine, M., Leenders, G. E., Teske, A. J., Wessel, H., Kirkels, J. H., Prinzen, F. W., Doevendans, P. A., Cramer, M. J., 2008. Practical and conceptual limitations of tissue doppler imaging to predict reverse remodelling in cardiac resynchronisation therapy. European journal of heart failure 10 (3), 281–290.

16. De Boeck, B. W., Teske, A. J., Meine, M., Leenders, G. E., Cramer, M. J., Prinzen, F. W., Doevendans, P. A., 2009. Septal rebound stretch reflects the functional substrate to cardiac resynchronization therapy and predicts volumetric and neurohormonal response. European journal of heart failure 11 (9), 863–871.

17. Delhaas, T., Arts, T., Prinzen, F. W., Reneman, R. S., 1994. Regional fibre stress-fibre strain area as an estimate of regional blood flow and oxygen demand in the canine heart. The Journal of Physiology 477 (3), 481–496.

18. Duncan, A., O'Sullivan, C., Carr-White, G., Gibson, D., Henein, M., 2001. Long axis electromechanics during dobutamine stress in patients with coronary artery disease and left ventricular dysfunction. Heart 86 (4), 397–404.

19. Gold, M. R., Birgersdotter-Green, U., Singh, J. P., Ellenbogen, K. A., Yu, Y., Meyer, T. E., Seth, M., Tchou, P. J., 2011. The relationship between ventricular electrical delay and left ventricular remodelling with cardiac resynchronization therapy. European heart journal 32 (20), 2516–2524.

20. Gonzales, M. J., Sturgeon, G., Krishnamurthy, A., Hake, J., Jonas, R., Stark, P., Rappel, W.-J., Narayan, S. M., Zhang, Y., Segars, W. P., 2013. A three-dimensional finite element model of human atrial anatomy: new methods for cubic hermite meshes with extraordinary vertices. Medical image analysis 17 (5), 525–537.

21. Holzapfel, G. A., Ogden, R. W., 2009. Constitutive modelling of passive myocardium: a structurally based framework for material characterization. Philosophical Transactions of the Royal Society of London A: Mathematical, Physical and Engineering Sciences 367 (1902), 3445–3475.

22. Kass, D. A., 2009. Pathobiology of cardiac dyssynchrony and resynchronization. Heart Rhythm 6 (11), 1660–1665.

23. Kerckhoffs, R. C., Omens, J. H., McCulloch, A. D., Mulligan, L. J., 2010. Ventricular dilation and electrical dyssynchrony synergistically increase regional mechanical nonuniformity but not mechanical dyssynchrony a computational model. Circulation: Heart Failure 3 (4), 528–536.

24. Kirk, J. A., Holewinski, R. J., Kooij, V., Agnetti, G., Tunin, R. S., Witayavanitkul, N., de Tombe, P. P., Gao, W. D., Van Eyk, J., Kass, D. A., 2014. Cardiac resynchronization sensitizes the sarcomere to calcium by reactivating gsk-3β. The Journal of clinical investigation 124 (1), 129.

25. Klotz, S., Hay, I., Dickstein, M. L., Yi, G.-H., Wang, J., Maurer, M. S., Kass, D. A., Burkhoff, D., 2006. Single-beat estimation of end-diastolic pressure-volume relationship: a novel method with potential for noninvasive application. American Journal of Physiology-Heart and Circulatory Physiology 291 (1), H403–H412.

26. Kors, J., Van Herpen, G., Sittig, A., Van Bemmel, J., 1990. Reconstruction of the frank vectorcardiogram from standard electrocardiographic leads: diagnostic comparison of different methods. European heart journal 11 (12), 1083–1092.

27. Krishnamurthy, A., Villongco, C. T., Chuang, J., Frank, L. R., Nigam, V., Belezzuoli, E., Stark, P., Krummen, D. E., Narayan, S., Omens, J. H., 2013. Patient-specific models of cardiac biomechanics. Journal of computational physics 244, 4–21.

28. Leenders, G. E., De Boeck, B. W., Teske, A. J., Meine, M., Bogaard, M. D., Prinzen, F. W., Doevendans, P. A., Cramer, M. J., 2012. Septal rebound stretch is a strong predictor of outcome after cardiac resynchronization therapy. Journal of cardiac failure 18 (5), 404–412.

29. Lumens, J., Delhaas, T., Kirn, B., Arts, T., 2009. Three-wall segment (triseg) model describing mechanics and hemodynamics of ventricular interaction. Annals of biomedical engineering 37 (11), 2234–2255.

30. Lumens, J., Leenders, G. E., Cramer, M. J., De Boeck, B. W., Doevendans, P. A., Prinzen, F. W., Delhaas, T., 2012. Mechanistic evaluation of echocardiographic dyssynchrony indices patient data combined with multiscale computer simulations. Circulation: Cardiovascular Imaging 5 (4), 491–499.

31. Masci, P. G., Marinelli, M., Piacenti, M., Lorenzoni, V., Positano, V., Lombardi, M., L'Abbate, A., Neglia, D., 2010. Myocardial structural, perfusion, and metabolic correlates of left bundle branch block mechanical derangement in patients with dilated cardiomyopathy a tagged cardiac magnetic resonance and positron emission tomography study. Circulation: Cardiovascular Imaging 3 (4), 482–490.

32. Nelson, G. S., Berger, R. D., Fetics, B. J., Talbot, M., Spinelli, J. C., Hare, J. M., Kass, D. A., 2000. Left ventricular or biventricular pacing improves cardiac function at diminished energy cost in patients with dilated cardiomyopathy and left bundle-branch block. Circulation 102 (25), 3053–3059.

33. Nielsen, P., Le Grice, I., Smaill, B., Hunter, P., 1991. Mathematical model of geometry and fibrous structure of the heart. Am. J. Physiol 260 (29), H1365–H1378.

34. Nishimura, R. A., Hayes, D. L., Holmes, D. R., Tajik, J., 1995. Mechanism of hemodynamic improvement by dual-chamber pacing for severe left ventricular dysfunction: an acute doppler and catheterization hemodynamic study. Journal of the American College of Cardiology 25 (2), 281–288.

35. Nowak, B., Stellbrink, C., Sinha, A. M., Kaiser, H.-J., Reinartz, P., Koos, R., Markus, K., Hanrath, P., Buell, U., Schaefer, W. M., 2004. Effects of cardiac resynchronization therapy on myocardial blood flow measured by oxygen-15 water positron emission tomography in idiopathic-dilated cardiomyopathy and left bundle branch block. The American journal of cardiology 93 (4), 496–499.

36. Ogano, M., Iwasaki, Y.-k., Tanabe, J., Takagi, H., Umemoto, T., Hayashi, M., Miyauchi, Y., Shimizu, W., 2014. Cardiac resynchronization therapy restored ventricular septal myocardial perfusion and enhanced ventricular remodeling in patients with nonischemic cardiomyopathy presenting with left bundle branch block. Heart Rhythm 11 (5), 836–841.

37. Patel, M. R., White, R. D., Abbara, S., Bluemke, D. A., Herfkens, R. J., Picard, M., Shaw, L. J., Silver, M., Stillman, A. E., Udelson, J., 2013. 2013 accf/acr/ase/asnc/scct/scmr appropriate utilization of cardiovascular imaging in heart failure: a joint report of the american college of radiology appropriateness criteria committee and the american college of cardiology foundation appropriate use criteria task force. Journal of the American College of Cardiology 61 (21), 2207–2231.

38. Prinzen, F. W., Augustijn, C. H., Arts, T., Allessie, M. A., Reneman, R. S., 1990. Redistribution of myocardial fiber strain and blood flow by asynchronous activation. American Journal of Physiology-Heart and Circulatory Physiology 259 (2), H300–H308.

39. Prinzen, F. W., Hunter, W. C., Wyman, B. T., McVeigh, E. R., 1999. Mapping of regional myocardial strain and work during ventricular pacing: experimental study using magnetic resonance imaging tagging. Journal of the American College of Cardiology 33 (6), 1735–1742.

40. Shah, A. M., Mann, D. L., 2011. In search of new therapeutic targets and strategies for heart failure: recent advances in basic science. The Lancet 378 (9792), 704–712.

41. Sogaard, P., Egeblad, H., Pedersen, A. K., Kim, W. Y., Kristensen, B. Ø., Hansen, P. S., Mortensen, P. T., 2002. Sequential versus simultaneous biventricular resynchronization for severe heart failure evaluation by tissue doppler imaging. Circulation 106 (16), 2078–2084.

42. ten Tusscher, K. H., Panfilov, A. V., 2006. Alternans and spiral breakup in a human ventricular tissue model. American Journal of Physiology-Heart and Circulatory Physiology 291 (3), H1088–H1100.

43. Valzania, C., Gadler, F., Winter, R., Braunschweig, F., Brodin, L.-Å., Gudmundsson, P., Boriani, G., Eriksson, M. J., 2008. Effects of cardiac resynchronization therapy on coronary blood flow: Evaluation by transthoracic doppler echocardiographyâŸĘ. European journal of heart failure 10 (5), 514–520.

44. van Everdingen, W. M., Paiman, M.-L., van Deursen, C. J., Cramer, M. J., Vernooy, K., Delhaas, T., Prinzen, F. W., 2014. Comparison of septal strain patterns in dyssynchronous heart failure between speckle tracking echocardiography vendor systems. Journal of Electrocardiology.

45. Vernooy, K., Verbeek, X. A., Peschar, M., Crijns, H. J., Arts, T., Cornelussen, R. N., Prinzen, F. W., 2005. Left bundle branch block induces ventricular remodelling and functional septal hypoperfusion. European Heart Journal 26 (1), 91–98.

46. Villongco, C. T., Krummen, D. E., Stark, P., Omens, J. H., McCulloch, A. D., 2014. Patient-specific modeling of ventricular activation pattern using surface ecg-derived

vectorcardiogram in bundle branch block. Progress in biophysics and molecular biology 115 (2), 305–313.

47. Wyman, B. T., Hunter, W. C., Prinzen, F. W., McVeigh, E. R., 1999. Mapping propagation of mechanical activation in the paced heart with mri tagging. American Journal of Physiology-Heart and Circulatory Physiology 276 (3), H881–H891.

48. Yancy, C. W., Jessup, M., Bozkurt, B., Butler, J., Casey, D. E., Drazner, M. H., Fonarow, G. C., Geraci, S. A., Horwich, T., Januzzi, J. L., 2013. 2013 accf/aha guideline for the management of heart failure: a report of the american college of cardiology foundation/american heart association task force on practice guidelines. Journal of the American College of Cardiology 62 (16), e147–e239.

Chapter 7

Dyssynchrony Biomarkers Predict and Optimize Long-term Outcomes of Cardiac Resynchronization Therapy

Abstract

The 12-lead body-surface electrocardiogram (ECG) is an important clinical data set for making routine, non-invasive assessments of electrical abnormalities, particularly in dyssynchronous heart failure (DHF) introduced by left bundle branch block (LBBB). Current clinical guidelines evaluate patient candidacy for cardiac resynchronization therapy (CRT) based primarily on the severity of electrical activation delay measured by QRS duration >150 ms. However, since the recorded QRS complex on the ECG is the result of complex interactions between ventricular electrophysiology, geometry, and orientation within the patient's chest, the baseline QRS width criteria is only 50% successful at predicting long-term, objective positive outcomes for CRT candidates.

Patient-specific computational models are to able deterministically simulate bundle branch block and compute the resulting ECG, providing a quantitative framework for making more precise estimates of electrical activation delays using the measured ECGs. We have found that a model-derived biomarker of total LV activation time at

baseline is a strong predictor ($R^2 = 0.95$) of long-term CRT outcomes. A biomarker of LV activation delay between the septum and LV lateral wall is also a strong predictor ($R^2 = 0.86$) of the degree of electrical resynchrony achieved by CRT. Extending this result further, we tested the ability of a kernel-based regularization learning algorithm to estimate the biomarkers from simulated ECG signals during CRT. By training with 33 CRT simulations in two patients each, we achieved good agreement (10% mean RMS error) between model-derived and estimated biomarkers in six other patients.

7.1 Introduction

The 12-lead body-surface electrocardiogram (ECG) is the standard clinical measurement for assessing cardiac electrical activity. The relative and absolute timing and magnitude of body surface potentials capture the various phases of electrical events (e.g. P, Q, R, S, T, U waves) in the heart. The QRS complex captures ventricular depolarization. Normal ventricular depolarization produces QRS complexes of approximately 90 ms in duration. In the case of dyssynchronous heart failure (DHF) introduced by left bundle branch block (LBBB), depolarization follows a characteristic, delayed pattern across the ventricle which exhibits a particular morphology in the ECG: the QRS complex is widened >120 ms, QS or rS complexes appear in lead V1, and mono-phasic R wave with absent Q waves appear in leads V6 and I [5]. Cardiac resynchronization therapy (CRT) has been shown by large randomized studies to improve survival for patients with mild and advanced DHF by improving synchrony of electrical activation [4, 1]. Subgroup analyses have frequently identified baseline QRS duration and morphology as independent predictors of CRT outcomes: patients with LBBB and prolonged QRS duration (>150 ms) exhibit better long-term outcomes, particularly LV reverse remodeling [3]. This reinforces the concept that LV electrical delay is an important factor for predicting benefit from CRT [16] and remains an essential clinical guideline for recommending patients for CRT.

The QRS duration is a coarse, global metric for electrical activation delay in patients with LBBB. In reality, the recorded ECG is the result of complex interactions between the intrinsic electrophysiological properties of the ventricular myocardium and

its geometry and orientation relative to the body-surface electrodes. Patient-specific computational models have the ability to deterministically simulate integrative processes and provide more detailed estimates of patient-specific electrophysiology. The estimated three-dimensional activation patterns predicted by the electrophysiology models (see Chapter 5) allow the derivation of biomarkers of electrical dyssynchrony, particularly in the LV, at baseline and during CRT. These markers can potentially provide better estimates of likely CRT responders before device implantation and guide optimal CRT settings for maximal long-term benefit. Moreover, since models of electrophysiology deterministically capture the complex relation between the observed ECG signal and model-derived biomarkers, we hypothesize that the biomarkers can be estimated using a kernel-based regularization algorithm trained with simulations from a subset of patients.

7.2 Methods

7.2.1 Clinical data

The clinical data used for this study has been described extensively in Chapter 6. In summary, 8 patients with dilated cardiomyopathy, left bundle branch block (LBBB), NYHA class III heart failure, and LVEF < 35% were enrolled from the Veteran's Administration San Diego Healthcare System (San Diego, CA) after obtaining informed, written consent to participate in an Institutional Review Board (IRB)-approved protocol. End-diastolic cardiac anatomy was obtained from CT and MR images. Standard 12-lead body-surface electrocardiograms were recorded (Bard Pro, Bard Electrophysiology, Lowell, MA) at 1 kHz sampling rate. Details of measured patient properties at baseline are described in the Methods section of Chapter 6.

Measurements of LV end-systolic volume were obtained for each patient after 6 months of pacing during an echocardiography study. CRT responders were identified by a reduction LV end-systolic volume $\Delta ESV_{LV} > 10\%$. Responders were BiV6 (+50 mL; +59%), BiV3 (+14 mL; +16%), BiV5 (+32 mL; +15%), and BiV1 (+17 mL; +12%). Non-responders with a sub-threshold reduction or increased ΔESV_{LV} included BiV8 (+8 mL; +7%), BiV2 (-3 mL; -2%), BiV4 (-22 mL; -12%), and BiV7 (-55 mL; -36%).

7.2.2 Patient-specific electrophysiology model and simulations

Patient-specific biventricular models of end-diastolic geometry and fiber architecture were constructed from the clinical images of each of the 8 patients. The details of geometric and fiber architecture models are given in the Methods sections of Chapters 2 and 3, respectively. The human ventricular electrophysiology model included a realistic description of ionic currents and monodomain reaction-diffusion. Transversely isotropic electrical conductivity was defined in a 7:1 (fiber:transverse) ratio according to the fiber architecture of the anatomical model. Details of the electrophysiology model are presented in the Methods section of Chapter 4.

Simulations of ventricular depolarization during LBBB were performed as described in the Methods section of Chapter 5 [21]. In summary, patient-specific activation patterns were estimated by optimizing stimulus and regional conductivity parameters to minimize the difference between simulated and measured vectorcardiograms (VCGs) derived from 12-lead body-surface ECG; a total of 608 parameter combinations were tested for each patient. The optimal parameter set minimized VCG angular deviations and matched the measured total activation time (QRS width) within 10 ms. The LBBB depolarization times at the mesh nodes were obtained from the resulting models.

Patient-specific activation patterns during CRT were simulated by applying ectopic stimuli at the ventricular lead positions and V-V delays of the pacing protocol prescribed at time of device implant; details of the pacing protocol can be found in the Methods section of Chapter 6. To explore the possibility for more optimal CRT pacing settings than that prescribed at time of implant, 33 depolarization simulations were performed for V-V delays in the range of -80 ms to 80 ms in 5 ms steps for each patient; V-V delay is defined as $t_{VLV} - t_{VRV}$. CRT depolarization times at the mesh nodes were obtained from the resulting models.

7.2.3 Derivation of electrical dyssynchrony biomarkers

Biomarkers of electrical dyssynchrony or delay between RV, septum, and LV regions were computed from the activation times solved at the mesh nodes (8448 in total) of the LBBB and CRT models. See Figure (7.1) for the definition of ventricular regions.

Regional dyssynchrony metrics are of several generic types: 1) durations or delays computed from the earliest and latest activation times within a region or between regions, 2) durations or delays computed from the mean activation time between regions, 3) regional volume fraction of myocardium with periods of simultaneous activation (overlap) with other regions, and 4) activation dyssynchrony defined as the mean difference in activated volume fraction between regions. All quantities are expressed as fractions of total regional dyssynchrony. See Table (7.1) for a description and associated equations of selected biomarkers.

7.2.4 Kernel-based regularization learning algorithm

We applied a kernel-based, regularized machine learning algorithm with demonstrated success for blood glucose monitoring [15] to estimate model-derived dyssynchrony biomarkers from simulated VCG signals. We develop the mathematical framework in this section.

Mathematical problem formulation

Without loss of generality, we can reformulate the problem of the dyssynchrony biomarker prediction from simulated VCG signals as the problem of the reconstruction of a real-valued function $f : X \to \mathbb{R}, X \subset \mathbb{R}^d$ from a given data set $\mathbf{z} = \{(x_i, y_i)\}_{i=1}^n \subset X \times \mathbb{R}$. In particular, a training set $\mathbf{z} = \{(x_i, y_i)\}_{i=1}^n$ consists of a simulated VCG signal $x_i \in \mathbb{R}^{200\times 3}$ for the given delay and the corresponding dyssynchrony biomarker $y_i \in \mathbb{R}$.

Our goal is to find a function f such that it minimizes the given data error, for example,

$$f := \underset{g\in\mathscr{H}}{\operatorname{argmin}} \sum_{i=1}^{n} (y_i - g(x_i))^2, \tag{7.1}$$

where $\mathscr{H}$ is some class of functions. In practice we usually do not know the class $\mathscr{H}$ and also we assume that given metric values y_i are not exact.

The choice of $\mathscr{H}$ could be a challenging task since if we choose $\mathscr{H}$ to be too large then the function f in (7.1) will interpolate the given noisy data, and we end up in over-fitting. However, our primary goal here is to predict biomarkers from VCG signals rather than describe the data at hand. On the other hand, if $\mathscr{H}$ is chosen to be too simple,

e.g. the space of linear polynomials, our function f may not even describe the training data adequately, and will provide similarly bad performance. Therefore, one has to trade off between the data fitting and the complexity of a data fitter.

Regularization provides us with one way to strike the appropriate balance in creating our model or, equivalently, choosing an appropriate $\mathscr{H}$ [8]. One way to do this is to introduce a penalization term in our minimization procedure as follows:

$$\underbrace{\mathrm{ERR}(f)}_{\text{empirical error}} + \lambda \underbrace{\mathrm{pen}(f)}_{\text{penalization term}},$$

where the regularization parameter λ governs a compromise between the attempt to fit the given data and the desire to reduce the complexity of a data fitter. This will cause the minimization to seek out simpler functions and incur less of a penalty.

One of the most efficient and well-known regularization methods is Tikhonov regularization that can be written as:

$$\frac{1}{|\mathbf{z}|}\sum_{i=1}^{n}(y_i - f(x_i))^2 + \lambda ||f||^2_{\mathscr{H}}, \tag{7.2}$$

where λ is a regularization parameter and $\|\cdot\|_{\mathscr{H}}$ is the norm in the function space $\mathscr{H}$. It is clear from this formulation that the penalization should force a choice of f which is as smooth as possible while still fitting the data. The norm of $\mathscr{H}$ will allow us to encode this criterion, but in order to do that we need to choose a rather general and powerful family of hypothesis spaces $\mathscr{H}$. In the sequel we assume that $\mathscr{H}$ belongs to a family of reproducing kernel Hilbert spaces (RKHS).

Reproducing kernel Hilbert spaces

A reproducing kernel Hilbert space $\mathscr{H}$ is a space of real-valued functions f defined on $X \subset \mathbb{R}^d$ such that for every $x \in X$ the point-wise evaluation functional $L_x(f) := f(x)$ is continuous in the topology induced by the inner product $\langle \cdot, \cdot \rangle$, which generates the norm of $\mathscr{H}$. By the Riesz representation theorem, to every RKHS $\mathscr{H}$ there corresponds a unique symmetric positive definite function $K : X \times X \to \mathbb{R}$, called a reproducing kernel of $\mathscr{H} = \mathscr{H}_K$, that has the following reproducing property: $f(x) = \langle f(\cdot), K(\cdot, x) \rangle$ for every $x \in X$ and $f \in \mathscr{H}_K$.

Having this general notion of a reproducing kernel is important because it allows us to define a RKHS in terms of its reproducing kernel, rather than attempting to derive the kernel from the definition of the function space directly. The following theorem formally establishes the relationship between the RKHS and a reproducing kernel.

Theorem 1. *A RKHS defines a corresponding reproducing kernel. Conversely, a reproducing kernel defines a unique RKHS.*

Examples of reproducing kernels

- Linear kernel
$$K(x,t) = x \cdot t$$
- Gaussian kernel
$$K(x,t) = \exp(-\frac{\|x-t\|^2}{\sigma^2}), \quad \sigma > 0$$
- Polynomial kernel
$$K(x,t) = (x \cdot t + 1)^d, \quad d \in \mathbb{N}$$

The concept of RKHS is widely used in learning, approximation, and regularization theory, as well as computer vision. In general, it is quite difficult to find useful function spaces that are not RKHS.

To summarize, if a space of functions can be represented as an RKHS, it has useful properties (namely the inner product and the ability for each function to be evaluated at each point) that allow us to use it to solve reconstruction and learning problems. A comprehensive theory of reproducing kernel Hilbert spaces can be found in [2].

Choice of a regularization parameter and space

The Tikhonov method, even in its simplest form (7.2), raises two issues that should be clarified before use of this scheme. One of them is how to choose a regularization parameter λ. This problem has been extensively discussed. A few selected references from the literature are [19, 7, 11].

Another issue which needs to be addressed is the choice of a space $\mathscr{H}$. In the case of RKHS setting the issue is, in fact, about the choice of a kernel for an RKHS. At

the same time, as it has been mentioned by Micchelli, Pontil [13], even for the classical RKHS-setting, a challenging and central problem is the choice of the kernel K itself. Indeed, since in view of Wahba's classical representer theorem [10] the minimizer f_λ of (7.2) can be written in the form:

$$f_\lambda = f^\lambda_{K,\mathbf{z}}(\cdot) = \sum_{i=1}^{n} c_i^\lambda K(\cdot, x_i),\ c_i \in \mathbb{R}^1,\ i = 1,2,\ldots,n, \tag{7.3}$$

the choice of the kernel K is tied to the problem of choosing the basis for the approximation of the unknown function f. Clearly, this choice is problem-dependent and can make a significant difference in practice.

In our case, we will use a specifically designed kernel choice rule, the kernel adaptive regularization (KAR) algorithm [14], which is based on a split of a given data set $\mathbf{z}$, oriented towards extrapolation. The development of the KAR algorithm was motivated by the problem of the blood glucose prediction in a diabetes patient from available past and present blood glucose measurements. The algorithm was successfully tested in extensive clinical trials and showed superior performance with respect to the state-of-the-art methods based on autoregressive models and neural network models [15].

A posteriori regularization parameter choice

Suppose a kernel K is fixed, then an appropriate choice of the regularization parameter λ is important to get a good performance of f_λ. For example, one can use a data-driven method for choosing the regularization parameter called the quasi-balancing principle [6]. This heuristic principle can be seen as a combination of the balancing-principle [6] and the quasi-optimality criterion [19]. In [6] and [11] it has been shown that the balancing-principle and the quasi-optimality criterion may potentially give an accuracy of optimal order for a given kernel K.

To apply the quasi-balancing principle [6] one needs to calculate the approximations f_λ given by (7.3) for λ from a finite geometric sequence

$$\Lambda^\nu_q = \{\lambda_s = \lambda_0 q^s, s = 0,1,2,\ldots,\nu\},\ q > 1. \tag{7.4}$$

Then one needs to calculate the norms

$$\begin{aligned}\sigma^2_{emp}(s) &= ||f^{\lambda_s}_{K,\mathbf{z}} - f^{\lambda_{s-1}}_{K,\mathbf{z}}||^2_{\{x_i\}_{i=1}^{|\mathbf{z}|}} \qquad (7.5)\\ &:= \frac{1}{|\mathbf{z}|}\sum_{i=1}^{|\mathbf{z}|}\left(\sum_{j=1}^{|\mathbf{z}|}(c_j^{\lambda_s} - c_j^{\lambda_{s-1}})K(x_i,x_j)\right)^2,\\ \sigma^2_{\mathscr{H}_K}(s) &= ||f^{\lambda_s}_{K,\mathbf{z}} - f^{\lambda_{s-1}}_{K,\mathbf{z}}||^2_K, \qquad (7.6)\end{aligned}$$

$$(7.7)$$

and find

$$\begin{aligned}\lambda_{emp} &= \lambda_h,\ h = \operatorname{argmin}\{\sigma^2_{emp}(s), s = 1,2,\ldots,\nu\},\\ \lambda_{\mathscr{H}_K} &= \lambda_p,\ p = \operatorname{argmin}\{\sigma^2_{\mathscr{H}_K}(s), s = 1,2,\ldots,\nu\}.\end{aligned}$$

Finally, in accordance with the quasi-balancing principle a value of the regularization parameter $\lambda = \lambda_+ \in \Lambda^\nu_q$ is given as

$$\lambda_+ = \min\{\lambda_{emp}, \lambda_{\mathscr{H}_K}\}. \qquad (7.8)$$

As can be easily seen, the choice of the regularization parameter is fully governed by the kernel and input data.

Kernel adaptive regularization algorithm

The general idea of the algorithm is to select a kernel from a set of admissible kernels which allows for accurate extrapolation. It consists of four steps:

1. Split the given data set $\mathbf{z} = \{(x_i,y_i)\}_{i=1}^{|\mathbf{z}|}$ into two parts $\mathbf{z} = \mathbf{z}_T \cup \mathbf{z}_P$ without common data points
$$\overline{co\{x_i : (x_i,y_i) \in \mathbf{z}_T\}} \cap \{x_i : (x_i,y_i) \in \mathbf{z}_P\} = \emptyset,$$
where $\overline{co\{x_i\}}$ is the closed convex hull of data points $\{x_i\}$.

2. Then for the fixed $\mathbf{z}_T$ and the corresponding Tikhonov-type regularization functional
$$T_{K,\lambda,\mathbf{z}_T}(f) = \frac{1}{|\mathbf{z}_T|}\sum_{i:(x_i,y_i)\in\mathbf{z}_T}(y_i - f(x_i))^2 + \lambda\|f\|^2_K, \qquad (7.9)$$
one considers a rule $\lambda = \lambda(K)$ that for any kernel K on X selects a regularization parameter from some fixed interval $[\lambda_{\min}, \lambda_{\max}],\ \lambda_{\min} > 0$.

3. Using the set $\mathbf{z}_T$, one constructs the regularized approximant

$$f^{\lambda}_{K,\mathbf{z}_T} = \arg\min T_{K,\lambda,\mathbf{z}_T}(f), \quad \lambda = \lambda(K),$$

and measures its extrapolation performance on the set $\mathbf{z}_P$ by the value of the functional $P(f^{\lambda}_{K,\mathbf{z}_T}, \mathbf{z}_P)$, where

$$P(f, \mathbf{z}_P) = \frac{1}{|\mathbf{z}_P|} \sum_{i:(x_i,y_i)\in\mathbf{z}_P} \rho(f(x_i), y_i), \tag{7.10}$$

and $\rho(\cdot,\cdot)$ is a continuous non-negative function of two variables.

4. Finally, the kernel K is chosen as the minimizer of the following functional

$$Q_\mu(K, \lambda, \mathbf{z}) = \mu T_{K,\lambda,\mathbf{z}_T}(f^{\lambda}_{K,\mathbf{z}_T}) + (1-\mu)(P(f^{\lambda}_{K,\mathbf{z}_T}, \mathbf{z}_P)) \tag{7.11}$$

over the set of admissible kernels $\mathscr{K}$, for example,

$$\mathscr{K} = \{K(x,u) = (xu)^{\alpha} + \beta e^{-\gamma(x-u)^2}, \alpha, \beta, \gamma \in [10^{-4}, 3]\}. \tag{7.12}$$

Note that the parameter $\mu \in [0,1]$ in (7.11) can be seen as a performance regulator on the sets $\mathbf{z}_T$ and $\mathbf{z}_P$. Taking μ closer to zero we put more emphasize on the ability to extrapolate, while for $\mu > \frac{1}{2}$ we are more interested in interpolation.

It has been shown in [14] that the existence of a kernel of choice can be guaranteed for a rather general form of set $\mathscr{K}$.

Theorem 2. *Let $\mathscr{K}(X)$ be the set of all kernels defined on X, Ω be a compact metric space, and $G : \Omega \to \mathscr{K}(X)$ be a continuous map in the sense that for any $x, u \in X$ the function $w \mapsto K_w(x,u) \in \mathbb{R}$ is continuous on Ω, where for $w \in \Omega$ the kernel $K_w \in \mathscr{K}(X)$ is given as $K_w = G(w)$. Define*

$$\mathscr{K} = \mathscr{K}(\Omega, G) = \{K : K = G(w), K \in \mathscr{K}(X), w \in \Omega\}$$

to be the set of kernels parametrized via G by elements of Ω.
Then for any parameter choice rule $\lambda = \lambda(K)$ there are $K^0 \in \mathscr{K}(\Omega, G)$ and $\lambda^0 \in [\lambda_{\min}, \lambda_{\max}]$ such that

$$Q_\mu(K^0, \lambda^0, \mathbf{z}) \quad = \quad \inf\{Q_\mu(K, \lambda(K), \mathbf{z}), K \in \mathscr{K}(\Omega, G)\}.$$

The proof of the Theorem can be found in [14].

7.2.5 Estimation of dyssynchrony biomarkers from simulated VCGs

We explored the possibility to use the Theorem 2 in the context of predicting a biomarker measuring the delay between the mean regional activation times of the septum and LV lateral wall. To illustrate this, we used simulated data sets of eight patients. The data set of each patient consisted of VCGs produced by CRT simulations where the pacing protocol was varied over a range of V-V delays (-80 ms to 80 ms in 5 ms steps; 33 in total for each patient). Each profile contained a VCG signal with 200 time steps. The corresponding biomarker value for each simulation was computed.

The training set $\mathbf{z}$ was formed by the data sets of the best and worst CRT responders (BiV6 and BiV7): $\mathbf{z} = \{(x_i, y_i)\}_{i=1}^{66}, x_i \in \mathbb{R}^{200\times 3}, y_i \in \mathbb{R}$. The training set was used to choose a kernel as described above. For this purpose, we split $\mathbf{z}$ into two parts $\mathbf{z}_T$ and $\mathbf{z}_P$, namely $\mathbf{z}_P = \{(x_i, y_i)\}_{i=1}^{10}$ formed by five minimum and five maximum values of y_i; and $\mathbf{z}_T = \mathbf{z} \backslash \mathbf{z}_P$. The purpose behind such a split is to incorporate more data in the construction of the estimator $f^{\lambda}_{K,\mathbf{z}_T}(\cdot)$, thus $|\mathbf{z}_T| > |\mathbf{z}_P|$. At the same time, we test the ability of the estimator to extrapolate to extreme cases from observed data. Then the kernel

$$K^0(x,t) = (xt)^{0.05} + 1.001 \exp(-0.25\|x-t\|^2),$$

was chosen as approximate minimizer of the functional (7.11), where $\mu = 0.1$ and $\lambda = \lambda(K)$ is given by the quasi-balancing criterion (7.4)–(7.8) with $\lambda_0 = 1.01 \cdot 10^{-4}, q = 1.01$. Moreover, in (7.11) the functional $P(f, \mathbf{z}_P)$ is given as a quadratic loss function, i.e., $P(f, \mathbf{z}_P) = \frac{1}{|\mathbf{z}_P|} \sum_{i:(x_i,y_i)\in \mathbf{z}_P} (y_i - f(x_i))^2$.

The minimization was performed by a full search over the grid of parameters $\alpha_i = 10^{-4} i, \beta_j = 10^{-4} j, \gamma_l = 10^{-4} l, \quad i, j, l = 1, 2, \ldots, 3 \cdot 10^4$. Of course, the application of the full search method in finding the minimum of (7.11) is computationally intensive, but in the present context it can be performed off-line.

For the other six patients this kernel K^0 was used to construct regularized estimators (7.3) that, starting from simulated VCG signal $x \in \mathbb{R}^{200\times 3}$, return an estimated dyssynchrony metric value $y = f_{\lambda(K^0)}(x)$, where $\lambda(K^0)$ was chosen from (7.4) in accordance with the quasi-balancing principle (7.8) for the kernel K^0.

7.3 Results

7.3.1 Biomarkers of baseline dyssynchrony predict CRT response

Several biomarkers of electrical delay during LBBB showed high correlation with CRT outcomes (ΔESV_{LV}) measured after 6 months. Table (7.1) lists the top ten predictive biomarkers of CRT outcome with R^2 coefficients greater than 0.75. Of note is the total LV activation time defined as the delay between the earliest and latest activated parts of the LV as a fraction of the total QRS duration; Figure (7.2) illustrates the derivation of the marker from the nodal activation times of the patient-specific models optimized to the measured baseline VCG. The degree of total LV activation delay during baseline LBBB explains up to 96% of the variance of CRT outcomes (Figure (7.3)), highlighting the significance of this biomarker for indicating patient-specific pathophysiological substrates that are highly amenable by CRT from baseline clinical measurements only. Other predictive biomarkers include various measures of intra-ventricular and inter-ventricular delay between the LV lateral wall and septum (late LV-early ST duration, mean LVlat-ST AT difference), RV lateral wall and septum (ST-RV AT duration difference, ST-RV early AT delay), and LV and RV (LV-RV early AT delay, LV-RV AT duration difference, LV-RV early AT delay, LV lateral-RV AT duration difference, LV lateral-RV early AT delay). Overall, these results suggest that the severity of regional dyssynchrony is an important predictor for the likelihood of positive long-term CRT outcomes.

7.3.2 Biomarker of dyssynchrony during CRT suggests optimal pacing protocol

A biomarker measuring the delay between the mean activation time of the septum and LV lateral wall (mean LVlat-ST activation delay) exhibited a high correlation ($R^2 = 0.91$) with ΔESV_{LV} at baseline as well as with the change due to CRT ($R^2 = 0.92$); Figure (7.4) illustrates the derivation of the marker from the nodal activation times of the patient-specific models during simulated CRT, where the effective V-V delay (adjusted for pacing capture delays) was determined by matching to the measured QRS duration

of the ECG recorded during acute CRT. The degree of reduction of delay between the septum and LV lateral wall due to CRT explained up to 92% of the variance of CRT outcomes (Figure (7.5)).

Using the mean LVlat-ST activation delay as a biomarker of acute CRT efficacy, the variation of this marker was recomputed from CRT simulations over a range of V-V delays in each patient. Figure (7.6) shows the generated curves for each patient with the effective V-V delay during acute CRT denoted by circles. The minimal dyssynchrony in the range of tested V-V delays occurs at the zero-crossings (x intercept) of the curves, though not all occur at a V-V delay of 0 ms. The shift of the point of minimal dyssynchrony away from simultaneous pacing is due to patient-specific variations in ventricular geometry, relative V-lead position, and myocardial conductivity. In the case of BiV2, a considerable shift of minimal dyssynchrony toward a negative V-V delay of -25 ms (RV lead before LV lead) is possibly due to the presence of an infero-septal infarct near the RV lead. All curves feature a steep, approximately linear slope about the point of minimal dyssynchrony, with flattened slopes at extreme V-V delays. This suggests that minimal dyssynchrony between septal and LV lateral activation is achieved mechanistically by well-timed stimuli such that their resulting depolarization waves meet between the septum and LV lateral wall. Sub-optimally programmed V-V delays give rise to situations where the depolarization waves meet closer to either wall, thereby increasing the delay in mean activation time of the regions. In extreme cases (flat regions of the curve), the depolarization wave from the early lead reaches the location of the late lead before the latter stimulates, introducing possibly worse dyssynchrony than baseline and reducing the sensitivity of dyssynchrony to local changes in V-V delay.

7.3.3 Machine-learned estimates of dyssynchrony biomarkers

We tested the ability of the kernel-based regularization learning algorithm to predict the mean LVlat-ST activation delay for a given patient and V-V delay using only the corresponding simulated VCG signal during CRT. The optimal kernel was trained by the biomarker values and simulated VCGs from BiV6 and BiV7, and estimates of the biomarker at a given V-V delay were made in the remaining 6 patients using the corresponding VCG signal. Figure (7.7) compares the estimated and computed values

of mean LVlat-ST activation delay over the range of tested V-V delays. Table (7.2) shows the mean relative error

$$RE = \frac{1}{n}\sum_{d=1}^{n}\frac{\|y_d - y_d^{\dagger}\|}{\|y_d^{\dagger}\|},$$

where y_d and $y_d^{\dagger}$ are the model and estimated biomarker values, respectively, for a given V-V delay d, over all n V-V delays tested in each patient. Estimated values from the learning algorithm showed very good agreement with the original model-derived values over the range of tested V-V delays, particularly at the V-V delay of minimal dyssynchrony, despite inter-patient variability in ventricular geometry, lead placement, and myocardial conductivity. This result demonstrates the possibility of machine learning algorithms to extract important physiological detail from relatively simple signals, given appropriate model assumptions and training data sample size.

7.4 Discussion

In this study, we used patient-specific computational models to predict electrical characteristics during LBBB and CRT that are predictive of long-term CRT outcomes. The combination of computational models with machine learning techniques is a powerful technique to derived detailed model-derived details of physiology from observed clinical measurements. The models can provide "ground truth" information to explain the variations in measured clinical data. This is a relatively new field given the complexity of computational physiological models. A recent example of combining model simulations with machine learning was by Prakosa et al. to estimate electrical activation times from cardiac image sequences using a simulated database of model-derived motion descriptors [17]. The results shown here demonstrate the possibility of using standard, routine clinical ECG measurements to provide clinicians with important physiological details for making clinical decisions. In addition to the dyssynchrony metrics, the estimated activation patterns reveal the earliest and latest activation sites in the ventricles which may guide optimal anatomical positioning of the LV and RV V-leads during CRT device implantation. The influence of lead position is an area of intense study. In this study, lead position was not varied to determine how much more the mod-

els could have improved. This could be an area of further study, as the lead position and V-V delays will undoubtedly affect the resulting electrical activation and mechanical contraction sequence.

Clinical investigations support the idea that more precise characterization of LV electrical dyssynchrony are associated with better CRT outcomes. Gold et al. demonstrated that the severity of electrical delay as measured by QLV strongly predicts reverse remodeling after 6 months of CRT [9]. A study by Lin et al. confirmed the predictive value of QLV, adding that the timing between the RV and LV lead positions be accounted for [12]. Similarly, Singh et al. [18] also demonstrated invasively that baseline LV activation delay correlates with reverse remodeling. Optimal CRT parameters are typically determined at time of implant by adjusting durations of the A-V and V-V delay to maximize ejection fraction. Van Deursen et al. [20] used vectorcardiography (VCG) to adjust the delay parameters, demonstrating that optimal acute hemodynamic improvement is obtained by adjusting the VV delay such that the mean amplitude of LV-only and RV-only pacing extremes is achieved. Optimal lead placement has been also been found to coincide with the latest activated parts of the LV wall [12, 9].

7.5 Conclusion

We have demonstrated that patient-specific models of LBBB and CRT electrophysiology can provide useful indices of electrical dyssynchrony and resynchrony that are predictive of CRT outcomes. A kernel-based regularization learning algorithm was employed to explore the possibility of estimating resynchrony metrics from simulated VCGs alone. This is a proof of concept that it may be possible to estimate baseline dyssynchrony, defined as total LV activation time, from standard clinical ECG measurements alone by training the learning algorithm with a comprehensive database of simulated VCGs of LBBB activation. If validated, this could potentially become a powerful tool for low-cost, non-invasive assessment of patient-specific CRT candidacy and prediction for likelihood for CRT response.

Acknowledgments

The majority of the content of this chapter comprises an original document. The author is especially grateful to Valeriya Naumova for authoring the Methods section "Kernel-based regularization learning algorithm" in this chapter, developing the original mathematical theory, performing the analysis, and producing the prediction results. Model simulation data was provided by the author as inputs to the algorithm. The author gives thanks to Andrew McCulloch and David Krummen for discussions on clinical data and model considerations.

Table 7.1: Table of selected dyssynchrony biomarkers.

	Metric Title	Description	State	Equation	R^2
1	Total LV AT duration (% QRS)	The total activation duration in the whole LV	Baseline	$\frac{AT_{LV\_max} - AT_{LV\_min}}{QRS_{LBBB}}$	0.93
2	Late LV-early ST duration (%QRS)	The total activation duration between the earliest activation time in the septum and the latest activation in the whole LV. This is similar to metric (1).	Baseline	$\frac{AT_{LV\_max} - AT_{ST\_min}}{QRS_{LBBB}}$	0.93
3	Mean LVlat-ST AT difference	The delay between the mean activation times in the septum and LV lateral wall	Baseline/CRT change	$\frac{AT_{LVlat\_mean} - AT_{ST\_mean}}{QRS_{LBBB}}$	0.91/0.92
4	ST-RV AT duration difference	The difference in total activation time between ST and RV regions.	Baseline	$\frac{(AT_{ST\_max} - AT_{ST\_min})}{AT_{ST\_max}} - \frac{(AT_{RV\_max} - AT_{RV\_min})}{AT_{RV\_max}}$	0.87
5	ST-RV early AT delay (%QRS)	The delay between the earliest activation times in the septum and RV	Baseline	$\frac{AT_{ST\_min} - AT_{RV\_min}}{QRS_{LBBB}}$	0.86
6	LV-RV electrical early AT delay (%QRS)	The delay between the earliest activation times in the whole LV and RV.	Baseline	$\frac{AT_{LV\_min} - AT_{RV\_min}}{QRS_{LBBB}}$	0.85
7	LV-RV AT duration difference	The difference in total activation time between LV and RV regions.	Baseline	$\frac{(AT_{LVlat\_max} - AT_{LVlat\_min})}{AT_{LVlat\_max}} - \frac{(AT_{RV\_max} - AT_{RV\_min})}{AT_{RV\_max}}$	0.85
8	LV-RV early AT delay (%QRS)	The delay between the earliest activation times in the LV and RV.	Baseline	$\frac{AT_{LV\_min} - AT_{RV\_min}}{QRS_{LBBB}}$	0.85
9	LV lateral-RV AT duration difference (%max ATs)	The difference in total activation time between LV lateral and RV regions.	Baseline	$\frac{(AT_{LVlat\_max} - AT_{LVlat\_min})}{AT_{LVlat\_max}} - \frac{(AT_{ST\_max} - AT_{ST\_min})}{AT_{ST\_max}}$	0.78
10	LV lateral-RV electrical early AT delay (%QRS)	The delay between the earliest activation times in the LV lateral wall and RV.	Baseline	$\frac{AT_{LVlat\_min} - AT_{RV\_min}}{QRS_{LBBB}}$	0.76

Table 7.2: Relative errors of biomarker estimates from simulated VCGs during CRT.

Patient	BiV1	BiV2	BiV3	BiV4	BiV5	BiV8
Error	0.086	0.183	0.011	0.167	0.129	0.050

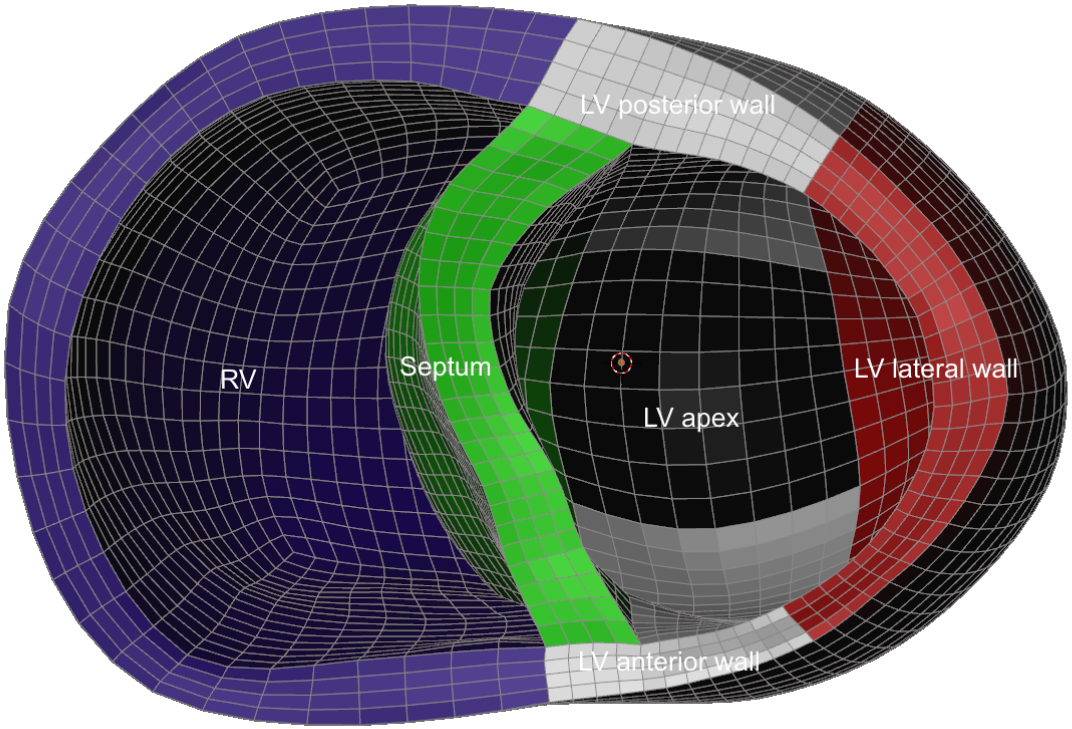

Figure 7.1: Ventricular regions for dyssynchrony biomarker derivations. Electrical activation times at the mesh nodes were used to compute biomarkers measuring the activation delay within and between ventricular regions. The biventricular mesh for BiV1 is shown here.

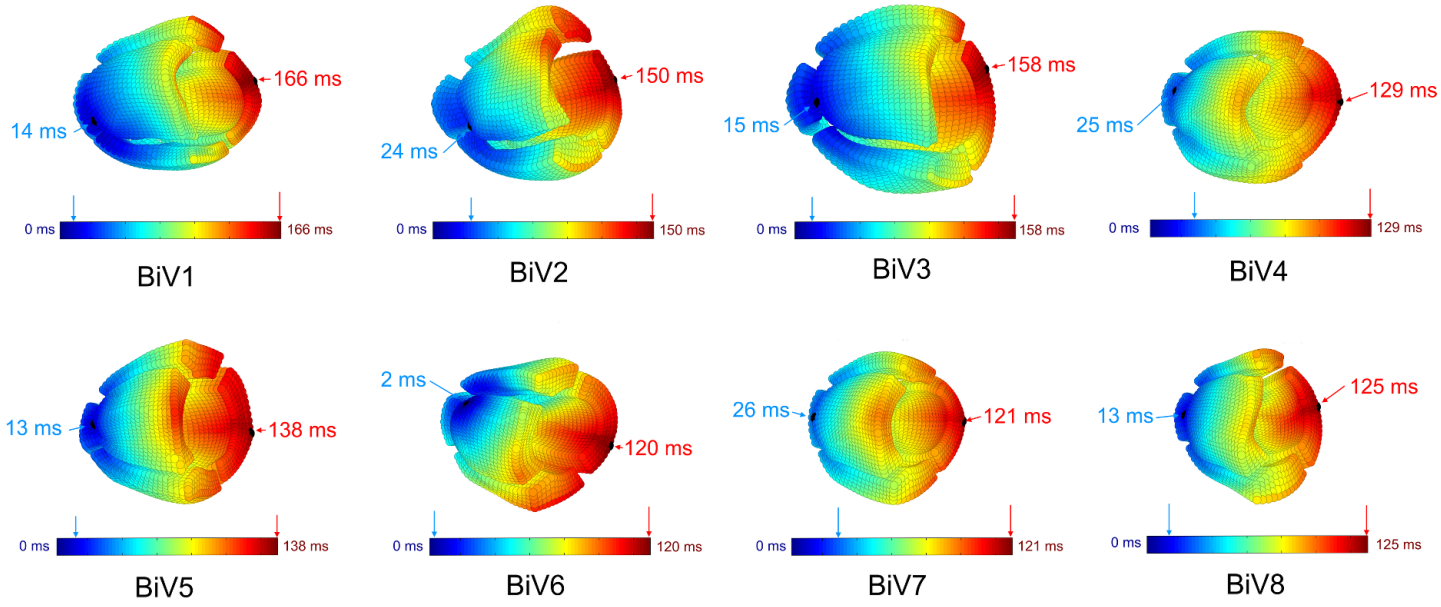

Figure 7.2: Derivation of total LV activation time dyssynchrony biomarker. The delay between the earliest activation time in the septum and latest activation time in the LV lateral wall define the extent of whole LV activation dyssynchrony.

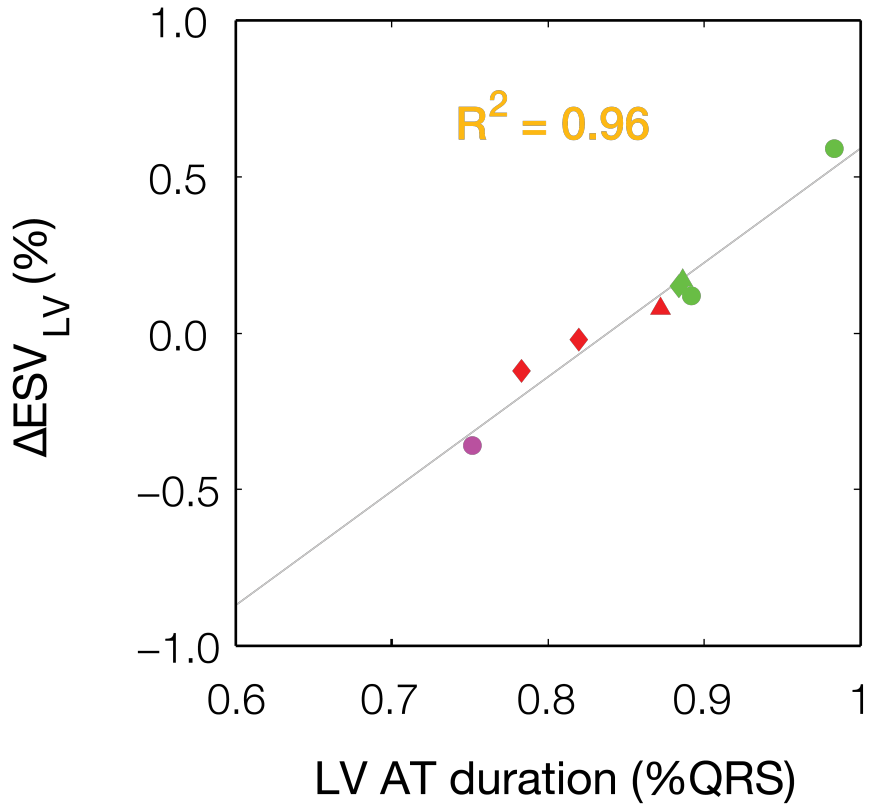

Figure 7.3: LV activation time biomarker correlates with CRT outcomes measured as the degree of LV reverse remodeling ΔESV_{LV} after 6 months of CRT.

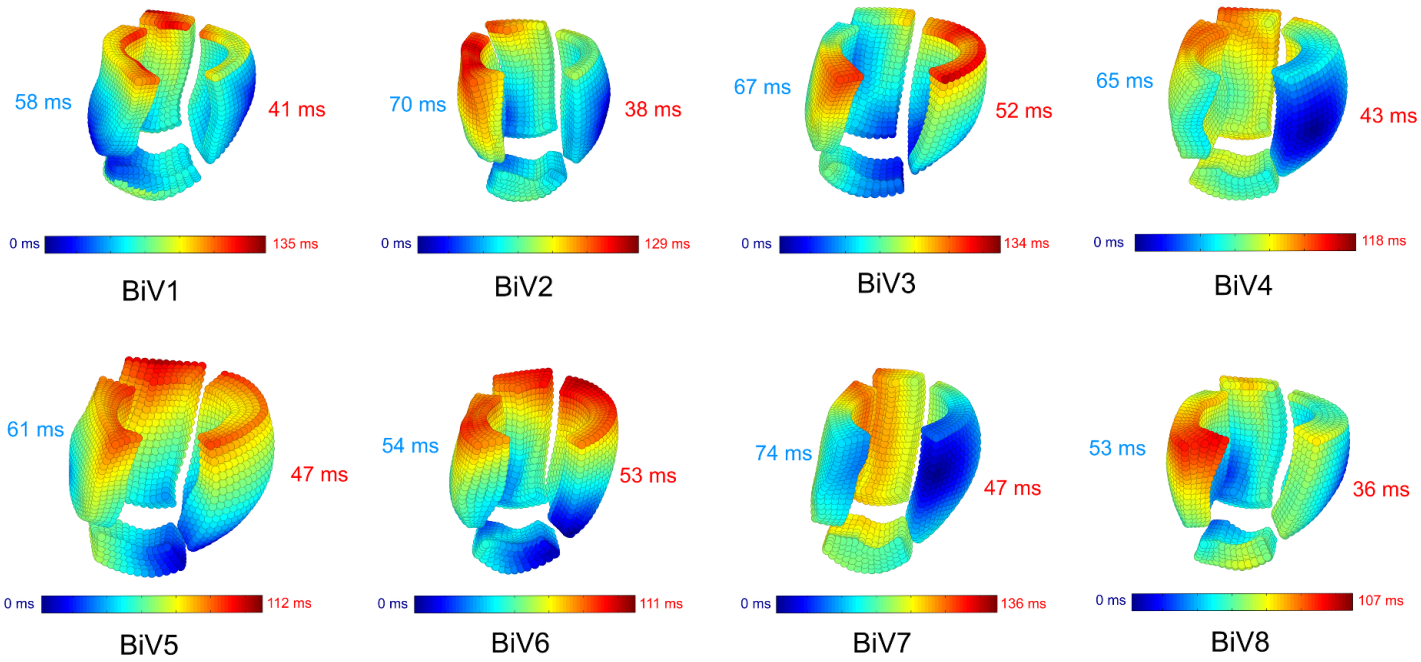

Figure 7.4: Derivation of mean LVlat-ST activation dyssynchrony biomarker. The mean activation time in the septum and latest activation time in the LV lateral wall estimates the extent of LV electrical resynchronization achieved while pacing at a particular VV delay during CRT.

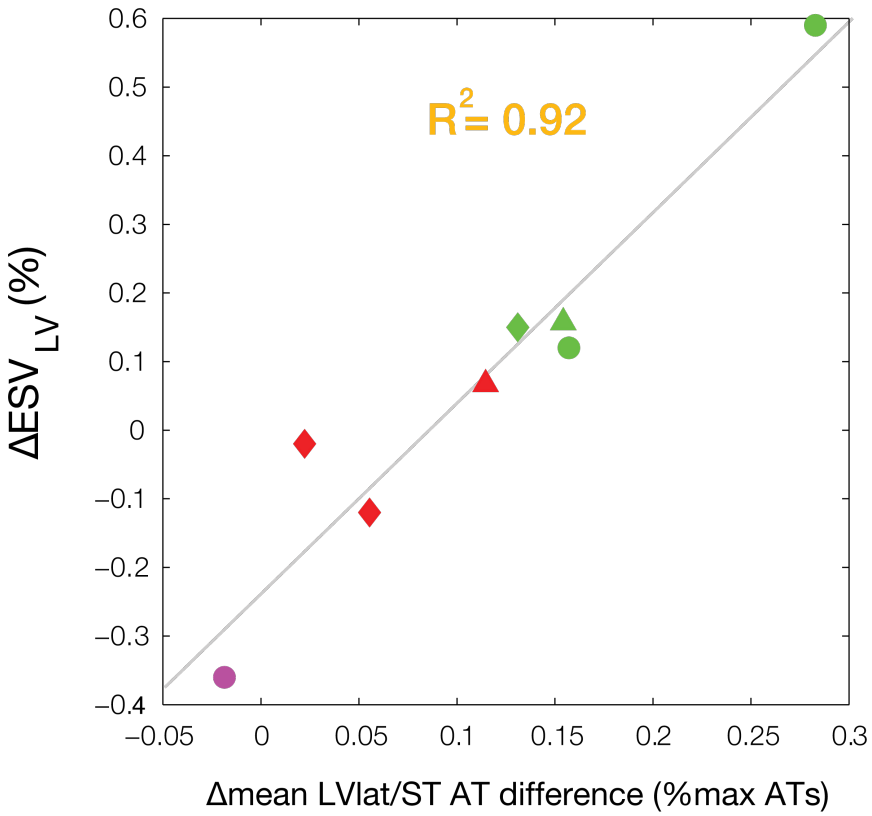

Figure 7.5: The change in mean LVlat-ST activation biomarker correlates with CRT outcomes. The difference between the mean activation times in the septum and LV lateral wall during CRT is a strong predictor of the degree of LV reverse remodeling after 6 months of CRT.

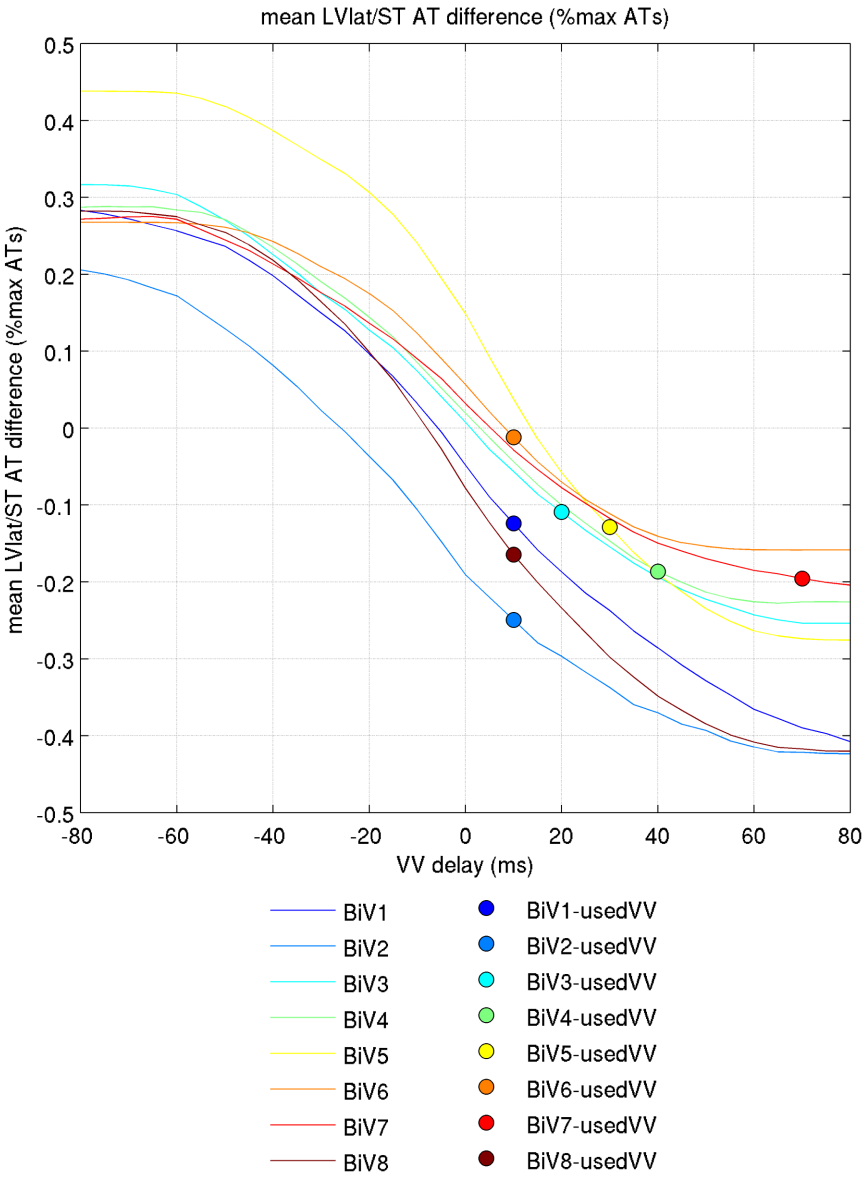

Figure 7.6: Variation of mean LVlat-ST delay over VV delay. The circles denote the effective VV delay (adjusted to measured QRS) programmed at time of implant. Optimal VV delays for maximal resynchronization should minimize the mean LVlat-ST delay to zero. Note that in some patients (BiV1, BiV2, BiV8) minimal mean LVlat-ST is achieved at negative VV delays where the RV lead is stimulated before the LV lead. The presence of an postero-septal infarct near the RV pacing site in BiV2 may explain the need to use a considerably negative VV delay.

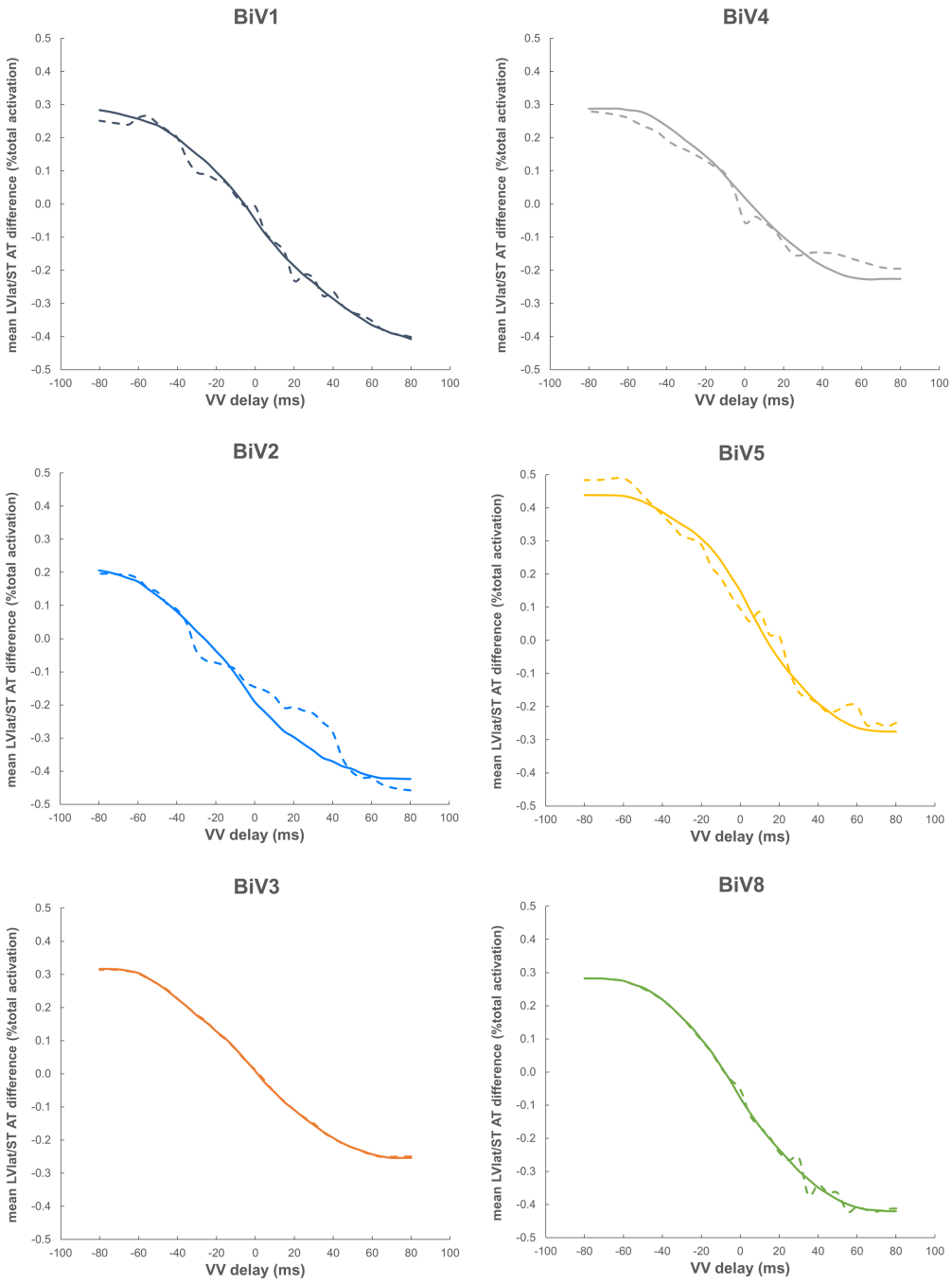

Figure 7.7: Estimated mean LVlat-ST biomarker values over VV delay by the learning algorithm. Mean relative errors over the curve are listed in Table (7.2). The learning algorithm was trained to relate the simulated VCGs to mean LVlat-ST over a range of VV delays using data from BiV6 and BiV7. The trained learning algorithm estimated the value of the biomarker using only the simulated VCGs correponding to each VV delay in the remaining six patients.

Bibliography

1. Abraham, W. T., Hayes, D. L., 2003. Cardiac resynchronization therapy for heart failure. Circulation 108 (21), 2596–2603.

2. Aronszajn, N., 1950. Theory of reproducing kernels. Trans. Amer. Math. Soc. 68, 337–404.

3. Cleland, J. G., Abraham, W. T., Linde, C., Gold, M. R., Young, J. B., Daubert, J. C., Sherfesee, L., Wells, G. A., Tang, A. S., 2013. An individual patient meta-analysis of five randomized trials assessing the effects of cardiac resynchronization therapy on morbidity and mortality in patients with symptomatic heart failure. European heart journal 34 (46), 3547–3556.

4. Cleland, J. G., Daubert, J.-C., Erdmann, E., Freemantle, N., Gras, D., Kappenberger, L., Tavazzi, L., 2005. The effect of cardiac resynchronization on morbidity and mortality in heart failure. New England Journal of Medicine 352 (15), 1539–1549.

5. Daubert, J.-C., Saxon, L., Adamson, P. B., Auricchio, A., Berger, R. D., Beshai, J. F., Breithard, O., Brignole, M., Cleland, J., DeLurgio, D. B., 2012. 2012 ehra/hrs expert consensus statement on cardiac resynchronization therapy in heart failure: implant and follow-up recommendations and management a registered branch of the european society of cardiology (esc), and the heart rhythm society; and in collaboration with the heart failure society of america (hfsa), the american society of echocardiography (ase), the american heart association (aha), the european association of echocardiography (eae) of the esc and the heart failure association of the esc (hfa). endorsed by the governing bodies of aha, ase, eae, hfsa, hfa, ehra, and hrs. Europace 14 (9), 1236–1286.

6. De Vito, E., Pereverzyev, S. V., Rosasco, L., 2010. Adaptive kernel methods using the balancing principle. Found. Comput. Math. 10 (4), 455–479.

7. De Vito, E., Rosasco, L., Caponnetto, A., Giovannini, U. D., Odone, F., 2005. Learning from examples as an inverse problem. J. Mach. Learn. Res. 6, 883–904.

8. Engl, H., Hanke, M., Neubauer, A., 1996. Regularization of Inverse Problems. Vol. 375 of Mathematics and Its Applications. Kluwer Academic Publishers, Dordrecht, Boston, London.

9. Gold, M. R., Birgersdotter-Green, U., Singh, J. P., Ellenbogen, K. A., Yu, Y., Meyer, T. E., Seth, M., Tchou, P. J., 2011. The relationship between ventricular electrical delay and left ventricular remodelling with cardiac resynchronization therapy. European heart journal 32 (20), 2516–2524.

10. Kimeldorf, G., Wahba, G., 1971. Some results on Tchebycheffian spline functions. J. Mathematical Analysis and Applications 33, 82–95.

11. Kindermann, S., Neubauer, A., 2008. On the convergence of the quasi-optimality criterion for (iterated) Tikhonov regularization. Inverse Problems and Imaging 2 (2), 291–299.

12. Lin, T., Crosby, P., Sugumar, H., Spencer, R., Flannery, M. D., O'Donnell, D., 2014. Implant electrical characteristics predict response to cardiac resynchronization therapy. World Journal of Cardiovascular Diseases 2014.

13. Micchelli, C. A., Pontil, M., 2005. Learning the kernel function via regularization. J. Mach. Learn. Res. 6, 1099–1125.

14. Naumova, V., Pereverzyev, S. V., Sivananthan, S., 2011. Extrapolation in variable RKHSs with application to the blood glucose reading. Inverse Problems 27 (7), 1–13.

15. Naumova, V., Pereverzyev, S. V., Sivananthan, S., 2012. A meta-learning approach to the regularized learning – case study: Blood glucose prediction. Neural Networks 33, 181–193.

16. Parreira, L., Santos, J., Madeira, J., Mendes, L., Seixo, F., Caetano, F., Lopes, C., Venancio, J., Mateus, A., Ines, J., 2005. Cardiac resynchronization therapy with sequential biventricular pacing: impact of echocardiography guided vv delay optimization on acute results. Revista portuguesa de cardiologia: orgao oficial da Sociedade Portuguesa de Cardiologia Portuguese journal of cardiology: an official journal of the Portuguese Society of Cardiology 24 (11), 1355–1365.

17. Prakosa, A., Sermesant, M., Allain, P., Villain, N., Rinaldi, C. A., Rhode, K., Razavi, R., Delingette, H., Ayache, N., 2014. Cardiac electrophysiological activation pattern estimation from images using a patient-specific database of synthetic image sequences. Biomedical Engineering, IEEE Transactions on 61 (2), 235–245.

18. Singh, J. P., Fan, D., Heist, E. K., Alabiad, C. R., Taub, C., Reddy, V., Mansour, M., Picard, M. H., Ruskin, J. N., Mela, T., 2006. Left ventricular lead electrical delay predicts response to cardiac resynchronization therapy. Heart Rhythm 3 (11), 1285–1292.

19. Tikhonov, A. N., Glasko, V. B., 1965. Use of the regularization methods in nonlinear problems. Vol. 5. USSR Comput. Math. Phys.

20. van Deursen, C. J., Strik, M., Rademakers, L. M., van Hunnik, A., Kuiper, M., Wecke, L., Crijns, H. J., Vernooy, K., Prinzen, F. W., 2012. Vectorcardiography as a tool for easy optimization of cardiac resynchronization therapy in canine left bundle branch block hearts. Circulation: Arrhythmia and Electrophysiology 5 (3), 544–552.

21. Villongco, C. T., Krummen, D. E., Stark, P., Omens, J. H., McCulloch, A. D., 2014. Patient-specific modeling of ventricular activation pattern using surface ecg-derived vectorcardiogram in bundle branch block. Progress in biophysics and molecular biology 115 (2), 305–313.

Chapter 8

Conclusion to the Dissertation

We have successfully demonstrated the novel use of patient-specific computational models of dyssynchronous heart failure (DHF) and cardiac resynchronization therapy (CRT) to gain new understanding of physiological mechanisms and predictors of LV reverse remodeling in order to support clinical decisions regarding CRT candidacy and personalization of therapy.

We first developed a process for constructing computational models of DHF from clinical data. Biventricular anatomy was modeled using high-order finite element methods to capture dilated geometry and myocardial infarction from CT, MR, and SPECT images (Chapter 2). The ventricular fiber architecture was estimated by mapping an atlas fiber model fitted to DT-MR measurements of a human organ donor heart to the patient-specific geometric models (Chapter 3). Within the biventricular geometric domain, a model of human ventricular myocyte action potential electrogenesis and propagation was described, and the numerical convergence of activation time solutions was validated to be on the order of certainty of gold–standard clinical electroanatomic measurements (Chapter 4). Finally, we estimated patient-specific, 3D electrical activation patterns due to LBBB by a novel method using ECG-derived VCG signals to localize an ectopic RV stimulus site and tune regional myocardial conductivities (Chapter 5). The estimated electrical activation patterns defined the local onset of LV systolic contraction and global ejection fraction using patient-specific models of biomechanics and hemodynamics developed with Adarsh Krishnamurthy.

The complete electromechanics models were used to test hypotheses for physi-

ological mechanisms and predictors of long-term CRT outcomes. We showed that the baseline and change in fraction of LV and septal myocardium performing net negative cardiac cycle work correlated with the degree of LV reverse remodeling (Chapter 6). This results suggests that the regional work could be an important tissue-level stimulus for cell-level reverse remodeling processes. Furthermore, myocardial work was found to be most sensitive to patient-specific hemodynamics, geometry, and electrical activation pattern due to LBBB and CRT. Finally, using biomarkers derived from reduced patient-specific models of electrophysiology only, we showed that the baseline and change in LV dyssynchrony also correlated with the degree of LV reverse remodeling (Chapter 7). This result suggests new criteria for recommending DHF patients for CRT and personalizing CRT pacing parameters to achieve maximal therapeutic benefit. Moreover, we provided initial proof of the concept that a kernel-based regularization learning algorithm can estimate LV dyssynchrony directly from VCG signals.

Future work can address several issues with model construction from clinical data. Further development and validation of models constructed from minimal clinical data are important for striking a balance between cost and accuracy. For example, sufficiently accurate geometries may be constructed from 2D or 3D echocardiography images rather than full 3D MR and CT scans. Mesh generation throughput can also improve from automated, image-based deformable registration of geometric atlases. We expect that the influence of patient-specific fiber architecture is minimal for computing work distributions and electrical activation patterns. Therefore, a fiber atlas from DT-MR data of excised hearts may be sufficient to estimate patient fiber architectures without *in vivo* DT-MR data. The parameterization of patient-specific electrophysiology models was a computationally expensive procedure that involved hundreds of depolarization simulations for each patient. However, machine learning techniques could train on simulation databases to estimate conductivity and ectopic activation sites from ECG signals.

The hypothesis that regional myocardial work drives cellular mechanisms leading to reverse remodeling can be further tested by coupling the current model to known mechano-energetic processes of cellular growth and remodeling. The validity of model-derived biomarkers for making baseline predictions of LV reverse remodeling should be

tested in a large, blinded patient study. Similarly, a biventricular pacing study should validate the relation between VCG morphology and V-V delay, lead position, and LV electrical activation. Finally, by incorporating and abstracting the information contained in large simulation databases of deterministic, biophysically detailed models, machine learning algorithms could possibly make predictions of long-term outcomes and suggestions for therapy planning and application from routine clinical measurements alone, given appropriate assumptions and use cases. The results of Chapter 7 should be validated in a large patient cohort using VCGs derived from measured standard 12-lead or reduced-lead ECGs .

As shown by the work in this dissertation, computational modeling holds great promise as a viable and important clinical tool to help cardiologists and other health care providers deliver the best personalized treatment for the individual heart failure patient.